



Provided by the author(s) and University of Galway in accordance with publisher policies. Please cite the published version when available.

Title	A computational and experimental investigation of the dissection of arterial tissue
Author(s)	FitzGibbon, Brian
Publication Date	2020-11-19
Publisher	NUI Galway
Item record	http://hdl.handle.net/10379/16309

Downloaded 2024-04-26T21:28:12Z

Some rights reserved. For more information, please see the item record link above.



A COMPUTATIONAL AND EXPERIMENTAL INVESTIGATION OF THE DISSECTION OF ARTERIAL TISSUE

Brian FitzGibbon, B.E.



NUI Galway
OÉ Gaillimh

A thesis submitted to the National University of Ireland as
fulfilment of the requirements for the Degree of Doctor of
Philosophy

July 2020

Discipline of Biomedical Engineering,
College of Engineering and Informatics,
National University of Ireland Galway

Supervisors of Research:

Dr. J. Patrick McGarry

ABSTRACT

The overall objective of this thesis is to provide a new understanding of the mechanisms underlying arterial fracture, and to extend this understanding to the initiation and propagation of aortic dissection using a combination of experimental testing and computational modelling.

Aortic dissection is a lethal disease that involves the separation of the arterial layers and carries mortality rates as high as 1-2% per hour untreated. However, to date the exact pathophysiological processes and related biomechanisms underlying aortic dissection have not been uncovered. We present the development and implementation of a novel experimental technique to generate and characterise mode II crack initiation and propagation in arterial tissue. We begin with a demonstration that lap-shear testing of arterial tissue results in mixed mode fracture, rather than mode II. A detailed computational design of a novel experimental method (shear fracture ring test (SFRT)) to robustly and repeatably generate mode II crack initiation and propagation in arteries is presented. This method is based on generating a localised region of high shear adjacent to a cylindrical loading bar. Placement of a radial notch in this region of high shear stress is predicted to result in a kinking of the crack during a mode II initiation and propagation of the crack over a long distance in the circumferential (c)-direction along the circumferential-axial (c - a) plane. Fabrication and experimental implementation of the SFRT on excised ovine aorta specimens confirms that the novel test method results in pure mode II initiation and propagation. We demonstrate that the mode II fracture strength along the c - a plane is eight times higher than the corresponding mode I strength determined from a standard peel test. We also calibrate the mode II fracture energy based on our measurement of crack propagation rates. The mechanisms of fracture uncovered, along with the quantification of mode II fracture properties have significant implications for current understanding of the biomechanical conditions underlying aortic dissection.

We observe that a standard exponential-CZM (E-CZM) is unable to capture the key trends associated with a collagenous interface undergoing fibrillation, namely, the non-linear crack growth observed during SFRT experiments. We propose an elastic fibrillation CZM (EF-CZM) and explore its conformability to the experimental data. An incremental improvement is obtained relative to the E-CZM; however, crack growth slows prematurely. It is found that the final regime of crack growth is insensitive to the model parameters. The EF-CZM fails to capture the key mechanisms underlying the fibrillation fracture process. It is hypothesised that the dissipative process of fibre pull-out may be an important consideration in phenomenologically capturing the experimental trends. Furthermore, we theorize that crack growth velocity and fibrillation may be related, and thus, a rate dependence may be necessary to phenomenologically capture the physics of the fibrillation process. Therefore, a viscoplastic CZM is developed, where the rate of strain hardening is dependent on the applied strain rate. We present a full exploration of the viscoplastic CZM and demonstrate a thermodynamic consideration of the CZM which demonstrates positive

instantaneous incremental dissipation of the elastic and plastic components of the CZM throughout all loading scenarios considered in the present study. Finally we explore the conformability of viscoplastic CZM to the fracture experiments of FitzGibbon and McGarry (2020) and demonstrate that the introduction of a rate-dependent plasticity captures the key trends observed experimentally, namely, the slow crack growth regime proceeded by fast crack growth and again by slow crack growth.

A realistic subject-specific aorta finite element model derived from a dual-ventricle MRI scan is developed. We investigate if spontaneous dissection will occur under extreme hypertensive lumen blood pressure loading, or if significant reduction in interface strength must occur in order for dissection to initiate. Importantly, it is also demonstrated that dissection initiation is a pure mode II fracture process, rather than a mixed mode or mode I process. We construct a parameterised idealised aorta model in order to assess the relative contribution for several anatomical and physiological factors to dissection risk. Such parametric analyses provide fundamental insight into the mechanics of stress localisation and delamination in the aorta. Overall, the detailed series of simulations suggest that variations in anatomical features and hypertensive loading will not result in a sufficient elevation of the stress state in the aorta wall to initiate dissection. Our results suggest that initiation of aortic dissection requires a significant reduction in the mode II fracture strength of the aortic wall, suggesting that dissection is preceded by structural and biomechanical remodelling.

Finally, we examine the risk of dissection in an artery with a range of pre-existing injuries. The risk of dissection is examined in an artery with an intimal tear (radial notch). Finite element cohesive zone analyses suggest propagation of an intimal tear is not predicted for pressures less than $P=275$ mmHg in a healthy aorta. The risk of dissection is then examined in an artery with a pre-existing intraluminal septum and a patent false lumen. Computational fluid dynamics (CFD) analyses are performed, and pressure data is extracted and applied to a solid fracture model. The results of the combined fluid dynamics and finite element cohesive zone analyses suggest extensive propagation of a false lumen is not predicted at a slightly hypertensive systolic pressure of 140 mmHg in a healthy aorta. Even in extreme hypertensive loading conditions AD propagation is arrested due to blunting of the crack tip and an increase in the mode angle towards mode II. The results of this study suggest an intimal tear will not develop into a false lumen in a healthy normotensive aorta

Acknowledgements

First and foremost, I would like to express my sincerest thanks and gratitude to my supervisor Dr. Patrick McGarry, for his unrelenting scientific curiosity, support, and direction throughout my studies. Without his encouragement, guidance, and generously given time, I could not have completed this PhD.

I would also like to thank Prof. Peter McHugh for his guidance, and time as I began and progressed in my research. His enthusiasm for computational methods is infectious and will remain with me.

To my clinical supervisors Prof. Sherif Sultan and Ms. Niamh Hynes, thank you for your endless enthusiasm for engineering research and your focus on clinical relevance and patientcare, which has shaped the way I think about research.

Thank you to the rest of the members of the McGarry group, to whom I owe my sanity. To Jamie and Sarah, thanks for many unforgettable memories and always being up for a *bitte* craic. To Lizanne, high council of the third floor, thank you for answering a million questions and always being up for a chat. To Eoin, Brían, honorary row-member Ciara, Ryan, Catherine, Juan, and Behrooz thanks for all the craic and memories of playing dice, cheating in fake blackjack, and partaking of Ryan's homemade mead. I am honoured to have worked alongside each one of you. Thank you to Donnacha for showing me the ropes of python and being so generous with your time. To all the rest of the PhD's on the third floor, thanks for all the conference memories, baked goods, and lunchtime talks, getting to work alongside all of you has been a pleasure. Thank you to Kevin for many masterclasses in Matlab wizardry. Thank you to Behrooz for many discussions about local orientations and UMATs and more proof-reads than I can count. Thanks to Dave and all of the technical staff, and a big thanks to William, whose good humour and enthusiasm for a good quiz or a piece of cake was always refreshing.

I would like to thank my funding sources; the Irish Research Council and the Western Vascular Institute along with the Irish Centre for High-End Computing (ICHEC) for the provision of essential computational facilities and technical support.

To my family, Mum and Dad, thank you for encouraging me throughout this entire process. You have been in my corner since day one with ceaseless support, encouragement, and prayer, for which I am beyond grateful. To my sister Caoimhe, thank you for always believing in me and supplying me with curated memes. To my sisters Aisling and Fiona, thank you for always being a supportive and loving force throughout my studies. To Villy, thanks for many games of poker and age of empires. To my "in-laws", Jim, Debbie, Christian, Kaitlin, Chelsea, and RJ, thank you so much for all the support, encouragement, and much-needed sunshine breaks.

To my dear wife Jordyn, your amazing support, patience, and love through the PhD has kept me going through the hardest times and inspired me during the best times. None of this would be possible without your unconditional love and support. Coming home to you and Polly was the highlight of every day, I love you. Finally, I am grateful to God, for His unconditional love, His grace for a distracted mind, and for His son Jesus, who has walked beside me all this way.

PUBLICATIONS & CONFERENCE PROCEEDINGS

List of Publications

Chapter 5: Under review in “*Acta Biomaterialia*”

Pre-print: FitzGibbon, B., McGarry, P., 2020. “Development of a novel test method to investigate mode II fracture and dissection of arteries”. DOI: 10.31224/osf.io/d3jbr

Chapter 6: Submitted to “*Engineering Fracture Mechanics*”

Chapter 7: Submitted to “*International Journal for Numerical Methods in Biomedical Engineering*”

Chapter 8: Under preparation for publication

Other Journal Publications

Fitzgibbon B, Jordan F, Hynes N, et al. “Endovascular versus open surgical repair for complicated chronic type B aortic dissection”. *Cochrane Database Syst Rev.* 2018;2018(4):CD012992. Published 2018 Apr 19. doi:10.1002/14651858.CD012992

Sultan, S., Kavanagh, E.P., Veerasingam, D., Costache, V., Elhelali, A., Fitzgibbon, B., Diethrich, E. and Hynes, N., 2019. Kinetic Elephant Trunk Technique: Early Results in Chronic Symptomatic Aortic Dissection Management. *Annals of vascular surgery*, 57, pp.244-252.

International Conference Proceedings

“Initiation of dissection in the aortic arch”, Summer Biomechanics, Bioengineering and Biotransport Conference 2019 (SB3C), Pittsburgh, PA, USA. 27th June 2019. *Podium presentation.*

“Biomechanics of an aortic dissection in a residually stressed aorta.”, 8th World Congress of Biomechanics (WCB2018), Dublin, July 8-12, 2018 *Podium presentation.*

“Biomechanical factors influencing aortic intra-mural dissection.”, 10th European Solid Mechanics Conference (ESMC2018), Bologna, July 2-6, 2018 *Podium presentation.*

Aortic Masterclass, Galway Clinic. 06th September 2018 **Podium Presentation (x2)**

“Modelling the dissection of arterial tissue”, Summer Biomechanics, Bioengineering, and Biotransport Conference 2017 (SB3C), Tucson, AZ, USA, June 21 – 24, 2017 *Podium presentation*

DECLARATION OF ORIGINALITY

I declare that the work presented in this thesis is my own.

Brian FitzGibbon

TABLE OF CONTENTS

1	INTRODUCTION	1
1.1	A brief history of aortic dissection	1
1.2	Thesis Objectives	2
1.3	Thesis Structure	3
	Bibliography.....	6
2	BACKGROUND AND LITERATURE	8
2.1	Anatomy of the Aorta.....	8
2.1.1	Arterial Tissue.....	8
2.1.2	Elastin in the Aorta.....	11
2.1.3	Collagen in the Aorta	12
2.2	Clinical Overview.....	14
2.2.1	What is Aortic Dissection?.....	14
2.3	Mechanical Behaviour of Aortic Tissue.....	19
2.3.1	Anisotropic material behaviour.....	19
2.3.2	Radial Failure properties	21
2.3.3	Shear Failure Properties and mechanisms.....	24
2.3.4	Residual Stress	28
2.4	Computational Modelling.....	29
2.5	Cohesive Zone Models	36
2.5.1	Potential Based.....	37
2.5.2	Non-potential based	38
	Bibliography.....	40
3	ESTABLISHED THEORY	53
3.1	Continuum Mechanics.....	53
3.1.1	Deformation and Motion.....	53
3.1.2	Strain tensors and strain rate measures	56
3.1.3	Strain invariants	57
3.1.4	Stress measures	58
3.1.5	Hyperelastic Materials	60
3.2	Finite Element Method (FEM)	62
3.2.1	Implicit solution scheme	62
3.2.2	Implementation of user-defined material subroutines.....	66
3.2.3	Implementation of user-defined surface interaction subroutines	66
	Bibliography.....	68

4	PRELIMINARY COHESIVE ZONE MODEL DEVELOPMENT AND ANALYSIS	69
4.1	Introduction	69
4.2	Development of non-potential based mixed-mode CZMs with exponential damage and overclosure penalisation (CZM1 and CZM2).....	71
4.3	Exploration of CZM1 and CZM2 behaviour.....	74
4.3.1	Proportional loading.....	76
4.3.2	Non-proportional loading.....	78
4.4	Comparison of CZM1 and CZM2 with Abaqus exponential softening formulation (CZM3).....	82
4.5	Construction of a potential-based CZM	86
	Bibliography.....	92
5	DEVELOPMENT OF A NOVEL TEST METHOD TO INVESTIGATE MODE ii FRACTURE AND DISSECTION OF ARTERIES	94
5.1	Introduction	94
5.1.1	Lap-shear testing of arterial tissue results in a mixed mode crack propagation.....	97
5.2	Design and computational validation of a novel experimental mode II fracture test (shear fracture ring test (SFRT)).....	99
5.2.1	Sample Preparation	107
5.3	Results	109
5.3.1	Determination of Hyperelastic Properties.....	109
5.3.2	Fracture Mechanics results.....	110
5.4	Discussion	120
5.5	Appendix A: Artery Material Model.....	124
5.6	Appendix B: Circumferential Notch Tests	126
5.7	Appendix C: Peel Tests	128
5.7.1	Methods.....	128
5.7.2	Results.....	129
5.8	Appendix D: Mesh convergence	131
5.9	Appendix E: Experimental Images.....	133
	Bibliography.....	136
6	VISCOPLASTIC COHESIVE ZONE MODELLING OF INTERFACIAL FIBRILLATION IN SOFT TISSUE.....	137
6.1	Introduction	137
6.1.1	General Background.....	137
6.1.2	Examination of fibrillation during mode II delamination of arteries uncovered in recent experimental study (McGarry and FitzGibbon (2020))....	138
6.1.3	Structure and aims of the study.....	140

6.2	Elastic fibrillation cohesive zone model (EF-CZM)	142
6.2.1	EF-CZM formulation	143
6.2.2	EF-CZM parametric investigation of mixed mode behaviour	147
6.2.3	Simulation of artery crack propagation experiment using EF-CZM .	154
6.3	Visco-plastic cohesive zone model (VP-CZM).....	156
6.3.1	VP-CZM formulation.....	158
6.3.2	Thermodynamic consideration in relation to a VP-CZM	164
6.3.3	VP-CZM parametric investigation of mixed-mode behaviour	166
6.3.4	Simulation of artery crack propagation experiment using VP-CZM.	175
6.4	Concluding remarks	177
	Bibliography.....	179
7	A NUMERICAL INVESTIGATION OF THE INITIATION OF TYPE A AORTIC DISSECTION	184
7.1	Introduction:	184
7.2	Development of a realistic subject-specific model of aortic dissection	186
7.2.2	Key results for subject-specific aorta model dissection analysis.....	189
7.3	Parametric investigation of the key factors that contribute to risk of vessel dissection.....	193
7.3.1	Development of an idealised and parameterised model of the aorta .	195
7.3.2	Results of parametric analysis of key factors in aorta shear tractions and dissection.....	203
7.4	Concluding remarks	215
7.5	Appendix A: Mesh Convergence	216
	Bibliography.....	218
8	A NUMERICAL INVESTIGATION OF THE PROPAGATION OF DISSECTION	223
8.1	Introduction	223
8.2	Examination of an artery with an intraluminal tear.....	225
8.3	Examination of a dissected artery with a patent false lumen	228
8.4	Conclusions	234
	Bibliography.....	236
9	CONCLUDING REMARKS & FUTURE PERSPECTIVES	239
9.1	Summary of Key Contributions	239
9.2	Future Perspectives.....	242
	Bibliography.....	245
10	DEVELOPED CODE: SUBROUTINES, AND OPTIMISATION SCHEMES	
	247	

Chapter 1

1 INTRODUCTION

1.1 A brief history of aortic dissection

The aorta is the largest vessel in the vascular system which supplies blood to all parts of the body and originates in the left ventricle. The aorta consists of three layers: the intima, which is the innermost layer; the media, which is the middle layer; and the adventitia, which is the outermost layer (Fuster *et al.*, 2007; Fox, 2011). Aortic dissection (AD) is a pathological process involving the separation or tearing of these layers (Rajagopal, Bridges and Rajagopal, 2007; Criado, 2011). The first clear description of AD is historically attributed to Frank Nicholls, who was the personal physician of George II, King of Britain, who died suddenly and unexpectedly. Having been instructed to open and embalm the royal body, Nicholls' account represents the first clear medical account of the disease now referred to as AD: “. . . the pericardium was found distended with a quantity of coagulated blood, nearly a pint . . .; the whole heart was so compressed as to prevent any blood contained in the veins from being forced into the auricles; therefore the ventricles were found absolutely void of blood . . .; and in the trunk of the aorta we found a transverse fissure on its inner side, about an inch and a half long, through which some blood had recently passed under its external coat and formed an elevated ecchymosis.” King George II died at Kensington palace “while straining on the toilet” (Nicholls and Parker, 1761), unbeknownst to the monarch, he was performing a closed glottis Valsalva manoeuvre resulting in

increased intrathoracic pressure, which was likely the cause of his aortic dissection, that propagated into his pericardial sac leading to a fatal cardiac tamponade (Miller *et al.*, 1984; MacDougall *et al.*, 1985; Narloch and Brandstater, 1995). The first major breakthrough in the treatment of AD came nearly 200 years later when Michael DeBakey pioneered the first successful surgical resection of an AD (Cooley and DeBakey, 1955; DeBakey *et al.*, 1964). Interestingly, DeBakey underwent the procedure that he pioneered after suffering from an AD and became the oldest human to have survived the surgery at 97 years old at the hands of the surgeons he trained.

The fracture mechanisms of arterial tissue in AD are poorly understood at present. It is unknown how or why a patient may present with an intimal tear. A major challenge to researchers is the lack of available dissected arterial tissue (taken from open surgical repair) for experimental testing. Open surgical repair of AD is rare due to the advent of endovascular repair using stent grafts (Fattori *et al.*, 2008; Nienaber *et al.*, 2009; FitzGibbon *et al.*, 2018). The majority of experimental characterisations of fracture properties of arterial tissue focus on peel tests, a mechanism which has little relevance for the initiation of dissection (Gasser and Holzapfel, 2006; Sommer *et al.*, 2008). To date, there has been no complete characterisation of the fracture properties of the aorta relevant to the initiation of aortic dissection. In order to understand the mechanisms that lead to AD, a complete characterisation of the fracture properties of the aorta is required.

1.2 Thesis Objectives

The overall objective of this thesis is to advance on the current understanding of the biomechanics of aortic dissection. Novel experimental and computational methodologies are developed that allow for the simulation of aortic dissection and its fracture mechanisms. This section provides motivation for each of the objectives of

this thesis. A comprehensive background and motivation for each objective is provided in the corresponding technical chapter. The specific aims are as follows:

- Develop a novel cohesive zone formulation to address shortcomings of the inbuilt Abaqus cohesive zone behaviour and develop novel methods of handling overclosure.
- Design and build a novel experimental-computational methodology to characterise the shear fracture properties of the aorta.
- Develop and implement physically motivated cohesive zone models to predict fibrillation observed in arterial tissue during fracture.
- Investigate the role of anatomical features, material conditions, and physiologically motivated boundary conditions on initiation of aortic dissection.
- Investigate the conditions necessary to propagate an intimal tear and to propagate a false lumen.

1.3 Thesis Structure

The following is a brief outline of each chapter in this thesis.

Chapter 2: A general review of the literature surrounding the aorta and aortic dissection is presented. With a focus on the aortic anatomy, the relevant clinical literature surrounding aortic dissection, mechanical testing and characterisation of aortic tissue and arteries in general, computational modelling of fracture in arteries and aortic dissection, and a general background on cohesive zone modelling. A critical review of the literature directly relevant to each individual study is presented in each technical chapter (Chapters 4-8), while Chapter 2 represents a more general review of the literature.

Chapter 3: A background on the theoretical and numerical methods implemented in the computational work of this thesis is provided. First presented is a general background in continuum mechanics with a discussion of hyperelastic materials. A background in the finite element method is then provided with discussion of user-defined material subroutines (UMATs) and user-defined interaction subroutines (UINTERS).

Chapter 4: Two novel non-potential based cohesive zone models are proposed, including a novel optional overclosure hardening behaviour. Full parametric investigation of mode-mixity behaviour is presented, as well as a demonstration of irreversible damage. A potential-based form of the model is also explored and compared to similar existing potential-based models. Finally, anomalous behaviours of the inbuilt Abaqus exponential damage evolution are discussed.

Chapter 5: Computational fracture analysis and anisotropic J-integral calculations are performed to design a new experimental test methodology to determine the mode II fracture properties of arterial tissue. This new experimental design is constructed and validated, and the pure mode II fracture properties of an artery are measured for the first time. As part of the study, it is shown that lap-shear testing of arteries does not result in mode II delamination due to high tissue deformability and toughness. It is argued that pure mode II fracture is the only possible mechanism by which arterial dissection can initiate in-vivo.

Chapter 6: Experimental evidence of interfacial fibrillation in arterial tissue is presented. The inability of a standard cohesive zone modelling approach to predict experimental fibrillation crack growth trends is demonstrated. A novel fibrillation CZM is proposed and presented with full parametric examination of the mixed mode

behaviour. The model shows an improvement over a standard CZM approach, but ultimately fails to capture the trends of the experiment. A novel viscoplastic cohesive zone model is proposed and presented with full parametric examination of the mixed mode behaviour. The proposed model captures the key experimental fibrillation crack growth trends.

Chapter 7: A subject specific aorta finite element cohesive zone analysis is presented. The risk of dissection is explored through reducing the aortic shear interface strength. It is found that a 100-fold reduction in mode II strength is required to initiate a dissection under physiological conditions. It is also shown that dissection must initiate in a mode II. The influence of other material, anatomical, and loading factors on dissection risk is also quantified using a parameterised idealised aorta model. It is shown that none of the factors considered pose a risk of dissection in a healthy aorta.

Chapter 8: The risk of dissection in an artery with a pre-existing intimal tear is examined computationally. Finite element cohesive zone analyses reveal a safe range of pressures at which an intimal tear will not propagate. The risk of dissection in an artery with a pre-existing intraluminal septum and a patent false lumen is investigated using a combined computational fluid dynamics and finite element cohesive zone modelling framework. The results indicate the range of pressures at which a false lumen will propagate.

Chapter 9: The key findings and implications of this thesis are outlined and summarised. Suggestions for future experimental work and computational work are also presented.

Bibliography

Cooley, D. A. and DeBakey, M. E. (1955) 'Resection of the thoracic aorta with replacement by homograft for aneurysms and constrictive lesions.', *The Journal of thoracic surgery*. Elsevier, 29(1), pp. 66–104. doi: 10.1016/S0096-5588(20)30733-9.

Criado, F. J. (2011) 'Aortic dissection: a 250-year perspective.', *Texas Heart Institute journal / from the Texas Heart Institute of St. Luke's Episcopal Hospital, Texas Children's Hospital*, 38(6), pp. 694–700. Available at: <http://www.pubmedcentral.nih.gov/articlerender.fcgi?artid=3233335&tool=pmcentrez&rendertype=abstract> (Accessed: 5 January 2016).

DeBakey, M. E. et al. (1964) 'Surgical Management of Dissecting Aneurysm Involving the Ascending Aorta.', *The Journal of cardiovascular surgery*, 5, pp. 200–211. Available at: <http://www.ncbi.nlm.nih.gov/pubmed/14168138> (Accessed: 14 July 2020).

Fattori, R. et al. (2008) 'Complicated Acute Type B Dissection: Is Surgery Still the Best Option?. A Report From the International Registry of Acute Aortic Dissection', *JACC: Cardiovascular Interventions*. *Journal of the American College of Cardiology*, 1(4), pp. 395–402. doi: 10.1016/j.jcin.2008.04.009.

FitzGibbon, B. et al. (2018) 'Endovascular versus open surgical repair for complicated chronic type B aortic dissection', *Cochrane Database of Systematic Reviews*. John Wiley & Sons, Ltd, 2018(4). doi: 10.1002/14651858.CD012992.

Fox, S. I. (2011) *Human Physiology*. 12th Edition. McGraw-Hill. Available at: http://www.maxdown.org/e-books-list/stuart-ira-fox-human-physiology-12th-edition_177j1.html (Accessed: 25 February 2015).

Fuster, V. et al. (2007) *Hurst's the heart*. McGraw Hill Professional.

Gasser, T. C. and Holzapfel, G. A. (2006) 'Modeling the propagation of arterial dissection', *European Journal of Mechanics - A/Solids*, 25(4), pp. 617–633. doi: 10.1016/j.euromechsol.2006.05.004.

MacDougall, J. D. et al. (1985) 'Arterial blood pressure response to heavy resistance exercise', *Journal of Applied Physiology*, 58(3), pp. 785–790. doi: 10.1152/jappl.1985.58.3.785.

Miller, D. C. et al. (1984) 'Independent determinants of operative mortality for patients with aortic dissections.', *Circulation*, 70(3 Pt 2), pp. I153-64. Available at: <http://europepmc.org/abstract/med/6235061> (Accessed: 4 January 2016).

Narloch, J. A. and Brandstater, M. E. (1995) 'Influence of breathing technique on arterial blood pressure during heavy weight lifting', *Archives of Physical Medicine and Rehabilitation*. W.B. Saunders, 76(5), pp. 457–462. doi: 10.1016/S0003-9993(95)80578-8.

Nicholls, F. and Parker, G. (1761) 'LI. Observations concerning the body of his late Majesty, October 26, 1760', *Philosophical Transactions of the Royal Society of London. The Royal Society*, 52, pp. 265–275. doi: 10.1098/rstl.1761.0052.

Nienaber, C. A. et al. (2009) 'Randomized comparison of strategies for type B aortic dissection: the INvestigation of STEnt Grafts in Aortic Dissection (INSTEAD) trial.', *Circulation*, 120(25), pp. 2519–28. doi: 10.1161/CIRCULATIONAHA.109.886408.

Rajagopal, K., Bridges, C. and Rajagopal, K. R. (2007) 'Towards an understanding of the mechanics underlying aortic dissection.', *Biomechanics and modeling in mechanobiology*, 6(5), pp. 345–59. doi: 10.1007/s10237-006-0069-3.

Sommer, G. et al. (2008) 'Dissection properties of the human aortic media: an experimental study.', *Journal of biomechanical engineering. American Society of Mechanical Engineers*, 130(2), p. 021007. doi: 10.1115/1.2898733.

Chapter 2

2 BACKGROUND AND LITERATURE

2.1 Anatomy of the Aorta

2.1.1 Arterial Tissue

Healthy elastic arteries are a complex anisotropic material consisting of three layers, each exhibiting unique material properties and microstructure. Each layer serves a mechanical and physiological function and are fundamental in the maintenance of a healthy artery.

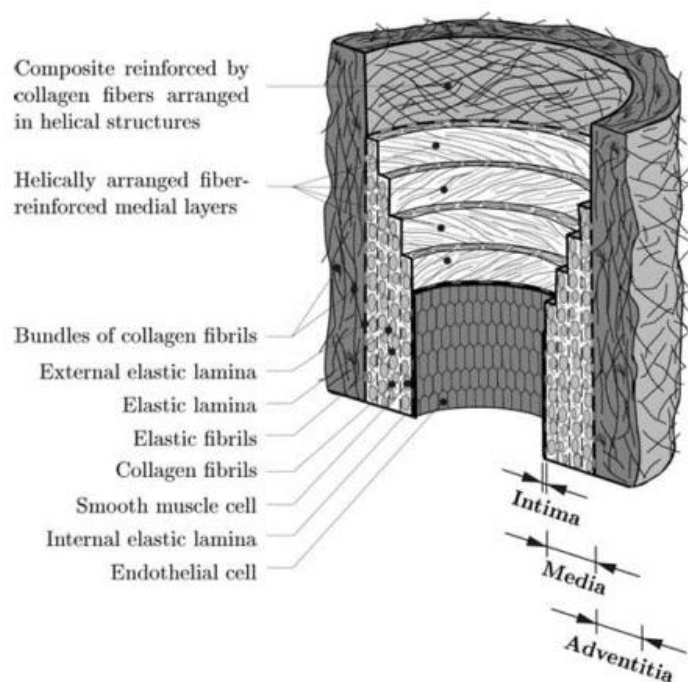


Figure 2.1: This idealised image of a healthy elastic artery shows the intima, media, adventitia, and the components of which they consist (Holzapfel, Gasser and Ogden, 2000).

2.1.1.1 Intima

The intima is the inner layer of the artery which interfaces with the flowing blood in the lumen. It consists of a single layer of endothelial cells on top of a thin basal

membrane. In healthy young arteries, the composition of the intima is not said to have any significant biomechanical influence in the arterial wall. There is, however, an additional layer of the intima below the endothelium which thickens with age, and disease. This thickening is thought to influence the biomechanical importance of the intima in the arterial wall (Weisbecker *et al.*, 2012).

2.1.1.2 Media

The media is the middle layer of the artery and provides the most significant mechanical support to the artery wall. It is composed primarily of smooth muscle cells, collagen, and elastin. Elastin is arranged in fenestrated sheets known as the elastic lamellae (López-Guimet *et al.*, 2017). These divide the media into separate layers (~60 in the thoracic aorta and ~28 in the abdominal aorta) which are fibre-reinforced and well-defined in a concentric pattern (Tsamis, Krawiec and Vorp, 2013). The organisation of these layers in their concentric manner allow for the deformation and high strength of the media. Aortic smooth muscle cells are primarily organised in a helical manner (Fuster *et al.*, 2007). Collagen fibres in the aortic media are aligned primarily in the circumferential direction which provides additional mechanical stiffness at high circumferential strains (Clark and Glagov, no date; Greenberg, 1986).

2.1.1.3 Adventitia

The adventitia is the third and outermost layer of the artery and is made up of fibroblasts and fibrocytes, ground matrix, and thick bundles of collagen fibrils. The adventitia is the most significant layer of the artery from a biochemical standpoint (Majesky, Dong, Høglund, *et al.*, 2011). There have been studies to suggest that the adventitia has the properties of a progenitor cell niche in the arterial wall, allowing it to respond to arterial injury (Majesky, Dong, Regan, *et al.*, 2011). The adventitia is the primary arterial layer in regulation of the health and disease of vessels (Witter,

Tonar and Schöpfer, 2016). Collagen fibres in the adventitia are generally less aligned than in the media, creating mechanical behaviour that is less anisotropic in nature (Schriefl *et al.*, 2012; Pierce *et al.*, 2015).

2.1.1.4 The Vasa Vasorum

The vasa vasorum (VV) is a network of small blood vessels which supply large elastic arteries (aorta) and veins (vena cava) with blood (Figure 2.2). The VV have been observed supplying porcine arteries and bovine aortae through the use of two families of vessels; the vasa vasorum interna (VVI) and the vasa vasorum externa (VVE) (Heistad and Marcus, 1979; Gössl *et al.*, 2003). The VVI originate in the lumen and extend into the arterial wall from the inside-out providing its blood supply. The VVE originate from major vessels in close proximity to the vessel in question (intercostal arteries for the aorta, major branches of the epicardial coronary arteries for the coronary arteries) and extend into the artery wall from the outside-in providing its blood supply (Wolinsky and Glagov, 1967). The number of VV present in a given section may be described as the spatial density of the VV. The VVI and VVE have been observed to exhibit a complementary relationship whereby a low density of VVE will often mean there will exist a high density of VVI in order to compensate for the reduced oxygen/nutrition to the artery wall. There is a spatially varying distribution of VV throughout the aorta, which may influence the prevalence of aortic diseases (Kampschulte *et al.*, 2010; Sano *et al.*, 2016).

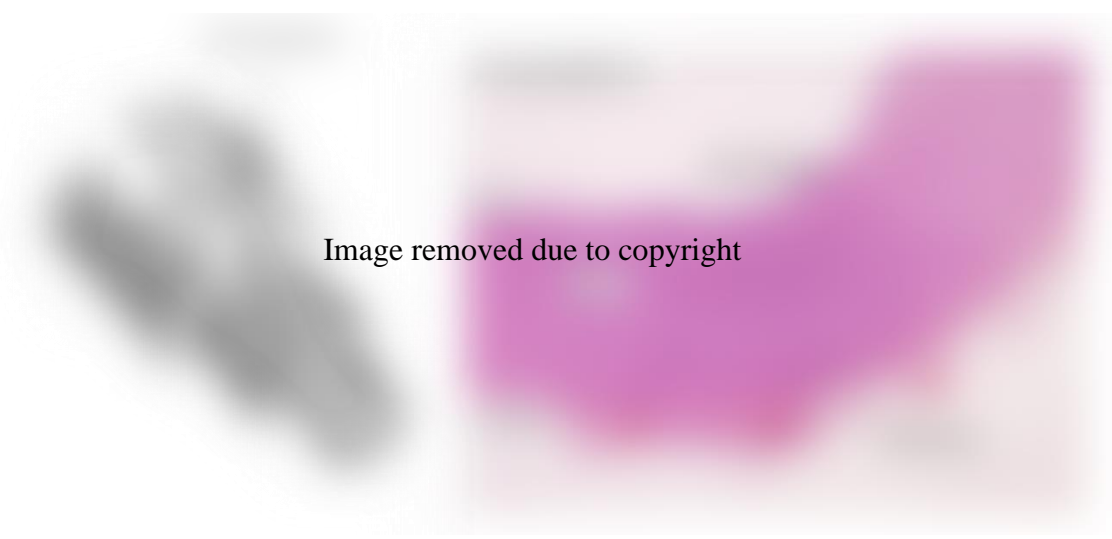


Image removed due to copyright

Figure 2.2: (Left): representative illustration of the aortic adventitia, media, and intima layers and the network of vasa vasorum contained within. (Right): Haematoxylin and eosin stain of a histological section of aorta. Vasa vasorum externa shown in red at the external adventitial surface. Image courtesy of (*Nervous tissue*, 2012).

2.1.2 Elastin in the Aorta

Elastin is a fundamental protein in the healthy aorta. It is the primary structural protein in the aorta at low strains (Schriebl *et al.*, 2015). It is highly elastic and fundamentally important in fluid-structure energetics in a physiological cardiac cycle (Mithieux and Weiss, 2005). Age and disease may negatively impact the physiological function of elastin *in vivo* through an assortment of different processes.

2.1.2.1 The effects of age:

As the aorta ages, there is a significant decrease in the concentration of elastin throughout the aorta (Hass, 1943). This decrease occurs through an increase in the other matrix components, such as collagen (Schlatmann and Becker, 1977; Greenberg, 1986; Sans and Moragas, 1993), and a maintenance of the current elastin content (Lansing, Alex and Rosenthal, 1950). There is also evidence to suggest that the elastin cross-linking is affected negatively by the ageing process. This is seen in one study where the amount of elastin cross-linking acids were decreased in older patients versus the control group (John and Thomas, 1972). Another study showed in the ascending

thoracic aorta the elastin concentration was found to decrease by 33% in patients in their 90's compared to patients in their 20's (Hosoda *et al.*, 1984). Despite the change in concentration, the content of elastin remained the same (Andreotti *et al.*, 1985). Elastin fibre fragmentation has also been linked with the natural ageing process of the human aorta (Toda *et al.*, 1980). The mechanism by which this occurs is unknown but it has been suggested that mechanical fatigue failure may play a primary role (Sans and Moragas, 1993; Greenwald, 2007). As well as mechanical failure, chemical degradation has also been suggested as an important mechanism due to an upregulation of matrix metalloproteinases (MMPs) due to decreased levels of their inhibitors (Wang and Lakatta, 2002).

2.1.2.2 *The effects of disease:*

Naturally, disease may alter the content, concentration, and morphology of elastin *in vivo*. In fact, the changes to these fundamental proteins are what underly many symptoms in various connective tissue diseases. In one study, the elastin content was decreased by almost 50% in patients with Marfan Syndrome (Abraham *et al.*, 1982). Patients with Marfan Syndrome suffer from larger interlamellar spaces and loss of interlamellar fibres. This may explain the prevalence of aneurysms and dissection in patients with Marfan Syndrome (Perejda *et al.*, 1985). In the ascending thoracic aorta, a significant decrease in elastin concentration was seen in dissected aortas when compared to healthy aortas. Furthermore, there was slightly less elastin cross-linking seen in these samples when compared with the control group (Cattell, Hasleton and Anderson, 1993).

2.1.3 **Collagen in the Aorta**

Collagen is the main structural protein in the arterial wall at high strains (Di Lullo *et al.*, 2002). It consists of amino acids bound together in a triple helix structure which

makes up a collagen fibril. Large fibrillar bundles are formed using various classes of proteins, glycoproteins, and proteoglycans (Perumal, Antipova and Orgel, 2008). Collagen fibres consist of many collagen fibrils. Similarly to elastin, collagen may pathologically degrade with age and disease.

2.1.3.1 The effects of age:

The increased content of collagen within the aortic wall due to increased age has been well documented (Schlatmann and Becker, 1977; Greenberg, 1986; Sans and Moragas, 1993). Importantly, this is a non-intimal collagenous increase (Smith, 1965). This means the intimal thickening associated with ageing is not responsible for the increased collagen content (Holzapfel *et al.*, 2007). Another study observed an increase in irregularly arranged collagen fibres in the media of the human thoracic aorta with age (Toda *et al.*, 1980). The increase of irregularly arranged collagen fibres leads to more isotropic behaviour with age, decreasing the aortas resistance to circumferential stretch, potentially resulting in increased incidences of aneurysms which are associated with old age (Kent, 2014). There is also an observed increase in collagen cross-linking with age. This is primarily due to the increase in content of cross-linking amino acids such as histidinoalanine (Fujimoto, 1982).

2.1.3.2 The effects of disease:

In one study, the content of collagen was found to be increased at the site of dissecting ascending thoracic aneurysms and collagen concentration was decreased (Whittle *et al.*, 1990). It has also been shown that the morphology of the collagen fibre bundle is dramatically altered in aortic dissection and ascending thoracic aortic aneurysms. In the disease cases, the fibres are thin and scattered as opposed to the thick well-arranged parallel fibres in the control (de Figueiredo Borges *et al.*, 2008).

2.2 Clinical Overview

2.2.1 What is Aortic Dissection?

The current understanding of Aortic Dissection (AD) in the clinical literature is varied and somewhat scarce when compared to other vascular disease, with several authors referring to it as a conundrum (Vilacosta *et al.*, 2010) . However, it is clinically accepted that AD occurs upon some intimal injury (commonly known as the tear/entry tear) which causes an initial separation of the arterial layers (Figure 2.3). The separation is thought to occur most commonly between the intima and media (Criado, 2011).

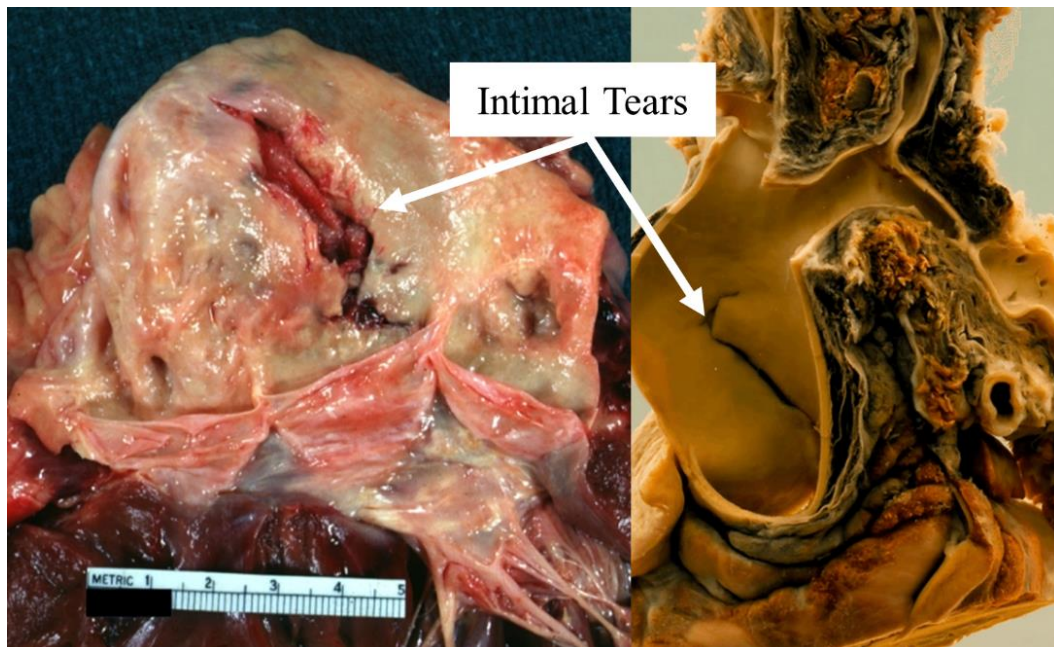


Figure 2.3: Pathology images of intimal tears in the ascending aorta. Images courtesy of (*Aortic aneurysm*, 2008; *Cardiac Pathology: Congenital: Coarctation of the aorta: aortic dissection*, 2011) (Creative Commons Attribution/Share-Alike License)

This intimo-medial tear is the pre-cursor for the progression of a further tearing which is thought to occur between the lamellar elastic layers of the media (Tam, Sapp and Roach, 1998; Gasser and Holzapfel, 2006; Sommer *et al.*, 2008) (see Figure 2.5). The propagation of this crack or tear allows a pathological blood flow between the medial layers. This blood flow exerts an internal pressure from within the media and leads to

expansion of this pathological conduit known as the “False lumen”. The expansion of this false lumen invariably leads to the compression of the original aortic lumen, commonly referred to as the “True lumen” (Figure 2.4).

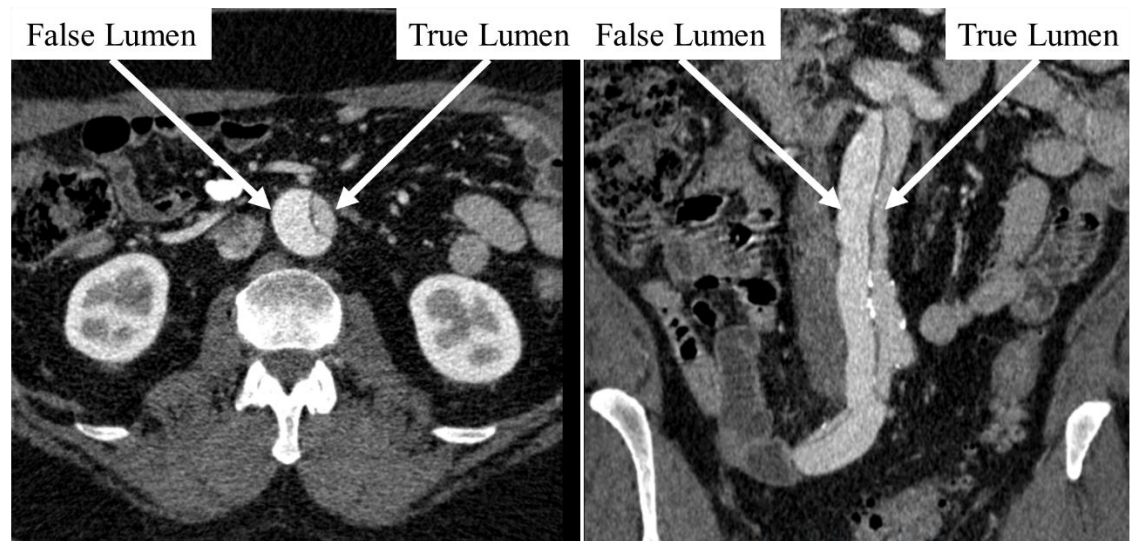


Figure 2.4: Computed Tomography (CT) scan showing an Axial (left) and Coronal (right) view of a type-B chronic aortic dissection. As can be seen in both views the true lumen is compressed by the false lumen. The lower attenuation in the true lumen also indicates reduction in blood flow from the true lumen and increased flow in the false lumen.

The compression of the true lumen is often problematic as it causes a reduction in blood flow to the major arteries which stem from the true lumen of the aorta; the celiac artery, the superior mesenteric artery (SMA), the renal arteries, the inferior mesenteric artery (IMA), the intercostal arteries, and the spinal arteries. If these arteries are occluded or malperfused, the results for the patient can be catastrophic (paraplegia, renal failure, bowel necrosis, etc.) (Eggebrecht *et al.*, 2006; Fattori *et al.*, 2008, 2013; Svensson *et al.*, 2008; Chou *et al.*, 2015; Chen *et al.*, 2017; Evangelista *et al.*, 2018).

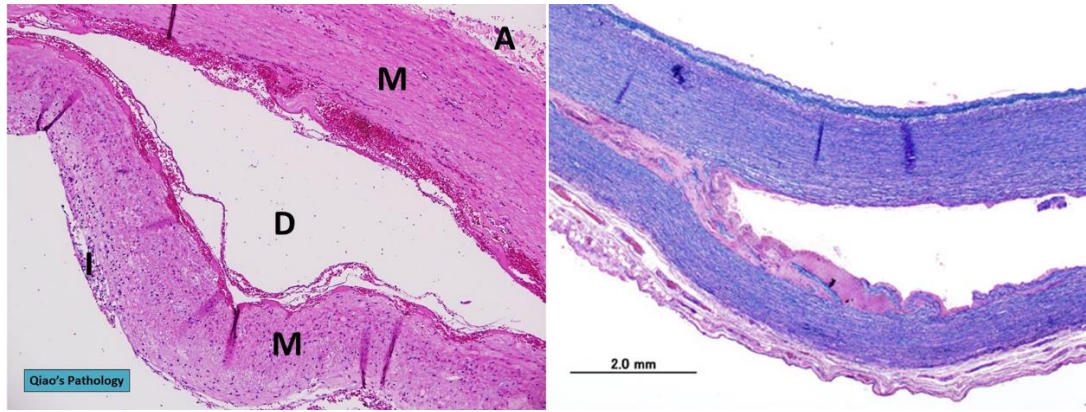


Figure 2.5: Histological image of dissected aorta. Dissection between the medial layers is evident in both images. The letters (left) refer to M-media, D-dissection, A-Adventitia. A buckle is also evident in the specimen on the left. Images courtesy of (*Qiao's Pathology*, 2018) (left) and (*Aortic dissection*, 2006) (right). (Creative Commons Attribution/Share-Alike License)

2.2.1.1 Anatomical Classification of Aortic Dissection.

There are two types of anatomical classification system with regards to aortic dissection: the Stanford classification and the DeBakey classification. These classifications describe the anatomical extent of the pathology and are frequently used to determine treatment pathways and patient outcomes. Between the two, the Stanford Classification is more commonly used in clinical practice and is sub-divided into Type-A and Type-B. A Type-A AD involves the ascending aorta, and the aortic arch, while a Type-B AD involves the remainder of the aorta beyond the supra-aortic vessels (the brachiocephalic artery, the left common carotid artery, and the left subclavian artery). The DeBakey classification divides AD into Type I, Type II, and Type III. Type I involves the ascending and descending aorta (Stanford Type A and B) infrequently referred to as a “pan-aortic dissection”, Type II involves the ascending aorta only (Stanford Type A), and type III involves the descending aorta only, beginning distal to the left subclavian artery (Stanford Type B). According to the International Registry of Acute Aortic Dissection approximately 62.3% of patients present with type-A dissection (Hagan *et al.*, 2000).



Figure 2.6: Illustration of the clinical classifications of aortic dissection based on the anatomical extent of the disease. Any dissection which involves the ascending aorta/aortic arch proximal to the left subclavian artery may be referred to as a Stanford Type-A. Stanford Type-B exclusively involves the descending aorta distal to the left subclavian artery (MacKnight *et al.*, 2016).

2.2.1.2 Temporal Classification of Aortic Dissection

AD is also classified based on the age of the dissection, typically beginning from the onset of symptoms or from first evidence of the disease with imaging (Evangelista *et al.*, 2018). Clinically, this is due to the variation in mortality rates as the dissection ages. Traditionally two classifications have been used: acute and chronic. These referred to less than 14 days old and older than 14 days. There are four classifications that are now used in clinical practice. These are (from the onset of symptoms); <24 hours (Hyper-acute); <2 weeks (Acute); 2-6 weeks (Sub-acute); >6 weeks (Chronic).

As the dissection progresses in chronicity, the separated arterial layers which divides the true and false lumen (the intraluminal septum) increase in rigidity and reduce in elasticity and mobility. This process occurs through the accumulation of granulation

tissue from the blood stream and fibrosis of the fractured surface (septum) (Hasleton and Leonard, 1979). There has been a recent shift in thought in the clinical literature away from arbitrary acute/chronic definitions and towards a more sophisticated method of dating the dissection based on septal mobility using 4D-MRI (Karmonik *et al.*, 2009, 2011; Clough *et al.*, 2012). These methods are still considered cutting-edge and have not been widely accepted by the medical community as of yet.

2.2.1.3 *Complicated versus Uncomplicated*

A Type-B AD is also classified based on the requirement for intervention and is referred to as uncomplicated or complicated. Complicated refers to AD which presents with: malperfusion or end organ ischaemia (ischaemia affecting the spinal cord, kidneys, viscera, or lower extremities), and uncontrolled severe hypertension. Uncomplicated refers to a patient without the aforementioned symptoms, these are generally treated with best medical therapy (Nienaber *et al.*, 2005; Tang and Dake, 2009; Ulug *et al.*, 2012; FitzGibbon *et al.*, 2018). This involves antihypertensive therapy through the use of beta blockers in attempt to reduce the haemodynamic load acting upon the initial entry tear and in order to avoid further propagation of the dissection.

2.2.1.4 *Aortic Dissection and Hypertension*

Hypertension is the most common comorbidity of aortic dissection, affecting approximately 77% of patients with aortic dissection (Evangelista *et al.*, 2018). Chronic hypertension is known to increase the stiffness of the arterial wall (Rorive and Carlier, 1983; Laurent, Boutouyrie and Lacolley, 2005; Arribas, Hinek and González, 2006; Greenwald, 2007). A study carried out on pigs with induced hypertension showed that the outer layer of the media becomes hypoxic due to restriction of blood flow to the vasa vasorum (Angouras, 2000). This leads to the formation of micro-

cracking at the region where the hypoxic tissue interfaces with the healthy tissue. Hypertension has also been shown to induce hypertrophy of the inner layer of the media (Henrichs *et al.*, 1980; Olivetti *et al.*, 1982; Owens, Rabinovitch and Schwartz, 2006). This is likely due to the increased smooth muscle cell activity required to compensate for the underactive outer hypoxic layer of media. Hypertension, therefore, can lead to thickening of the inner layer of the media, and arteriosclerosis of the outer layer of the media or of the entire vessel. The morphology of elastin and collagen has also been shown to vary in hypertension (Angouras, 2000; Laurent and Boutouyrie, 2015).

2.3 Mechanical Behaviour of Aortic Tissue

2.3.1 Anisotropic material behaviour

Extensive research has been conducted on the characterisation of the mechanical behaviour of the healthy aorta and various disease states of the aorta. The anisotropic nature of the aorta has been well established in innumerable experimental studies (Labrosse *et al.*, 2009; García-Herrera *et al.*, 2012; Weisbecker *et al.*, 2012; Nolan *et al.*, 2014; Pierce *et al.*, 2015). The mechanical behaviour of the individual layers has also been examined in great detail in healthy and diseased arteries (Holzapfel *et al.*, 2005; Schriefl *et al.*, 2012; Weisbecker *et al.*, 2012; Sassani, Tsangaris and Sokolis, 2015).

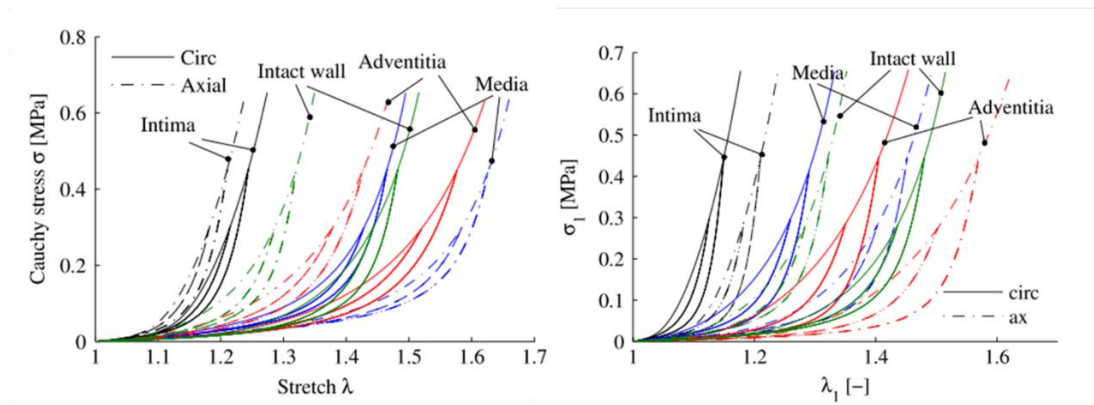


Figure 2.7: Layer-specific mechanical behaviour of thoracic (left) and abdominal (right) aorta undergoing uniaxial extension. Image with permission from Weisbecker *et al.* (Weisbecker *et al.*, 2012). Behaviour of each layer in circumferential and axial extension is shown.

There are a few contributing factors that lead to the anisotropy of arterial tissue including tissue microstructure, smooth muscle cell orientation, axial, radial, and circumferential heterogeneity in the wall properties. However, the primary determinant of anisotropy is the aligned nature of collagen fibres within the arterial wall. The degree and direction of alignment of these fibres varies radially throughout the aortic layers. These layer-specific orientations within the aorta have been well documented experimentally in the thoracic aorta, abdominal aorta and the iliac arteries (Schriefl *et al.*, 2012). This is achieved through analysis of polarised light micrographs (Figure 2.8). Generally, two fibre families are identified in the intima, media, and adventitia with a third and fourth sometimes appearing in the intima (Schriefl *et al.*, 2012).

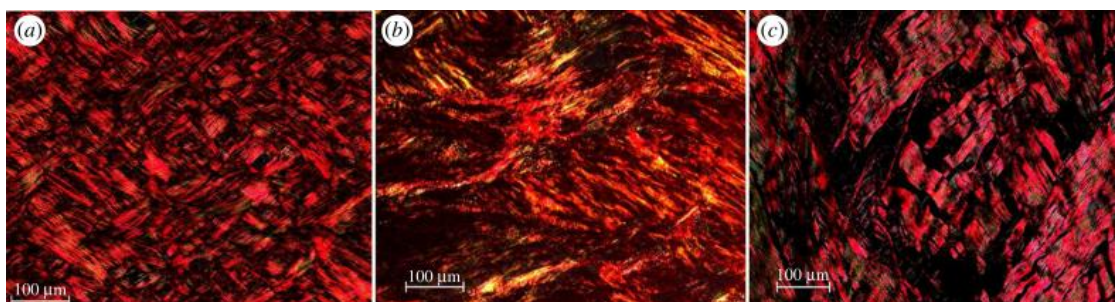


Figure 2.8: Polarized light micrographs of picosirius red stained sections of the (a)

intima, (b) media, and (c) adventitia. Two distinct fibre families are evident from the images. Images with permission courtesy of (Schriebl *et al.*, 2012).

2.3.2 Radial Failure properties

The radial failure properties of the aorta have been documented in a number of studies, the majority of these are peel tests. The resistance of the aorta to normal (mode I) opening is an important quantity which can be readily measured with peel tests. This resistance is typically quantified as a force per unit width (F/w) or a dissection energy (W_{diss}). Sommer *et al.* carried out peel tests on medial specimens of the human abdominal aorta and found a mean force per width of $22.9 \pm 2.9 \text{ mN/mm}$ in the circumferential direction which was lower than the axial counterpart of $34.8 \pm 15.5 \text{ mN/mm}$ (Sommer *et al.*, 2008). These levels of anisotropy are also observed in other peeling studies (presented in Table 2.1). Histology reveals damage to several lamellar layers in the medial peel tests (Figure 2.9c-d). Another interesting finding is the smooth fracture surface left in the circumferential peel when compared to the rough surface of the axial peel (Figure 2.9a-b), indicating microstructural causation of the observed anisotropy. The surface roughness of the histological samples is reflected in the standard deviations of the circumferential and axial specimens, respectively. Pasta *et al.* carried out peel tests on aneurysmal aortas with tricuspid aortic valves (TAVs) and bicuspid aortic valves (BAVs) (Pasta *et al.*, 2012). The motivation behind testing aneurysmal BAVs and TAVs is clear, BAVs carry significantly increased risk of AD, aneurysm, and dissecting aneurysm (Edwards, Leaf and Edwards, 1978; Michelena *et al.*, 2011; Girdauskas *et al.*, 2014). The results of the peel test help to explain the underlying mechanics behind the clinical observation. TAVs had a significantly higher resistance to peeling than BAVs. Both test groups were significantly lower than the non-aneurysmal TAV control group. A study by Kozuń *et al.* found contrasting results for dissected descending thoracic aorta, and dissected aneurysmal descending thoracic

aorta (Kozuń *et al.*, 2019). No significant decrease in mean peeling resistance (F/w) was observed in the aneurysmal group compared to the non-aneurysmal group. Another study from the same group demonstrated that anisotropy in force/width exists in atherosclerotic thoracic aortas (Kozuń *et al.*, 2018). In particular, a significantly higher resistance to peeling was reported in the axial direction than the circumferential direction.

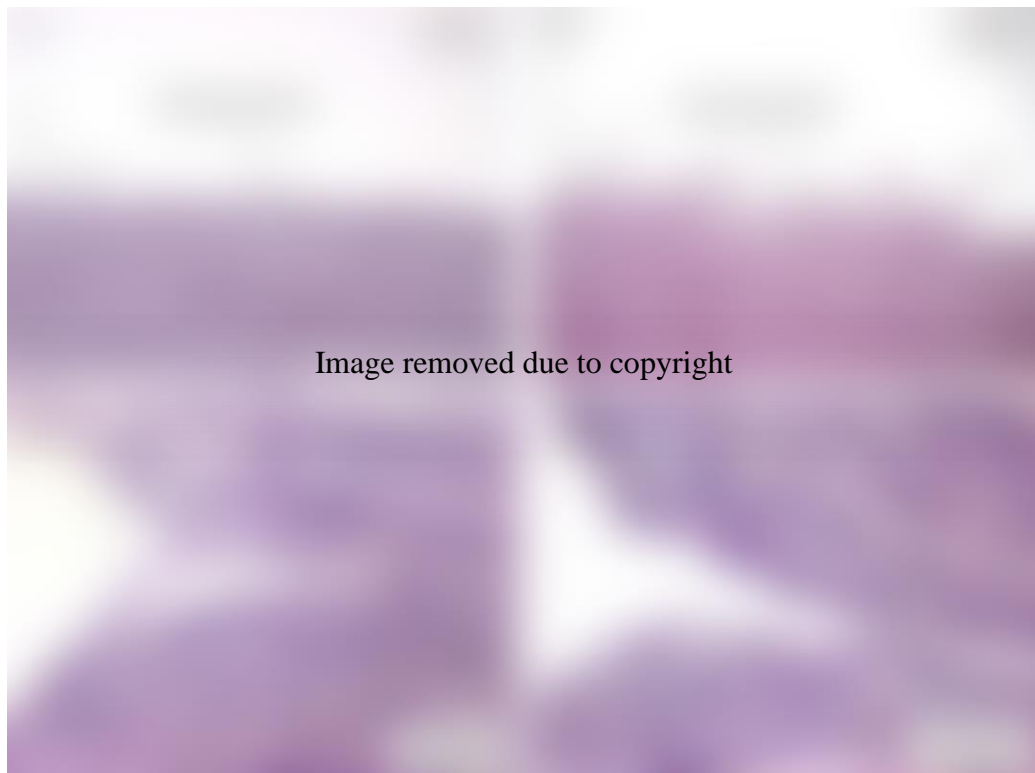


Figure 2.9: Peel tests carried out by Sommer *et al.* (Sommer *et al.*, 2008). Fracture surface of the smooth circumferential (a) and rough axial (b) peel tests. (c) Circumferential and (d) Axial crack tips showing damage to several lamellar layers.

Noble *et al.* carried out peel tests on porcine thoracic aorta to investigate the influence of elastin, and collagen on the resistance to peeling (Noble *et al.*, 2016). Specifically, individual groups of specimens are treated using collagenase, elastase, and glutaraldehyde. Significant loss of peeling resistance is observed in the collagenase treated group; implying collagen fibres play a significant role in resistance to peeling. Conversely, no statistically significant difference is observed with elastin knockout,

implying elastin plays little to no role in resisting peeling. The collagenase results are consistent with the clinical observation that Vascular Ehlers-Danlos Syndrome (EDS) patients are at a significantly higher risk to dissection (Goldfinger *et al.*, 2014). Vascular EDS involves a mutation of the COL3A1 gene, which is responsible for type III procollagen (Brandt *et al.*, 2001; Ulbricht *et al.*, 2004). It is shown that relatively low levels of anisotropy in the mean force per width exist in the circumferential and axial directions across all subgroups.

Leng *et al.* most recently carried out peel tests on porcine abdominal aortic media (Leng *et al.*, 2018). The authors carried out two types of peel tests: T-shape peel tests (traditional peel tests) in axial and circumferential directions and mixed mode peel tests at loading angles in axial and circumferential directions. Testing reveals a similar mean force per width in both orientations and in both loading configurations ($F/w = 60$ mN/mm) indicating isotropic behaviour in a mixed mode peel.

Table 2.1: Overview of peel tests conducted on arterial tissue. H: Healthy, AN: Aneurysmal, AT: Atherosclerotic, AA: Abdominal Aorta, ATA: Ascending Thoracic Aorta, TA: Thoracic Aorta, F/w : Force per width, W_{diss} : Dissection energy.

Study	Species	Tissue State	Location	Layer	Direction	mean F/w (mN/mm)	W_{diss} (mJ/cm^2)
Sommer et al. (Sommer <i>et al.</i> , 2008)	Human	H	AA	Media	Circ	22.9 ± 2.9	5.1 ± 0.6
					Long.	34.8 ± 15.5	7.6 ± 2.7
Pasta et al. (Pasta <i>et al.</i> , 2012)	Human	H	ATA	Media	Circ	126 ± 6.6	-
					Long.	149 ± 7.6	-
Tong et al.	Human	AN	AA	Media- Intima	Circ	-	10.1 ± 1.7

(Tong <i>et al.</i> , 2011a)					Long.	-	9.3 ± 0.9
Kozuń <i>et al.</i> (Kozuń <i>et al.</i> , 2018)	Human	AT	TA	Adventitia-Media	Circ.	24.5 ± 7.5	5.6 ± 0.9
					Long.	32.4 ± 6.5	7.6 ± 1.7
Noble <i>et al.</i> (Noble <i>et al.</i> , 2016)	Porcine	H	TA	Media	Circ.	67.4 ± 11.7	15.18 ± 2.70
					Long.	76.7 ± 25.9	18.33 ± 6.42
Witzenburg <i>et al.</i> (Witzenburg <i>et al.</i> , 2017)	Porcine	H	ATA	Media	Circ.	68.8 ± 14.2	-
					Long.	97.0 ± 12.7	-
Leng <i>et al.</i> (Leng <i>et al.</i> , 2018)	Porcine	H	AA	Media	Circ.	60	-
					Long.	60	-

Another type of radial experiment was proposed by Sommer *et al.*, the direct tension test (Sommer *et al.*, 2008). This test involves punching a coin-shaped specimen out of the aortic wall and gluing the top and bottom to the grips. A small notch is introduced around the circumference of the sample midway through the height. The sample is then tested to failure. The authors assume a homogenous stress state in the material to estimate an average radial failure stress of $140.1 \pm 15.9 \text{ kPa}$.

2.3.3 Shear Failure Properties and mechanisms

There have been fewer studies characterising the shear failure properties of the aorta when compared to the many peel tests characterising normal failure of the aorta. In

recent years Sommer et al. carried out in-plane and out-of-plane shear tests on human aneurysmatic and dissected thoracic aorta. Small rectangular cuboid samples are prepared ($4\text{mm} \times 4\text{mm} \times 5\text{mm}$), a notch is cut into the sample midway through the sample height such that it lies on the face in the direction of applied shear. Samples are then glued top and bottom and sheared to failure. The authors find nearly an order of magnitude difference in the ultimate shear stresses for the in-plane shear when compared to the out of plane shear tests in aneurysmatic specimens ($115 \pm 41 \text{ kPa}$, $918 \pm 313 \text{ kPa}$). The findings across axial and circumferential for in plane shear tests from the study do not reveal statistically significant anisotropy in failure properties. The mean shear at ultimate shear stress was $\gamma^u = 1.53 \pm 0.28$ in the circumferential direction and $\gamma^u = 1.24 \pm 0.22$ in the axial direction for aneurysmatic specimens, indicating these specimens undergo extremely high levels of deformation before reaching an ultimate shear stress.

Another study characterising the shear failure properties of the ascending porcine aorta was carried out by Witzenburg et al. (Witzenburg *et al.*, 2017). Lap-shear tests were carried out in the axial and circumferential directions. Contrary to previous shear experiments, the authors found a statistically significant difference in the peak shear stress in the circumferential direction when compared to the axial direction ($185.4 \pm 28.4 \text{ kPa}$ versus $143.7 \pm 16.0 \text{ kPa}$ respectively). It is difficult to compare the two experiments, as they consist of different experimental methods and specimen geometries, however, the failure properties of the tissue should be insensitive to experimental methodology. This may indicate that lap-shear is a more appropriate experiment than in-plane shear in determining failure characteristics of aortic tissue.

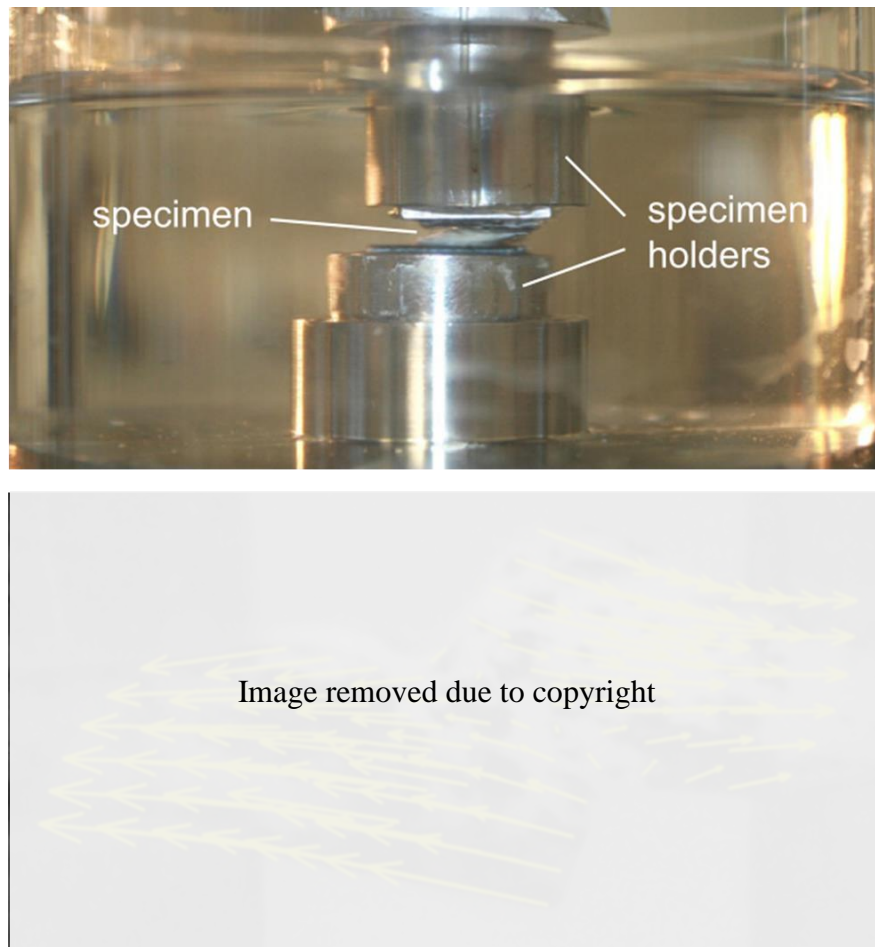


Figure 2.10: Images of two shear experiments carried out on aortic tissue. (top): In-plane shear tests with permission (Sommer *et al.*, 2016). A notched specimen is glued to holders on top and bottom and sheared to failure. (bottom): Lap-shear tests (Witzenburg *et al.*, 2017). Aorta is cut into a z-shape specimen and free edges are placed in colinear grips. Specimens are sheared to failure.

Haslach *et al.* carried out shear testing of aneurysmal and non-pathological human ascending aortic tissue and found relatively isotropic material behaviour in shear (Haslach, Gipple, *et al.*, 2018). The authors predict significantly lower shear stresses than the previous two studies, however they may not be directly compared as the experimental apparatus is quite dissimilar.

More recently, Haslach *et al.* examined the shear mechanisms that underly aortic fracture mechanics and discovered some interesting phenomena (Haslach, Siddiqui, *et al.*, 2018). Pressure inflation tests are carried out on aortic ring specimens containing notches of varying orientations. Notches are cut such that they initiate at the intima

and travel perfectly radially (perpendicular to the circumferential plane) or they travel at varying angles towards the adventitia. Crack growth is observed propagating radially over a very small distance followed by a discrete change in direction to propagate circumferentially. This phenomenon is observed regardless of notch orientation. This indicates that it is energetically favourable for the notch to propagate circumferentially in a mode II crack and not a mode I. This study represents the best evidence that aortic dissection and all other rupture processes in the aorta are the results of a mode II crack growth, not a mode I. Previously, ultimate tensile strength was used as an indicator for rupture in the aorta (Vorp, Raghavan and Webster, 1998; Vande Geest, 2005; Vande Geest *et al.*, 2006). Following ultimate tensile strength, many considered the normal strength of the aortic layers to be the gold standard and as such carried out peel tests to characterise this strength. The best evidence currently suggests aortic dissection occurs in a mode II propagation (Haslach *et al.*, 2015; Haslach, Siddiqui, *et al.*, 2018).

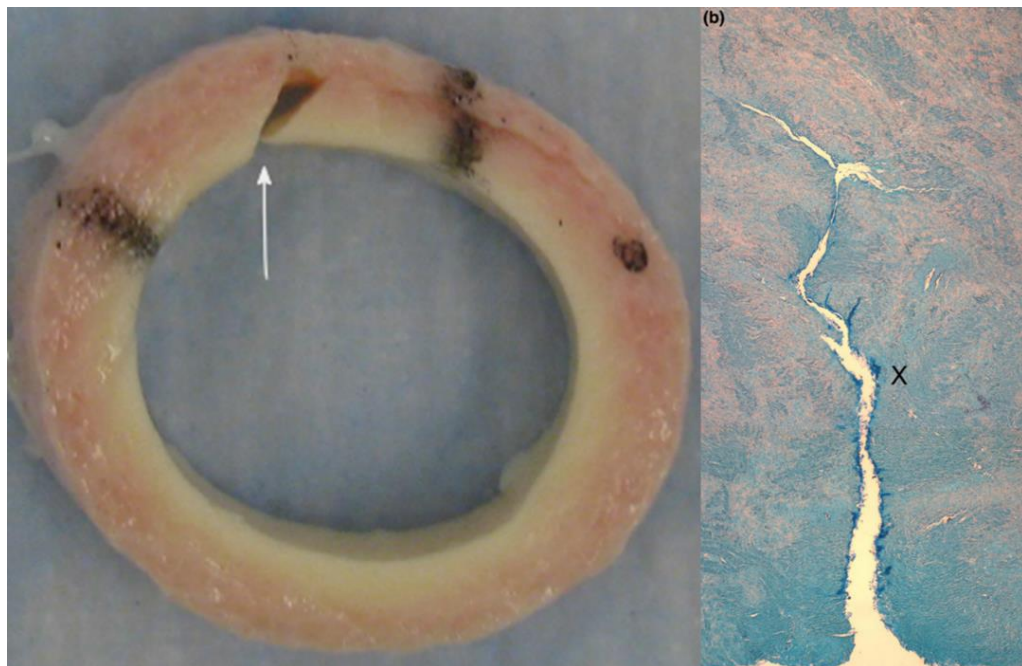


Figure 2.11: Results of pressure inflation tests on bovine aorta. Extensive circumferential crack growth is observed. (Left) with permission from (Haslach,

Siddiqui, *et al.*, 2018): The initial radial notch shown by the white arrow. The crack turns 90 degrees and propagates circumferentially in a mode II. (Right): Histological sample stained with safranin-O. The X marks the boundary position of the initial radial notch. Small radial growth is observed, after which the crack turns 90 degrees and propagates bi-directionally in shear in the circumferential plane (Haslach *et al.*, 2015).

2.3.4 Residual Stress

An interesting feature of aortic tissue is the lack of a zero-stress state when it remains circumferentially intact. Circumferentially intact aortic rings are in a state of equilibrium and zero-pressure; however, they are not in a “zero-stress” state. There exist stresses in the aorta which cause a ring specimen to spring open if radially cut (Liu and Fung, 1988). These exist due to a compressive circumferential stress at the intima and a tensile circumferential stress at the adventitia. Experimentally this phenomenon is measured by cutting aortic rings and measuring the angle they spring open to, known as the opening angle. This opening angle varies spatially throughout the aorta indicating a spatial variation in residual stress throughout the aorta. Experiments carried out on rat aortae observed that the maximum change in opening angle occurs in the ascending aorta (Fung and Liu, 1989). Another study carried out on rat aortae showed that hypertension significantly increases the residual stress in the aorta (Matsumoto and Hayashi, 1996a). In a study carried out on human aortas a very strong correlation between vessel radius and opening angle was observed (Saini, Berry and Greenwald, 1995). The same study also revealed a strong correlation between the opening angle and the wall thickness. It is also shown that residual stress increases with the presence of atherosclerosis. A more recent study provides the most complete and comprehensive dataset regarding residual stress in the human aorta (Sokolis *et al.*, 2017).

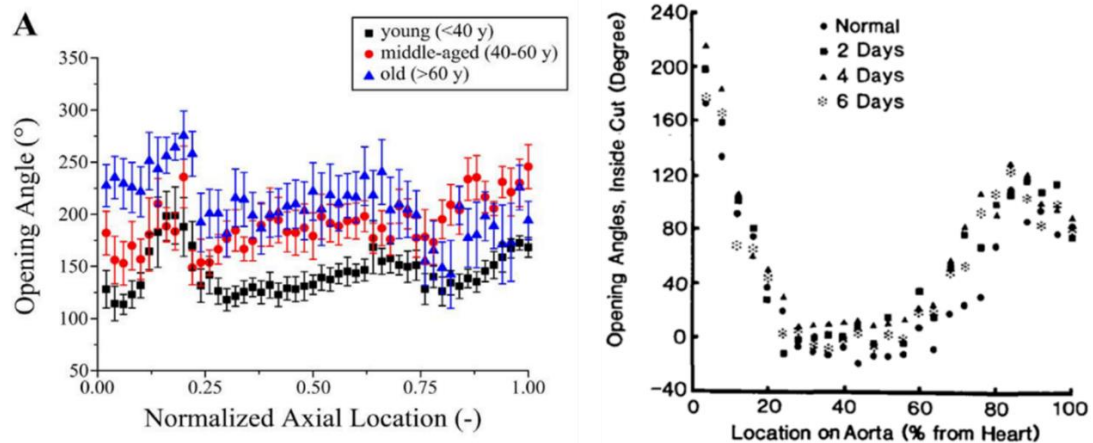


Figure 2.12: Opening angle data for human aorta (left) and rat aorta (right). Images with permission from (Liu and Fung, 1988; Sokolis *et al.*, 2017).

2.4 Computational Modelling

There have been significant improvements over the past decade in computational modelling of aortic dissection and the fracture processes involved. These computational models are frequently used to gain further insight to experiments and to predict disease progression. Just as there have been a number of experimental peel tests carried out on aortic tissue, there have also been a number of computational studies carried out on peel tests and related experiments. The first of these was performed by Gasser and Holzapfel (Gasser and Holzapfel, 2006). The authors use the partition of unity finite element method (PUFEM) in order to model the delamination occurring between arterial layers. A normal cohesive strength of 140 kPa is calculated to propagate a tear at a quasi-steady state force/width of 23.0 mN/mm . The authors assume a plastic like behaviour of the exponential cohesive interface which avoids a fast decay of the traction after reaching the peak. A second numerical study of peel tests was carried out by Ferrara *et al.* (Ferrara and Pandolfi, 2010). In said study, the authors use a cohesive zone modelling approach to model the peeling process. A linear damage model is used with varying interface strengths and fracture energies. No dependence of the mean force/width on the fracture energy is found and it is shown

that the mean force/width is primarily sensitive to the interface strength. An interface strength of $140kPa$ predicts a steady-state force/width of $28.8 mN/mm$. These results show good agreement with the previous study. More recently, simulation of peel tests were carried out by Witzenburg et al. (Witzenburg *et al.*, 2017). The authors approach the problem differently by using multiscale modelling. The scales consist of the FE domain (mm scale), representative volume elements (RVEs) (μm scale), and individual fibres (the nm scale). The authors demonstrate good agreement between their own experimental and computational data but do not report a normal interface strength due to the nature of the modelling framework. The mean circumferential peel tension is found to be $68.8 \pm 14.2 mN/mm$ for porcine ascending aorta. The most recent study on peeling of aortic tissue was carried out by Leng et al. (Leng *et al.*, 2018). The study focuses on the numerical modelling of two types of peel tests, T-shaped (traditional peel test) and mixed mode. The arterial tissue is modelled as a HGO material and the CZM is an exponential type traction separation law taken from (Ortiz and Pandolfi, 1999). The mode mixity at the crack tip as a function of loading angle for the mixed mode peeling experiments is also presented.

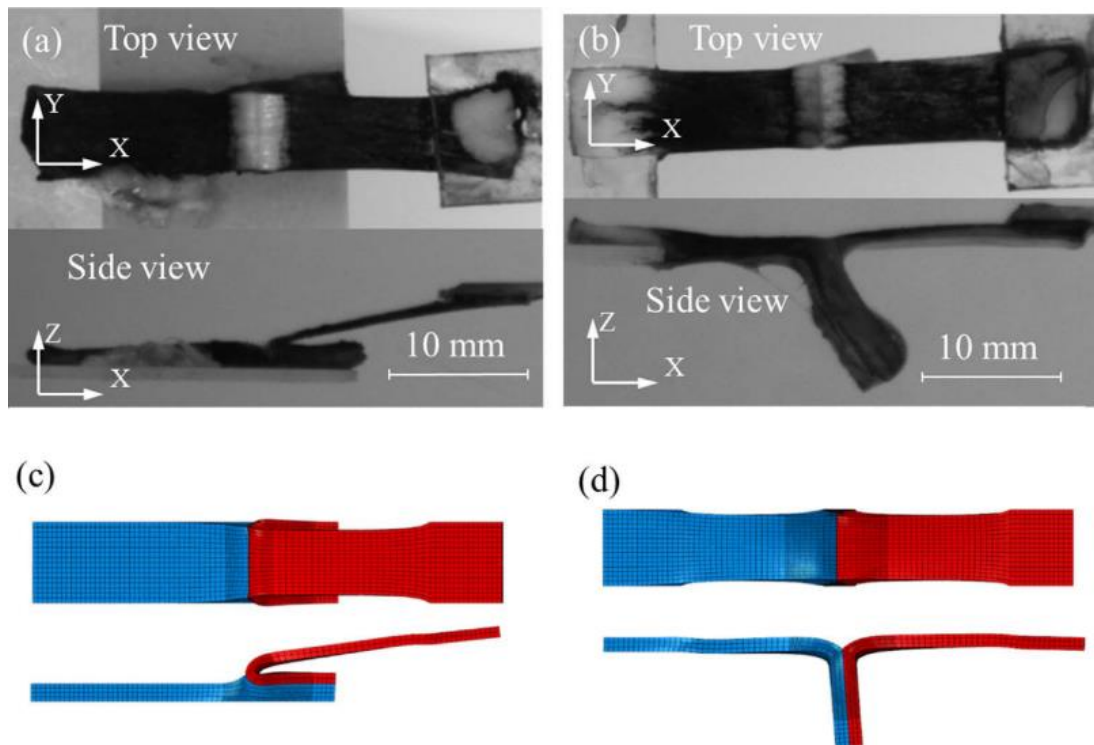


Figure 2.13: Mixed mode peel test experiment (a) and simulation (c) and traditional T-shape peel test experiment (b) and simulation (d) from Leng *et al.* with permission (Leng *et al.*, 2018)

There have been a number of studies that use the results of experimental and numerical simulations of peel tests in order to calibrate their cohesive strengths. Noble *et al.* carried out an investigation into iatrogenic dissection of arterial tissue (Noble *et al.*, 2017). Iatrogenic dissection occurs typically in the catheterisation process or during balloon angioplasty (Núñez-Gil *et al.*, 2015; Ramasamy *et al.*, 2017; Hiraide *et al.*, 2018). It predominantly occurs in the coronary arteries and is initiated by a mode I opening induced by the catheter (Leontyev *et al.*, 2012; Fiddler, Avadhani and Marmur, 2015; Hiraide *et al.*, 2018). The authors use a cohesive zone modelling approach using the large displacement formulation as described by Van Den Bosch *et al.* (van den Bosch, Schreurs and Geers, 2007). They report numerical dissection energies approximately four times larger than the experimentally calculated values.

Many studies assume the primary mechanism of the propagation of tears in arterial tissue is a mode I opening. One such study by Wang, et al presents evidence that tear propagation and arrest is dictated by surrounding connective tissues that are sufficiently stiff (Wang *et al.*, 2015). Another study from the same group examines the role of residual stress in crack propagation in an artery model (Wang *et al.*, 2017). Extended finite element method (XFEM) is used with the same linear damage evolution law as Ferrara et al. It is assumed that dissection must propagate due to some internal pressure acting within the aortic wall and report critical pressures which lead to crack propagation. The authors model an initial crack of various lengths and report the propagation paths (Figure 2.14). Their findings suggest a balance between the residual stress present in the artery and the initial tear length.

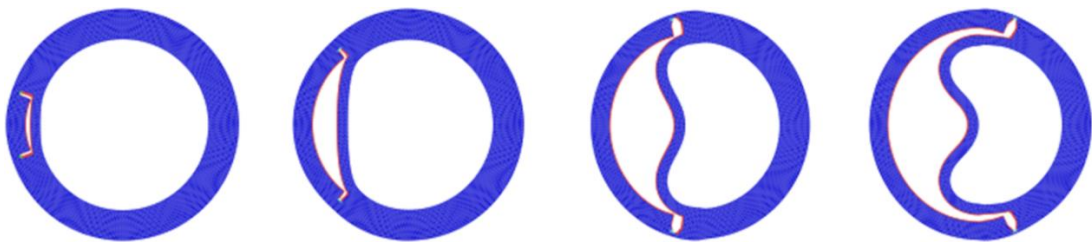


Figure 2.14: Simulations from Wang et al. showing a residually stressed artery with several configurations of initial crack length. Radial propagation is predicted in each case (Wang *et al.*, 2017). Images presented under a creative commons license.

A similar study from the same group presents findings regarding initial tear depth and length (Wang *et al.*, 2018). The same method as the previous study is used and it is shown that deeper shorter tears are more difficult to propagate than long shallow tears (Figure 2.15). It is also hypothesised that the buckling of the true lumen may work to slow down crack propagation as it redistributes the energy and stresses within the wall. Their claim is supported by the prediction that deep tears without buckling tend to propagate radially at lower pressures.

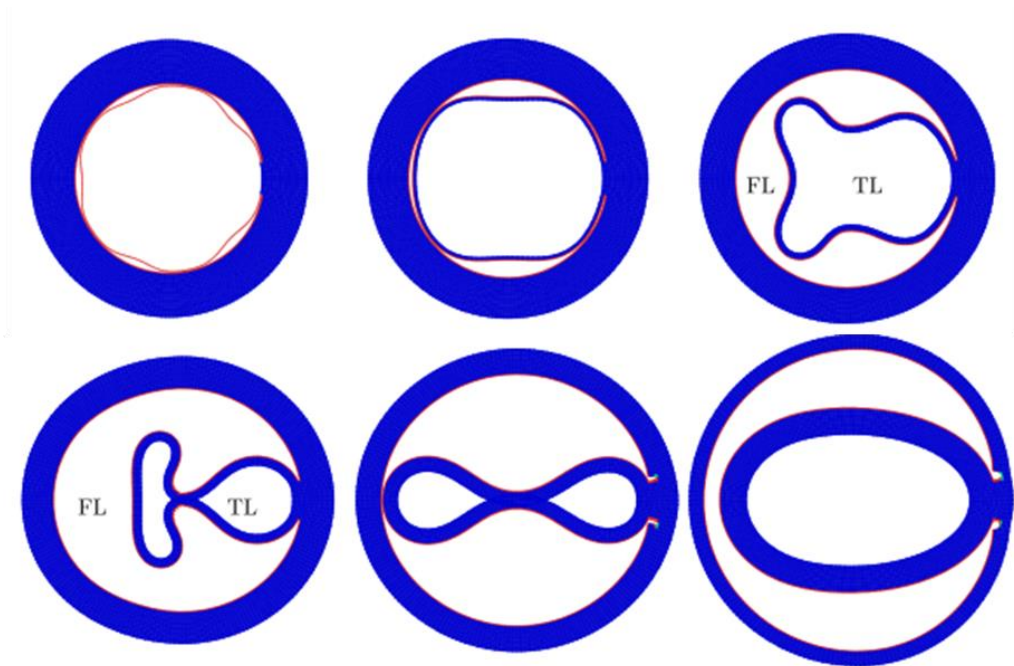


Figure 2.15: Simulations from Wang et al. show the influence of initial tear depth on propagation and morphology of the true lumen. Deep tears tend to propagate radially whilst shallow tears cause compression and distortion of the true lumen. Image courtesy of (Wang *et al.*, 2018) Images presented under a creative commons license.

A recent study carried out by Gültekin et al. simulates the experiments of Sommer et al. using a phase field approach (Gültekin, Dal and Holzapfel, 2016). The authors do not model the exact specimen geometries seen in the experiments, instead representative specimens are modelled, and the data is fit using said geometries. The approach is similar to previous studies in its phenomenological nature, it involves a failure criterion based on the components of the material model i.e. critical fracture energy of the ground matrix and a critical fracture energy of the collagen fibre. A more recent study by Gültekin et al. may be thought of as an extension of the previous study. The same phase field approach is taken, and the authors come to similar conclusions to Haslach et al. that aortic dissection is dominated by a mode II fracture process.



Figure 2.16: Simulations from Gültekin et al. (Gültekin *et al.*, 2019) Initial tear is seen in the image on the left. Crack evolution during pressurisation (centre) and twist (right) is observed. In this framework the crack propagates in a mode II with a compressive mode I component due to the lumen pressure. Images presented under a creative commons license.

There are very few computational studies investigating the mechanics of the aortic arch as they pertain to Type A AD. In fact, to the authors knowledge, only one such study exists. Beller et al. presented a preliminary finite element analysis of a semi-idealised aortic arch (Beller *et al.*, 2004). The material behaviour was assumed to be linear elastic and isotropic with a Young's Modulus of $E = 3$ MPa and a Poisson's ratio of $\nu = 0.49$. The supra-aortic vasculature (the left common carotid artery, brachiocephalic artery, and left subclavian artery) were assumed to be four times stiffer than the aorta ($E = 12$ MPa) and the branch ends were modelled as rigid. The authors report significant stress concentrations by the ostia of the supra-aortic vessels for given displacements of the aortic root. It is difficult to ascertain the validity of these findings given the profound disparity in material properties between the branches and the aorta and the rigid nature of the boundary conditions. The authors conclude that displacement of the aortic root may be an initiating factor in aortic

dissection. This study is somewhat limited however, given that peak wall stress was the metric used to determine risk of dissection.

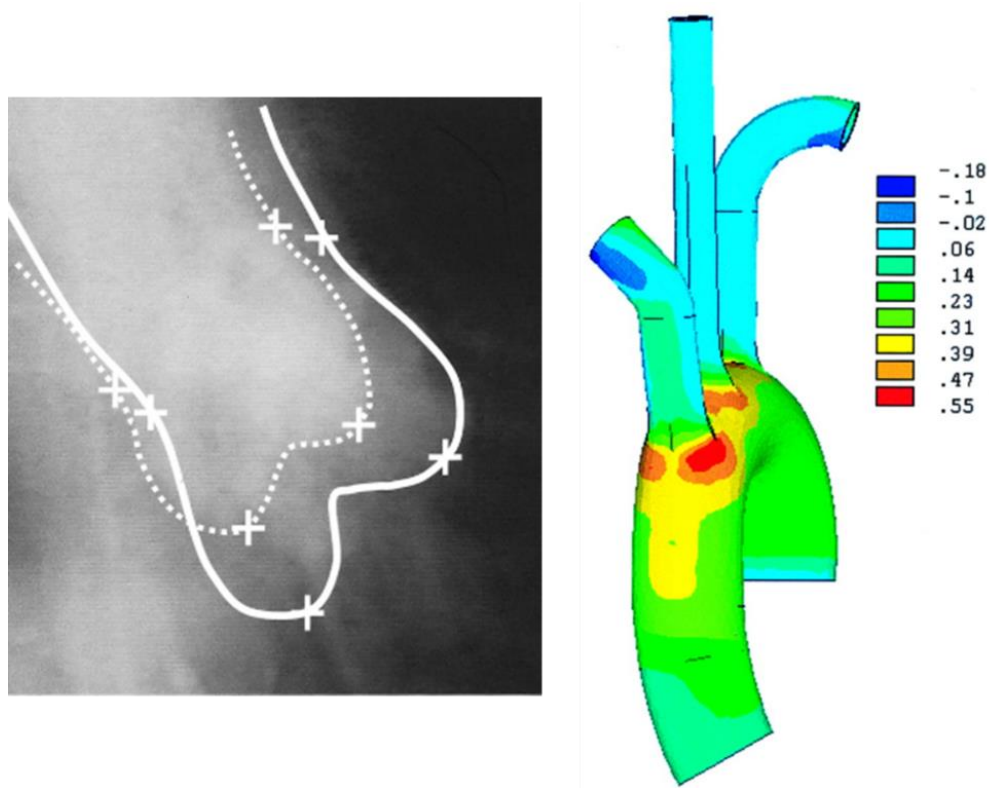


Figure 2.17: CT showing displacement of the aortic root from Beller *et al.* (Images with permission from Beller *et al.*, 2004) (left). Finite element analysis of aortic arch undergoing axial displacement and resultant stress concentrations at the ostia of the branching vessels (right).

Due to the simplicity of constructing patient specific geometries from contrast CT scans and contrast MRI's, there are innumerable studies regarding computational fluid dynamics on patient specific geometries of aortic dissection. Many of these investigate the effect of stent graft repair on the false lumen flow and pressure. Although these studies are vitally important for clinicians they are beyond the scope of this chapter, for an overview of this topic the reader is referred to the comprehensive review paper by Doyle *et al.* and other similar studies (Cheng *et al.*, 2010, 2013, 2014; Doyle and Norman, 2016).

There have been a relatively high number of fluid-structure-interaction (FSI) studies in the literature surrounding aortic dissection also (Qiao, Yin and Chu, 2015; Bonfanti *et al.*, 2018; Bäumlner *et al.*, 2020). The majority of these studies focus on the late stages of the disease progression (fully developed false lumen, treatment, etc.). However, one FSI study investigates the role of pressure and flow acting on an initial intimal flap (Chen *et al.*, 2016). In this study, the geometry has been partially dissected and the pressures acting on the flap are explored. The solid domain is assumed to be linear elastic and isotropic with a Young's Modulus of $E = 2$ MPa and a Poisson's ratio of $\nu = 0.45$. Fluid density is set to be $\rho = 1050$ kg/m³, and the dynamic viscosity $\mu = 0.004$ Pa-s. The fluid was modelled using Newtonian flow. Pressures at the crack tip are only reported as a pressure difference either side of the flap. The authors hypothesise that the stress concentrations at the flap tip are evidence that crack propagation is likely in these areas.

2.5 Cohesive Zone Models

Cohesive zone models (CZMs) are used to describe the cohesive forces which exist at an interface that is undergoing delamination, cracking, or some other mechanism of separation (Barenblatt, 1959). Cohesive zone models are particularly useful in scenarios where linear elastic fracture mechanics (LEFM) laws cannot be applied (Elices *et al.*, 2002). There have been a plethora of cohesive zone models proposed in the literature for applications varying from concrete cracking to soft tissue fracture mechanics (Gasser and Holzzapfel, 2006; Song, Paulino and Buttlar, 2006; Aure and Ioannides, 2010; Noble *et al.*, 2017). Cohesive zone models involve a mathematical description of the damage behaviour that occurs at the interface, this is sometimes referred to as the traction-separation law. CZMs can be coupled or uncoupled, this refers to how the traction behaves as a function of the individual components of the

separation vector. For example, in an uncoupled CZM, the normal traction would be independent of the tangential separation, and likewise for the tangential traction and normal separation. These formulations are typically only useful in problems that are exclusively a mode I or mode II opening. As such, for the vast majority of engineering applications, coupled CZMs are favourable. A coupled CZM means that all components of the traction vector (normal and tangential) are a function of all components of the separation vector (normal and tangential). This aids in providing a physically realistic response, for example if an interface undergoes complete tangential separation there should be no further resistance to a normal separation. There have been two main types of cohesive zone models presented in the literature, potential-based and non-potential based.

2.5.1 Potential Based

A potential based CZM is path-independent and the traction separation law is derived from an interface potential function which describes the work of separation of the interface at any given point on the interface. Many in the literature have favoured these models for their path independence and ease of implementation. A very well-known potential based model is the Xu-Needleman model (Xu *et al.*, 1993), although many others have been used in a variety of mixed mode applications (Needleman, 1987; Rice and Beltz, 1994; van den Bosch, Schreurs and Geers, 2006). The traction-separation law is obtained through the partial derivative of the potential function in the desired traction direction. For example:

$$T_i = \frac{\partial \phi}{\partial \Delta_i}, \quad i = \{n, t\} \quad (2.1)$$

Where ϕ is some potential function that describes the work of separation throughout the interface, T_i is the traction in the i direction, and Δ_i is the separation in the i

direction. Potential-based cohesive zone formulations do however have some limitations (Máirtín *et al.*, 2014). Due to the traction separation law being derived from an interface potential function, it is possible to compute un-physical repulsive normal tractions at any given point where the partial derivative of the potential surface becomes negative. Furthermore, by the same reasoning, unphysical residual non-zero tractions may also be computed even upon extreme separation of an interface. In this scenario complete separation of an interface may be considered path-dependant, given that the interface may never completely separate.

2.5.2 Non-potential based

A non-potential based CZM refers to a traction separation law that is not derived from an interface potential function (Máirtín *et al.*, 2014). These formulations are path-dependant, and the work of separation depends then on the traction separation law, and path taken. There have been a number of these models proposed in the literature. These include rigid-linear fracture models (Camacho and Ortiz, 1996), piece-wise trapezoidal models (Tvergaard and Hutchinson, 1992), bilinear models (Geubelle and Baylor, 1998; Camanho, Dávila and De Moura, 2003) and exponential type models (McGarry *et al.*, 2014). Of course, non-potential-based cohesive zone models have their own shortcomings. It is possible that certain laws may calculate unusual fracture energies for given paths. This can result in non-monotonic behaviour of the total work of separation, which is considered by most to be unphysical behaviour in the vast majority of cases. A non-potential based formulation is used in Abaqus (Providence, RI: Dassault Systèmes Simulia Corp) unless a UINTER is being used. Using the model proposed by Camanho *et al.* (Camanho, Dávila and De Moura, 2003), the developers add functionality for an exponential type softening as well as the original linear softening.

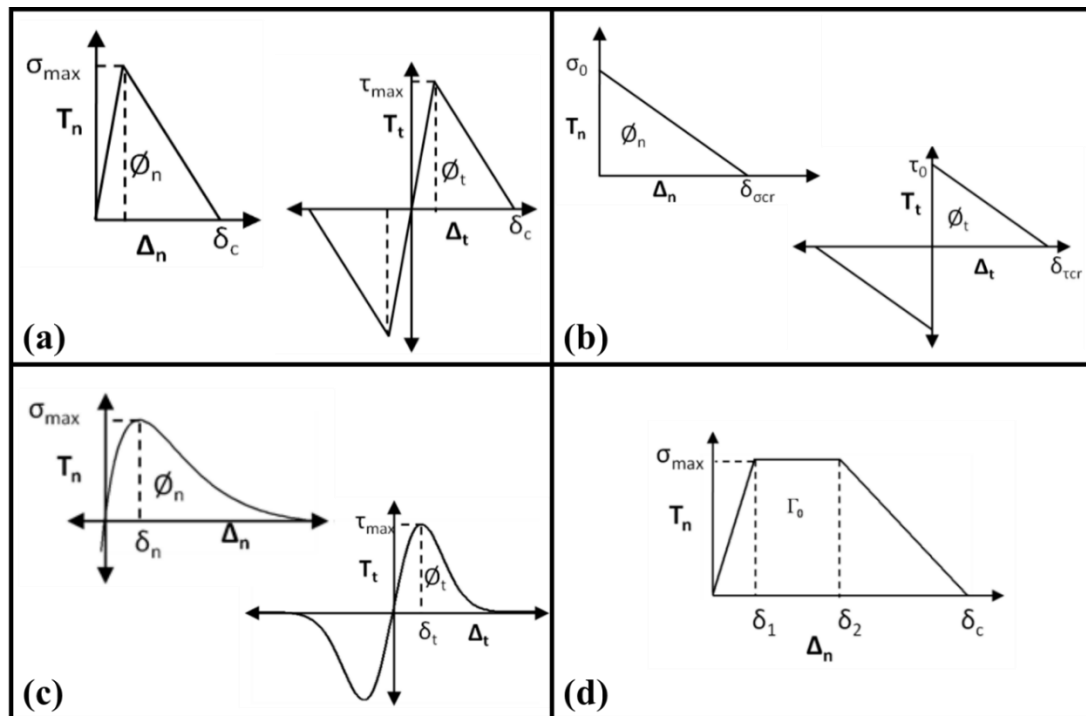


Figure 2.18: (a): Example of a bilinear model such as the one used in Abaqus as presented by Camanho et al. (Camanho, Dávila and De Moura, 2003) (b): Rigid linear model (Camacho and Ortiz, 1996). (c): Exponential type model (McGarry *et al.*, 2014). (d): piecewise trapezoidal model (Tvergaard and Hutchinson, 1992).

Bibliography

Abraham, P. A. et al. (1982) ‘Marfan syndrome. Demonstration of abnormal elastin in aorta’, *Journal of Clinical Investigation*. American Society for Clinical Investigation, 70(6), pp. 1245–1252. doi: 10.1172/JCI110723.

Andreotti, L. et al. (1985) ‘Aortic Connective Tissue in Ageing A Biochemical Study’, *Angiology*. Sage PublicationsSage CA: Thousand Oaks, CA, 36(12), pp. 872–879. doi: 10.1177/000331978503601206.

Angouras, D. (2000) ‘Effect of impaired vasa vasorum flow on the structure and mechanics of the thoracic aorta: implications for the pathogenesis of aortic dissection’, *European Journal of Cardio-Thoracic Surgery*, 17(4), pp. 468–473. doi: 10.1016/S1010-7940(00)00382-1.

Aortic aneurysm (2008). Available at: https://www.wikidoc.org/index.php/File:Aortic_aneurysm_59.jpg (Accessed: 14 July 2020).

Aortic dissection (2006). Available at: [https://commons.wikimedia.org/wiki/File:Aortic_dissection_\(1\)_Victoria_blue-HE.jpg](https://commons.wikimedia.org/wiki/File:Aortic_dissection_(1)_Victoria_blue-HE.jpg) (Accessed: 14 July 2020).

Arribas, S. M., Hinek, A. and González, M. C. (2006) ‘Elastic fibres and vascular structure in hypertension’, *Pharmacology and Therapeutics*, 111(3), pp. 771–791. doi: 10.1016/j.pharmthera.2005.12.003.

Aure, T. and Ioannides, A. (2010) ‘Simulation of crack propagation in concrete beams with cohesive elements in ABAQUS’, *Transportation Research Record*. SAGE PublicationsSage CA: Los Angeles, CA, 2154(2154), pp. 12–21. doi: 10.3141/2154-02.

Barenblatt, G. I. (1959) ‘The formation of equilibrium cracks during brittle fracture. General ideas and hypotheses. Axially-symmetric cracks’, *Journal of Applied Mathematics and Mechanics*. Pergamon, 23(3), pp. 622–636. doi: 10.1016/0021-8928(59)90157-1.

Bäumler, K. et al. (2020) ‘Fluid–structure interaction simulations of patient-specific aortic dissection’, *Biomechanics and Modeling in Mechanobiology*. Springer Berlin Heidelberg, pp. 1–22. doi: 10.1007/s10237-020-01294-8.

Beller, C. J. et al. (2004) ‘Role of Aortic Root Motion in the Pathogenesis of Aortic Dissection’, *Circulation*. American Heart Association, Inc., 109(6), pp. 763–769. doi: 10.1161/01.CIR.0000112569.27151.F7.

Bonfanti, M. et al. (2018) ‘A simplified method to account for wall motion in patient-specific blood flow simulations of aortic dissection: Comparison with fluid-structure interaction’, *Medical Engineering & Physics*. Elsevier, 58, pp. 72–79. doi: 10.1016/J.MEDENGGPHY.2018.04.014.

van den Bosch, M. J., Schreurs, P. J. G. and Geers, M. G. D. (2006) ‘An improved description of the exponential Xu and Needleman cohesive zone law for mixed-mode decohesion’, *Engineering Fracture Mechanics*. Pergamon, 73(9), pp. 1220–1234. doi: 10.1016/j.engfracmech.2005.12.006.

van den Bosch, M. J., Schreurs, P. J. G. and Geers, M. G. D. (2007) ‘A cohesive zone model with a large displacement formulation accounting for interfacial fibrillation’, *European Journal of Mechanics, A/Solids*. Elsevier Masson, 26(1), pp. 1–19. doi: 10.1016/j.euromechsol.2006.09.003.

Brandt, T. et al. (2001) ‘Pathogenesis of cervical artery dissections: Association with connective tissue abnormalities’, *Neurology*. Wolters Kluwer Health, Inc. on behalf of the American Academy of Neurology, 57(1), pp. 24–30. doi: 10.1212/WNL.57.1.24.

Camacho, G. T. and Ortiz, M. (1996) ‘Computational modelling of impact damage in brittle materials’, *International Journal of Solids and Structures*. Pergamon, 33(20–22), pp. 2899–2938. doi: 10.1016/0020-7683(95)00255-3.

Camanho, P. P., Dávila, C. G. and De Moura, M. F. (2003) ‘Numerical simulation of mixed-mode progressive delamination in composite materials’, *Journal of Composite Materials*. SAGE Publications, 37(16), pp. 1415–1438. doi: 10.1177/0021998303034505.

Cardiac Pathology: Congenital: Coarctation of the aorta: aortic dissection (2011). Available at: <https://www.thenakedscientists.com/podcasts/video-podcasts/naked-pathology/cardiac-pathology-congenital-coarctation-aorta-aortic-dissection> (Accessed: 14 July 2020).

Cattell, M. A., Hasleton, P. S. and Anderson, J. C. (1993) ‘Increased elastin content and decreased elastin concentration may be predisposing factors in dissecting aneurysms of human thoracic aorta’, *Cardiovascular Research*. Oxford University Press, 27(2), pp. 176–181. doi: 10.1093/cvr/27.2.176.

Chen, H. Y. et al. (2016) ‘Editor’s Choice – Fluid–Structure Interaction Simulations of Aortic Dissection with Bench Validation’, *European Journal of Vascular and Endovascular Surgery*, 52(5), pp. 589–595. doi: 10.1016/j.ejvs.2016.07.006.

Chen, Y. et al. (2017) ‘Analysis of the timing of thoracic endovascular aortic repair and its indications and outcomes in type b aortic dissection’, *Journal of the American College of Cardiology*, 69 (11 Sup(PG-2077)), p. 2077. doi: <http://dx.doi.org/10.1016/S0735-1097%2817%2935466-9>.

Cheng, Z. et al. (2010) ‘Analysis of Flow Patterns in a Patient-Specific Aortic Dissection Model’, *Journal of Biomechanical Engineering*. American Society of Mechanical Engineers Digital Collection, 132(5). doi: 10.1115/1.4000964.

Cheng, Z. et al. (2013) ‘Initial findings and potential applicability of computational simulation of the aorta in acute type B dissection.’, *Journal of vascular surgery*, 57(2 Suppl), pp. 35S-43S. doi: 10.1016/j.jvs.2012.07.061.

Cheng, Z. et al. (2014) ‘Predicting flow in aortic dissection: comparison of computational model with PC-MRI velocity measurements.’, *Medical engineering & physics*. Elsevier Ltd, 36(9), pp. 1176–84. doi: 10.1016/j.medengphy.2014.07.006.

Chou, H. P. et al. (2015) ‘Outcome comparison between thoracic endovascular and open repair for type B aortic dissection: A population-based longitudinal study’, *Journal of the Chinese Medical Association*, 78(4 PG-241–248), pp. 241–248. doi: <http://dx.doi.org/10.1016/j.jcma.2014.10.003>.

Clark, J. M. and Glagov, S. (no date) Transmural Organization of the Arterial Media The Lamellar Unit Revisited. Available at: <http://ahajournals.org>.

Clough, R. E. et al. (2012) 'A new imaging method for assessment of aortic dissection using four-dimensional phase contrast magnetic resonance imaging.', *Journal of vascular surgery*, 55(4), pp. 914–23. doi: 10.1016/j.jvs.2011.11.005.

Criado, F. J. (2011) 'Aortic dissection: a 250-year perspective.', *Texas Heart Institute journal / from the Texas Heart Institute of St. Luke's Episcopal Hospital, Texas Children's Hospital*, 38(6), pp. 694–700. Available at: <http://www.pubmedcentral.nih.gov/articlerender.fcgi?artid=3233335&tool=pmcentrez&rendertype=abstract> (Accessed: 5 January 2016).

Doyle, B. J. and Norman, P. E. (2016) 'Computational Biomechanics in Thoracic Aortic Dissection: Today's Approaches and Tomorrow's Opportunities.', *Annals of biomedical engineering*, 44(1), pp. 71–83. doi: 10.1007/s10439-015-1366-8.

Edwards, W. D., Leaf, D. S. and Edwards, J. E. (1978) 'Dissecting aortic aneurysm associated with congenital bicuspid aortic valve', *Circulation. American Heart Association, Inc.*, 57(5), pp. 1022–1025. doi: 10.1161/01.CIR.57.5.1022.

Eggebrecht, H. et al. (2006) 'Endovascular stent-graft placement in aortic dissection: a meta-analysis.', *European heart journal*, 27(4), pp. 489–98. doi: 10.1093/eurheartj/ehi493.

Elices, M. et al. (2002) 'The cohesive zone model: advantages, limitations and challenges', *Engineering Fracture Mechanics. Pergamon*, 69(2), pp. 137–163. doi: 10.1016/S0013-7944(01)00083-2.

Evangelista, A. et al. (2018) 'Insights from the international registry of acute aortic dissection: A 20-year experience of collaborative clinical research', *Circulation. Lippincott Williams & Wilkins Hagerstown, MD*, pp. 1846–1860. doi: 10.1161/CIRCULATIONAHA.117.031264.

Fattori, R. et al. (2008) 'Complicated Acute Type B Dissection: Is Surgery Still the Best Option?. A Report From the International Registry of Acute Aortic Dissection', *JACC: Cardiovascular Interventions. Journal of the American College of Cardiology*, 1(4), pp. 395–402. doi: 10.1016/j.jcin.2008.04.009.

Fattori, R. et al. (2013) 'Interdisciplinary expert consensus document on management of type B aortic dissection.', *Journal of the American College of Cardiology. Journal of the American College of Cardiology*, 61(16), pp. 1661–78. doi: 10.1016/j.jacc.2012.11.072.

Ferrara, A. and Pandolfi, A. (2010) 'A numerical study of arterial media dissection processes', in *International Journal of Fracture. Springer Netherlands*, pp. 21–33. doi: 10.1007/s10704-010-9480-y.

Fiddler, M., Avadhani, S. A. and Marmur, J. D. (2015) 'Guide Catheter-Induced Aortic Dissection Complicated by Pericardial Effusion with Pulsus Paradoxus: A Case Report of Successful Medical Management', *Case Reports in Medicine*, 2015, pp. 1–6. doi: 10.1155/2015/480242.

- de Figueiredo Borges, L. et al. (2008) 'Collagen is reduced and disrupted in human aneurysms and dissections of ascending aorta', *Human Pathology*. W.B. Saunders, 39(3), pp. 437–443. doi: 10.1016/j.humpath.2007.08.003.
- FitzGibbon, B. et al. (2018) 'Endovascular versus open surgical repair for complicated chronic type B aortic dissection', *Cochrane Database of Systematic Reviews*. John Wiley & Sons, Ltd, 2018(4). doi: 10.1002/14651858.CD012992.
- Fujimoto, D. (1982) 'Aging and cross-linking in human aorta', *Biochemical and Biophysical Research Communications*, 109(4), pp. 1264–1269. doi: 10.1016/0006-291X(82)91913-1.
- Fung, Y. C. and Liu, S. Q. (1989) 'Change of residual strains in arteries due to hypertrophy caused by aortic constriction.', *Circulation research*, 65(5), pp. 1340–9. doi: 10.1161/01.RES.65.5.1340.
- Fuster, V. et al. (2007) *Hurst's the heart*. McGraw Hill Professional.
- García-Herrera, C. M. et al. (2012) 'Mechanical characterisation of the human thoracic descending aorta: experiments and modelling.', *Computer methods in biomechanics and biomedical engineering*, 15(2), pp. 185–93. doi: 10.1080/10255842.2010.520704.
- Gasser, T. C. and Holzapfel, G. A. (2006) 'Modeling the propagation of arterial dissection', *European Journal of Mechanics - A/Solids*, 25(4), pp. 617–633. doi: 10.1016/j.euromechsol.2006.05.004.
- Vande Geest, J. P. (2005) 'TOWARDS AN IMPROVED RUPTURE POTENTIAL INDEX FOR ABDOMINAL AORTIC ANEURYSMS: ANISOTROPIC CONSTITUTIVE MODELING AND NONINVASIVE WALL STRENGTH ESTIMATION'. Available at: http://d-scholarship.pitt.edu/8585/1/vandegeest_edt2005.pdf (Accessed: 3 February 2015).
- Vande Geest, J. P. et al. (2006) 'Towards a noninvasive method for determination of patient-specific wall strength distribution in abdominal aortic aneurysms.', *Annals of biomedical engineering*, 34(7), pp. 1098–106. doi: 10.1007/s10439-006-9132-6.
- Geubelle, P. H. and Baylor, J. S. (1998) 'Impact-induced delamination of composites: A 2D simulation', *Composites Part B: Engineering*. Elsevier, 29(5), pp. 589–602. doi: 10.1016/S1359-8368(98)00013-4.
- Girdauskas, E. et al. (2014) 'Risk of proximal aortic dissection in patients with bicuspid aortic valve: how to address this controversy?', *Interactive cardiovascular and thoracic surgery*. Oxford University Press, 18(3), pp. 355–9. doi: 10.1093/icvts/ivt518.
- Goldfinger, J. Z. et al. (2014) 'Thoracic aortic aneurysm and dissection', *Journal of the American College of Cardiology*. Elsevier, pp. 1725–1739. doi: 10.1016/j.jacc.2014.08.025.
- Gössl, M. et al. (2003) 'Functional anatomy and hemodynamic characteristics of vasa vasorum in the walls of porcine coronary arteries.', *The anatomical record. Part A, Discoveries in molecular, cellular, and evolutionary biology*. Wiley Subscription Services, Inc., A Wiley Company, 272(2), pp. 526–537. doi: 10.1002/ar.a.10060.

Greenberg, S. R. (1986) ‘The association of medial collagenous tissue with atheroma formation in the aging human aorta as revealed by a special technique’, *Histology and Histopathology*. Murcia : F. Hernández, 1(4), pp. 323–326.

Greenwald, S. E. (2007) ‘Ageing of the conduit arteries’, *Journal of Pathology*. John Wiley & Sons, Ltd., pp. 157–172. doi: 10.1002/path.2101.

Gültekin, O. et al. (2019) ‘Computational modeling of progressive damage and rupture in fibrous biological tissues: application to aortic dissection’, *Biomechanics and Modeling in Mechanobiology*. Springer Berlin Heidelberg, 18(6), pp. 1607–1628. doi: 10.1007/s10237-019-01164-y.

Gültekin, O., Dal, H. and Holzapfel, G. A. (2016) ‘A phase-field approach to model fracture of arterial walls: Theory and finite element analysis’, *Computer Methods in Applied Mechanics and Engineering*. North-Holland, 312, pp. 542–566. doi: 10.1016/j.cma.2016.04.007.

Hagan, P. G. et al. (2000) ‘The International Registry of Acute Aortic Dissection (IRAD)’, *The Journal of American Medical Association*. American Medical Association, 283(7), pp. 897–903. doi: 10.1001/jama.283.7.897.

Haslach, H. W. et al. (2015) ‘Crack Propagation and Its Shear Mechanisms in the Bovine Descending Aorta.’, *Cardiovascular engineering and technology*, 6(4), pp. 501–18. doi: 10.1007/s13239-015-0245-7.

Haslach, H. W., Gipple, J., et al. (2018) ‘Comparison of aneurysmal and non-pathologic human ascending aortic tissue in shear’, *Clinical Biomechanics*. Elsevier, 58, pp. 49–56. doi: 10.1016/j.clinbiomech.2018.07.002.

Haslach, H. W., Siddiqui, A., et al. (2018) ‘Fracture mechanics of shear crack propagation and dissection in the healthy bovine descending aortic media’, *Acta Biomaterialia*. Elsevier, 68, pp. 53–66. doi: 10.1016/j.actbio.2017.12.027.

Hasleton, P. S. and Leonard, J. C. (1979) ‘Dissecting aortic aneurysms: a clinicopathological study. II. Histopathology of the aorta.’, *The Quarterly journal of medicine*, 48(189), pp. 63–76. Available at: <http://www.ncbi.nlm.nih.gov/pubmed/482592> (Accessed: 15 February 2020).

Hass, G. M. (1943) ‘Elastic tissue. II. A study of the elasticity and tensile strength of elastic tissue isolated from the human aorta’, *American Heart Journal*. Elsevier, 25(6), p. 842. doi: 10.1016/S0002-8703(43)90687-8.

Heistad, D. D. and Marcus, M. L. (1979) ‘Role of Vasa Vasorum in Nourishment of the Aorta’, *Journal of Vascular Research*. Karger Publishers, 16(5), pp. 225–238. doi: 10.1159/000158209.

Henrichs, K. J. et al. (1980) ‘Is arterial media hypertrophy in spontaneously hypertensive rats a consequence of or a cause for hypertension?’, *Clinical Science*, 59 Suppl 6, pp. 331s-333s. Available at: <http://www.ncbi.nlm.nih.gov/pubmed/7449279> (Accessed: 21 June 2017).

Hiraide, T. et al. (2018) ‘Impact of catheter-induced iatrogenic coronary artery dissection with or without postprocedural flow impairment: A report from a Japanese multicenter percutaneous coronary intervention registry.’, *PloS one*. Public Library of Science, 13(9), p. e0204333. doi: 10.1371/journal.pone.0204333.

Holzapfel, G. A. et al. (2005) ‘Determination of layer-specific mechanical properties of human coronary arteries with nonatherosclerotic intimal thickening and related constitutive modeling.’, *American journal of physiology. Heart and circulatory physiology*, 289(5), pp. H2048–58. doi: 10.1152/ajpheart.00934.2004.

Holzapfel, G. A. et al. (2007) ‘Layer-specific 3D residual deformations of human aortas with non-atherosclerotic intimal thickening.’, *Annals of biomedical engineering*, 35(4), pp. 530–45. doi: 10.1007/s10439-006-9252-z.

Holzapfel, G. A., Gasser, T. C. and Ogden, R. W. (2000) ‘A new constitutive framework for arterial wall mechanics and a comparative study of material models’, *Journal of Elasticity*. Kluwer Academic Publishers, 61(1–3), pp. 1–48. doi: 10.1023/A:1010835316564.

Hosoda, Y. et al. (1984) ‘Age-Dependent Changes of Collagen and Elastin Content in Human Aorta and Pulmonary Artery’, *Angiology*. Sage Publications Sage CA: Thousand Oaks, CA, 35(10), pp. 615–621. doi: 10.1177/000331978403501001.

John, R. and Thomas, J. (1972) ‘Chemical compositions of elastins isolated from aortas and pulmonary tissues of humans of different ages’, *Biochemical Journal*, 127(1).

Kampschulte, M. et al. (2010) ‘Quantitative CT imaging of the spatio-temporal distribution patterns of vasa vasorum in aortas of apoE^{-/-}/LDL^{-/-} double knockout mice’, *Atherosclerosis*, 212(2), pp. 444–450. doi: 10.1016/j.atherosclerosis.2010.07.010.

Karmonik, C. et al. (2009) ‘An image processing algorithm for the in-vivo quantification and visualization of septum motion in type III B - aortic dissections with cine magnetic resonance imaging.’, *Conference proceedings : ... Annual International Conference of the IEEE Engineering in Medicine and Biology Society. IEEE Engineering in Medicine and Biology Society. Annual Conference, 2009*, pp. 4391–4. doi: 10.1109/IEMBS.2009.5333811.

Karmonik, C. et al. (2011) ‘Correlation between hemodynamic parameters and intra-arterial septum motion in DeBakey Type III aortic dissections using 2D pcMRI and 4D MRA.’, *Conference proceedings : ... Annual International Conference of the IEEE Engineering in Medicine and Biology Society. IEEE Engineering in Medicine and Biology Society. Annual Conference, 2011*, pp. 2809–12. doi: 10.1109/IEMBS.2011.6090777.

Kent, K. C. (2014) ‘Abdominal aortic aneurysms’, *New England Journal of Medicine*. Edited by C. G. Solomon. Massachusetts Medical Society, 371(22), pp. 2101–2108. doi: 10.1056/NEJMcp1401430.

Kozuń, M. et al. (2018) ‘The impact of development of atherosclerosis on delamination resistance of the thoracic aortic wall’, *Journal of the Mechanical Behavior of Biomedical Materials*. Elsevier, 79, pp. 292–300. doi: 10.1016/J.JMBBM.2018.01.009.

Kozuń, M. et al. (2019) ‘Effect of dissection on the mechanical properties of human ascending aorta and human ascending aorta aneurysm’, *Acta of Bioengineering and Biomechanics*, 21(2), pp. 127–134. doi: 10.5277/ABB-01376-2019-01.

- Labrosse, M. R. et al. (2009) ‘Mechanical behavior of human aortas: Experiments, material constants and 3-D finite element modeling including residual stress’, *Journal of Biomechanics*, 42(8), pp. 996–1004. doi: 10.1016/j.jbiomech.2009.02.009.
- Lansing, A. I., Alex, M. and Rosenthal, T. B. (1950) ‘Calcium and Elastin in Human Arteriosclerosis’, *Journal of Gerontology*, 5(2), pp. 112–119. doi: 10.1093/geronj/5.2.112.
- Laurent, S. and Boutouyrie, P. (2015) ‘The Structural Factor of Hypertension: Large and Small Artery Alterations’, *Circulation Research*. American Heart Association, Inc., pp. 1007–1021. doi: 10.1161/CIRCRESAHA.116.303596.
- Laurent, S., Boutouyrie, P. and Lacolley, P. (2005) ‘Structural and genetic bases of arterial stiffness’, *Hypertension*. American Heart Association, Inc., pp. 1050–1055. doi: 10.1161/01.HYP.0000164580.39991.3d.
- Leng, X. et al. (2018) ‘Experimental and numerical studies of two arterial wall delamination modes’, *Journal of the Mechanical Behavior of Biomedical Materials*. Elsevier, 77, pp. 321–330. doi: 10.1016/j.jmbbm.2017.09.025.
- LEONARD, J. C. and HASLETON, P. S. (1979) ‘Dissecting Aortic Aneurysms: a Clinicopathological Study’, *QJM*, 48(1).
- Leontyev, S. et al. (2012) ‘Iatrogenic type A aortic dissection during cardiac procedures: early and late outcome in 48 patients’, *European Journal of Cardio-Thoracic Surgery*, 41(3), pp. 641–646. doi: 10.1093/ejcts/ezr070.
- Liu, S. Q. and Fung, Y. C. (1988) ‘Zero-stress states of arteries.’, *Journal of biomechanical engineering*. American Society of Mechanical Engineers, 110(1), pp. 82–84. doi: 10.1115/1.3108410.
- López-Guimet, J. et al. (2017) ‘High-Resolution Morphological Approach to Analyse Elastic Laminae Injuries of the Ascending Aorta in a Murine Model of Marfan Syndrome’, *Scientific Reports*. Nature Publishing Group, 7(1), p. 1505. doi: 10.1038/s41598-017-01620-8.
- Di Lullo, G. A. et al. (2002) ‘Mapping the ligand-binding sites and disease-associated mutations on the most abundant protein in the human, type I collagen’, *Journal of Biological Chemistry*. American Society for Biochemistry and Molecular Biology, 277(6), pp. 4223–4231. doi: 10.1074/jbc.M110709200.
- MacKnight, B. M. et al. (2016) ‘Advances in Imaging for the Management of Acute Aortic Syndromes: Focus on Transesophageal Echocardiography and Type-A Aortic Dissection for the Perioperative Echocardiographer’, *Journal of Cardiothoracic and Vascular Anesthesia*. W.B. Saunders, pp. 1129–1141. doi: 10.1053/j.jvca.2016.01.020.
- Máirtín, É. Ó. et al. (2014) ‘Potential-based and non-potential-based cohesive zone formulations under mixed-mode separation and over-closure—Part II: Finite element applications’, *Journal of the Mechanics and Physics of Solids*. Pergamon, 63, pp. 363–385. doi: 10.1016/J.JMPS.2013.08.019.
- Majesky, M. W., Dong, X. R., Høglund, V., et al. (2011) ‘The adventitia: A dynamic interface containing resident progenitor cells’, *Arteriosclerosis, Thrombosis, and*

- Vascular Biology. NIH Public Access, pp. 1530–1539. doi: 10.1161/ATVBAHA.110.221549.
- Majesky, M. W., Dong, X. R., Regan, J. N., et al. (2011) ‘Vascular smooth muscle progenitor cells: building and repairing blood vessels.’, *Circulation research*, 108(3), pp. 365–77. doi: 10.1161/CIRCRESAHA.110.223800.
- Matsumoto, T. and Hayashi, K. (1996) ‘Stress and strain distribution in hypertensive and normotensive rat aorta considering residual strain’, *J Biomech Eng. American Society of Mechanical Engineers*, 118(1), pp. 62–73. doi: 10.1115/1.2795947.
- McGarry, J. P. et al. (2014) ‘Potential-based and non-potential-based cohesive zone formulations under mixed-mode separation and over-closure. Part I: Theoretical analysis’, *Journal of the Mechanics and Physics of Solids*, 63(1), pp. 336–362. doi: 10.1016/j.jmps.2013.08.020.
- Michelena, H. I. et al. (2011) ‘Incidence of Aortic Complications in Patients With Bicuspid Aortic Valves’, *JAMA*, 306(10), p. 1104. doi: 10.1001/jama.2011.1286.
- Mithieux, S. M. and Weiss, A. S. (2005) ‘Elastin’, *Advances in Protein Chemistry*. Academic Press, 70, pp. 437–461. doi: 10.1016/S0065-3233(05)70013-9.
- Needleman, A. (1987) ‘A Continuum Model for Void Nucleation by Inclusion Debonding’, *Journal of Applied Mechanics. American Society of Mechanical Engineers Digital Collection*, 54(3), pp. 525–531. doi: 10.1115/1.3173064.
- Nervous tissue (2012). Available at: <https://pt.slideshare.net/kohlschuetter/nervous-tissue-ii/13?smtNoRedir=1> (Accessed: 14 July 2020).
- Nienaber, C. A. et al. (2005) ‘INvestigation of STEnt grafts in patients with type B Aortic Dissection: design of the INSTEAD trial--a prospective, multicenter, European randomized trial.’, *American heart journal*, 149(4), pp. 592–9. doi: 10.1016/j.ahj.2004.05.060.
- Noble, C. et al. (2016) ‘Controlled peel testing of a model tissue for diseased aorta’, *Journal of Biomechanics*, 49(15), pp. 3667–3675. doi: 10.1016/j.jbiomech.2016.09.040.
- Noble, C. et al. (2017) ‘Simulation of arterial dissection by a penetrating external body using cohesive zone modelling’, *Journal of the Mechanical Behavior of Biomedical Materials*, 71(Submitted), pp. 95–105. doi: 10.1016/j.jmbbm.2017.03.004.
- Nolan, D. R. et al. (2014) ‘A robust anisotropic hyperelastic formulation for the modelling of soft tissue’, *Journal of the Mechanical Behavior of Biomedical Materials*, 39, pp. 48–60. doi: 10.1016/j.jmbbm.2014.06.016.
- Núñez-Gil, I. J. et al. (2015) ‘Incidence, Management, and Immediate- and Long-Term Outcomes After Iatrogenic Aortic Dissection During Diagnostic or Interventional Coronary Procedures.’, *Circulation*, 131(24), pp. 2114–9. doi: 10.1161/CIRCULATIONAHA.115.015334.
- Olivetti, G. et al. (1982) ‘Quantitative structural changes of the rat thoracic aorta in early spontaneous hypertension. Tissue composition, and hypertrophy and hyperplasia of smooth muscle cells’, *Circulation Research. American Heart Association, Inc.*, 51(1), pp. 19–26. doi: 10.1161/01.RES.51.1.19.

- Ortiz, M. and Pandolfi, A. (1999) 'Finite-deformation irreversible cohesive elements for three-dimensional crack-propagation analysis', *International Journal for Numerical Methods in Engineering*. John Wiley & Sons, Ltd, 44(9), pp. 1267–1282. doi: 10.1002/(SICI)1097-0207(19990330)44:9<1267::AID-NME486>3.0.CO;2-7.
- Owens, G. K., Rabinovitch, P. S. and Schwartz, S. M. (2006) 'Smooth muscle cell hypertrophy versus hyperplasia in hypertension.', *Proceedings of the National Academy of Sciences*. National Academy of Sciences, 78(12), pp. 7759–7763. doi: 10.1073/pnas.78.12.7759.
- Pasta, S. et al. (2012) 'Effect of aneurysm on the mechanical dissection properties of the human ascending thoracic aorta.', *The Journal of thoracic and cardiovascular surgery*, 143(2), pp. 460–7. doi: 10.1016/j.jtcvs.2011.07.058.
- Perejda, A. J. et al. (1985) 'Marfan's syndrome: Structural, biochemical, and mechanical studies of the aortic media', *The Journal of Laboratory and Clinical Medicine*, 106(4), pp. 369–375. doi: 10.5555/uri:pii:0022214385901076.
- Perumal, S., Antipova, O. and Orgel, J. P. R. O. (2008) 'Collagen fibril architecture, domain organization, and triple-helical conformation govern its proteolysis', *Proceedings of the National Academy of Sciences of the United States of America*, 105(8), pp. 2824–2829. doi: 10.1073/pnas.0710588105.
- Pierce, D. M. et al. (2015) 'Human thoracic and abdominal aortic aneurysmal tissues: Damage experiments, statistical analysis and constitutive modeling', *Journal of the Mechanical Behavior of Biomedical Materials*, 41, pp. 92–107. doi: 10.1016/j.jmbbm.2014.10.003.
- Qiao's Pathology (2018). Available at: https://www.flickr.com/photos/jianhua_qiao_md (Accessed: 14 July 2020).
- Qiao, A., Yin, W. and Chu, B. (2015) 'Numerical simulation of fluid–structure interaction in bypassed DeBakey III aortic dissection', *Computer Methods in Biomechanics and Biomedical Engineering*. Taylor & Francis, 18(11), pp. 1173–1180. doi: 10.1080/10255842.2014.881806.
- Ramasamy, A. et al. (2017) '16 Iatrogenic catheter induced coronary artery dissection: incidence, management and outcomes', *Heart*. BMJ Publishing Group Ltd and British Cardiovascular Society, 103(Suppl 7), pp. A7–A8. doi: 10.1136/heartjnl-2017-bcis.16.
- Rice, J. R. and Beltz, G. E. (1994) 'The activation energy for dislocation nucleation at a crack', *Journal of the Mechanics and Physics of Solids*. Pergamon, 42(2), pp. 333–360. doi: 10.1016/0022-5096(94)90013-2.
- Rorive, G. L. and Carlier, P. G. (1983) 'Hypertension and the arterial wall.', *Acta Clinica Belgica*, 38(6), pp. 353–359. Available at: <http://www.ncbi.nlm.nih.gov/pubmed/7036052> (Accessed: 21 June 2017).
- Saini, A., Berry, C. and Greenwald, S. (1995) 'Effect of age and sex on residual stress in the aorta.', *Journal of vascular research*. Karger Publishers, 32(6), pp. 398–405. doi: 10.1159/000159115.

- Sano, M. et al. (2016) 'Topologic distributions of vasa vasorum and lymphatic vasa vasorum in the aortic adventitia - Implications for the prevalence of aortic diseases', *Atherosclerosis*, 247, pp. 127–134. doi: 10.1016/j.atherosclerosis.2016.02.007.
- Sans, M. and Moragas, A. (1993) 'Mathematical morphologic analysis of the aortic medial structure. Biomechanical implications', *Analytical and Quantitative Cytology and Histology*, 15(2), pp. 93–100. Available at: <http://www.ncbi.nlm.nih.gov/pubmed/8318132> (Accessed: 10 February 2017).
- Sassani, S. G., Tsangaris, S. and Sokolis, D. P. (2015) 'Layer- and region-specific material characterization of ascending thoracic aortic aneurysms by microstructure-based models.', *Journal of biomechanics*, 48(14), pp. 3757–65. doi: 10.1016/j.jbiomech.2015.08.028.
- Schlatmann, T. J. M. and Becker, A. E. (1977) 'Histologic changes in the normal aging aorta: Implications for dissecting aortic aneurysm', *The American Journal of Cardiology*, 39(1), pp. 13–20. doi: 10.1016/S0002-9149(77)80004-0.
- Schriebl, a. J. et al. (2012) 'Determination of the layer-specific distributed collagen fibre orientations in human thoracic and abdominal aortas and common iliac arteries', *Journal of The Royal Society Interface*, 9(71), pp. 1275–1286. doi: 10.1098/rsif.2011.0727.
- Schriebl, A. J. et al. (2015) 'Selective enzymatic removal of elastin and collagen from human abdominal aortas: Uniaxial mechanical response and constitutive modeling', *Acta Biomaterialia*. Elsevier Ltd, 17, pp. 125–136. doi: 10.1016/j.actbio.2015.01.003.
- Smith, E. B. (1965) 'The influence of age and atherosclerosis on the chemistry of aortic intima: Part 2. Collagen and mucopolysaccharides', *Journal of Atherosclerosis Research*, 5(2), pp. 241–248. doi: 10.1016/S0368-1319(65)80065-5.
- Sokolis, D. P. et al. (2017) 'Regional distribution of circumferential residual strains in the human aorta according to age and gender', *Journal of the Mechanical Behavior of Biomedical Materials*. Elsevier, 67, pp. 87–100. doi: 10.1016/j.jmbbm.2016.12.003.
- Sommer, G. et al. (2008) 'Dissection properties of the human aortic media: an experimental study.', *Journal of biomechanical engineering*. American Society of Mechanical Engineers, 130(2), p. 021007. doi: 10.1115/1.2898733.
- Sommer, G. et al. (2016) 'Mechanical strength of aneurysmatic and dissected human thoracic aortas at different shear loading modes', *Journal of Biomechanics*, pp. 2374–2382. doi: 10.1016/j.jbiomech.2016.02.042.
- Song, S. H., Paulino, G. H. and Buttlar, W. G. (2006) 'A bilinear cohesive zone model tailored for fracture of asphalt concrete considering viscoelastic bulk material', *Engineering Fracture Mechanics*. Pergamon, 73(18), pp. 2829–2848. doi: 10.1016/j.engfracmech.2006.04.030.
- Svensson, L. G. et al. (2008) 'Expert consensus document on the treatment of descending thoracic aortic disease using endovascular stent-grafts.', *The Annals of thoracic surgery*, 85(1 Suppl), pp. S1-41. doi: 10.1016/j.athoracsur.2007.10.099.
- Tam, A. S., Sapp, M. C. and Roach, M. R. (1998) 'The effect of tear depth on the propagation of aortic dissections in isolated porcine thoracic aorta.', *Journal of*

- biomechanics, 31(7), pp. 673–6. Available at: <http://www.ncbi.nlm.nih.gov/pubmed/9796691> (Accessed: 18 July 2019).
- Tang, D. G. and Dake, M. D. (2009) ‘TEVAR for acute uncomplicated aortic dissection: immediate repair versus medical therapy.’, *Seminars in vascular surgery*, 22(3), pp. 145–51. doi: 10.1053/j.semvascsurg.2009.07.005.
- Toda, T. et al. (1980) ‘Morphometrical analysis of the aging process in human arteries and aorta.’, *Acta anatomica*. Karger Publishers, 106(1), pp. 35–44. doi: 10.1159/000145167.
- Tong, J. et al. (2011) ‘Dissection properties and mechanical strength of tissue components in human carotid bifurcations’, *Annals of Biomedical Engineering*. Springer US, 39(6), pp. 1703–1719. doi: 10.1007/s10439-011-0264-y.
- Tsamis, A., Krawiec, J. T. and Vorp, D. A. (2013) ‘Elastin and collagen fibre microstructure of the human aorta in ageing and disease: a review.’, *Journal of the Royal Society, Interface / the Royal Society*, 10(83), p. 20121004. doi: 10.1098/rsif.2012.1004.
- Tvergaard, V. and Hutchinson, J. W. (1992) ‘The relation between crack growth resistance and fracture process parameters in elastic-plastic solids’, *Journal of the Mechanics and Physics of Solids*. Pergamon, 40(6), pp. 1377–1397. doi: 10.1016/0022-5096(92)90020-3.
- Ulbricht, D. et al. (2004) ‘Cervical artery dissection: An atypical presentation with Ehlers-Danlos-like collagen pathology?’, *Neurology*. Wolters Kluwer Health, Inc. on behalf of the American Academy of Neurology, 63(9), pp. 1708–1710. doi: 10.1212/01.WNL.0000142970.09454.30.
- Ulug, P. et al. (2012) ‘Endovascular versus conventional medical treatment for uncomplicated chronic type B aortic dissection.’, *The Cochrane database of systematic reviews*, 11, p. CD006512. doi: 10.1002/14651858.CD006512.pub2.
- Vilacosta, I. et al. (no date) ‘Acute aortic syndrome: a new look at an old conundrum’, *pmj.bmj.com*. Available at: <https://pmj.bmj.com/content/86/1011/52.short> (Accessed: 15 February 2020).
- Vorp, D. a., Raghavan, M. L. and Webster, M. W. (1998) ‘Mechanical wall stress in abdominal aortic aneurysm: Influence of diameter and asymmetry’, *Journal of Vascular Surgery*, 27(4), pp. 632–639.
- Wang, L. et al. (2015) ‘Modelling of tear propagation and arrest in fibre-reinforced soft tissue subject to internal pressure’, *Journal of Engineering Mathematics*. Springer Netherlands, 95(1), pp. 249–265. doi: 10.1007/s10665-014-9757-7.
- Wang, L. et al. (2017) ‘Propagation of dissection in a residually-stressed artery model’, *Biomechanics and Modeling in Mechanobiology*. Springer Berlin Heidelberg, 16(1), pp. 139–149. doi: 10.1007/s10237-016-0806-1.
- Wang, L. et al. (2018) ‘Modelling peeling- and pressure-driven propagation of arterial dissection’, *Journal of Engineering Mathematics*. Springer Netherlands, 109(1), pp. 227–238. doi: 10.1007/s10665-017-9948-0.

- Wang, M. and Lakatta, E. G. (2002) 'Altered regulation of matrix metalloproteinase-2 in aortic remodeling during aging', *Hypertension*, 39(4), pp. 865–873. doi: 10.1161/01.HYP.0000014506.13322.66.
- Weisbecker, H. et al. (2012) 'Layer-specific damage experiments and modeling of human thoracic and abdominal aortas with non-atherosclerotic intimal thickening.', *Journal of the mechanical behavior of biomedical materials*, 12, pp. 93–106. doi: 10.1016/j.jmbbm.2012.03.012.
- Whittle, M. A. et al. (1990) 'Collagen in dissecting aneurysms of the human thoracic aorta. Increased collagen content and decreased collagen concentration may be predisposing factors in dissecting aneurysms.', *The American journal of cardiovascular pathology*, 3(4), pp. 311–9. Available at: <http://www.ncbi.nlm.nih.gov/pubmed/2129573> (Accessed: 14 February 2017).
- Witter, K., Tonar, Z. and Schöpfer, H. (2016) 'How many Layers has the Adventitia? - Structure of the Arterial Tunica Externa Revisited', *Anatomia, Histologia, Embryologia*. doi: 10.1111/ahe.12239.
- Witzenburg, C. M. et al. (2017) 'Failure of the porcine ascending aorta: Multidirectional experiments and a unifying microstructural model', *Journal of Biomechanical Engineering. American Society of Mechanical Engineers Digital Collection*, 139(3). doi: 10.1115/1.4035264.
- Wolinsky, H. and Glagov, S. (1967) 'Nature of species differences in the medial distribution of aortic vasa vasorum in mammals.', *Circulation research*. Lippincott Williams & Wilkins, 20(4), pp. 409–421. doi: 10.1161/01.RES.20.4.409.
- Xu, X.-P. et al. (1993) 'Void nucleation by inclusion debonding in a crystal matrix', *Modelling and Simulation in Materials Science and Engineering*. IOP Publishing, 1(2), pp. 111–132. doi: 10.1088/0965-0393/1/2/001.

Chapter 3

3 ESTABLISHED THEORY

3.1 Continuum Mechanics

Continuum mechanics involves the analysis of the kinematics and mechanical behaviour of materials (Malvern, 1969). This section outlines the essential elements of continuum mechanics required for the interpretation of the subsequent chapters. Vectors, tensors, and matrices are denoted by **bold** type face. Index notation is also frequently used in order to simplify the representation of vector equations. For example, the dot product of two 3D vectors (\mathbf{u} , \mathbf{v}) may be written using summation convention:

$$\mathbf{u} \cdot \mathbf{v} = u_1 v_1 + u_2 v_2 + u_3 v_3 = \sum_{i=1}^3 u_i v_i = u_i v_i \quad (3.1)$$

Where $i = 1,2,3$. In the case of a 3x3 tensor, the location of each component may be defined by subscripts $i, j = 1,2,3$.

3.1.1 Deformation and Motion

A classic representation of the configuration of a continuum body undergoing motion and deformation is illustrated in Figure 3.1. Where the reference configuration of a body (undeformed/Lagrangian configuration) is defined by the domain Ω_0 , at time $t = 0$. If such a body is considered to undergo motion χ , such that the current configuration, (which is the deformed/Eulerian configuration) can be described as the region encompassed by Ω . The position of a material point P in the reference configuration, with respect to the origin O , is denoted by the vector \mathbf{X} . A vector such

as \mathbf{X} can be described for all points within Ω_0 . Points within Ω_0 are known as material (Lagrangian) coordinates. In the current configuration the position of P is given by

$$\mathbf{x} = \boldsymbol{\chi}(\mathbf{X}, t) \quad (3.2)$$

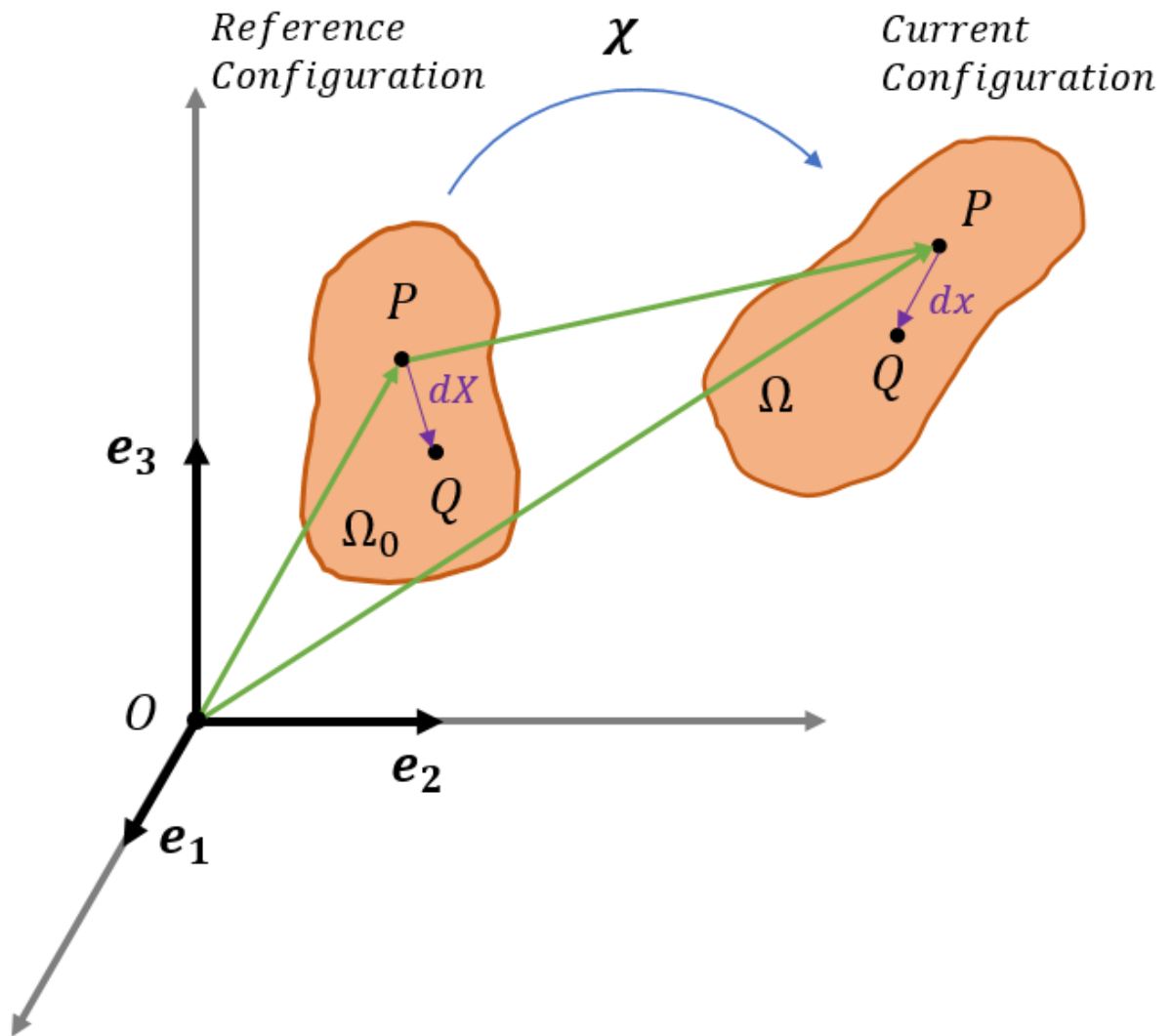


Figure 3.1: Classical schematic of a continuum body undergoing motion and deformation.

Similar to the reference configuration, the coordinates of \mathbf{x} are referred to as the spatial (Eulerian) coordinates. The displacement \mathbf{u} that the material point P undergoes

between the reference and current configuration is defined as $\mathbf{u} = \mathbf{x} - \mathbf{X}$. Rearranging in terms of \mathbf{X} and t gives:

$$\mathbf{u} = \chi(\mathbf{X}, t) - \mathbf{X} \quad (3.3)$$

The quantification of deformation and strain in a body is of primary importance here, rather than the rigid body displacement. A second material point Q is considered on Ω_0 and an infinitesimal line $d\mathbf{X}$, which is bound by the points P and Q . This infinitesimal line $d\mathbf{X}$ is transformed to $d\mathbf{x}$ in the current configuration. In order to calculate the strain, this transformation must be described through a second order tensor known as the deformation gradient, \mathbf{F} , and it is defined as:

$$\mathbf{F} = \frac{\partial \chi}{\partial \mathbf{X}} = \frac{\partial \mathbf{x}}{\partial \mathbf{X}} \quad (3.4)$$

The determinant of \mathbf{F} is known as the Jacobian of the deformation gradient. The Jacobian of the deformation gradient describes the ratio of volume change between the current configuration and the reference configuration at the material point P with the expression:

$$J = \det(\mathbf{F}) \quad (3.5)$$

The velocity, \mathbf{v} , of the material point P may be defined as:

$$\mathbf{v} = \frac{\partial \mathbf{x}}{\partial t} \quad (3.6)$$

Where the partial derivative with respect to time is equal to the rate of change of \mathbf{x} for a fixed \mathbf{X} . The gradient of the spatial velocity, \mathbf{L} , then is defined as:

$$\mathbf{L} = \frac{\partial \mathbf{v}}{\partial \mathbf{x}} \quad (3.7)$$

Which can also be expressed as:

$$\mathbf{L} = \dot{\mathbf{F}}\mathbf{F}^{-1} \text{ or } \dot{\mathbf{F}} = \mathbf{L}\mathbf{F} \quad (3.8)$$

Where $\dot{\mathbf{F}}$ is the derivative of the deformation gradient with respect to time. This spatial velocity gradient \mathbf{L} is commonly decomposed into the symmetric rate of deformation tensor \mathbf{D} and the antisymmetric spin tensor \mathbf{W} with the following expressions:

$$\mathbf{L} = \mathbf{D} + \mathbf{W} \quad (3.9)$$

$$\mathbf{D} = \frac{1}{2}(\mathbf{L} + \mathbf{L}^T) = \text{sym}(\mathbf{L}), \text{ and} \quad (3.10)$$

$$\mathbf{W} = \frac{1}{2}(\mathbf{L} - \mathbf{L}^T) = \text{asym}(\mathbf{L}) \quad (3.11)$$

3.1.2 Strain tensors and strain rate measures

There are a number of different measures we can construct from the deformation gradient in order to describe various strain states. One such measure is the Green-Lagrange strain, \mathbf{E} , defined as:

$$\mathbf{E} = \frac{1}{2}(\mathbf{F}^T\mathbf{F} - \mathbf{I}) \quad (3.12)$$

Where \mathbf{F}^T is the transpose of \mathbf{F} , and \mathbf{I} is the identity tensor. We may also describe the Green-Lagrange strain using index notation: $E_{ij} = \frac{1}{2}\left(\frac{\partial u_i}{\partial X_j} + \frac{\partial u_j}{\partial X_i} + \frac{\partial u_k}{\partial X_i} \frac{\partial u_k}{\partial X_j}\right)$. This means the infinitesimal strain is found through assuming the product of the infinitesimal terms is zero, giving the expression:

$$\epsilon_{ij} = \frac{1}{2}\left(\frac{\partial u_i}{\partial X_j} + \frac{\partial u_j}{\partial X_i}\right) \quad (3.13)$$

The right Cauchy-Green deformation tensor, \mathbf{C} , defined in material (Lagrangian) coordinates, is often used as a fundamental measure of deformation in hyperelastic constitutive laws. It is defined as:

$$\mathbf{C} = \mathbf{F}^T \mathbf{F} \quad (3.14)$$

Its counterpart in spatial (Eulerian) coordinates is the left Cauchy-Green deformation tensor, \mathbf{B} , which is written as:

$$\mathbf{B} = \mathbf{F} \mathbf{F}^T \quad (3.15)$$

The deformation gradient \mathbf{F} may be decomposed into an orthogonal rotation tensor \mathbf{R} , and right (material), and left (spatial) symmetric stretch tensors, \mathbf{U} and \mathbf{V} respectively

$$\mathbf{F} = \mathbf{R} \mathbf{U} = \mathbf{V} \mathbf{R} \quad (3.16)$$

We may then consider deformation to be a rotation followed by a stretch ($\mathbf{F} = \mathbf{R} \mathbf{U}$) or a stretch followed by a rotation ($\mathbf{F} = \mathbf{V} \mathbf{R}$). These stretch tensors can be easily related to the right and left Cauchy-Green deformation tensors through the following expressions:

$$\mathbf{V}^2 = \mathbf{B}; \quad \mathbf{U}^2 = \mathbf{C} \quad (3.17)$$

The eigenvalues of \mathbf{U} are known as the principal stretches λ_i , and the logarithmic strain tensor can be calculated from \mathbf{V} :

$$\boldsymbol{\varepsilon}_{\log} = \ln(\mathbf{V}) \quad (3.18)$$

Recall from \mathbf{L} , that \mathbf{D} is the symmetric rate of deformation tensor (3.10). The logarithmic strain rate then is:

$$\dot{\boldsymbol{\varepsilon}}_{\log} = \mathbf{D} \quad (3.19)$$

3.1.3 Strain invariants

Let \mathbf{S} be a real symmetric second-order tensor: $\bar{\mathbf{S}} = \mathbf{S} = \mathbf{S}^T$. The eigenvalues of \mathbf{S} are the roots $\lambda_1, \lambda_2, \lambda_3$ of the cubic polynomial equation:

$$\det(\mathbf{S} - \lambda \mathbf{I}) = 0 \quad (3.20)$$

This can be expanded as:

$$-\lambda^3 + I_1 \lambda^2 - I_2 \lambda + I_3 = 0 \quad (3.21)$$

Where the quantities I_1, I_2, I_3 are the first three principal invariants of \mathbf{S} , these are defined as:

$$I_1 = \text{tr}(\mathbf{S}) \quad (3.22)$$

$$I_2 = \frac{1}{2} \left[(\text{tr}(\mathbf{S}))^2 - \text{tr}(\mathbf{S}^2) \right] \quad (3.23)$$

$$I_3 = \det(\mathbf{S}) \quad (3.24)$$

The first three principal invariants of the right Cauchy-Green tensor (\mathbf{C}) are commonly used in hyperelastic constitutive laws and are given as follows:

$$I_1 = \text{tr}(\mathbf{C}) = \lambda_1^2 + \lambda_2^2 + \lambda_3^2 \quad (3.25)$$

$$I_2 = \frac{1}{2} \left[(\text{tr}(\mathbf{C}))^2 - \text{tr}(\mathbf{C}^2) \right] = \lambda_1^2 \lambda_2^2 + \lambda_1^2 \lambda_3^2 + \lambda_2^2 \lambda_3^2 \quad (3.26)$$

$$I_3 = \det(\mathbf{C}) = J^2 = \lambda_1^2 \lambda_2^2 \lambda_3^2 \quad (3.27)$$

3.1.4 Stress measures

Let the deformed body Ω now be cut by a planar surface which separates the body into two portions (Figure 3.2). The body has a traction vector \mathbf{t} derived from the surface forces, and a vector \mathbf{n} , which is normal to the section surface. Cauchy stress $\boldsymbol{\sigma}$ is the second order symmetric tensor as the force per unit deformed surface area ds given by:

$$\mathbf{t} = \boldsymbol{\sigma} \mathbf{n} \quad (3.28)$$

The Kirchhoff stress is given as:

$$\boldsymbol{\tau} = J \boldsymbol{\sigma} \quad (3.29)$$

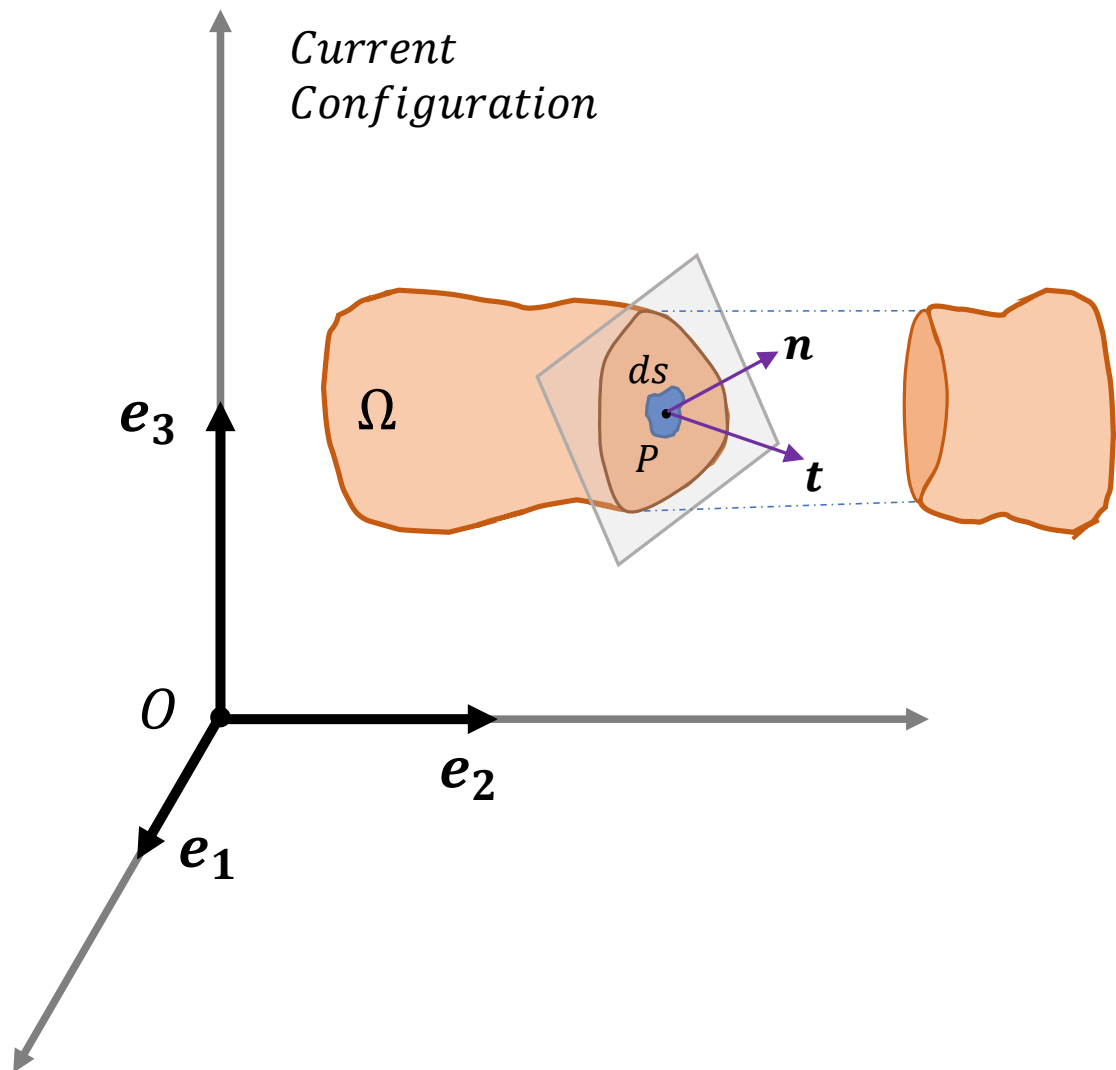


Figure 3.2: Traction vectors \mathbf{t} acting on infinitesimal surface elements ds with outward unit normals \mathbf{n} .

Where J has its usual meaning of the determinant of the deformation gradient \mathbf{F} , which is a measure of the volume change between the reference configuration and the current configuration. The First Piola-Kirchhoff stress (PK1), \mathbf{P} , is defined as the force per unit surface area in the reference (undeformed) configuration. The transpose of the unsymmetric tensor \mathbf{P} is frequently called the nominal stress tensor \mathbf{N} , such that $\mathbf{N} =$

\mathbf{P}^T . Using Nanson's formula, we may relate the First Piola-Kirchhoff stress to the Cauchy stress $\boldsymbol{\sigma}$ in the current configuration as:

$$\mathbf{P} = J\boldsymbol{\sigma}\mathbf{F}^{-T} \quad (3.30)$$

Closely related to \mathbf{P} is the symmetric Second Piola-Kirchhoff (PK2) stress tensor, \mathbf{S} . The PK2 may be expressed in terms of the PK1 or the Cauchy stress as follows:

$$\mathbf{S} = \mathbf{P}\mathbf{F}^T; \quad \mathbf{S} = J\mathbf{F}^{-1}\boldsymbol{\sigma}\mathbf{F}^{-T} \quad (3.31)$$

3.1.5 Hyperelastic Materials

A so-called Hyperelastic material (often referred to as a Green-elastic material) postulates the existence of an elastic free-energy function Ψ , from which a constitutive material response may be derived (Holzapfel, 2000). It is particularly useful for large deformation applications. For this reason, it is widely used in the description of the mechanical behaviour of soft tissues (Holzapfel, Gasser and Ogden, 2000; Nolan *et al.*, 2014). We may express the second Piola-Kirchhoff stress as the derivative of Ψ with respect to the right Cauchy-Green tensor:

$$\mathbf{S} = 2 \frac{\partial \Psi(\mathbf{C})}{\partial \mathbf{C}} \quad (3.32)$$

We may then also transform the second Piola-Kirchhoff stress into the current configuration to yield the Cauchy stress. Which can also be expressed this in terms of the left Cauchy-Green tensor:

$$\boldsymbol{\sigma} = 2J^{-1}\mathbf{F} \frac{\partial \Psi(\mathbf{C})}{\partial (\mathbf{C})} \mathbf{F}^T = 2J^{-1}\mathbf{B} \frac{\partial \Psi(\mathbf{B})}{\partial (\mathbf{B})} \quad (3.33)$$

The strain energy potential can then be expressed as a function of the strain invariants shown in (3.25),(3.26),(3.27). For an isotropic material, the strain energy potential

becomes a function of the first three invariants such that $\Psi(\mathbf{B}) = \Psi(I_1, I_2, I_3)$. In such a case the strain energy potential may be expressed as the derivative of Ψ with respect to \mathbf{B} , giving:

$$\frac{\partial \Psi(\mathbf{B})}{\partial \mathbf{B}} = \frac{\partial \Psi}{\partial I_1} \frac{\partial I_1}{\partial \mathbf{B}} + \frac{\partial \Psi}{\partial I_2} \frac{\partial I_2}{\partial \mathbf{B}} + \frac{\partial \Psi}{\partial I_3} \frac{\partial I_3}{\partial \mathbf{B}} \quad (3.34)$$

The derivatives of the invariants with respect to the left Cauchy-Green tensor are then:

$$\frac{\partial I_1}{\partial \mathbf{B}} = \mathbf{I}, \quad \frac{\partial I_2}{\partial \mathbf{B}} = I_1 \mathbf{I} - \mathbf{B}, \quad \frac{\partial I_3}{\partial \mathbf{B}} = I_3 \mathbf{B}^{-1} \quad (3.35)$$

Using the relation of (3.34) and (3.33) we may express the Cauchy stress as a function of \mathbf{B} , giving:

$$\boldsymbol{\sigma} = 2J^{-1} \left[I_3 \left(\frac{\partial \Psi}{\partial I_3} \right) \mathbf{I} + \left(\frac{\partial \Psi}{\partial I_1} + I_1 \frac{\partial \Psi}{\partial I_2} \right) \mathbf{B} - \frac{\partial \Psi}{\partial I_2} \mathbf{B}^2 \right] \quad (3.36)$$

Assuming incompressibility gives $I_3 = J = 1$. This results in the strain energy potential becoming a function of the first two strain invariants, I_1, I_2 , for an incompressible, isotropic strain energy potential such that:

$$\Psi(\mathbf{B}) = \Psi(I_1, I_2) \quad (3.37)$$

We can then express the Cauchy stress for any given incompressible isotropic hyperelastic material as follows:

$$\boldsymbol{\sigma} = -p \mathbf{I} + 2W_1 \mathbf{B} - 2W_2 \mathbf{B}^{-1} \quad (3.38)$$

Where $W_1 = \left(\frac{\partial \Psi}{\partial I_1} \right)$ and $W_2 = \left(\frac{\partial \Psi}{\partial I_2} \right)$, and p is the hydrostatic pressure which functions as a Lagrangian multiplier to enforce the incompressibility.

The Lagrangian multiplier must be determined through imposing equilibrium and boundary conditions.

3.2 Finite Element Method (FEM)

The finite element method is employed throughout this thesis to solve each of the continuum mechanics problems presented. These problems are predominantly solved using the commercial FE code, Abaqus (DS SIMULIA, R.I., USA). The advantages of using Abaqus (as opposed to a custom code) include in-built meshing techniques, and the ease of implementing novel surface interaction laws (UINTERs) and novel user-defined material laws (UMATs). Here, a brief background on the implicit solution scheme is provided, as well as the implementation of user-defined surface interactions and material laws.

3.2.1 Implicit solution scheme

In the implicit FE method, the stress state in a mesh is incrementally updated. The stress state at time $t + \Delta t$ is solved iteratively via convergence of a residual force vector within a specified tolerance. The Abaqus solver implements a form of the Newton-Raphson method to get convergence at each increment. The principle of virtual work (PVW) provides the fundamental equation of the finite element method (Hughes, 2012):

$$\int_{\Omega} \delta \boldsymbol{\varepsilon}^T \boldsymbol{\sigma} d\Omega = \int_S \delta \mathbf{u}^T \mathbf{t} dS \quad (3.39)$$

Where $\boldsymbol{\sigma}$ and \mathbf{t} are the stress and surface traction and $\delta \boldsymbol{\varepsilon}$ and $\delta \mathbf{u}$ are the virtual strain and virtual displacement vectors. Ω is a reference volume on which equilibrium is enforced, and Ω is bounded by the surface S . The FE approximation can now be introduced over each element (e) of volume (Ω_e) and surface (S_e), allowing us to express the stresses and strains as follows:

$$\delta \boldsymbol{\varepsilon} = \hat{\mathbf{B}}_e \delta \mathbf{u}_e \quad (3.40)$$

$$\delta \mathbf{u} = \widehat{\mathbf{N}}_e \delta \mathbf{u}_e \quad (3.41)$$

Where $\delta \mathbf{u}_e$ are the nodal displacements, $\widehat{\mathbf{B}}_e$ is the elemental shape function gradient matrix, and where $\widehat{\mathbf{N}}_e$ is the global shape function matrix. The principle of virtual work then becomes:

$$\sum_e \int_{\Omega_e} \delta \mathbf{u}_e^T \widehat{\mathbf{B}}_e^T \boldsymbol{\sigma}(\mathbf{u}_e) d\Omega = \sum_e \int_{S_e} \delta \mathbf{u}_e^T \widehat{\mathbf{N}}_e^T \mathbf{t} dS \quad (3.42)$$

$$\delta \mathbf{u}^T \int_{\Omega} \widehat{\mathbf{B}}^T \boldsymbol{\sigma}(\mathbf{u}) d\Omega - \delta \mathbf{u}_e^T \int_S \widehat{\mathbf{N}}^T \mathbf{t} dS = 0 \quad (3.43)$$

$$\delta \mathbf{u}^T \left(\int_{\Omega} \widehat{\mathbf{B}}^T \boldsymbol{\sigma}(\mathbf{u}) d\Omega - \int_S \widehat{\mathbf{N}}^T \mathbf{t} dS \right) = 0 \quad (3.44)$$

Given that the virtual displacement, $\delta \mathbf{u}$, is arbitrary, it then follows that:

$$\int_{\Omega} \widehat{\mathbf{B}}^T \boldsymbol{\sigma}(\mathbf{u}) d\Omega - \int_S \widehat{\mathbf{N}}^T \mathbf{t} dS = 0 \quad (3.45)$$

Introducing linear elasticity gives:

$$\boldsymbol{\sigma} = \mathbf{D} \boldsymbol{\varepsilon} = \mathbf{D} \widehat{\mathbf{B}} \mathbf{u}_e \quad (3.46)$$

Where \mathbf{D} is a fourth order elasticity tensor. We then define the external force vector, \mathbf{F}_{ext} , as follows:

$$\mathbf{F}_{ext} = \int_S \widehat{\mathbf{N}} \mathbf{t} dS \quad (3.47)$$

We may then express the PVW with consideration of linear elasticity in the following equations:

$$\int_{\Omega} \widehat{\mathbf{B}}^T \mathbf{D} \widehat{\mathbf{B}} \mathbf{u}_e d\Omega - \mathbf{F}_{ext} = 0 \quad (3.48)$$

$$\left(\int_{\Omega} \widehat{\mathbf{B}}^T \mathbf{D} \widehat{\mathbf{B}} d\Omega \right) \mathbf{u}_e - \mathbf{F}_{ext} = 0 \quad (3.49)$$

$$\mathbf{K} \mathbf{u}_e - \mathbf{F}_{ext} = 0 \quad (3.50)$$

Where \mathbf{K} is the familiar form of the global FE stiffness matrix. Returning to the PVW given in equation (3.45) we can develop a set of global equations for the out of balance residual force \mathbf{G} :

$$\mathbf{G}(\mathbf{u}) = \int_{\Omega} \widehat{\mathbf{B}}^T \boldsymbol{\sigma}(\mathbf{u}) d\Omega - \int_S \widehat{\mathbf{N}}^T \mathbf{t} dS \quad (3.51)$$

This non-linear set of equations must be solved for convergence to attain an equilibrium stress state in the body, such that

$$\mathbf{G}(\mathbf{u}) = 0 \quad (3.52)$$

Generally, for boundary value problems requiring a non-linear analysis and complex geometries, such a minimisation for convergence must be solved iteratively. As previously stated, the implicit solver used in Abaqus/Standard uses a Newton-Raphson scheme to step from time t to time $t + \Delta t$ by making an initial guess and iterating until the solution converges. In the Newton-Raphson scheme, a tangent taken to the function $f(x)$ is used to approximate to a converged solution:

$$x_{n+1} = x_n - \frac{f(x_n)}{f'(x_n)} \quad (3.53)$$

The approximation is deemed to be accurate when a tolerance is achieved.

$$|x_{i+1} - x_i| < tol \quad (3.54)$$

Following an initial guess for all nodal displacements $\mathbf{u}_i^{t+\Delta t}$ within an increment of an implicit analysis, the numerical scheme iterates until a stable equilibrium is achieved.

The Newton-Raphson minimisation process is applied to the residual force vector:

$$\mathbf{G}(\mathbf{u}^{t+\Delta t}) = 0 \quad (3.55)$$

For the i^{th} iteration:

$$\mathbf{u}_{i+1}^{t+\Delta t} = \mathbf{u}_i^{t+\Delta t} - \left[\frac{\partial \mathbf{G}(\mathbf{u}_i^{t+\Delta t})}{\delta \mathbf{u}} \right]^{-1} \mathbf{G}(\mathbf{u}_i^{t+\Delta t}) \quad (3.56)$$

Therefore, a change in nodal displacements yields:

$$\partial \mathbf{u}_{i+1} = \mathbf{u}_{i+1}^{t+\Delta t} - \mathbf{u}_i^{t+\Delta t} = - \left[\frac{\partial \mathbf{G}(\mathbf{u}_i^{t+\Delta t})}{\partial \mathbf{u}} \right]^{-1} \mathbf{G}(\mathbf{u}_i^{t+\Delta t}) \quad (3.57)$$

This can be written in terms of the tangent stiffness matrix, $\bar{\mathbf{K}}$, to form the linear equation for the problem:

$$\bar{\mathbf{K}}(\mathbf{u}_{i+1}^{t+\Delta t}) = \frac{\partial \mathbf{G}(\mathbf{u}_i^{t+\Delta t})}{\partial \mathbf{u}} \quad (3.58)$$

$$\bar{\mathbf{K}}(\mathbf{u}_{i+1}^{t+\Delta t}) \partial \mathbf{u}_{i+1} = \mathbf{G}(\mathbf{u}_i^{t+\Delta t}) \quad (3.59)$$

Finally, \mathbf{K} may be expressed as:

$$\mathbf{K}(\mathbf{u}) = \frac{\partial \mathbf{G}(\mathbf{u})}{\partial \mathbf{u}} = \frac{\partial}{\partial \mathbf{u}} \left(\int_V \mathbf{B}^T \boldsymbol{\sigma}(\mathbf{u}) \, dV - \mathbf{F}_{\text{ext}} \right) \quad (3.60)$$

$$= \frac{\partial}{\partial \mathbf{u}} \left(\int_V \mathbf{B}^T \boldsymbol{\sigma}(\mathbf{u}) \, dV \right) \quad (3.61)$$

$$\int_V \mathbf{B}^T \frac{\partial \boldsymbol{\sigma}(\mathbf{u})}{\partial \mathbf{u}} dV = \int_V \mathbf{B}^T \frac{\partial \boldsymbol{\sigma}(\mathbf{u})}{\partial \boldsymbol{\varepsilon}} \frac{\partial \boldsymbol{\varepsilon}}{\partial \mathbf{u}} dV \quad (3.62)$$

$$= \int_V \mathbf{B}^T \frac{\partial \boldsymbol{\sigma}(\mathbf{u})}{\partial \boldsymbol{\varepsilon}} \mathbf{B} dV \quad (3.63)$$

$$\mathbf{K}(\mathbf{u}) = \int_V \mathbf{B}^T \mathbf{D} \mathbf{B} dV \quad (3.64)$$

Where \mathbf{D} is the consistent tangent matrix, which is equal to the Jacobian of the constitutive law $\partial \boldsymbol{\sigma} / \partial \boldsymbol{\varepsilon}$. In each iteration of the Newton-Raphson method, \mathbf{K} must be calculated and inverted. Though computationally expensive, this ensures an accurate solution. For more details on the finite element method, the reader is referred to Bathe (2006) and Fagan (1992).

3.2.2 Implementation of user-defined material subroutines

In addition to the in-built library of constitutive laws, Abaqus caters for the use of novel material formulations through user defined material subroutines (UMATs). At each iteration of each time increment, the UMAT is called and the material deformation is passed into the subroutine. The UMAT calculates the stress and passes it out to the main program. To calculate the stress, the material Jacobian, defined as the change in stress at the end of a given time increment caused by an infinitesimal perturbation of the strain ($\partial \Delta \boldsymbol{\sigma} / \partial \Delta \boldsymbol{\varepsilon}$), needs to be calculated.

3.2.3 Implementation of user-defined surface interaction subroutines

In addition to the built-in library of surface interaction properties, Abaqus allows for the description of user-defined surface interaction subroutines (UINTERs). At each iteration of each time increment the UINTER is called at points (nodes) on the slave surface of a contact pair. The surface (nodal) deformation (RDISP) is passed into the UINTER and the stress is calculated in the form of a normal and tangential traction. Similarly to the UMAT, in order to calculate the stress in the UINTER, the interface

stiffness matrix (interface Jacobian) is required. This is defined as the change in the i^{th} stress component at the end of the time increment caused by an infinitesimal perturbation of the j^{th} component of the relative displacement increment array. In simple applications it can be computationally favourable to treat the Jacobian as symmetric and negate the additional non-symmetric terms. However, given the nonlinear, complex nature of the problems considered in this thesis, the majority of Abaqus computations involving UINTERs require the full unsymmetric interface stiffness matrix in the calculation of the stress components.

Bibliography

Holzapfel, A. G. (2000) *Nonlinear solid mechanics II*. John Wiley & Sons, Inc.

Holzapfel, G. A., Gasser, T. C. and Ogden, R. W. (2000) 'A new constitutive framework for arterial wall mechanics and a comparative study of material models', *Journal of Elasticity*. Kluwer Academic Publishers, 61(1–3), pp. 1–48. doi: 10.1023/A:1010835316564.

Hughes, T. (2012) *The finite element method: linear static and dynamic finite element analysis*. Available at: https://books.google.com/books?hl=en&lr=&id=cHH2n_qBK0IC&oi=fnd&pg=PP1&ots=vsynv9b-X_&sig=PG1-7hRpaSuztxDPkUeF82xkXRQ.

Malvern, L. E. (1969) *Introduction to the Mechanics of a Continuous Medium*.

Nolan, D. R. et al. (2014) 'A robust anisotropic hyperelastic formulation for the modelling of soft tissue', *Journal of the Mechanical Behavior of Biomedical Materials*, 39, pp. 48–60. doi: 10.1016/j.jmbbm.2014.06.016.

Chapter 4

4 PRELIMINARY COHESIVE ZONE MODEL DEVELOPMENT AND ANALYSIS

4.1 Introduction

Cohesive zone models (CZMs) have been extensively used to describe an interface undergoing separation (Barenblatt, 1959; Xu *et al.*, 1993; van den Bosch, Schreurs and Geers, 2006; Máirtín *et al.*, 2014). CZMs have been used to model crack propagation in ductile metals (Nielsen and Hutchinson, 2012), polyethylene (Ivankovic, Pandya and Williams, 2004), porous materials (Nakamura and Wang, 2001) and concrete beams (Aure and Ioannides, 2010). They have also been used to model the delamination of cells from substrates (McGarry and McHugh, 2008), polymer coatings from stents (Hopkins, McHugh and McGarry, 2010; Máirtín *et al.*, 2014), inter-laminar failure in carbon-fibre laminates (Gallagher, Lamorinière and McGarry, 2018, 2019), and failure of coatings of diamond-coated cutting tools (Hu, Chou and Thompson, 2008).

The calibration of CZM parameters requires experimental testing data (Ivankovic, Pandya and Williams, 2004; Di Leo *et al.*, 2014; Wu *et al.*, 2016). The primary outputs of these tests are interface strength and fracture energy. It is extremely difficult to measure the stiffness of interfaces in highly elastic materials. The characteristic length (δ) or the modulus (K) of the initial elastic region of some CZMs often dictates the fracture energy (G) and vice-versa. This is common in exponential CZM formulations as seen in (Xu *et al.*, 1993; van den Bosch, Schreurs and Geers, 2006; Dimitri *et al.*, 2015). Therefore, the choice of fracture energy may anomalously influence the

stiffness and characteristic length of the interface. Piecewise CZMs allow for the specification of K (and by extension δ) and G independently (Camanho, Dávila and De Moura, 2003; Park, Paulino and Roesler, 2009). Choice of CZM should be motivated by experimental data and boundary conditions.

CZMs may be coupled or uncoupled. In a coupled CZM the traction depends on the separation vector which will include both normal and tangential opening (Δ_n, Δ_t) whereas in an uncoupled CZM the normal traction (T_n) depends only on the normal opening (Δ_n). Most engineering applications involve mixed separation and therefore should implement mixed mode (coupled) CZMs. Achieving a physically realistic mixed mode response is important in such applications.

Many constitutive relationships of traction-separation laws have been proposed, these include but are not limited to, linear softening (Camacho and Ortiz, 1996), bilinear softening, cubic polynomial, exponential (Xu *et al.*, 1993; van den Bosch, Schreurs and Geers, 2006; McGarry *et al.*, 2014), exponential softening, and trapezoidal (Tvergaard and Hutchinson, 1992). Here we present two forms of an exponential softening model and introduce a feature whereby tangential interface strength can be augmented as a function of compressive normal traction. We also explore the model in a potential-based form and demonstrate undesirable behaviour common to potential based models. We then compare to the exponential softening model available in the commercial FEA software ABAQUS when damage evolution is specified according to energy and demonstrate anomalous behaviour of the traction in certain scenarios. We propose an alternative formulation of exponential softening than what is currently available in Abaqus.

4.2 Development of non-potential based mixed-mode CZMs with exponential damage and overclosure penalisation (CZM1 and CZM2)

For a given interface displacement vector $\mathbf{\Delta}$ with normal and tangential (shear) components Δ_n and Δ_t , respectively, the corresponding displacement magnitude is given as $\Delta_m = (\Delta_n^2 + \Delta_t^2)^{1/2}$ and the mode angle is given as $\varphi = \tan^{-1}(\Delta_t/\Delta_n)$. The magnitude of the interface traction is expressed as a function of Δ_m and φ by the following formulation:

$$T_m(\Delta_m, \varphi) = \begin{cases} K_m \Delta_m, & \Delta_m < T_m^{max}(\varphi)/K_m \\ K_m T_m^{max}(\varphi)/K_m \Psi(\varphi), & \Delta_m \geq T_m^{max}(\varphi)/K_m \end{cases} \quad (4.1)$$

We refer to Ψ as the integrity of the interface (i.e. $\Psi = (1 - D)$, where D is referred to as the interface damage). Ψ monotonically decreases from 1 to 0 with increasing interface separation, such that

$$\Psi(\varphi) = \exp\left(-\frac{\Delta_m^{max} - T_m^{max}(\varphi)/K_m}{\delta_m^*(\varphi)}\right) \frac{\Delta_m}{\Delta_m^{max}} \quad (4.2)$$

where K_m is the intrinsic elastic stiffness of the interface. K_m is assumed to be mode-independent. $T_m^{max}(\varphi)$ is the specified mode-dependent interface strength; the corresponding displacement ($\delta_m^{el}(\varphi) = T_m^{max}(\varphi)/K_m$) represents the elastic limit of interface separation at the point of damage initiation. The mode-dependent parameter $\delta_m^*(\varphi)$ governs the rate of softening in the damage region ($\Delta_m \geq T_m^{max}(\varphi)/K_m$). The interface strength is defined as a function of the mode as follows:

$$T_m^{max}(\varphi) = \tau_{max} - \left(\frac{\tau_{max} - \sigma_{max}}{1 - \exp\left(-\frac{\pi}{\Omega^T}\right)} \right) \left(1 - \exp\left(-\frac{\varphi}{\Omega^T}\right) \right) \quad (4.3)$$

where τ_{max} is the mode II interface strength, Ω^T sets the non-linearity of the transition from mode II to mode I, and σ_{max} is the mode I interface strength. The mode mixity of the initial interface damage parameter $\delta_m^*(\varphi)$ is obtained from

$$\delta_m^*(\varphi) = \frac{G_m(\varphi)}{\Gamma_m^{max}(\varphi)} - \frac{\Gamma_m^{max}(\varphi)}{2K_m} \quad (4.4)$$

where $G_m(\varphi)$ is the mode-dependent fracture energy

$$\begin{aligned} G_m(\varphi) &= \frac{1}{2} K_m \delta_m^{el}(\varphi)^2 \\ &+ \int_{\Gamma_m^{max}(\varphi)/K_m}^{\infty} \Gamma_m^{max}(\varphi) \exp\left(-\frac{\Delta_m^{max} - \Gamma_m^{max}(\varphi)/K_m}{\delta_m^*}\right) d\Delta_m \end{aligned} \quad (4.5)$$

We may specify the mode-dependence of $G_m(\varphi)$ using the following function:

$$G_m(\varphi) = G_t^0 - \left(\frac{G_t^0 - G_n^0}{1 - \exp\left(-\frac{\pi}{2\Omega^G}\right)} \right) \left(1 - \exp\left(-\frac{\varphi}{\Omega^G}\right) \right) \quad (4.6)$$

where G_t^0 is the mode II fracture energy and G_n^0 is the mode I fracture energy, Ω^G sets the non-linearity of the transition from mode II to mode I. Finally, we complete the description of the cohesive zone formulation by decomposing T_m into the normal and tangential components, T_n and T_t , respectively, such that

$$T_n = \begin{cases} K_{noc} \Delta_n, \Delta_n < 0 \\ T_m \sin(\varphi), \Delta_n \geq 0 \end{cases} \quad (4.7)$$

$$T_t = T_m \cos(\varphi) \quad (4.8)$$

where K_{noc} is the overclosure penalty stiffness.

We include a dependence of the mode II interface strength, τ_{max} , on normal compression at the interface, such that

$$\tau_{max}(T_n) = \begin{cases} \tau_{max}^{nc}(T_n), & \Delta_n < 0 \\ \tau_{max}^0, & \Delta_n \geq 0 \end{cases}$$

as described in equation (4.9). The mode II interface strength increases within increasing (negative) normal traction, such that

$$\tau_{max}^{nc}(T_n) = \tau_{max}^0 + \tau_{max}^0(F_{oc} - 1.0) * \left(1 - \exp\left(\frac{T_n \frac{K_{noc}^*}{\sigma_{max}}}{K_m}\right) \right) \quad (4.9)$$

where $\tau_{max}^{nc}(\Delta_n)$ is the increased value of tangential strength due to a normal compression at the interface. τ_{max}^0 is the maximum tangential strength, as encountered during a pure mode II separation when $\Delta_n = 0$ and $T_n = 0$. The parameter F_{oc} prescribes the maximum (plateau) value of increased shear strength due to compressive normal tractions at the interface. The parameter K_{noc}^* governs the sensitivity of maximum (plateau) shear stress to compressive normal tractions. Unless otherwise stated in this thesis, we assume that $\tau_{max} = \tau_{max}^0$, i.e. maximum tangential strength is not increased due to normal compression at the interface.

Alternative form of damage and softening (CZM2)

To demonstrate that alternative forms of damage softening laws can be readily incorporated into our CZM framework, we next present a small modification of (4.2) whereby in which exponential damage is assumed to depend on the square of the interface separation. Again, starting with equation ((4.1), and the integrity of the interface (Ψ) is now defined as

$$\Psi(\varphi) = \exp\left(-\left(\frac{\Delta_m^{max} - \frac{T_m^{max}(\varphi)}{K_m}}{\delta_m^*(\varphi)}\right)^2\right) \frac{\Delta_m}{\Delta_m^{max}} \quad (4.10)$$

We make use of the same relation of $G(\varphi) = \int_0^\infty T_m(\Delta_m, \varphi) d\Delta_m$ in order to obtain an expression for δ_m^* . The description of $G_m(\varphi)$ is given as follows

$$\begin{aligned}
G_m(\varphi) &= \frac{1}{2} K_m \delta_m^{el}(\varphi)^2 \\
&+ \int_{\Gamma_m^{max}(\varphi)/K_m}^\infty \Gamma_m^{max}(\varphi) \exp\left(-\left(\frac{\Delta_m^{max} - \frac{\Gamma_m^{max}(\varphi)}{K_m}}{\delta_m^*(\varphi)}\right)^2\right) d\Delta_m
\end{aligned} \tag{4.11}$$

Integrating we get the following expression which includes the error function

$$\begin{aligned}
G_m &= \frac{1}{2} K_m \delta_m^{el}(\varphi)^2 \\
&+ \Gamma_m^{max}(\varphi) \left(\lim_{\Delta_m \rightarrow \infty} \left(\frac{1}{2} \sqrt{\pi} \delta_m^*(\varphi) \operatorname{erf}\left(\frac{\Delta_m - \frac{\Gamma_m^{max}(\varphi)}{K_m}}{\delta_m^*(\varphi)}\right) \right) \right)
\end{aligned} \tag{4.12}$$

As $\Delta_m \rightarrow \infty$ we arrive at the final expression for $\delta_m^*(\varphi)$

$$\delta_m^*(\varphi) = -\frac{\Gamma_m^{max}(\varphi)}{K_m \sqrt{\pi}} + \frac{2G_m(\varphi)}{\sqrt{\pi} \Gamma_m^{max}(\varphi)} \tag{4.13}$$

4.3 Exploration of CZM1 and CZM2 behaviour

We firstly present the response of CZM1 and CZM2 to pure mode II loading, as shown in Figure 4.1(A). Normalised tangential traction (T_t/τ_{max}) is presented as a function of normalised tangential separation (Δ_t/δ_t). Traction increases according to the interfacial stiffness K_m until the prescribed mode II strength τ_{max} is reached. Further deformation results in damage and softening. Due to the form of the respective exponential damage laws, CZM1 initially softens at a faster rate than CZM2. An expression for the instantaneous incremental energy dissipation (Cazes *et al.*, 2009) is

given as $d\phi_i = 0.5(Td\underline{\Delta} - \underline{\Delta}dT)$. As shown in Figure 4.1(B), positive instantaneous energy dissipation is observed throughout the mode II separation for both CZM1 and CZM2.

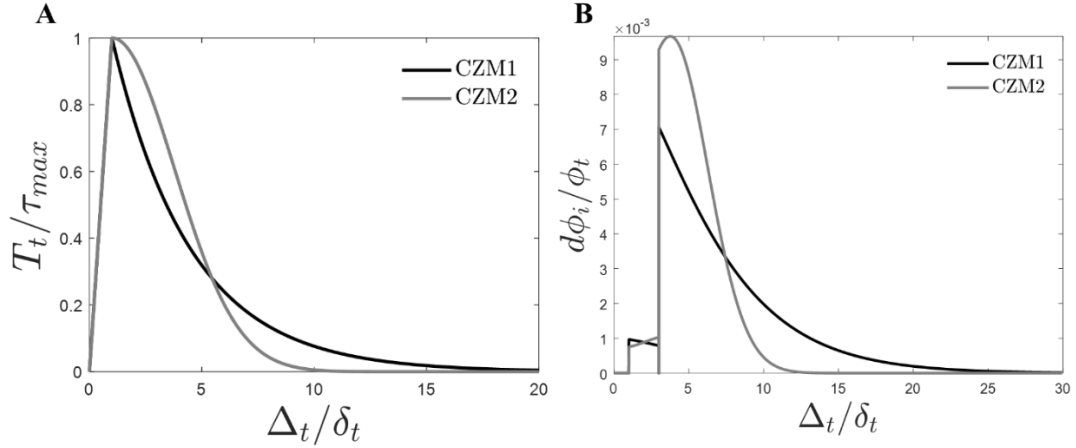


Figure 4.1. (A) Normalised traction separation curves for a mode II separation for both formulations of the proposed model. $K_m = 10$ MPa, $\tau_{max} = 5$ MPa, $G_t^0 = 10$ N/mm; (B) Instantaneous incremental energy dissipation ($d\phi_i/\phi_t$) as a function of normalised tangential separation for CZM1 and CZM2 during a mode II displacement.

In Figure 4.2(A) we explore the influence of normal compressive tractions on tangential fracture. An increase in magnitude of a compressive normal traction T_n (with $T_n < 0$) results in an increase in $\tau_{max}^{nc}(T_n)$, up to a plateau value of $\tau_{max}^0 F_{oc}$ as $T_n \rightarrow -\infty$. In Figure 4.2(B) further explores influence of a fixed applied normal separation on the maximum tangential traction, T_{max} , encountered during a subsequent tangential separation. As expected, normal interface separation ($\Delta_n > 0$) results in a reduction in T_{max} . In contrast, if $\Delta_n < 0$ a negative normal traction ($T_n < 0$) is obtained through the overclosure penalty term (equation (4.9)). This results in an increase in $\tau_{max}^{nc}(T_n)$ up to a plateau value with increasingly negative normal traction.

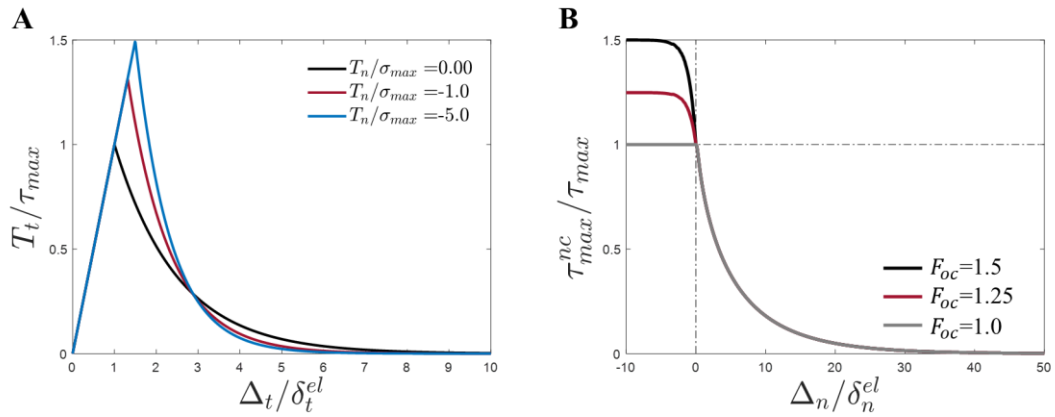


Figure 4.2. (A) Influence of compressive normal tractions on tangential fracture. (B) Maximum tangential traction shown as a function of the F_{oc} parameter.

4.3.1 Proportional loading

Proportional loading paths: CZM1 and CZM2 are examined under mixed-mode proportional loading conditions whereby Δ_m increases at a constant mode angle φ . Computed traction-separation responses are presented in Figure 4.3 for the case of $K_m = 10$ MPa, $\tau_{max} = 5(\sigma_{max})$, $G_t = 5(G_n)$, $\Omega^T = \pi/16$, $\Omega^G = \Omega^T$ for both models. CZM1 is shown in Figure 4.3(A,B), CZM2 in Figure 4.3(C, D). Consistent mixed-mode behaviour is observed for both formulations, with a gradual transition from mode II behaviour to mode I behaviour. In accordance with equations (4.3) and (4.6), identical fracture energy is obtained for both formulations for such proportional loading paths, as shown in Figure 4.4. The computed total fracture energy G_{total} monotonically increases from G_n^0 to G_t^0 .

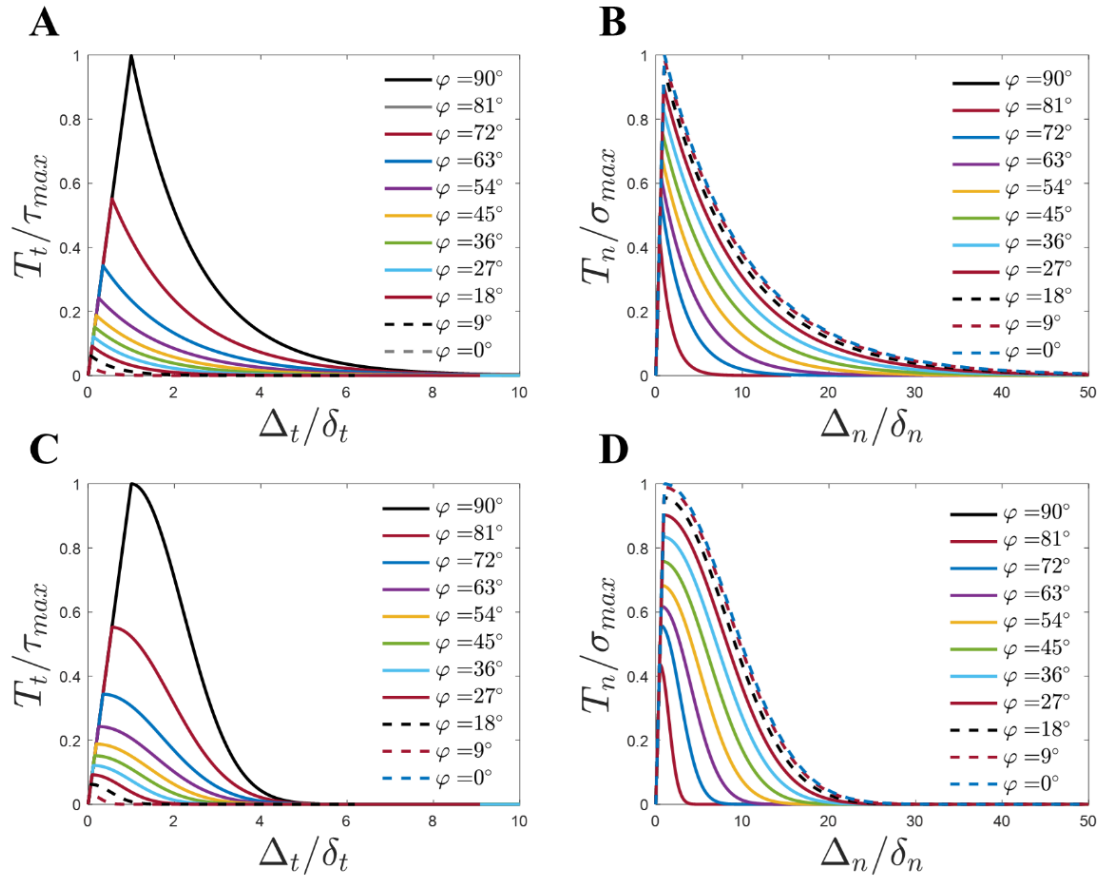


Figure 4.3: Mixed mode response of each CZM undergoing proportional loading ranging from mode II to mode I. Normalised traction vs. separation in the normal direction (B,D) and tangential direction (A,C) for CZM1 (A&B), CZM2 (C&D) undergoing proportional loading. $K_m = 10$ MPa, $\tau_{max} = 5(\sigma_{max})$, $G_t = 5(G_n)$.

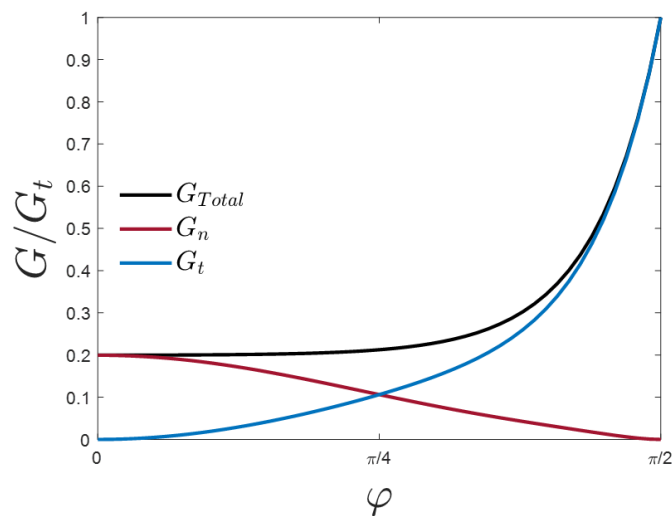


Figure 4.4. Computed fracture energy as a function of mode angle φ for CZM1 and

CZM2 under proportional loading in the case of $K_m = 10 \text{ MPa}$, $\tau_{max} = 5(\sigma_{max})$, $G_t = 5(G_n)$, $\Omega^T = \pi/16$, $\Omega^G = \Omega^T$.

4.3.2 Non-proportional loading

Non-proportional loading paths: We next consider non-proportional loading path whereby the interface undergoes an initial mode II separation to a prescribed value of $\Delta_t = \Delta_t^{max}$, followed by a subsequent normal separation to complete failure. Figure 4.5 shows the traction-separation response, again for the case of $K_m = 10 \text{ MPa}$, $\tau_{max} = 5(\sigma_{max})$, $G_t = 5(G_n)$, $\Omega^T = \pi/16$, $\Omega^G = \Omega^T$ for both models. CZM1 is shown in Figure 4.5(A,B), CZM2 in (C,D). Consistent behaviour is again observed for both models. If significant damage is computed during the initial mode II separation, the maximum normal traction computed during subsequent normal separation is reduced. This demonstrates that sensible mixed mode coupling is provided by both CZM1 and CZM2. Computed fracture energy during such non-proportional loading paths is presented in Figure 4.6. for the non-proportional loading paths presented Figure 4.5. While identical fracture energy is not obtained for both formulations, a monotonic increase as a function of increasing Δ_t^{max} is computed both formulations. Additionally, monotonically increasing/decreasing tangential/normal fracture energy contributions are also computed.

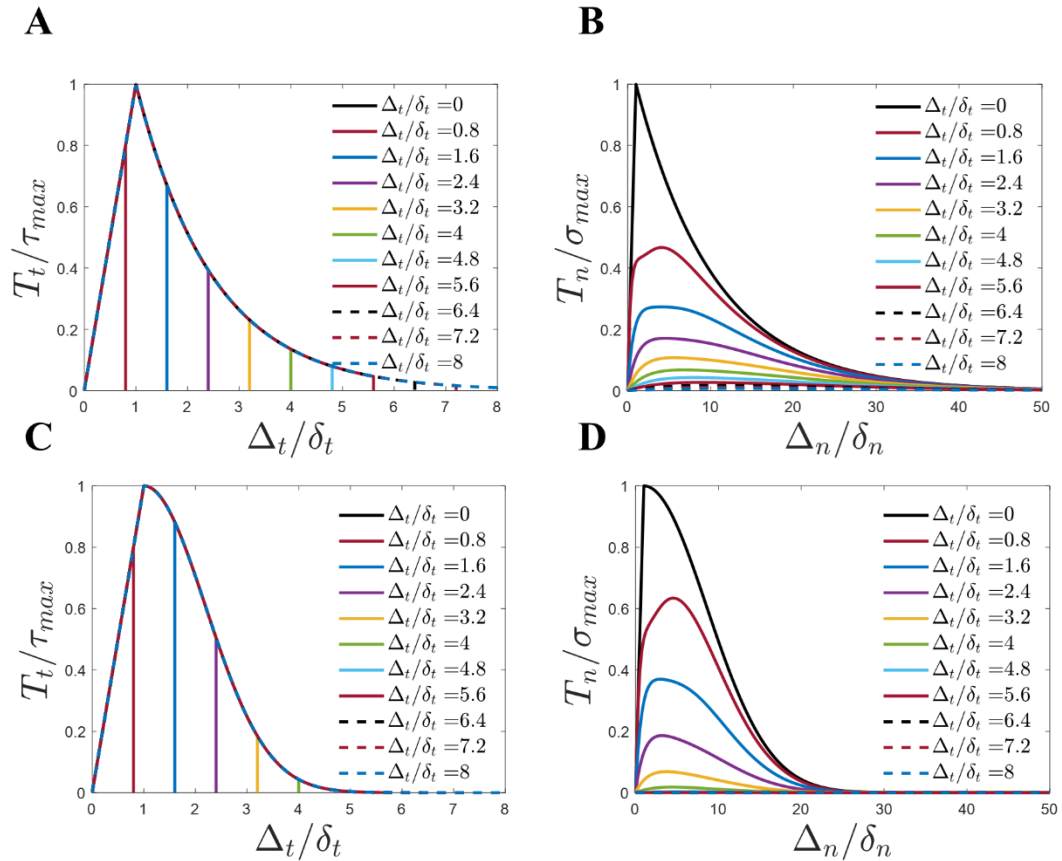


Figure 4.5: Normalised traction vs. separation in the normal direction (B,D) and tangential direction (A,C) for CZM1 (A&B), CZM2 (C&D) undergoing non-proportional loading. Each simulation involves incrementally increasing tangential displacements beginning at $\Delta_t/\delta_t = 0$ and increasing until the interface is fully debonded in the tangential direction followed by a complete normal separation ($\Delta_n/\delta_n = 50$). $K_m = 10$ MPa, $\tau_{max} = 5(\sigma_{max})$, $G_t = 5(G_n)$.

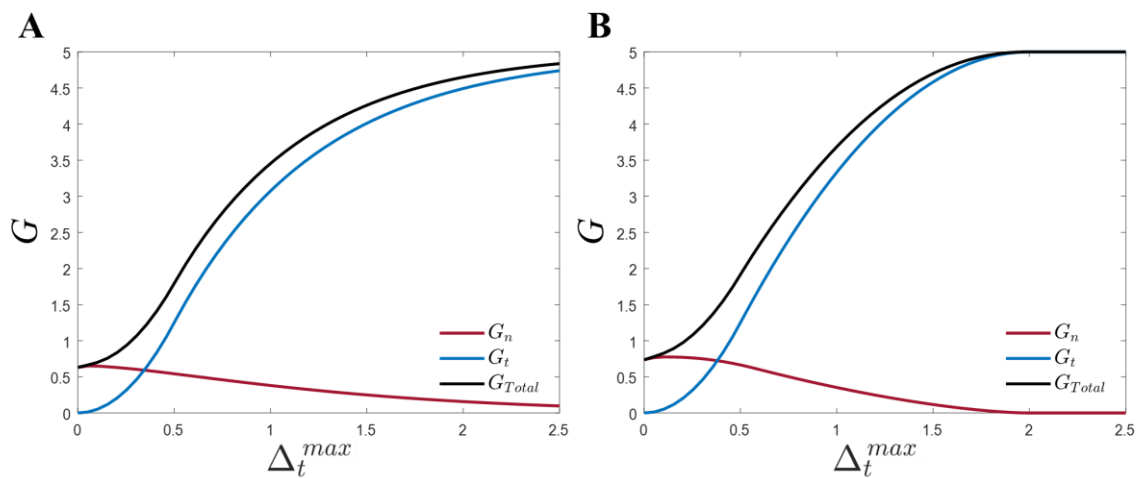


Figure 4.6: Fracture energy (G) for CZM1 (A), CZM2 (B) undergoing non-proportional loading paths of varying initial tangential separation (Δ_t) followed by

normal separation (Δ_n) until complete failure. Parameters are the same as those seen in Figure 4.5.

The dissipation of CZM1 is presented in Figure 4.7(A,C) and CZM2 is presented in Figure 4.7(C,D) for the proportional loading (A, B) and non-proportional loading (C, D). Positive instantaneous incremental dissipation is computed throughout each of the analyses presented.

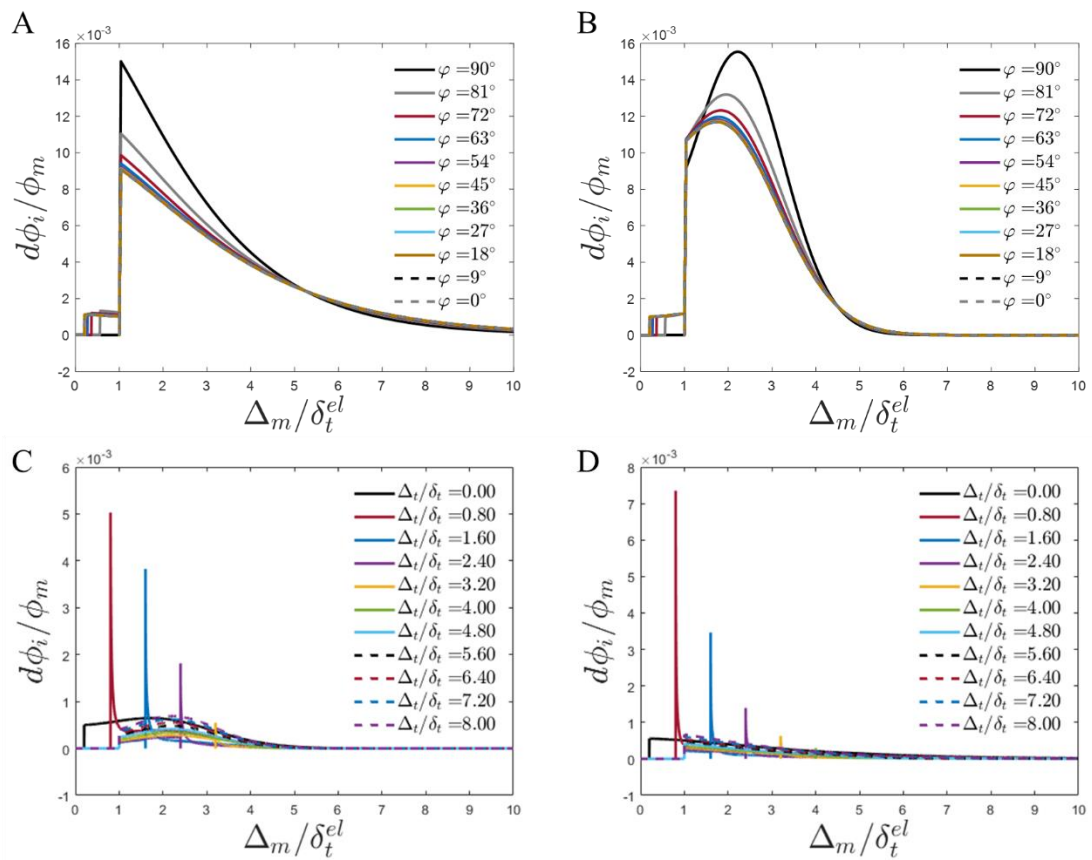


Figure 4.7: instantaneous incremental energy dissipation of CZM1 (A, C) and CZM2 (B, D) under proportional loading (A, B) and non-proportional loading (C, D).

The response of CZM1 and CZM2 to load-unload boundary conditions is demonstrated in Figure 4.8. Specifically, as shown in Figure 4.8(A), a mixed-mode proportionate loading path is followed so that partial damage is computed. The interface is then unloaded along the same mode angle, until it returns to its original

configuration ($\Delta_n = \Delta_t = 0$). The interface is then subjected to the same mode angle in the reverse direction ($\Delta_t < 0$) to failure. As shown in Figure 4.8(B-D), consistent behaviour is obtained for all mode angles. In all cases the prescribed strength for the given mode angle is exceeded and softening/damage is computed. Reversal of loading results in elastic unloading at a reduced/damaged interface stiffness. Reversal of the direction of tangential loading direction for the final mixed mode component of the loading path results in a continuation of elastic deformation at the reduced damaged interface stiffness (note that the damaged interface stiffness is not dependent on the current loading mode; rather, it is merely a function of the loading/damage history). Eventually, the tangential traction reaches the reduced/damaged tangential strength and further interface softening proceeds during ultimate mode II separation and failure. Similar consistent trends are computed for both CZM1 and CZM2. Figure 4.8(F,G) demonstrate that instantaneous incremental dissipation is positive throughout the entire mixed mode loading histories shown in Figure 4.8(B-E).

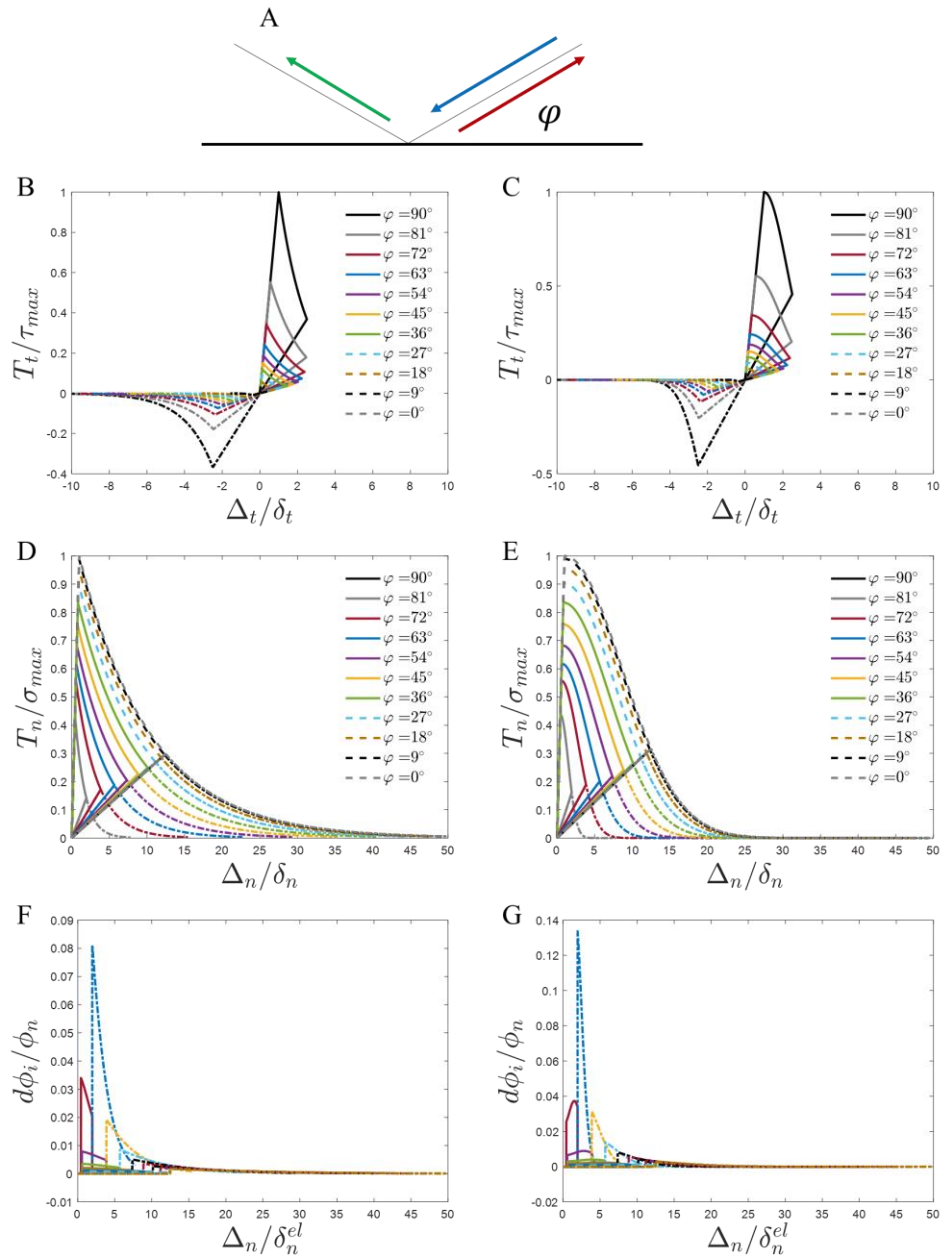


Figure 4.8. Loading-unloading path shown (A); Demonstration of the interface integrity variable in CZM1 (B,D) and CZM2 (C, E) for a series of proportional loading modes ranging from mode II to mode I. $K_m = 10$ MPa, $\tau_{max} = 5(\sigma_{max})$, $G_t = 5(G_n)$. Instantaneous incremental dissipation is shown in (F, G) for CZM1 and CZM2, respectively.

4.4 Comparison of CZM1 and CZM2 with Abaqus exponential softening formulation (CZM3)

The commercial finite element software Abaqus provides a cohesive zone functionality in which damage evolution may be specified in terms of mixed mode

fracture energy. In this section we describe this formulation, which we refer to as CZM3, and we provide critical comparisons with CZM1 and CZM2. The constitutive law for the traction is specified as follows

$$T = \begin{matrix} T_n \\ T_t \end{matrix} = \begin{bmatrix} K_{nn} & 0 \\ 0 & K_{tt} \end{bmatrix} \begin{Bmatrix} \Delta_n \\ \Delta_t \end{Bmatrix} = \mathbf{K}\Delta \quad (4.14)$$

where K_{nn} is a prescribed mode I stiffness and K_{tt} is a prescribed mode II stiffness. The traction increases elastically in accordance with (4.14) until the chosen damage initiation criterion is met. As an example, the quadratic failure criterion (Tsai and Wu, 1971) can readily be chosen, such that damage initiates when

$$\left\{ \frac{\langle T_n \rangle}{\sigma_{max}} \right\}^2 + \left\{ \frac{T_t}{\tau_{tmax}} \right\}^2 = 1 \quad (4.15)$$

where the Macauley brackets describe the ramp function

$$\langle T_n \rangle = \begin{cases} 0, & T_n < 0 \\ T_n, & T_n \geq 0 \end{cases} \quad (4.16)$$

Once the damage initiation criterion is satisfied, the scalar damage variable (D) increases monotonically from 0 to 1 with increasing separation until complete failure of the interface occurs. The traction during damage evolution is given as

$$T = (1 - D)\bar{T} \quad (4.17)$$

where \bar{T} is the peak elastic traction calculated in the absence of damage according to (4.14). This applies in both tangential directions, however, in normal displacement the traction is given as follows

$$T_n = \begin{cases} (1 - D)\bar{T}_n, & \bar{T}_n \geq 0 \\ \bar{T}_n, & \bar{T}_n < 0 \end{cases} \quad (4.18)$$

This ensures the stiffness of the interface in overclosure cannot be affected by the damage variable (D) whilst allowing stiffness of the interface in normal opening

(K_{nn}) to be affected in the same manner as (4.17). For exponential damage evolution specified according to energy the damage variable (D) reduces to

$$D = \int_{\delta_m^{el}}^{\delta_m^*} \frac{T_m d\Delta_m}{G_m - G_0} \quad (4.19)$$

Where T_m is the effective traction and Δ_m is the effective separation. G_0 is the stored elastic energy at damage initiation. G_m is the mixed mode fracture energy.

In Figure 4.9(A) we show the response of CZM3 to a simple mode II separation. The computed tangential traction exceeds the prescribed mode II fracture strength of the interface, providing a non-physical prediction. In contrast, CZM1 and CZM2 correctly reproduce the prescribed mode II fracture strength, in addition to the prescribed mode II fracture energy.

Figure 4.9(B) shows the computed tangential traction for CZM3 as a function of the damage ($D = (1 - \Psi)$, where Ψ is the interface integrity) during a mode II separation. The relationship is non-monotonic, whereby the mode II interface strength incorrectly increases with increasing interface damage. Peak tangential traction occurs when the scalar damage variable $D \approx 0.3$. Furthermore, the tangential traction does not decrease to the specified mode II fracture strength until $D \approx 0.7$, i.e. when the interface is 70% damaged. In contrast, tangential tractions are correctly computed to decrease monotonically with increasing interface damage for CZM1 and CZM2.

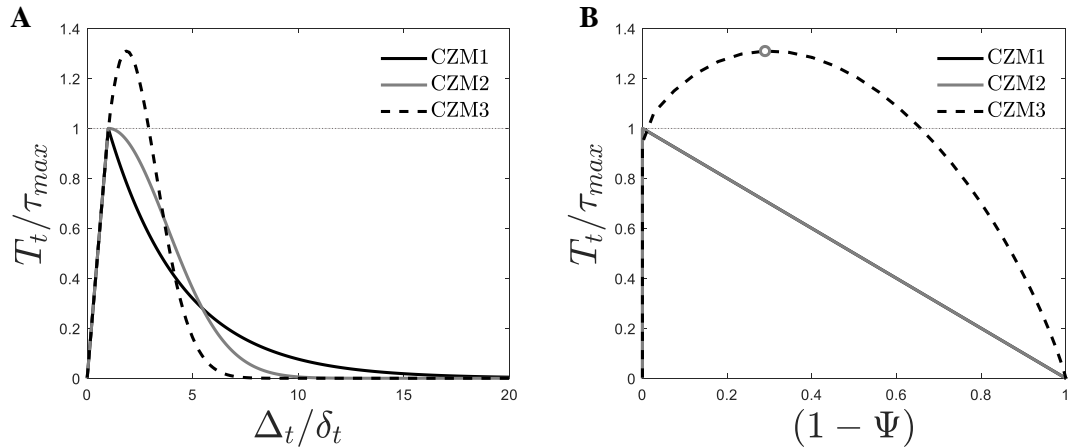


Figure 4.9: (A): Normalised traction-separation response of CZM3 (Abaqus exponential softening) formulation presented with CZM1 and CZM2 for a pure mode II separation. Note $T_t > \tau_{max}$ for the Abaqus exponential softening. $K_m = 10 \text{ MPa}$, $\tau_{max} = 5 \text{ MPa}$, $G = 10 \text{ N/mm}$. (B): Normalised tangential traction as a function of damage D (where $D = (1 - \Psi)$). Monotonic reduction is mode II interface strength with increasing damage for CZM1 and CZM2, but not for CZM3.

Such anomalous behaviour in CZM3 is further exposed in Figure 4.10. Figure 4.10(a) shows the computed maximum normal traction as a function of mode angle during proportional mixed mode separation. In the case of CZM1 and CZM2 the prescribed mode I strength is reached only for a pure mode I, as expected. However, for CZM3 the prescribed mode I strength is incorrectly exceeded for a wide range of applied mode angles. Similar results are presented in Figure 4.10(B) for non-proportionate mixed-mode loading paths.

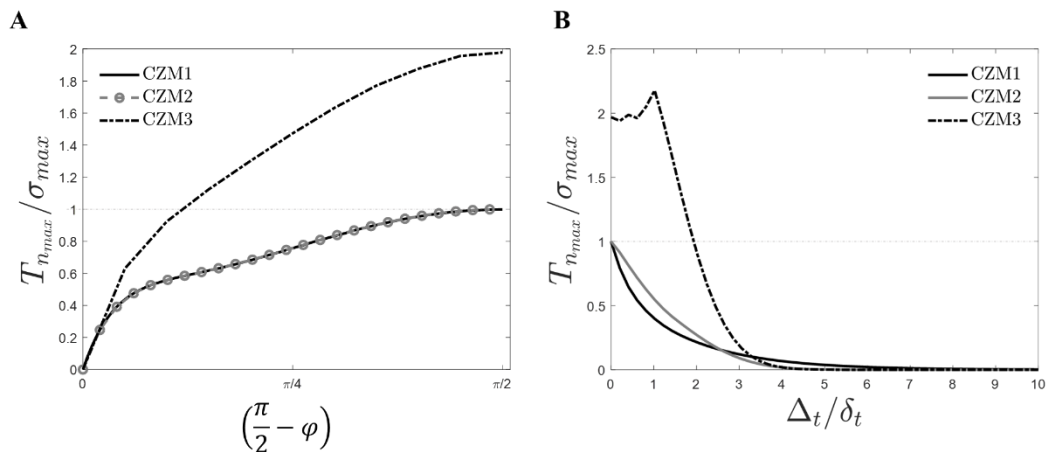


Figure 4.10: (A): Normalised normal traction ($T_{n_{max}}/\sigma_{max}$) as a function of mode angle (φ) for the three models in proportional loading scenarios (as seen in Figure 4.3). Note the dotted grey line indicates σ_{max} in both A and B. (B): Normalised traction as a function of maximum normalised tangential displacement prior to complete normal separation (as seen in Figure 4.5). Note the non-monotonic behaviour of the Abaqus exponential softening model.

4.5 Construction of a potential-based CZM

Several previous studies have used traction-separation laws derived from a potential function (Xu *et al.*, 1993; Park, Paulino and Roesler, 2009), based on the philosophy that the work of separation associated with a given interface separation vector should be path independent. A study by McGarry *et al.* uncovered problematic behaviour associated with potential-based cohesive zone models, such as repulsive tractions during mixed mode loading paths (McGarry *et al.*, 2014). We next propose a potential-based extension of CZM1, and we investigate if this formulation provides improvements upon existing potential-based models in terms of limiting unphysical repulsive tractions during mixed mode loading paths.

We construct a potential surface by integrating the traction magnitude-separation magnitude relationships specified for CZM1 along proportional loading paths for $0 \leq \varphi_{MA} \leq \pi/2$, giving the following piece-wise expression potential function $\phi(\Delta_m, \varphi_{MA})$:

$$\phi(\Delta_m, \varphi) = \begin{cases} \frac{1}{2} K_m \delta_m^{el}(\varphi)^2, & \Delta_m < T_m^{max}(\varphi)/K_m \\ \int_{\frac{T_m^{max}(\varphi)}{K_m}}^{\infty} T_m^{max}(\varphi) \exp\left(-\frac{\Delta_m^{max} - \frac{T_m^{max}(\varphi)}{K_m}}{\delta_m^*}\right) d\Delta_m, & \Delta_m \geq T_m^{max}(\varphi)/K_m \end{cases} \quad (4.20)$$

We refer to this formulation as PF-CZM1 (potential function extension of CZM1). Figure 4.11(A) shows ϕ for PF-CZM1 for the case where the specified mode II fracture energy is two times higher than the mode I fracture energy. For comparison we also show the potential function (ϕ) of the PPR model (Park, Paulino and Roesler, 2009) and the XU-Needleman model (Xu *et al.*, 1993).

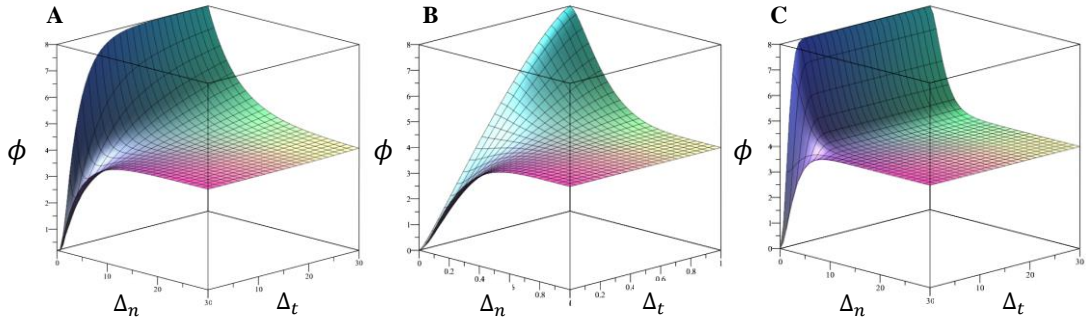


Figure 4.11: Potential surfaces shown as a function of normal separation and tangential separation. (A) PF-CZM1 $K = 1, \phi_t = 2(\phi_n), \tau_{max} = \sigma_{max}, \varphi^0 = \pi/8$. (B) PPR $\sigma_{max} = \tau_{max}, \phi_t = 2(\phi_n), \delta_n = \delta_t$. (C): Xu-Needleman $r = 0, q = 2$

We next derive the traction separation relationships for the PF-CZM1 model using the standard approach as follows:

$$\begin{aligned}
T_n &= \frac{\partial \phi}{\partial \Delta_n} \\
&= \frac{\partial}{\partial \Delta_n} \left(\frac{1}{2} K_m \delta_m^{el} (\varphi_{MA})^2 \right. \\
&\quad \left. + \int_{T_m^{max}(\varphi_{MA})/K_m}^{\infty} T_m^{max}(\varphi_{MA}) \exp\left(-\frac{\Delta_m^{max} - T_m^{max}(\varphi_{MA})/K_m}{\delta_m^*}\right) d\Delta_m \right) \\
T_t &= \frac{\partial \phi}{\partial \Delta_t} \tag{4.21} \\
&= \frac{\partial}{\partial \Delta_t} \left(\frac{1}{2} K_m \delta_m^{el} (\varphi_{MA})^2 \right. \\
&\quad \left. + \int_{T_m^{max}(\varphi_{MA})/K_m}^{\infty} T_m^{max}(\varphi_{MA}) \exp\left(-\frac{\Delta_m^{max} - T_m^{max}(\varphi_{MA})/K_m}{\delta_m^*}\right) d\Delta_m \right)
\end{aligned}$$

Figure 4.12(A) shows the normal traction ($\partial\phi/\partial\Delta_n$) derived from the PF-CZM potential function ϕ as a function of normal separation (Δ_n) and tangential separation (Δ_t). As clearly shown in Figure 4.12(B) repulsive tractions are computed for increasing tangential separation, even when no normal separation exists ($\Delta_n = 0$). The transparent surface indicates $\partial\phi/\partial\Delta_n = 0$. Residual tractions can also be computed on the potential surface.

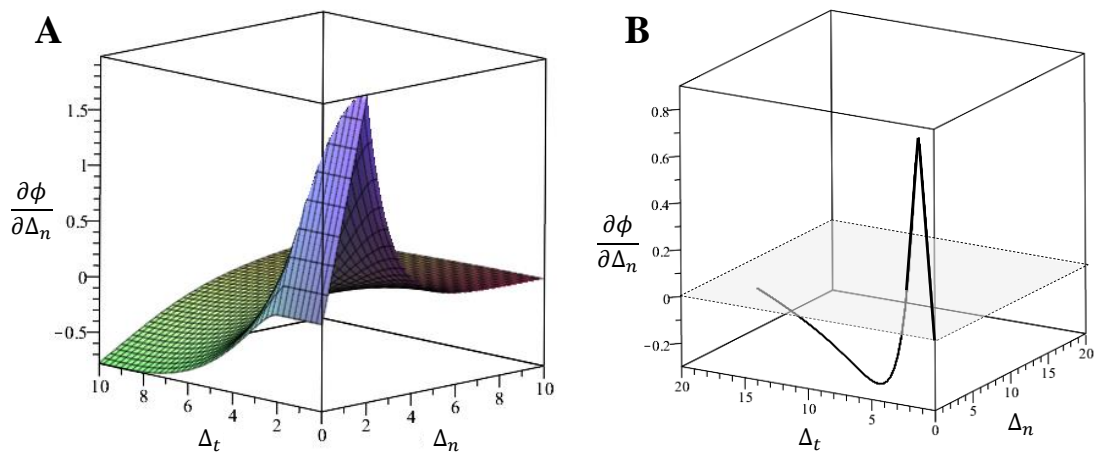


Figure 4.12. (A): Normal traction derived from the potential function ($\phi(\Delta_n, \Delta_t)$) seen

in Figure 4.12. Note repulsive normal tractions exist for increasing tangential opening even for $\Delta_n = 0$. (B): Repulsive normal tractions are further demonstrated for a proportional loading of $\Delta_t = 2(\Delta_n)$. The transparent surface indicates $\partial\phi/\partial\Delta_n = 0$.

This limitation of potential-based models has been expounded previously (McGarry *et al.*, 2014) and as such we do not present an exhaustive analysis in the current study however we do show that repulsive tractions are present in other popular potential-based models. For a balanced comparison we look to potential-based models with independent control of the initial elastic stiffness of the interface (K_m) and the fracture energy (G_m) similar to the model presented in the present study. One such model that meets these requirements is the PPR model (Park, Paulino and Roesler, 2009) presented here in Figure 4.13.

Figure 4.13 shows the mixed-mode response of the PPR model is shown as it undergoes a proportional separation ($\Delta_n = \Delta_t$). Figure 4.13(A) clearly demonstrates that repulsive tractions can arise for a simple mixed-mode loading path. Normalised normal traction (T_n/σ_{max}) is shown as a function of normal separation (Δ_n). During the damage evolution the traction decreases until negative, followed by a gradual increase to zero traction. Figure 4.13(B) shows the normalised tangential traction (T_t/τ_{max}) as a function of tangential separation (Δ_t). Figure 4.13(C) shows the instantaneous incremental energy dissipation ($d\phi_i/\phi_n$) as a function of normal separation (Δ_n). Negative instantaneous incremental energy dissipation is observed in this loading path.

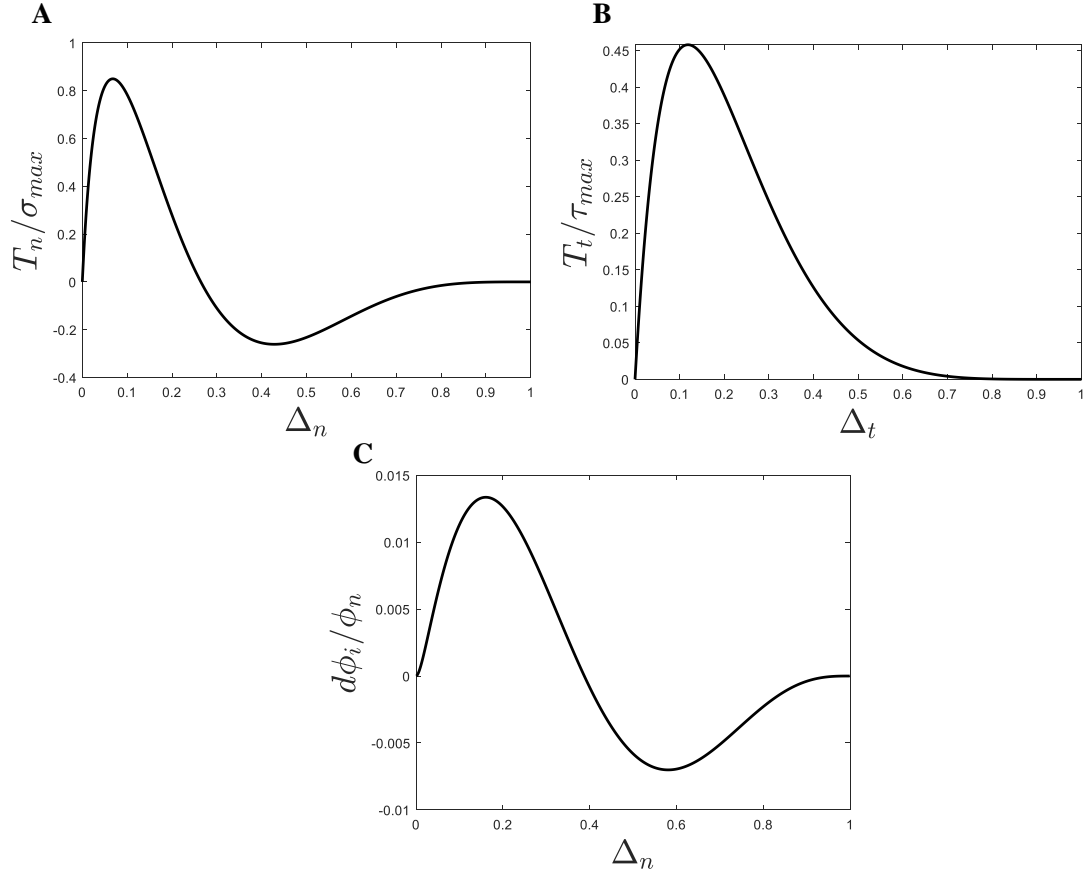


Figure 4.13: PPR model subject to a proportional loading path where $\varphi = 45^\circ$. Model parameters are the same as those seen in Figure 4.5. $\tau_{max} = 5(\sigma_{max})$, $\phi_t = 5(\phi_n)$, $\delta_t = 0.5$, $\delta_n = \delta_t/5$ (A): normalised normal traction (T_n/σ_{max}) as a function of normal separation (Δ_n). Repulsive (negative) tractions are computed. (B): Normalised tangential traction (T_t/τ_{max}) as a function of tangential separation (Δ_t). Tractions remain positive throughout. (C): Instantaneous incremental energy dissipation ($d\phi_i/\phi_n$) as a function of normal separation (Δ_n). Negative instantaneous incremental energy dissipation is observed during the loading history.

Summary of key contributions of CZM1 and CZM2

- The proposed path-dependent non-potential based cohesive zone models CZM1 and CZM2 are shown to provide consistent behaviour during mixed-mode loading paths, exhibiting a robust implementation of prescribed mode-dependent interface fracture strength and mode-dependent fracture energy and consistent coupling between normal and tangential separations and tractions.
- CZM1 and CZM2 provide robust penalisation of unphysical overclosure due to compressive normal tractions. Furthermore, CZM1 and CZM2 implement a

formulation to generate increased tangential strength as a result of compressive normal tractions.

- The cohesive zone model formulation CZM3, as implemented in Abaqus, does not provide robust implementation of prescribed interface strength during interface separations in which the fracture energy is specified.
- A potential based CZM formulation (PF-CZM1) is constructed based on the proportionate loading path behaviour of CZM1. We demonstrate the computation of unphysical normal tractions, inherent in all potential based models, remains problematic, despite the robust mixed-mode basis for the PF-CZM.

Bibliography

- Aure, T. and Ioannides, A. (2010) ‘Simulation of crack propagation in concrete beams with cohesive elements in ABAQUS’, *Transportation Research Record*. SAGE Publications/Sage CA: Los Angeles, CA, 2154(2154), pp. 12–21. doi: 10.3141/2154-02.
- Barenblatt, G. I. (1959) ‘The formation of equilibrium cracks during brittle fracture. General ideas and hypotheses. Axially-symmetric cracks’, *Journal of Applied Mathematics and Mechanics*. Pergamon, 23(3), pp. 622–636. doi: 10.1016/0021-8928(59)90157-1.
- van den Bosch, M. J., Schreurs, P. J. G. and Geers, M. G. D. (2006) ‘An improved description of the exponential Xu and Needleman cohesive zone law for mixed-mode decohesion’, *Engineering Fracture Mechanics*. Pergamon, 73(9), pp. 1220–1234. doi: 10.1016/j.engfracmech.2005.12.006.
- Camacho, G. T. and Ortiz, M. (1996) ‘Computational modelling of impact damage in brittle materials’, *International Journal of Solids and Structures*. Pergamon, 33(20–22), pp. 2899–2938. doi: 10.1016/0020-7683(95)00255-3.
- Camanho, P. P., Dávila, C. G. and De Moura, M. F. (2003) ‘Numerical simulation of mixed-mode progressive delamination in composite materials’, *Journal of Composite Materials*. SAGE Publications, 37(16), pp. 1415–1438. doi: 10.1177/0021998303034505.
- Cazes, F. et al. (2009) ‘A thermodynamic method for the construction of a cohesive law from a nonlocal damage model’, *International Journal of Solids and Structures*. Pergamon, 46(6), pp. 1476–1490. doi: 10.1016/j.ijsolstr.2008.11.019.
- Dimitri, R. et al. (2015) ‘Coupled cohesive zone models for mixed-mode fracture: A comparative study’, *Engineering Fracture Mechanics*. Pergamon, 148, pp. 145–179. doi: 10.1016/j.engfracmech.2015.09.029.
- Gallagher, E. A., Lamorinière, S. and McGarry, P. (2018) ‘Multi-axial damage and failure of medical grade carbon fibre reinforced PEEK laminates: Experimental testing and computational modelling’, *Journal of the Mechanical Behavior of Biomedical Materials*. Elsevier, 82, pp. 154–167. doi: 10.1016/j.jmbbm.2018.03.015.
- Gallagher, E. A., Lamorinière, S. and McGarry, P. (2019) ‘Finite element investigation into the use of carbon fibre reinforced PEEK laminated composites for distal radius fracture fixation implants’, *Medical Engineering and Physics*. Elsevier, 67, pp. 22–32. doi: 10.1016/j.medengphy.2019.03.006.
- Hopkins, C. G., McHugh, P. E. and McGarry, J. P. (2010) ‘Computational investigation of the delamination of polymer coatings during stent deployment’, *Annals of Biomedical Engineering*. Springer US, 38(7), pp. 2263–2273. doi: 10.1007/s10439-010-9972-y.
- Hu, J., Chou, Y. K. and Thompson, R. G. (2008) ‘Cohesive zone effects on coating failure evaluations of diamond-coated tools’, *Surface and Coatings Technology*. Elsevier, 203(5–7), pp. 730–735. doi: 10.1016/j.surfcoat.2008.08.029.

- Ivankovic, A., Pandya, K. C. and Williams, J. G. (2004) 'Crack growth predictions in polyethylene using measured traction-separation curves', *Engineering Fracture Mechanics*. Pergamon, 71(4–6), pp. 657–668. doi: 10.1016/S0013-7944(03)00030-4.
- Di Leo, C. V. et al. (2014) 'A new methodology for characterizing traction-separation relations for interfacial delamination of thermal barrier coatings', *Acta Materialia*. Pergamon, 71, pp. 306–318. doi: 10.1016/j.actamat.2014.02.034.
- Máirtín, É. Ó. et al. (2014) 'Potential-based and non-potential-based cohesive zone formulations under mixed-mode separation and over-closure—Part II: Finite element applications', *Journal of the Mechanics and Physics of Solids*. Pergamon, 63, pp. 363–385. doi: 10.1016/J.JMPS.2013.08.019.
- McGarry, J. P. et al. (2014) 'Potential-based and non-potential-based cohesive zone formulations under mixed-mode separation and over-closure. Part I: Theoretical analysis', *Journal of the Mechanics and Physics of Solids*, 63(1), pp. 336–362. doi: 10.1016/j.jmps.2013.08.020.
- McGarry, J. P. and McHugh, P. E. (2008) 'Modelling of in vitro chondrocyte detachment', *Journal of the Mechanics and Physics of Solids*. Pergamon, 56(4), pp. 1554–1565. doi: 10.1016/j.jmps.2007.08.001.
- Nakamura, T. and Wang, Z. (2001) 'Simulations of crack propagation in porous materials', *Journal of Applied Mechanics, Transactions ASME*. American Society of Mechanical Engineers, 68(2), pp. 242–251. doi: 10.1115/1.1356029.
- Nielsen, K. L. and Hutchinson, J. W. (2012) 'Cohesive traction-separation laws for tearing of ductile metal plates', *International Journal of Impact Engineering*. Pergamon, 48, pp. 15–23. doi: 10.1016/j.ijimpeng.2011.02.009.
- Park, K., Paulino, G. H. and Roesler, J. R. (2009) 'A unified potential-based cohesive model of mixed-mode fracture', *Journal of the Mechanics and Physics of Solids*. Pergamon, 57(6), pp. 891–908. doi: 10.1016/j.jmps.2008.10.003.
- Tsai, S. W. and Wu, E. M. (1971) 'A General Theory of Strength for Anisotropic Materials', *Journal of Composite Materials*. Sage PublicationsSage CA: Thousand Oaks, CA, 5(1), pp. 58–80. doi: 10.1177/002199837100500106.
- Tvergaard, V. and Hutchinson, J. W. (1992) 'The relation between crack growth resistance and fracture process parameters in elastic-plastic solids', *Journal of the Mechanics and Physics of Solids*. Pergamon, 40(6), pp. 1377–1397. doi: 10.1016/0022-5096(92)90020-3.
- Wu, C. et al. (2016) 'On determining mixed-mode traction–separation relations for interfaces', *International Journal of Fracture*. Springer Netherlands, 202(1), pp. 1–19. doi: 10.1007/s10704-016-0128-4.
- Xu, X.-P. et al. (1993) 'Void nucleation by inclusion debonding in a crystal matrix', *Modelling and Simulation in Materials Science and Engineering*. IOP Publishing, 1(2), pp. 111–132. doi: 10.1088/0965-0393/1/2/001.

Chapter 5

5 DEVELOPMENT OF A NOVEL TEST METHOD TO INVESTIGATE MODE II FRACTURE AND DISSECTION OF ARTERIES

5.1 Introduction

Aortic dissection is a lethal disease which can lead to stroke, spinal cord infarction, renal failure, cardiac tamponade, aortic rupture, and death (Criado, 2011; Fattori *et al.*, 2013; Evangelista *et al.*, 2018). Mortality rates can be as high as 1% per hour (Chikwe *et al.*, 2013; Evangelista *et al.*, 2018). However, to date the exact pathophysiological processes and related biomechanisms underlying aortic dissection have not been uncovered. Previous investigations of the damage and fracture properties of arterial tissue have primarily relied on peel tests (Gasser and Holzapfel, 2006; Sommer *et al.*, 2008; Ferrara and Pandolfi, 2010; Tong *et al.*, 2011a; Noble *et al.*, 2016). Such a test methodology results in a mode I fracture and allows for the calibration of a mode I fracture strength (reported to be in the region of 140 kPa (Ferrara and Pandolfi, 2010)). However, given the anisotropic mechanical behaviour of arterial due to its complex microstructure, which consists of families of aligned collagen and elastin fibres, the mode and mechanism of crack propagation induced by a standard peel test is of limited relevance to the physiological process of artery dissection and rupture. Given that the high blood pressure in the lumen is the primary source of loading of arterial tissue in vivo, we argue that aortic dissection results from mode II fracture initiation, rather than mode I. Lumen pressure loading induces a high compressive radial component of stress throughout the artery wall, such that a mode I initiation of a dissection in the

orthogonal circumferential-axial plane is highly improbable. Iatrogenic dissections may follow from mixed mode fracture initiation (Noble *et al.*, 2017), but such dissections primarily result from catheterisation, percutaneous transluminal coronary angioplasty, or cardiac surgery (Hagan *et al.*, 2000). In any event, iatrogenic dissections are reported to occur in the radial-axial plane (Eshtehardi *et al.*, 2010), which, given the highly anisotropic arterial microstructure, is not at all reflective of the mode I fracture in the circumferential-axial plane induced by a standard peel test. Every aortic dissection involves circumferential and axial crack propagation, whereas not all are associated with a radial crack propagation (Hagan *et al.*, 2000; Trimarchi *et al.*, 2007; Evangelista *et al.*, 2018). A recent experimental study qualitatively observed a similar trend of dissection in the circumferential-axial plane of excised aortas subjected to hypertensive levels of lumen fluid pressure (Haslach, Siddiqui, *et al.*, 2018). Such dissection propagation in the circumferential-axial plane is also reported for canine thoracic aortas, where it is qualitatively suggested that bond strength between lamellae are weaker than the lamellae material strength (van Baardwijk and Roach, 1987).

To gain further insight into the clinical observation of arterial dissection in the circumferential-axial plane it is essential to accurately characterise the fracture properties of arterial tissue under such mode II loading conditions. Classical mode II lap-shear fracture mechanics experiments have been carried out by Witzenburg *et al.* (Witzenburg *et al.*, 2017) on porcine ascending aorta and by Sommer *et al.* (Sommer *et al.*, 2016) on excised human aneurysmatic and dissected aorta. However, we present a preliminary finite element analysis of lap-shear testing of arterial tissue in Section 5.1.1 (below) in which we demonstrate that the high levels of material deformation at the point of fracture initiation consequently results in a mixed mode initiation and

propagation, rather than the intended mode II fracture. The generation of a mode II crack in highly deformable, high toughness fibrous soft tissue under controlled experimental conditions remains a significant challenge. This challenge cannot be addressed by standard test methodologies developed for traditional engineering materials, such as lap shear tests. A further challenge is that fracture testing of naturally occurring biological materials such as arteries does not facilitate the engineering of standardised fracture specimen geometries. Therefore, implementation and interpretation of fracture testing subject to the limitation of non-standard geometries, such as arteries, requires in-depth mechanistic analysis.

In the current study we design, develop, and validate a novel test methodology for the initiation and propagation of mode II dissection in arterial tissue in the circumferential-axial plane. We demonstrate that this pattern of mode II dissection is highly repeatable. Such mode II fracture always preferentially occurs in our experiments, in contrast to mode I fracture in the radial-axial plane, which never occurs due to the significant toughening mechanism of collagen alignment at the crack-tip. Using our novel experimental methodology, in parallel with cohesive zone modelling of our experiments, we determine the pure mode II fracture strength and fracture energy of ovine aortas. We demonstrate that the mode II fracture strength is approximately eight times higher than the mode I fracture strength measured using a traditional peel test. Finally, we discuss the implications of our results in terms of advancing the current understanding of the biomechanics of artery dissection.

5.1.1 Lap-shear testing of arterial tissue results in a mixed mode crack propagation

Due to the high strength and toughness of arterial tissue, significant material deformation occurs in lap-shear tests prior to damage initiation and crack propagation. This is clearly illustrated by the experiments of Sommer et al. (Sommer *et al.*, 2016) (referred to hereafter as *constrained lap-shear testing*) and Witzenburg et al. (Witzenburg *et al.*, 2017) (referred to hereafter as *unconstrained lap-shear testing*). In the *constrained lap-shear tests* the top and bottom surfaces of the artery sample are bonded to rigid horizontal plates. In the *unconstrained lap-shear tests* the top and bottom surfaces of the artery sample are unconstrained. In Figure 5.1 we present finite element cohesive zone analysis of the constrained experiments of Sommer et al. (Sommer *et al.*, 2016) and the unconstrained experiments of Witzenburg et al. (Witzenburg *et al.*, 2017) in which crack initiation and propagation is simulated using a cohesive zone formulation. The fracture strength is calibrated so that predicted crack initiation occurs at an identical level of applied shear deformation as reported experimentally. Mode mixity is defined as $\varphi_{MM} = \tan^{-1}(T_t/T_n)$ and is presented as a function of normalised crack tip position, where T_t and T_n are the tangential (shear) and normal tractions, respectively, at the crack-tip. Full details of the artery anisotropic hyperelastic material law are presented in Appendix A, and the calibration of the material law to arterial tissue is presented in Section 5.3.1. The cohesive zone fracture model utilised in this study is presented in Chapter 4 and provides an advance on previous coupled mixed mode formulations by facilitating independent specification of mode-dependent fracture strength and fracture energy independent of intrinsic interface stiffness, while ensuring positive instantaneous incremental positive dissipation (McGarry *et al.*, 2014).

As shown in Figure 5.1(a), simulation of a *constrained lap-shear test*, predicts a mode mixity of ~ 0.2107 at fracture initiation, with a mean mode mixity of $\varphi_{MM} = \sim 0.1157$ rad ($\sim 6.63^\circ$) during subsequent crack propagation. Remarkably, this represents a mode mixity that is closer to mode I, rather than the intended mode II fracture. Figure 5.1(b) illustrates the high level of material deformation at the crack-tip throughout, resulting in a localised mode of loading that resembles a peel test rather than a mode II fracture test. Also shown in Figure 5.1, simulation of an *unconstrained lap-shear test* predicts a mode mixity of ~ 1.229 at fracture initiation, with a mean mode mixity of $\varphi_{MM} = \sim 1.236$ rad ($\sim 70.85^\circ$) during subsequent crack propagation. Again, this is quite different from the intended mode II fracture ($\varphi_{MM} = \pi/2$ rad). Figure 5.1(c) demonstrates the high levels of material deformation at initiation and during propagation, resulting in normal tractions at the crack-tip that are comparable in magnitude to corresponding tangential tractions.

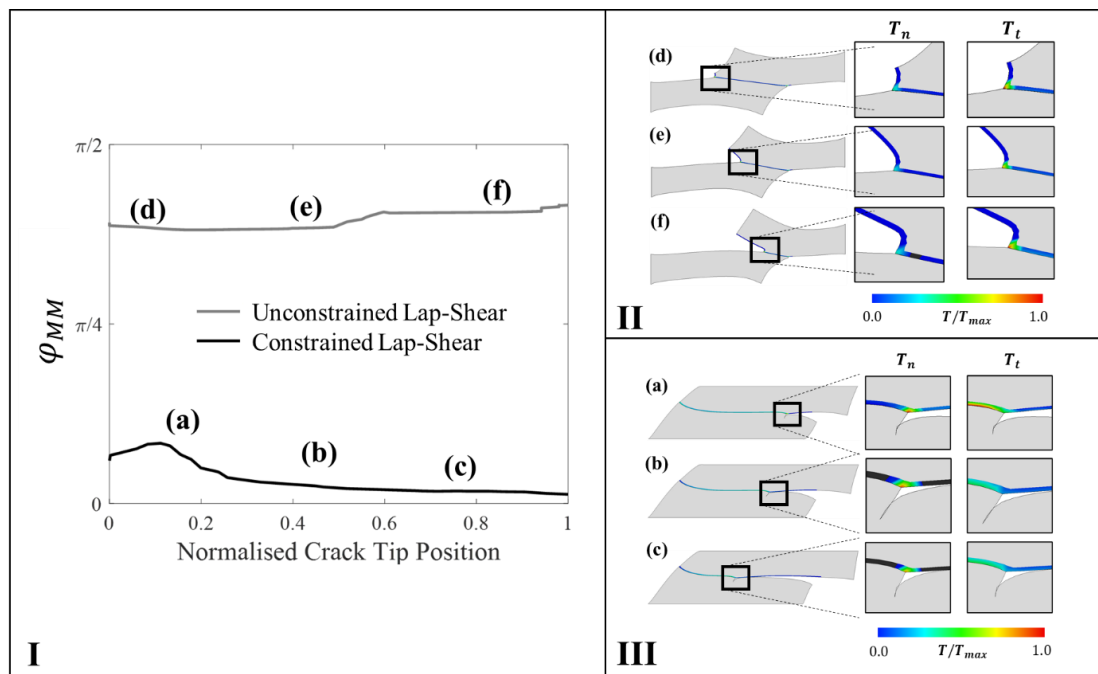


Figure 5.1. (I) Mode mixity (φ_{MM}) as a function of normalised crack tip position for a constrained in-plane lap shear test and an unconstrained lap-shear test; (II) Simulation of an unconstrained lap-shear test where normal and tangential traction is shown.

Cohesive zone parameters used were ($\sigma_{max} = 200 \text{ kPa}$, $G_n^0 = 0.003 \text{ N/mm}$, $\tau_{max} = 400 \text{ kPa}$, $G_t^0 = 0.003 \text{ N/mm}$); (III) Simulation of a constrained lap-shear test. The traction at the crack tip is predominantly a mode I traction. Cohesive zone parameters used were ($\sigma_{max} = 200 \text{ kPa}$, $G_n^0 = 0.003 \text{ N/mm}$, $\tau_{max} = 400 \text{ kPa}$, $G_t^0 = 0.003 \text{ N/mm}$). Full details of the artery anisotropic hyperelastic material law and the cohesive zone fracture model are presented in Appendix A and Chapter 4, respectively.

As neither unconstrained nor constrained lap-shear test protocols result in mode II fracture, in the current study we aim to develop a novel test methodology to induce pure mode II fracture initiation and crack propagation in arterial tissue. We argue that the quantitative analysis of pure mode II fracture resistance of arterial tissue is of critical importance. Lumen blood pressure is the primary source of mechanical loading on an artery wall in vivo, resulting in a compressive radial component of stress. The presence of an intramural haematoma could potentially result in a mixed mode or mode I fracture initiation in the c-a plane. However, the high compressive radial component of stress in the vessel wall due to lumen pressure will promote mode II initiation, particularly in the absence of an intramural hematoma.

Therefore, we suggest that (in the absence of other conditions such as intramural haematoma) mode I initiation of fracture is not possible under in vivo loading and that arterial dissection results from mode II fracture of arterial tissue. Therefore, we suggest that mode I initiation of fracture is not possible under in vivo loading and that arterial dissection results from mode II fracture of arterial tissue.

5.2 Design and computational validation of a novel experimental mode II fracture test (shear fracture ring test (SFRT))

In this section we outline the analysis and design of a novel experimental methodology that results in pure mode II crack propagation in aortic tissue. Motivated by an analytical solution developed by Parry and McGarry (Parry and McGarry, 2012) for the stress state of a bi-layered composite arch, we note that interface tractions vary from mode I at the top of the arch to mode II at the side of the arch. Attachment of a

straight bi-layered composite strut to the bi-layered arch (representing a typical stent design) further increases the shear stress at the base of the arch (Parry and McGarry, 2012). Extending this analysis of the transition of interface from normal stress at the top of an arch to a shear stress at the side of the arch, we propose a test method in which a section (“ring”) of excised artery is mounted on two cylindrical loading bars. The loading bars are then moved apart, imposing a deformation on the artery ring such that that two curved “arch-type” sections (top and bottom) are developed, connected by straight “strut-type” sections, as shown in Figure 5.2(a). This generates a localised region of high shear stress at the sides of the cylindrical loading bars (analogous to the maximum shear stress at the base of the stent arch uncovered in the study by McGarry and Parry (Parry and McGarry, 2012)).

Computational design of experiment

A schematic of the computational design of experiment modelling procedure is outlined in Figure 5.2(a). A ring of excised aortic tissue with radius R_s is placed onto two steel bars of radius r_b . The bottom bar is fixed throughout the analysis while the top bar is displaced at a constant strain rate such that at any time point the distance travelled by the top bar is equal to u . We define a deformed interface coordinate S (shown in Figure 5.2(a)) which describes the position along a quarter circumference of the deformed configuration. S begins at the top of the bar and describes the position that is distance d through the thickness t and ends at $S = L$. We also define a radial coordinate r_{ct} which describes the radial position of the crack tip through the wall. The original circumference of the ring is described as $C_0 = 2(L_0) + 2\pi(r_b + t/2)$ where L_0 is the distance from the midpoint of one loading bar to the other. The change in circumference is described as follows: $\Delta C = \Delta L$ where ΔL is the displacement applied to the upper loading bar. Also shown in Figure 5.2(a) is a local/material

coordinate system for the artery ring; r, c, a indicating axes corresponding to the physiological radial, circumferential, axial axes, respectively. Collagen fibres are assumed to lie in the c - a plane (Gasser, Ogden and Holzapfel, 2006; Nolan *et al.*, 2014). A measure of nominal strain in the c -direction (the physiological circumferential direction) is then given as the $E_{cc} = \Delta C/C_0$ where C_0 is the undeformed circumference of the ring. Hereafter, for brevity, E_{cc} is referred to as the nominal *circumferential strain* imposed on the artery ring. The novel test methodology is referred to as the *SFRT* hereafter.

A finite element analysis of the *SFRT* is presented in Figure 5.2(b). Figure 5.2(b) shows a contour plot of circumferential stress σ_{cc} (normalised by the initial shear modulus μ) for the case of a loading bar of radius $r_b/R_s = 0.18$. The circumferential stress is the dominant stress component in the artery ring; it is five times higher than the corresponding peak maximum shear stress τ (when $r_b/R_s = 0.18$) which occurs at the side of the arch region, as shown in Figure 5.2(c). The magnitude of τ at the side of the bar is strongly influenced by the loading bar radius. Three bar radii are shown in Figure 5.2(b) ($r_b/R_s = 0.18, 0.36, 1.0$). The peak value of τ is increased when the radius of the bar is decreased. In Figure 5.2(e) the distribution shear traction T_t along the c - a plane mid-way through the arterial section ($r=t/2$) is examined. Similar to the distribution of τ in the arterial material, T_t along a c - a plane is highest at the side of the loading bar ($S = \pi(r_b + d)/2$) and increases with decreasing value of r_b .

The effect of the radial coordinate of a c - a plane through the thickness was also examined, placing the plane a quarter-way through the thickness, such that the plane lies on S when $d = t/4$, results in a 7.3% decrease in T_t compared to $d = t/2$. However, placing the plane three quarters through the thickness, such that the plane

lies on S when $d = 3t/4$, results in a 44% decrease in T_t . The plane lies on S when $d = t/2$ in Figure 5.2(d-f).

Figure 5.2(f) shows the normal tractions (i.e. in the r -direction acting on a c - a plane) are negative (i.e. compressive) throughout the arch region and are negligible in the straight section of the specimen.

In terms of experimental design of a mode II fracture test, the analyses presented in Figure 5.2 provide the following insights:

- Maximum shear stress and shear traction on a c - a plane occur at the side of the loading bars ($S = \pi(r_b + d)/2$).
- A smaller loading bar generates highest magnitude of shear stress and shear traction on a c - a plane.
- Crack propagation along a c - a plane (as reported clinically) is expected to be pure mode II, based on computed compressive normal tractions throughout the arterial specimen.

We therefore select a small loading bar radius of 1.5 mm (corresponding to $r_b/R_s = 0.18$ for an aorta specimen radius of 8.33 mm).

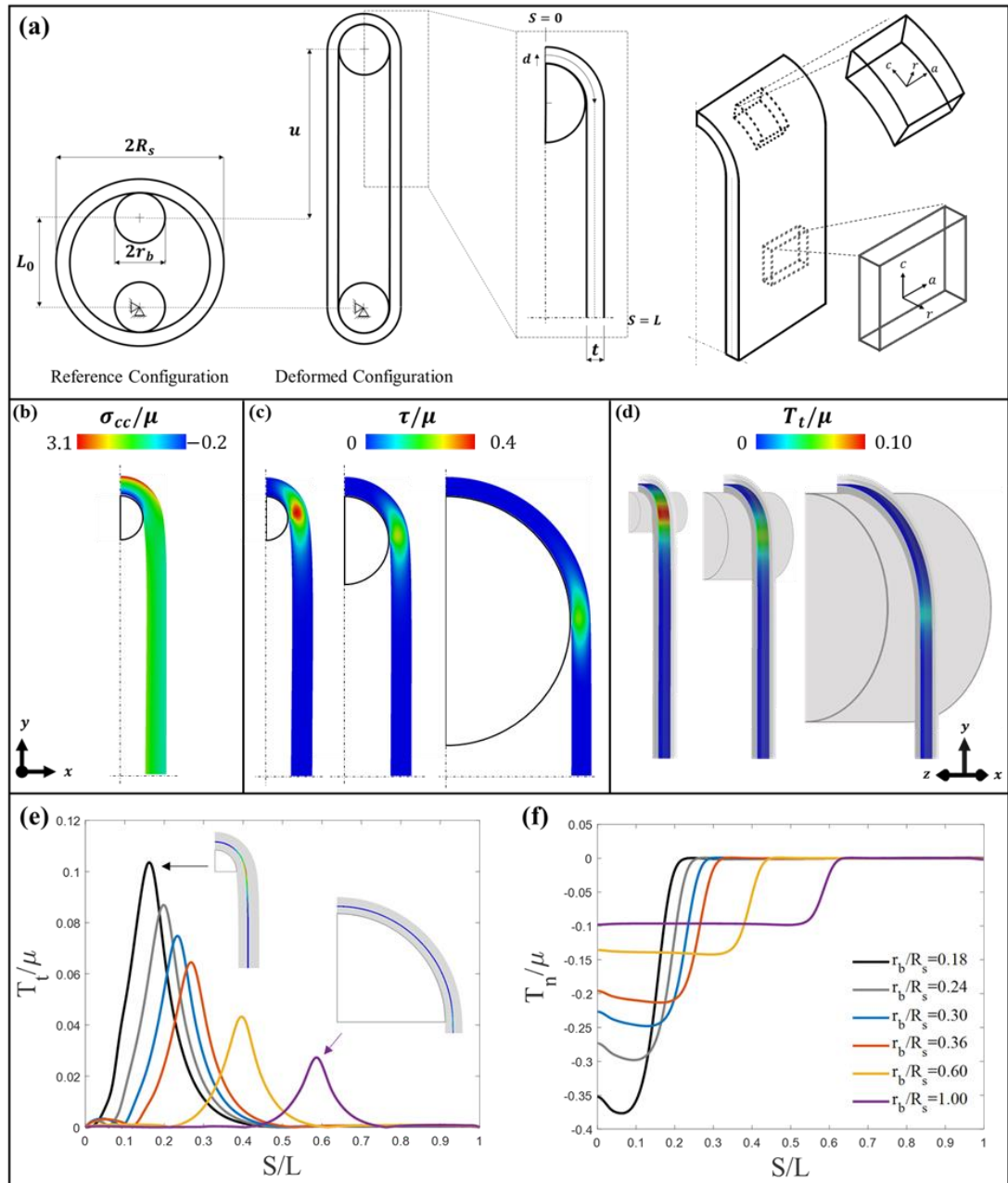


Figure 5.2. (a) Schematic of the *SFRT*. An excised aortic ring specimen is shown mounted on two bars in the reference configuration. R_s is the radius of the specimen and r_b is the radius of the bar. The bottom bar is fixed and u is the displacement of the top bar. S is the deformed interface coordinate which is a distance d offset from the bar. A schematic of the local material coordinate system is shown with local circumferential, axial, and radial directions (c - a - r); (b) Local circumferential stress is presented for a $r_b/R_s = 0.18$ configuration; (c) Maximum local shear stress (τ/μ) contour is plot for three bar radii ($r_b/R_s = 0.18, 0.36, 1.0$); (d) Normalised interface shear traction (T_t/μ) contour for the same radii as shown in (c); Tangential traction (e) and normal traction (f) as a function function of the normalised interface coordinate (S/L) for each of the bar radii analysed. Full details of the artery anisotropic hyperelastic material law used are presented in Appendix A.

In Figure 5.3, using a cohesive zone, we examine the mode mixity during crack initiation and propagation in our *SFRT* test. We next hypothesise that the insertion of a notch in the radial direction at the location of maximum shear stress ($S = \pi(r_b + d)/2$), as illustrated in the schematic in Figure 5.3(a), will result in a kinking of the notch such that mode II initiation and propagation will occur along the *c-a* plane through the notch-tip, as shown in the illustrations of Figure 5.3(a) (we define kinking as the growth of the radial notch directly in the circumferential direction with no prior radial crack growth). A cohesive surface is placed along the *c-a* plane through the notch-tip. Simulated crack initiation and propagation is presented in Figure 5.3. The evolution of T_t along the *c-a* plane through the notch tip ($r=t/2$) is shown in Figure 5.3(b), in addition to the computed specimen deformation. Following initiation at the side of the loading bar ($S = \pi(r_b + d)/2$), at an applied circumferential strain of $\Delta C/C_0 = 0.64$, the crack front propagates a long distance along the *c-a* plane. The delaminated portion of artery (i.e. the evolving crack flank) remains flat on the *c-a* plane, suggesting that the crack growth is pure mode II throughout. This is confirmed by plotting the mode mixity φ_{MM} at the crack-tip as a function of crack-tip position during propagation, as shown in Figure 5.3(c). Corresponding plots for lap-shear test simulations are shown once-again for comparison, highlighting the significant improvement of the *SFRT* in generating mode II initiation and propagation in arterial tissue. The normal interface calibrated from standard peel tests is $\sigma_{max} = 202 \text{ kPa}$.

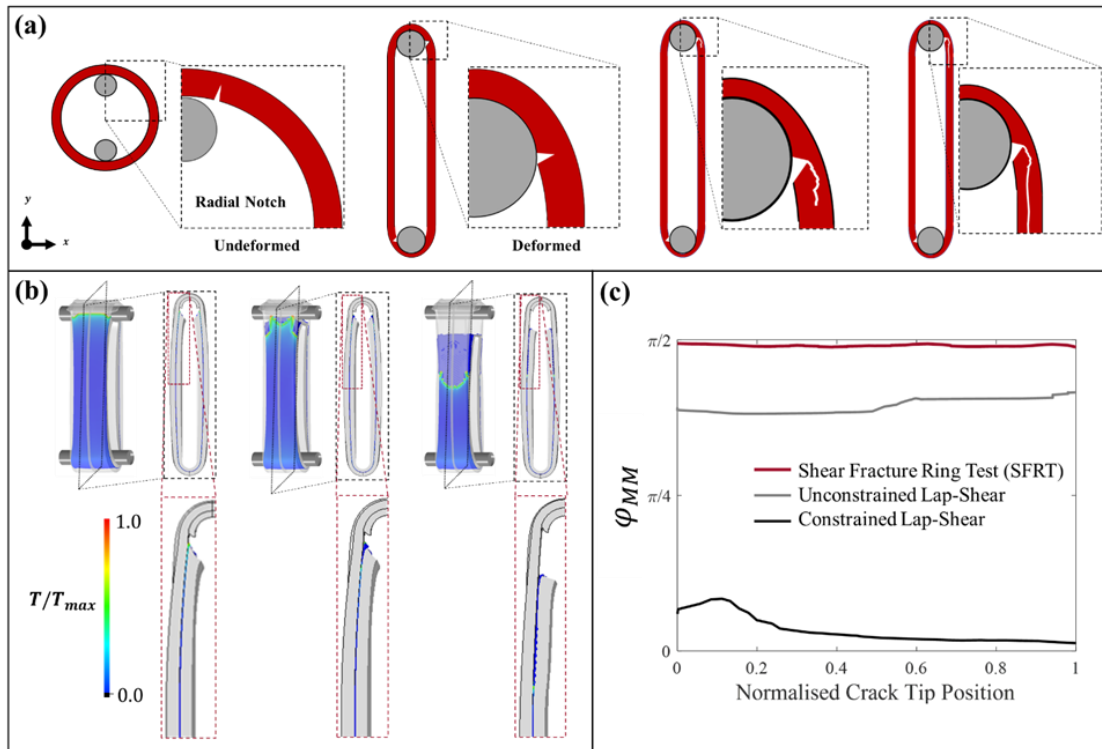


Figure 5.3. (a) Schematic of the proposed radial notch and the evolution throughout testing; (b) Section views of the finite element simulation of the *SFRT* carried out in the present study. Sections are taken in the middle of the aortic ring as the crack propagates. Crack tip is shown by the black arrow; (c) Mode mixity (ϕ_{MM}) as a function of normalised crack tip position for each of the shear experiments analysed in this study. Cohesive zone parameters are as follows: the normal interface strength is calibrated from peel tests, $\sigma_{max} = 202 \text{ kPa}$ (see supplementary material I); the shear interface strength is assumed to be approximately twice the normal interface strength, $\tau_{max} = 400 \text{ kPa}$; the mode I and mode II fracture energies are assumed to be $G_n^0 = 0.003 \text{ N/mm}$ and $G_t^0 = 0.003 \text{ N/mm}$. Full details of the cohesive zone model are presented in Chapter 4.

Following from the key computational design and analysis presented in Figures 5.1-5.3, a proposed experimental test rig is shown in Figure 5.4(a). Cantilevered stainless steel loading bars are attached to the base-plate and the cross-head fixture of a mechanical test machine. Selection of loading bar radius is a key design consideration. While, as shown above, a smaller radius enhances the level of shear stress, bars must be large enough to support the forces imposed by the deforming arterial specimen without exceeding the elastic limit of stainless steel. The force imposed by the deforming specimen is, of course, dependent on the chosen specimen width, w .

Specimens are prepared such that $w/t \approx 4.14$, so that specimens are sufficiently wide to approximate generalised plane strain conditions, but not so wide that significant anatomical variations are introduced in the a-direction (i.e. specimens are approximately cylindrical). For a typical specimen thickness of $t=2.35$ mm, a width $w=9.73$ mm is chosen. Specimens are placed as close as possible to the cantilevered ends of the loading bars (while contacting only the loading bars). Preliminary testing suggests that a specimen exerts a uniformly distributed load of ~ 0.97 N/mm on the loading bars at $\sim \Delta C/C_0 \approx 0.6$ prior to rupture. Figure 5.4(a) shows the stress in stainless steel loading bars, normalised by the yield stress of stainless steel (200 MPa). Clearly, a bar radius in the range $r_b/R_s \leq 0.135$ (corresponding to $r_b \leq 1.125$ mm based on a mean artery radius of 8.33 mm) does not provide an adequate factor of safety for the structural integrity of the loading bar. On the otherhand, large bar radii $r_b/R_s \geq 0.25$ result in lower magnitudes of shear stress and, consequently, a reduced probability of mode II fracture. Therefore a bar of radius $r_b/R_s = 0.18$ (i.e. $r_b = 1.5$ mm) is chosen to provide a high level of shear stress while ensuring that the yield stress of the loading bar is not exceeded. This bar size also facilitates straight-forward positioning of the radial notch at the position of maximum shear to the side of the bar ($S = \pi(r_b + d)/2$). A high-resolution camera (60 fps, 1080p) and digital microscope (10 fps, 1080p) are positioned in front of the sample to record specimen deformation and crack propagation throughout each test. A photograph of the final test set-up is shown in Figure 5.4(c).

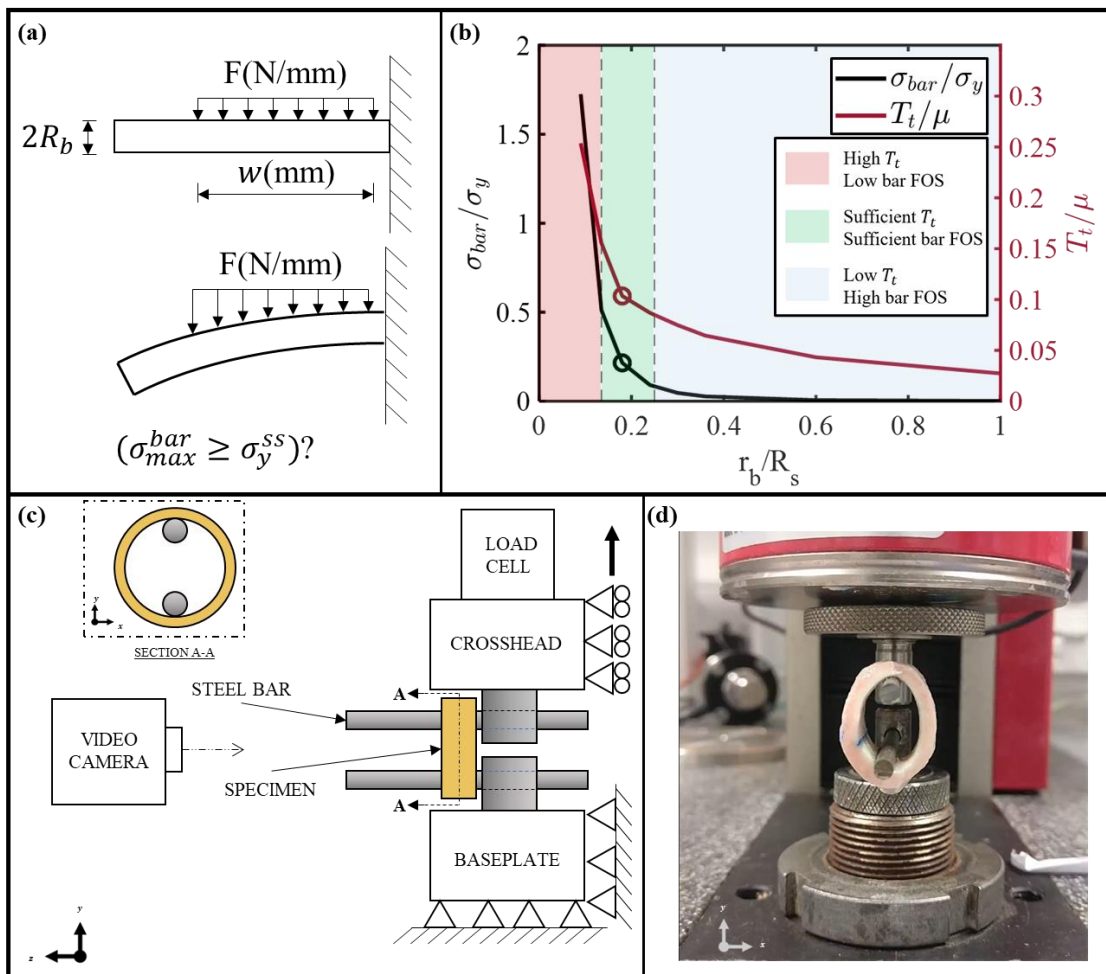


Figure 5.4. (a) Schematic of structural bending of loading bar during stretching of artery SFRT specimen; (b) Identification of optimal experimental design based on required loading bar flexural strength and generation of high shear stress in arterial tissue. The blue shaded region indicates a high loading-bar factor of safety (FOS) and low shear traction. The red region indicates a low loading-bar FOS and a high shear traction. The green region indicates the optimal experimental design whereby high shear tractions are generated in the artery while a sufficiently high loading-bar FOS is achieved; (c) Schematic of the computationally designed experimental test rig. The section view (Section A-A) shows the front view of the specimen; (d) Finalised test-rig design with mounted arterial SFRT specimen.

5.2.1 Sample Preparation

The ascending aorta and aortic arch were excised from 6 sheep sourced from a local abattoir (Brady's Athenry, Galway, Ireland). Excess connective tissue was carefully removed from the external (adventitial) surface of the vessel. Notched and un-notched specimens were prepared through cutting cylindrical sections out of the aorta to form circumferentially intact rings. Sample dimensions were taken using a digital Vernier

callipers and a digital thickness gauge. Tissue samples were stored at 0-4°C in phosphate buffer solution prior to testing to ensure adequate tissue hydration and preservation. Unnotched intact ring extension tests (n=6) and notched ring extension tests (n=11) were carried out. Samples were mounted on a rigid bar to allow for constrained, precise notching. Two notches were introduced using a No. 10 scalpel blade at opposite ends of the sample. Notches were approximately a half of the tissue thickness in depth ($r_{ct} \approx t/2$). The boundary of the notch was marked with blue waterproof all-surface ink. Samples were mounted on the extension bars and tested to failure at a strain rate of 10 mm/minute. The samples were rotated such that the notches were aligned with $S = \pi(r_b + d)/2$.

To determine the anisotropic hyperelastic properties and anisotropy of the material, three experiments were carried out: axial extension, circumferential extension, and unnotched intact ring extension. Uniaxial testing in two directions was carried out rather than biaxial testing due to the non-uniform strain states in biaxial samples (Nolan and McGarry, 2016b). Strips were excised from the ascending aorta and cut to uniform rectangular shapes in the axial and circumferential directions maintaining a mean aspect ratio of $L:w = 3.8:1$ (all mean specimen dimensions are presented in Table 5.1). The samples were gripped using Zwick pneumatic specimen jaws. Axial (n=10) and circumferential (n=6) extension tests were carried out individually with a crosshead speed of 10 mm/min. Each of the samples were tested to failure.

Table 5.1. Mean specimen dimensions \pm SD for each of the experiments. Reported values for SFRT length and unnotched intact ring extension length refer to the diameter of the specimen pre-test. Circumferential extension length is the initial grip to grip separation. *Peel test experiment is presented in supplementary material I.

Experiment	Length or Radius (mm)	Width (mm)	Thickness (mm)
Peel Tests* (n=7)	37.96 ± 6.59	12.77 ± 1.07	1.95 ± 0.5
Circumferential Extension (n=6)	19.06 ± 2.28	4.60 ± 1.17	1.39 ± 0.16
Axial Extension (n=10)	27.68 ± 4.35	7.89 ± 0.92	2.06 ± 0.33
Unnotched Intact Ring Extension (n=7)	$8.85 \pm 0.23 (R_S)$	5.15 ± 0.49	2.05 ± 0.14
SFRT (n=11)	$9.09 \pm 0.60 (R_S)$	9.73 ± 2.32	2.35 ± 0.16

5.3 Results

5.3.1 Determination of Hyperelastic Properties

Prior to simulation of fracture experiments, the anisotropic hyperelastic behaviour of the arterial tissue must first be calibrated using uniaxial tension testing of the tissue in the circumferential and axial directions, as described in Section 5.2.1. Additional validation of the calibrated material model is performed by experimental and computational analysis of the response of unnotched artery sections to our *SFRT*. Experimental tensile testing reveals significant anisotropy and material non-linearity, as shown in Figure 5.5a. The material exhibits a higher initial stiffness in the circumferential direction. Furthermore, in the circumferential direction the material transitions to a high stiffness regime at a strain of ~ 0.4 . Strain stiffening is less pronounced in the axial direction. The model provides an accurate representation of the material anisotropy and strain stiffening both in the circumferential direction ($RMSE_{circ} = 0.0059$) and in the axial direction ($RMSE_{axial} = 0.0144$) for the unique material parameter set presented in Table 5.2. Simulation of the stretching of an unnotched intact ring using the calibrated material model parameters, is shown in

Figure 5.5(b). Results are in strong agreement with corresponding experimental measurements for the entire range of applied deformation ($RMSE_{ring} = 0.0081$).

Table 5.2. Table of best fit material parameters for the arterial material model.

D_1^m	D_2^m	E_1^m (MPa)	E_2^m (MPa)	K (MPa)	D_1^f	D_2^f	E_1^f (MPa)	E_2^f (MPa)	α (°)	β
0.15	0.9	0.075	0.5	1.52	0.4	0.5	0.16	4.5	28.5	15.0

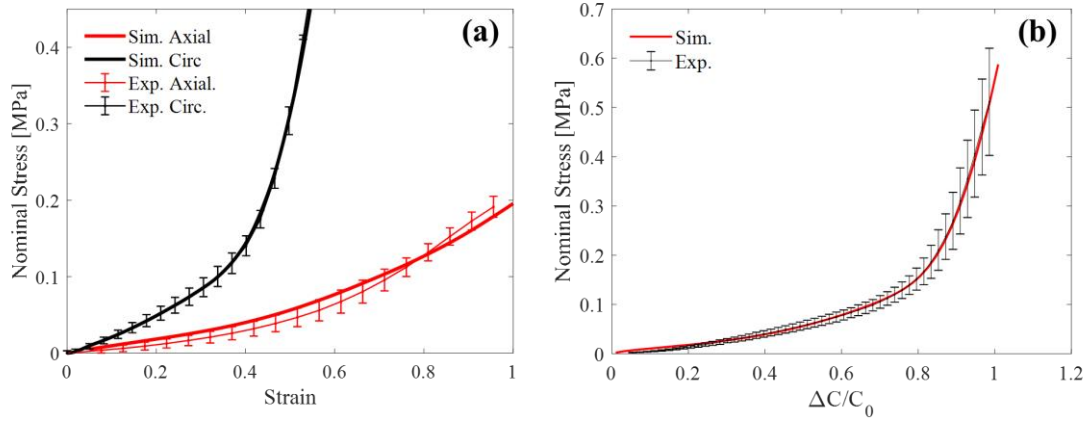


Figure 5.5. (a) Nominal stress (MPa) as a function of nominal strain for the uniaxial extension of the axial and circumferential datasets. Experimental data and numerical data are shown. The root mean squared error (RMSE) of the axial and circumferential data sets are 0.0144 and 0.0059 respectively; (b) Nominal stress (MPa) as a function of the circumferential strain for the unnotched intact ring extension tests. RMSE for the unnotched intact ring extension test is 0.0081. Final material parameters are presented in Table 5.2. Full details of the artery anisotropic hyperelastic material law are presented in Appendix A.

5.3.2 Fracture Mechanics results

Firstly, we introduce the results of our SFRT fracture mechanics investigation by presenting the details of a representative aorta test sample, Figure 5.6 shows the measured force (F/wt) versus applied nominal circumferential strain ($\Delta C/C_0$). The measured force continues to increase beyond the point of crack initiation at $\Delta C/C_0 = 0.72$. This is due to the continued load bearing capacity of the outer section of the ring ($r > r_{ct}$) up to the point of ultimate rupture.

Fracture initiation (shown in Figure 5.6(a)) appears to be a pure mode II initiation with no evidence of normal separation of the fracture surfaces at the crack-tip; i.e. fracture

initiation entails an immediate kinking of the radial notch so that a mode II initiation along the c - a plane occurs. This experimental result demonstrates that toughening mechanisms due to fibre alignment behind the crack-tip will result in crack kinking and mode II fracture along the c - a plane, rather than mode I fracture along the r - a plane. Following initiation, significant crack propagation is observed in the c -direction through the c - a plane over a long distance (Figure 5.6(a-d)). This crack propagation appears to be close to pure mode II with no visible normal separation at the crack-tip. A relatively smooth fracture surface is observed along the c - a plane and the crack flank (delaminated material) is observed to remain flat to the c - a plane throughout the test. As shown in Figure 5.6(b), at $\Delta C/C_0 = 0.86$, propagation appears to be a pure mode II in nature. This pattern of mode II propagation continues through $\Delta C/C_0 = 0.93$ (Figure 5.6(c)) up to, and including, the point of ultimate rupture ($\Delta C/C_0 = 0.97$; Figure 5.6(d)). This observed pattern of mode II initiation and propagation in the c -direction along the c - a plane is remarkably similar to that predicted by experimental design calculations (Figure 5.2). This exact pattern of mode II initiation and propagation was observed in all samples ($n=11$) subjected to our novel SFRT test. In no case was mode II cracking in the r -direction observed, despite the high levels of circumferential nominal strain applied to the specimen during our SFRT tests. This highlights the benefit of detailed computational analysis to uncover competing mechanism of material damage when designing biomechanical tests for biological materials.

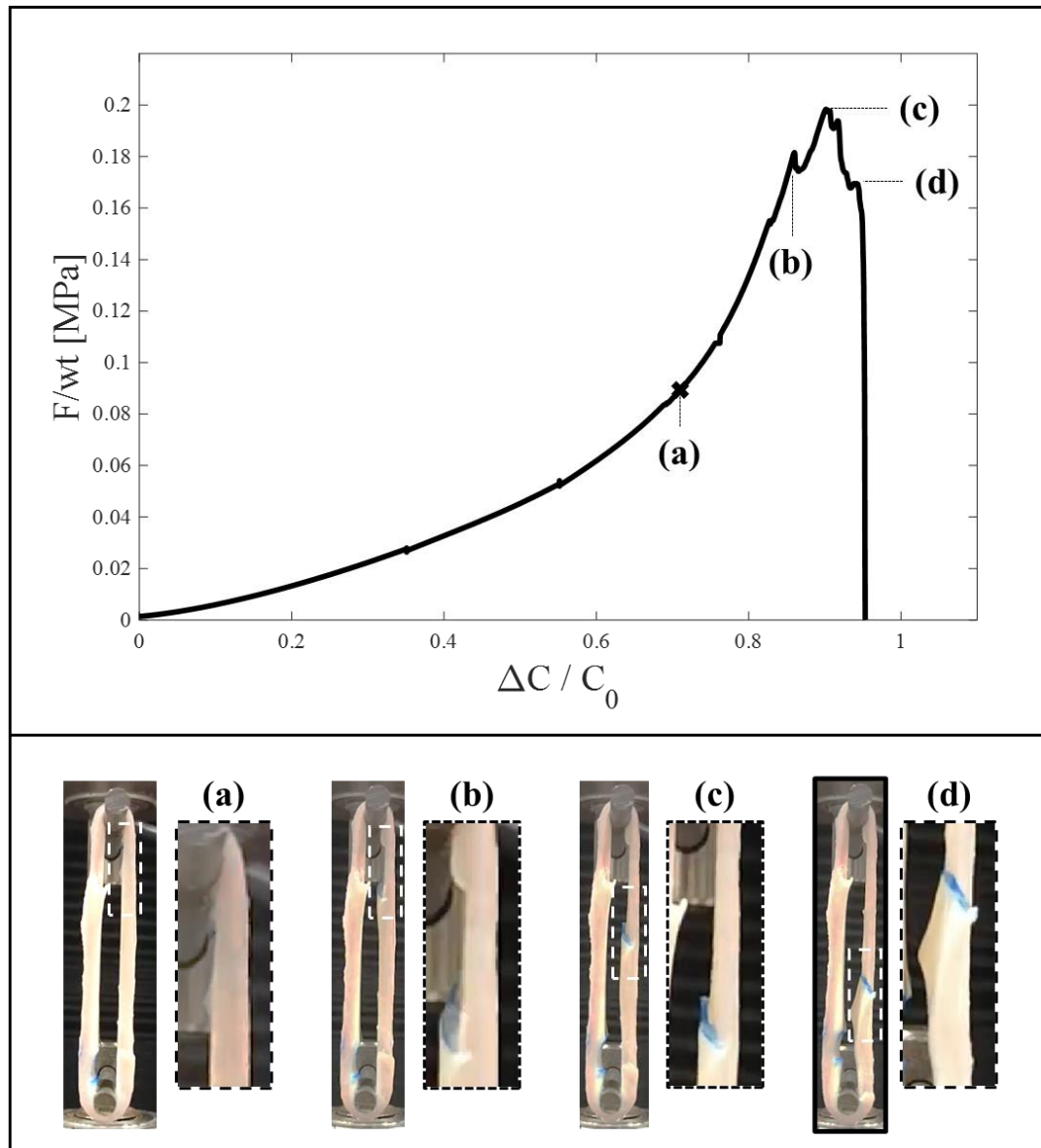


Figure 5.6. The graph shows force normalised by the cross-sectional area, F/wt (MPa) as a function of the circumferential strain ($\Delta C/C_0$). The point of crack initiation is marked with an X. Experimental results of the *SFRT* for a representative sample. (a-d) Progression of the crack tip from the point of initiation to ultimate rupture of specimen (S3). The original notch is seen in blue.

Figure 5.7(a) shows the measured force (F/wt) versus applied nominal circumferential strain ($\Delta C/C_0$) for all *SFRT* samples ($n=11$). Points of crack initiation are indicated for all cases. As stated above, mode II crack propagation in the c direction through the c - a plane is observed in all cases. Generally, fracture initiation is observed to occur in the transition between the initial low stiffness regime and the

high stiffness regime. The range of nominal strain at initiation is observed as $0.53 \leq \Delta C_i/C_0 \leq 0.82$; $\text{mean} \pm \text{SD} = 0.64 \pm 0.23$. This illustrates the quantitative repeatability of the SFRT methodology, despite high levels of inter-sample variability typically reported for mechanical behaviour of aortic tissue. Finally, in all samples ($n=11$), crack initiation does not eliminate the load bearing capacity of the specimen due to the intact outer layer of each specimen ($r > r_{ct}$). However, superposition of the corresponding mean curve for an intact unnotched specimen subjected to the same loading regime (Figure 5.7(a)) confirms that the presence of the notch, and consequent mode II crack propagation, leads to a reduction in measured force throughout each test. Figure 5.7(b) shows measurements of the cracked plane as a function of the interface length (S). \tilde{t} is the measurement of deviation from the original crack plane, it is defined as $t(S)/t(S_i)$ where $t(S)$ is the thickness of the remaining intact wall at the position S , and $t(S_i)$ is the thickness of the remaining wall at the position where the crack initiated. Mean measured values and standard deviation is shown by the boxes and error bars, respectively. The dashed line indicates no deviation from the original crack plane ($\tilde{t} = 1$). A t-test reveals no statistically significant difference between any of the measured values ($p=2.39\text{e-}9$).

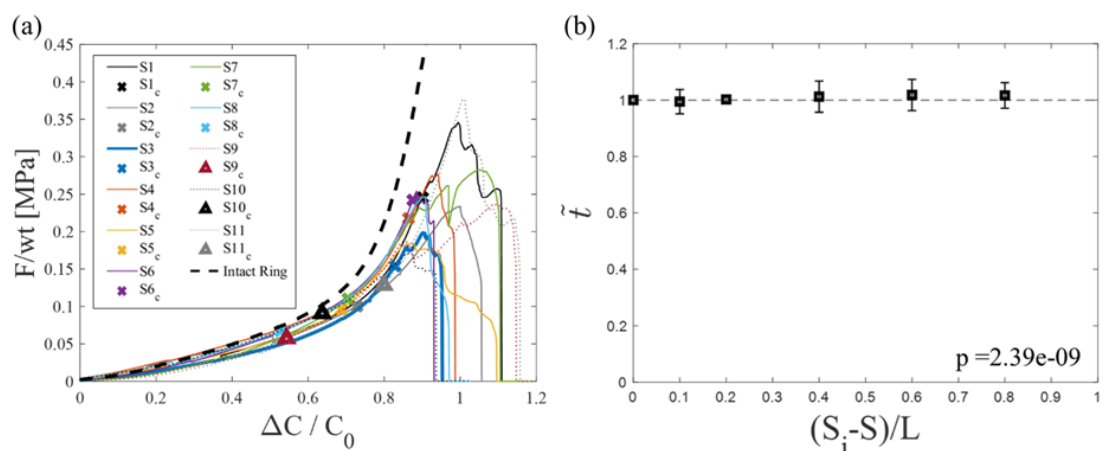


Figure 5.7. (a) Force normalised by the cross-sectional area, F/wt (MPa) as a function

of the circumferential strain ($\Delta C/C_0$) for each of the radial notch test specimens. The points of crack initiation are marked with the symbol shown in the legend and are denoted by S_n_c where n is the specimen number. The mean stress strain data of all the samples for the unnotched intact ring extension test is shown as the thick dotted black line. The notched samples exhibit a lower stiffness in the high strain regime compared to the unnotched intact ring. (b) Measurements of the crack plane as a function of the interface length (S). \tilde{t} is the deviation of the crack plane from the original crack plane. Figure 5.8 shows the deformed crack length as a function of applied deformation beyond the point of initiation ($(\Delta C - C_i)/C_i$). The mean final deformed crack length was 22.65 ± 9.68 mm. The typical fracture pattern is characterised by a regime of slow crack growth post-initiation followed by a regime of rapid growth. One likely cause for the initial slow growth followed by the rapid growth is the experimentally observed fibrillation during early stages of crack growth. Extension and pull-out of fibres between fracture surfaces will provide partial resistance to crack propagation. In 4 samples, a third regime of further slow crack growth subsequent to the fast growth regime is observed.

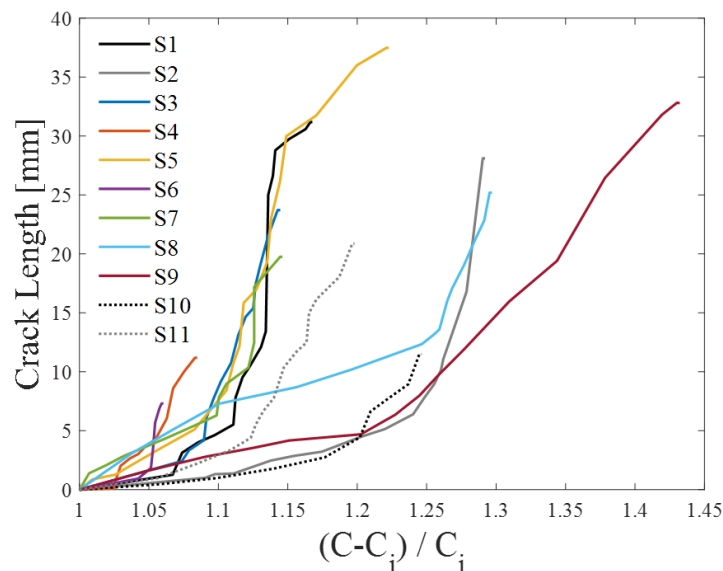


Figure 5.8. Crack length as a function of circumferential stretch past initiation. $(C - C_i)/C_i = 1$ indicates the point of crack initiation and the final point on each curve is the point at which the specimen underwent final rupture.

Images of the fracture surfaces are shown for eight samples in Figure 5.9. The original notch is marked with blue ink in each of the images. Images confirm that crack propagation is restricted to the same c - a plane (through the original notch-tip) for the entirety of the test, up to the point of final rupture, again confirming the mechanism of mode II fracture predicted in our design of experiment calculations (Figure 5.2). Fibrillation is observed at the crack-tip at the end of SFRTs, as shown Figure 5.9(h), in addition to the early stages of fracture propagation and initiation.

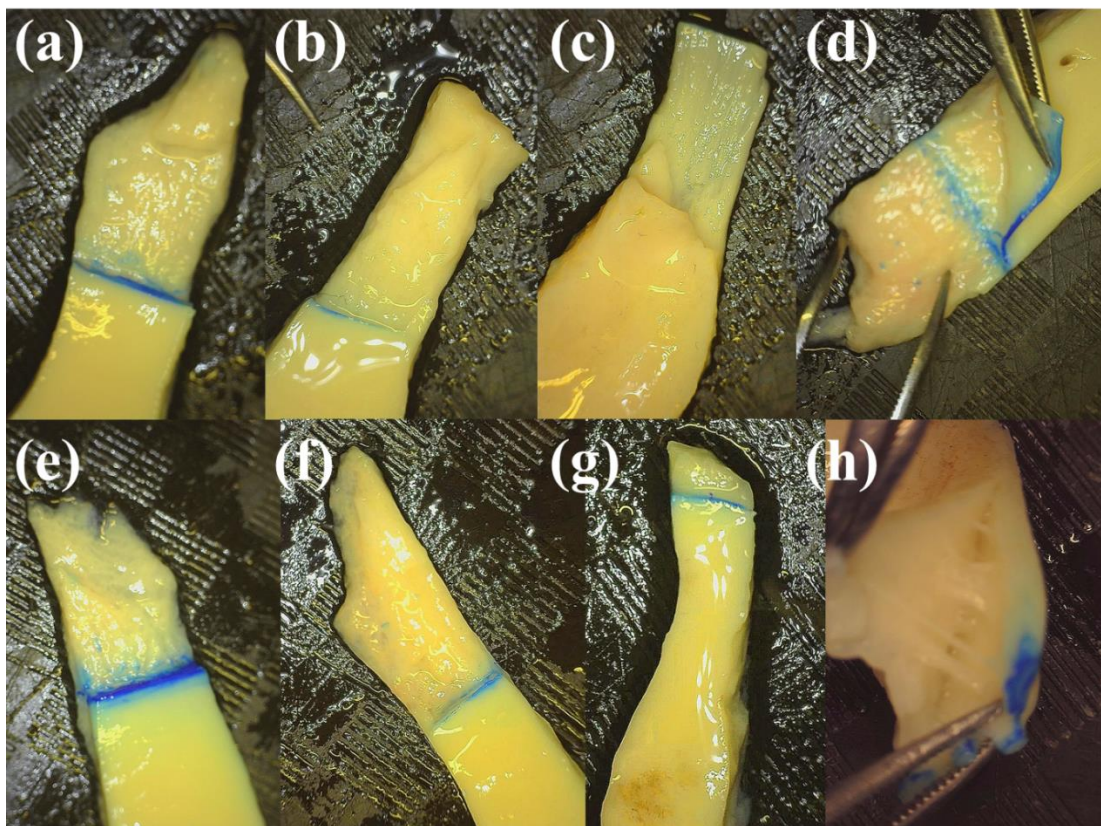


Figure 5.9. Fracture surfaces of the specimens. Original notches are shown with blue ink. Fibrils formed during fibrillation are shown in (h).

5.3.2.1 Computational analysis of SFRT experiments to determine mode II fracture properties

Deformed finite element meshes during crack initiation and propagation are shown in Figure 5.10(a). In all simulations the mixed-mode CZM described in Appendix A is

implemented. The value of the parameter σ_{max} of 202 *kPa* (the mode I fracture strength along the *c-a* plane) is determined from the implementation of standard peel test experiments, described in Appendix C. The sensitivity of SFRT crack initiation to the mode II fracture strength, τ_{max} , is presented in Figure 5.10(b). τ_{max} values of 1.4 MPa and 1.8 MPa predict fracture initiation within the experimentally observed standard deviations (in terms of circumferential strain and measured force), and a value of $\tau_{max} = 1.6$ MPa leads to the prediction at $\Delta C/C_0 = 0.63$ and $F/wt = 0.84$ MPa, which is within 0.86% of the experimentally measured mean values of $\Delta C/C_0 = 0.63$ and $F/wt = 0.84$ MPa, respectively. This suggests that the mode II fracture strength for initiation along the *c-a* plane is eight times higher than the corresponding mode I strength along the *c-a* plane. It should be emphasised that this is not reflective of the mode I strength for fracture along the *r-a* plane, which we expect to be considerably higher than τ_{max} or σ_{max} along the *c-a* plane. Similar to experimental measurements, the computed force (F/wt) increases following fracture initiation. Additionally, similar to experiments, computed forces for notched SFRTs

are lower than corresponding curves without the presence of a notch/crack propagation.

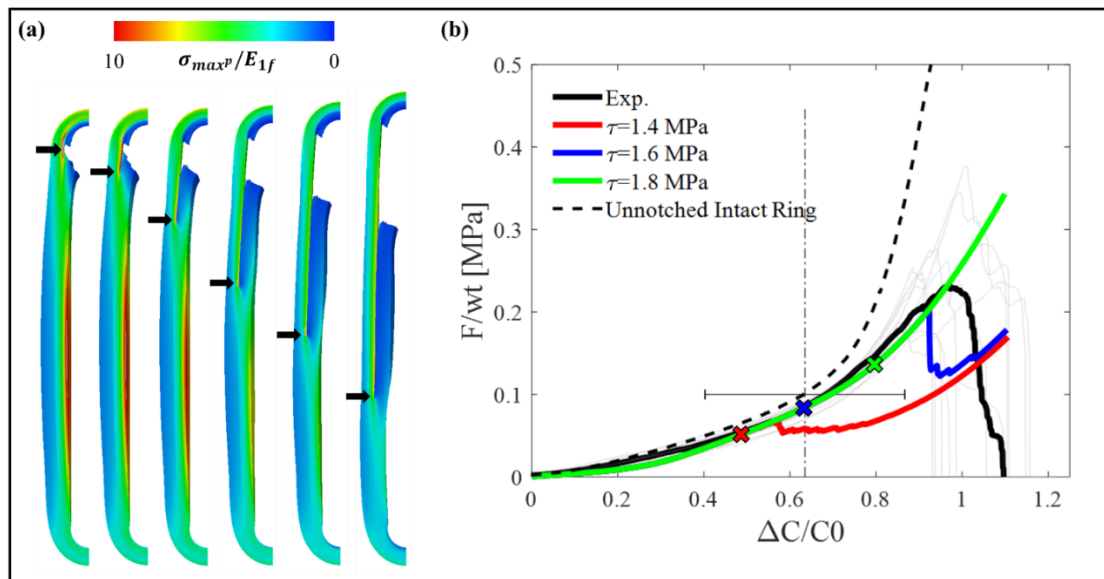


Figure 5.10. (a) Contour plot of max principal stress showing the progression of a mode II crack propagation, black arrows indicate the area of the crack tip; (b) Sensitivity of the crack initiation to the mode II interface strength. Mean force normalised by the cross-sectional area as a function of circumferential strain ($\Delta C/C_0$) for the SFRT. Points of crack initiation are shown with an 'X'. In each simulation the mode I interface strength was $\sigma = 202 \text{ kPa}$, the mode II fracture energy was $G_t^0 = 0.001 \text{ N/mm}$, and the mode I fracture energy was $G_n^0 = 0.001 \text{ N/mm}$. The mean circumferential strain ($\Delta C/C_0$) at initiation is shown by the vertical dotted black line and the standard error is shown by the horizontal error bar. Full details of the artery anisotropic hyperelastic material law and cohesive zone model are presented in Appendix A and Chapter 4, respectively.

Figure 5.11 shows the evolution of the J1 and J2 components of the J integral at the crack tip in addition to the fibre alignment evolution during the simulation. The mean circumferential strain at fracture is shown by the dotted line and the standard deviation is shown in the highlighted region. As seen in Figure 5.11, J1 is 8 times higher than J2 at the mean point of initiation. Fracture initiation occurs in the circumferential direction only when fibres are almost fully aligned in the c - a plane. This suggests that the J_{crit} is at least 8 times higher for crack propagation in the radial direction than the circumferential direction. The experiment generates a sufficiently high J2 component

of the J-integral at the crack tip to result in circumferential propagation, while fibre alignment results in a significant toughening mechanism against radial crack initiation so that $J_1 < J_{1crit}$ and propagation does not occur in the radial direction. In arterial tissue, collagen fibres lie along $c-a$ planes, as structural investigations indicate this depends on age, pathology, and type of artery (Whittle *et al.*, 1990; Tsamis, Krawiec and Vorp, 2013; Pierce *et al.*, 2015). Therefore, collagen alignment due to increased circumferential strain acts as a toughening mechanism only for fracture in the radial direction (through the aligned fibres). Crack propagation in the circumferential direction does not benefit from the toughening mechanism of fibre alignment (essentially cracks propagate between the collagen).

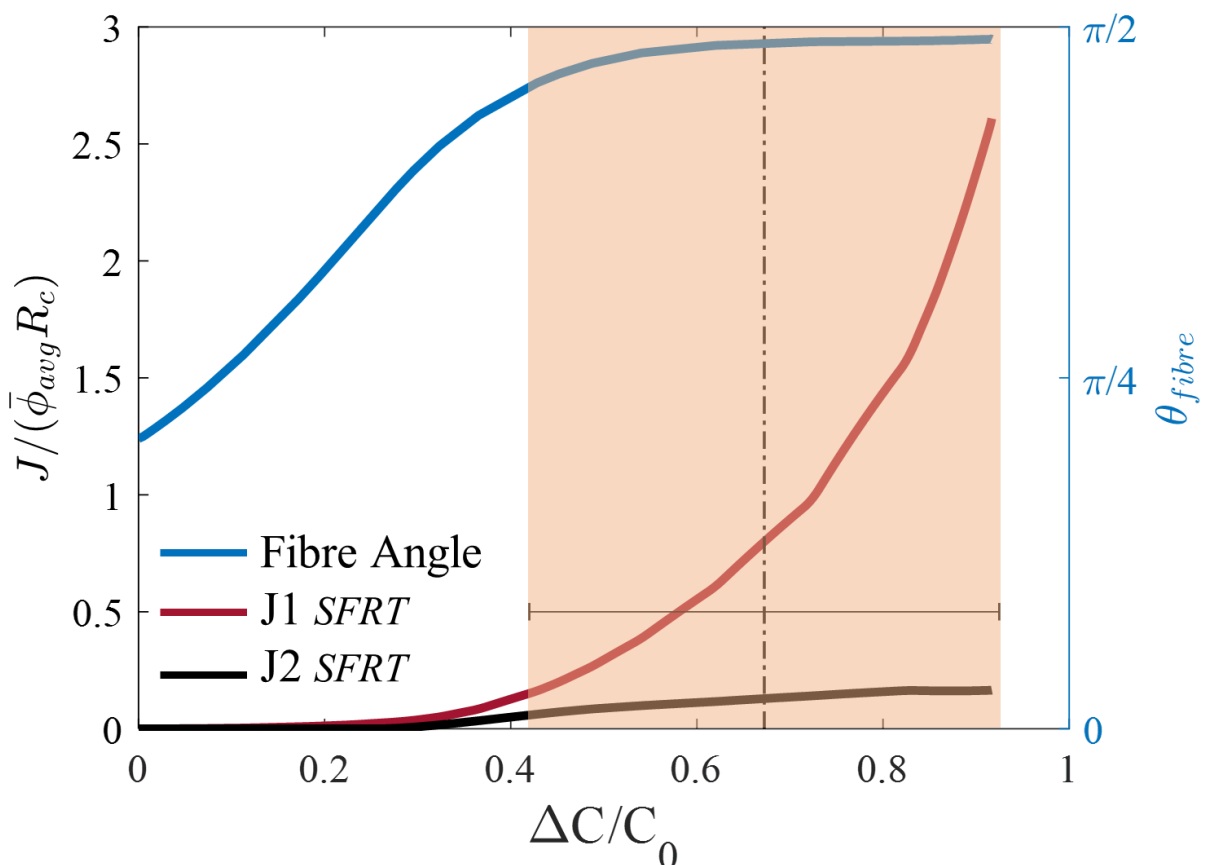


Figure 5.11. (left y-axis): J-Integral calculations for fracture paths in the radial and circumferential directions as a function of circumferential strain in a SFRT. (right y-axis): Fibre angle as a function of circumferential strain. Fibres are almost fully

aligned in the c -direction at a circumferential strain of 0.6. A non-dimensional fracture resistance is presented as $J/(\bar{\phi}_{avg}R_c)$ where $\bar{\phi}_{avg}$ is the volume averaged strain energy density in the arterial tissue within a radius R_c from the notch-tip. Note that $\bar{\phi}_{avg}R_c$ is identical for both crack paths so the figure presents a direct comparison of the J-integrals.

While the point of fracture initiation is highly sensitive to the parameter τ_{max} , it is not found to be sensitive to the mode II fracture energy (G_t^0). However, as shown in Figure 5.12, simulations reveal that the rate of crack propagation exhibits sensitivity to G_t^0 . Simulations reveal that a value of $G_t^0 = 0.25$ N/mm results in a rate of crack propagation that is slower than that observed experimentally. On the other end of the spectrum, values of $G_t^0 \geq 0.0005$ N/mm result in excessively high rates of propagation compared to experimental measurements. A value of $G_t^0 = 0.005$ N/mm is predicted to provide a reasonable approximation of experimental measurement, both during early and later stages of crack initiation.

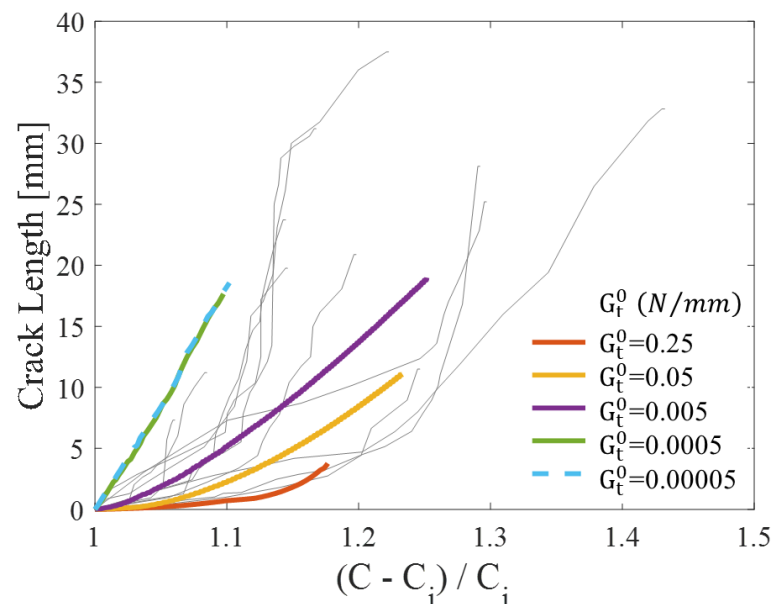


Figure 5.12. Simulated crack length as a function of circumferential stretch past initiation presented alongside the experimental data (shown in light grey). The crack length and velocity are shown to depend on the mode II fracture energy. Cohesive zone parameters are $\sigma_{max} = 202$ kPa, $\tau_{max} = 1.6$ MPa, the mode I fracture energy is scaled with the mode II fracture energy according to $G_n^0 = (\sigma_{max}/\tau_{max})G_t^0$. Full

details of the artery anisotropic hyperelastic material law and cohesive zone model are presented in Appendix A and Chapter 4, respectively.

5.4 Discussion

The current study presents the development and implementation of a novel experimental technique (SFRT) to generate and characterise mode II crack initiation and propagation in arterial tissue. A mechanistic consideration of a large body of clinical studies suggest that artery dissection results from mode II initiation and crack propagation along a c - a plane in the artery wall, rather than mode I propagation. However, the majority of artery fracture experiments rely on mode I peel test. Recently the studies of Sommer et al. (Sommer *et al.*, 2016) and Witzenburg et al. (Witzenburg *et al.*, 2017) adopt standard lap-shear test techniques to measure mode II fracture properties. The current study begins with a demonstration that lap-shear testing of arterial tissue results in mixed mode fracture, rather than mode II due to the high levels of tissue deformation at the crack-tip at the point of initiation. The combination of high toughness and high deformability of arterial tissue presents a considerable challenge in generating mode II fracture. A further challenge, albeit an obvious one, is that fracture testing of naturally occurring biological materials such as arteries does not facilitate the engineering of standardised fracture specimen geometries. Therefore, implementation and interpretation of fracture testing subject to the limitation of non-standard geometries such as arteries requires in-depth mechanistic analysis. In the current study we perform a detailed computational design of a novel experimental method (which we refer to as a shear fracture ring test (SFRT)) to robustly and repeatably generate mode II crack initiation and propagation in the c - a plane of arteries. This method is based on generating a localised region of high shear adjacent to a cylindrical loading bar. Placement of a radial notch in this region of high shear

stress is predicted to result in a kinking of the crack during a mode II initiation and propagation of the crack over a long distance in the c -direction along the c - a plane. A J-integral analysis suggests radial mode I crack propagation will not occur due to significant fracture toughening as a result of collagen alignment in the c -direction behind the crack-tip. Fabrication and experimental implementation of the SFRT on excised ovine aorta specimens confirms that the novel test method results in pure mode II initiation and propagation, as predicted by our computational design of experiment. Using a cohesive zone formulation, we simulate our mode II experimental tests, and we demonstrate that the mode II fracture strength along the c - a plane is eight times higher than the corresponding mode I strength determined from a standard peel test. We also calibrate the mode II fracture energy based on our measurement of crack propagation rates. The mechanisms of fracture uncovered in the current study, along with our quantification of mode II fracture properties have significant implications current understanding of the biomechanical conditions underlying in vivo aortic dissection.

The present study provides an explanation why every dissection is associated with circumferential and axial crack propagation, but not always radial (i.e. the majority of aortic dissections do not rupture (Hagan *et al.*, 2000; Trimarchi *et al.*, 2007)). Aortic rupture requires radial crack propagation, and collagen fibre alignment provides high levels of toughening against radial fracture. The results of this study suggest radial crack propagation is only likely to occur between collagen fibres or in areas where there is less fibre toughening. The majority of aortic dissection-induced ruptures occur in the ascending aorta leading to cardiac tamponade and death (Miller *et al.*, 1984; Hagan *et al.*, 2000). This may be due to the discontinuous and irregular collagen structure observed in the wall of ascending aortic dissections (Sariola, Viljanen and

Luosto, 1986; Tsamis, Krawiec and Vorp, 2013). Such irregular and discontinuous structure reduces the radial toughening mechanism in the aortic wall. This is also a possible mechanistic explanation for the high incidence of aortic dissection amongst patients with connective tissue diseases such as Marfan syndrome and Ehler-Danlos syndrome (Abraham *et al.*, 1982; Nakashima, Shiokawa and Sueishi, 1990; Lemaire and Russell, 2011; Yuan and Jing, 2011). Connective tissue disorders significantly alter the intramural and inter-lamellar aortic microstructure and strength through abnormal fibrillin (Marfan), and collagen deterioration (Ehler-Danlos). This puts patients with connective tissue disorders at higher risk of aortic dissection (Brandt *et al.*, 2001; Ulbricht *et al.*, 2004).

The propagation of a pure mode II crack following insertion of a notch is suggestive that the intimal tear or initiation tear acts in a similar fashion *in vivo* to the notch (Criado, 2011). The notch acts as a concentrator of stress at the notch tip and causes shear stress localisations (Anderson, 2005). The notch also significantly reduces the strain in the inner layer of the artery relative to the outer layer which results in a shear concentration. The results of the present experiment serve as supporting evidence to the theory that aortic dissection is far more likely to occur in the presence of an intimal tear (Larson and Edwards, 1984; Dake *et al.*, 2013). This is highlighted further by the additional testing carried out using circumferential notches (see appendix B). Only 3 of the 8 samples tested with circumferential notches resulted in mode II crack propagation, indicating crack growth in the aorta is much more likely to occur in the presence of a radial tear or notch.

The use of the bilinear material model in the present study allows for the elimination of unphysical auxetic behaviour commonly associated with other anisotropic fibre material models in which the fibre is described using an exponential or power law

term. Furthermore, it circumvents other known issues associated with these models, such as unphysically high stress states in regions of localised high strain. Accurate calculation of material stress is fundamental to accurately calibrating the cohesive zone model fracture properties.

The cohesive zone model used in the present study allows for the accurate calibration of a mode II interface strength and mode II fracture energy. However, it is not capable of capturing the complex rate-dependant plastic nature of the fracture, this is reflected in the predicted crack lengths which are linear and do not sufficiently capture the two crack growth regimes (fibrillation and rapid crack growth). Future work should focus on the development of a rate-dependant cohesive zone model capable of capturing the complex nature of viscoplastic fibrillation in soft tissues. The cohesive zone parameters calculated in the present study should be applied to patient-specific geometries to assess the risk of dissection. They should also be used to examine a range of biomechanical factors which may influence arterial dissection. A companion study to the present study is currently underway examining the application of these CZM parameters to an MRI derived subject-specific aortic geometry to analyse the risk of aortic dissection.

The residual stress state in the aorta has been well documented previously (Sokolis et al. 2017). The aortic residual stress state is heterogenous through the thickness of the wall varying in each arterial layer (Holzapfel et al. 2007). Under a zero pressure state an aortic ring is under a constant circumferential stress due to the presence of elastin. Selective enzymatic digestion of elastin in an aortic ring results in dilation of the zero pressure state artery (Schriefl et al. 2015) suggesting elastin is a significant contributor to residual strain in the aorta. Inclusion of residual stress in the form of an elastin pre-

stretch in the material model may lead to a more accurate calibration of the cohesive zone fracture model parameters.

The test methodology (*SFRT*) developed in the present study could readily be applied to large veins such as the pulmonary veins or other large arteries (left subclavian artery, left common carotid artery, brachiocephalic artery, iliac arteries, renal arteries). The apparatus could be scaled to work on coronary arteries, femoral arteries, carotid arteries, and other arteries of a similar size). Furthermore, it could potentially be used with any other tubular soft tissue of interest such as the urethra, bronchial tubes, trachea, and skin to name but a few.

5.5 Appendix A: Artery Material Model

In order to simulate the anisotropic non-linear hyperelastic behaviour of arterial tissue we use a recently proposed formulation by Fereidoonzhad and McGarry (Fereidoonzhad, O'Connor and McGarry, 2020). Full details are presented in Fereidoonzhad et al. (Fereidoonzhad, O'Connor and McGarry, 2020), including extensive demonstration that this new formulation robustly avoids the computation of non-physiological auxetic behaviour during large deformation of anisotropic soft tissue, in contrast to established formulations. Here we briefly present the key features of the model and we demonstrate that it accurately captures the mechanical behaviour of the ovine arterial specimens used in this study. The anisotropic strain energy density function due to the presence of two fibre families is given as $\Psi_{aniso} = \sum_{i=1,2} \Psi_{fi}$, where

$$\Psi_{fi} = \begin{cases} E_{1f} \left(\frac{2}{3} \lambda_{fi}^3 - \lambda_{fi}^2 + \frac{1}{3} \right), & \lambda_{fi} - 1 \leq D_{1f} \\ \frac{2}{3} \lambda_{fi}^3 (q - 2p) + \frac{p}{2} \lambda_{fi}^4 + \lambda_{fi}^2 (p - q + r) + \psi_{01}, & D_{1f} < \lambda_{fi} - 1 < D_{2f} \\ \frac{2E_{2f}}{3} \lambda_{fi}^3 + \lambda_{fi}^2 (pD_{2f}^2 + qD_{2f} + r - E_{2f} - E_{2f}D_{2f}) + \psi_{02}, & \lambda_{fi} - 1 \geq D_{2f} \end{cases} \quad (\text{A1})$$

λ_{fi} is the fibre stretch of the i_{th} fibre family, D_{1f} and D_{2f} are material parameters, and p , q and r are given as:

$$p = \frac{E_{1f} - E_{2f}}{2(D_{1f} - D_{2f})}, \quad q = E_{1f} - 2D_{1f}p, \quad r = (E_{1f} - q)D_{1f} - pD_{1f}^2, \quad (\text{A2})$$

in which E_{1f} and E_{2f} are material parameters. The isochoric strain energy density function is given as

$$\psi_{iso}(\bar{\lambda}_1, \bar{\lambda}_2, \bar{\lambda}_3) = \sum_{i=1}^3 \bar{\psi}(\bar{\lambda}_i),$$

$$\bar{\psi}(\bar{\lambda}_i) = \begin{cases} E_1(\bar{\lambda}_i - \ln \bar{\lambda}_i - 1) & |\bar{\lambda}_i - 1| \leq D_1 \\ p \left(\frac{\bar{\lambda}_i^2}{2} - 2\bar{\lambda}_i + \ln \bar{\lambda}_i \right) + q(\bar{\lambda}_i - \ln \bar{\lambda}_i) + r \ln \bar{\lambda}_i + \psi_{01} & D_1 < |\bar{\lambda}_i - 1| < D_2 \\ E_2(\bar{\lambda}_i - (1 + D_2) \ln \bar{\lambda}_i) + (pD_2^2 + qD_2 + r) \ln \bar{\lambda}_i + \psi_{02} & |\bar{\lambda}_i - 1| \geq D_2 \end{cases} \quad (\text{A3})$$

where D_1, D_2, E_1 , and E_2 are material parameters, $\bar{\lambda}_i$ ($i = 1, 2, 3$) are the isochoric principal stretches, $J = \lambda_1 \lambda_2 \lambda_3$ is the jacobian, and ψ_{01} and ψ_{02} are two constants which ensure the continuity of strain energy. Moreover p , q , and r are not independent parameters; in order to maintain C^0 and C^1 continuity the following relations must be enforced:

$$p = \frac{E_1 - E_2}{2(D_1 - D_2)}, \quad q = E_1 - 2D_1p, \quad r = (E_1 - q)D_1 - pD_1^2 \quad (\text{A4})$$

The volumetric strain energy density function is given as

$$\Psi_{vol} = \frac{K}{2} \{J - 1\}^2 \quad (\text{A5})$$

A value of $\kappa = 1.52$ MPa is used resulting in slight material compressibility is based on the experiments of Nolan and McGarry (Nolan and McGarry, 2016a).

For further information regarding the material model the reader is directed to Fereidoon nezhad et al. (Fereidoon nezhad, O'Connor and McGarry, 2020). A *user defined material subroutine* (UMAT) has been developed for this formulation so that it can be implemented in the Abaqus finite element solver.

5.6 Appendix B: Circumferential Notch Tests

Circumferential notch tests ($n=8$) were also performed. Notches ($\approx 2.1\text{mm}$) were introduced through puncturing the aortic media through the entire specimen width. Notches were then grown manually to ensure a sharp crack tip was present. Notched samples were mounted onto the loading bars as described previously in Figure 5.3. The extent of the notch was marked with ink prior to testing to allow for accurate measurement of crack growth. Crack growth was also measured after the experiment.

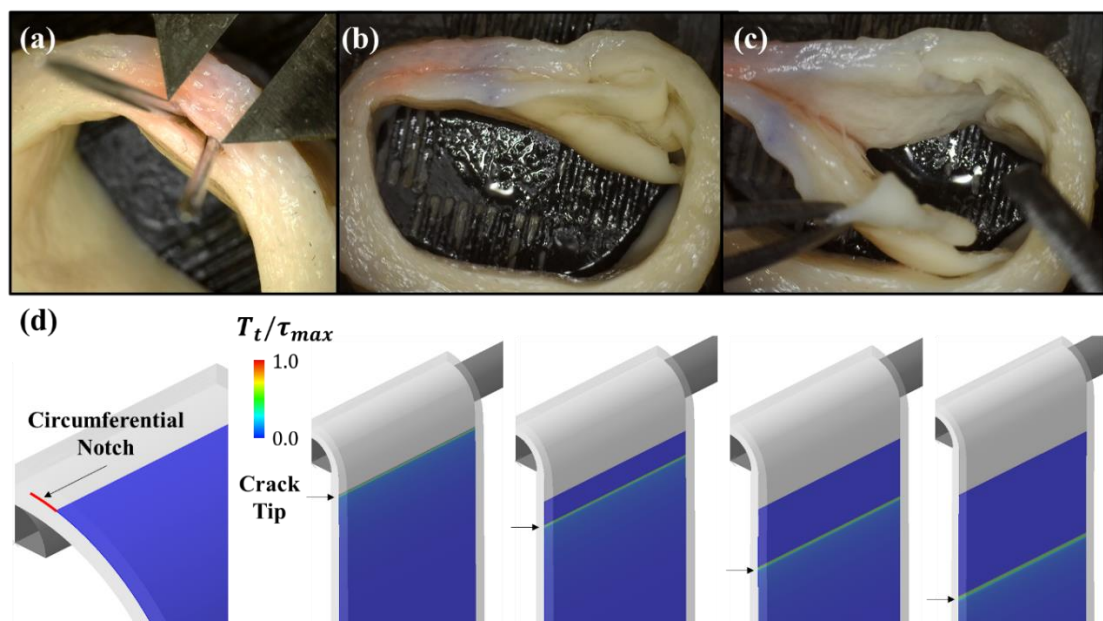


Figure 5.B1 (a) Image of the circumferential notch pre-testing. Circumferential notch

is shown measuring approximately ~ 2 mm; (b) Image of the specimen after testing and prior to ultimate failure. Significant crack growth is observed; (c) Image showing the extent of the circumferential crack growth. Dissected flap is peeled back to reveal the extent of fracture; (d) Finite element simulation of SFRT with a circumferential notch. Extensive crack growth is observed in the c -direction in the c - a plane. The black arrow indicates the position of the crack tip.

Crack growth was observed in 3 specimens out of the 8 tested. Average crack length was $11.79\text{mm} \pm 4.1\text{mm}$. Aortic dissection is most commonly associated with an intimal tear or notch (Larson and Edwards, 1984; Karthikesalingam *et al.*, 2010; Aun, 2013; Clough and Nienaber, 2015), however it can and does occur (although less commonly) without a visible entry tear in certain cases (Hirst, Johns and Kime, 1958; Wilson and Hutchins, 1982; Lui, Menkis and McKenzie, 1992; Colli *et al.*, 2018). This is reflected in the results of our study, all samples tested with a radial notch exhibited extensive mode II crack growth whereas only 3 out of 8 samples with a circumferential notch exhibited mode II crack growth. The mode mixity for the circumferential notch test is also explored in Figure . It shows the same as Figure 5.3(c) with the addition of the circumferential notch test. The mean mode mixity for the circumferential notch test is 89.18° .

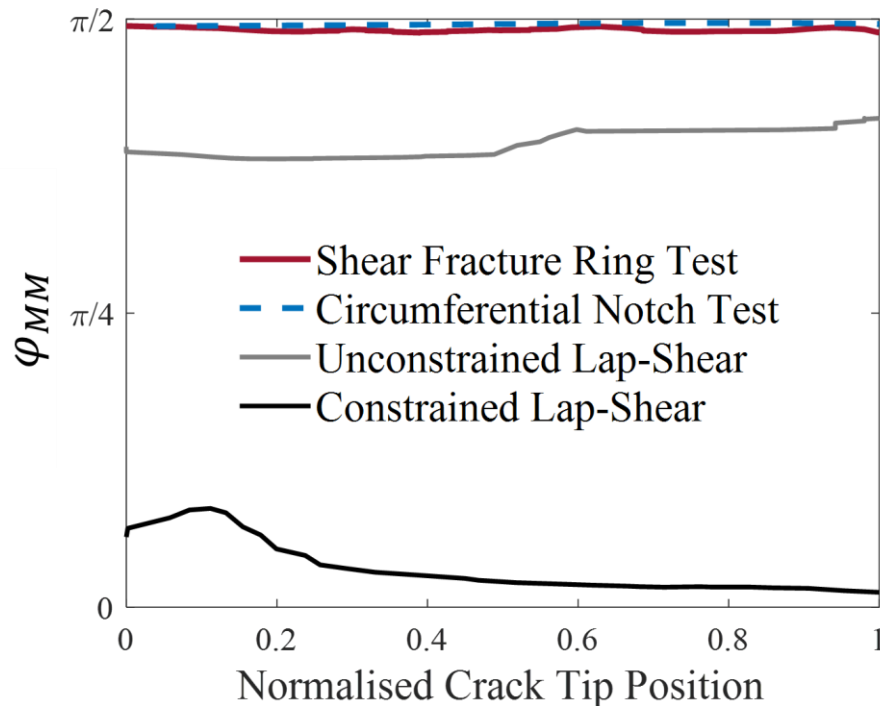


Figure 5.B2 Mode mixity φ_{MM} as a function of normalised crack tip position for the SFRT, circumferential notch test, unconstrained lap-shear, and constrained lap-shear. The mean mode mixity in the circumferential notch test is 89.18° .

5.7 Appendix C: Peel Tests

5.7.1 Methods

To characterise the mode I strength of the tissue, peel tests ($n=7$) were performed. Tubular sections of aorta were cut along the axial length of the artery resulting in planar sheet specimens. Using a scalpel with a No.10 blade, a notch was introduced at one of the boundary faces (Sommer *et al.*, 2008; Noble *et al.*, 2016) such that the notch was in the circumferential plane. The notch was then manually grown approximately 2mm to ensure a sharp crack tip. This created two layers (~ 8 -10mm) to be gripped in sandpaper and inserted into the grips of the test machine. Due to the well documented nature of the relatively low levels of anisotropy associated with peel tests and large standard deviation (Sommer *et al.*, 2008; Tong *et al.*, 2011b; Noble *et al.*, 2016) peel tests ($n=7$) were conducted in the circumferential direction. The tongues of prepared

samples were gripped on either side with sandpaper and placed into the grips of the test machine. A controlled displacement rate of 10.0mm/min was applied to the sample and the resultant reaction force was recorded. The zero level of the force was defined as the force after total separation had occurred.

5.7.2 Results

Experimental curve

Figure shows force/width (mN/mm) as a function of the applied displacement (mm). The mean curve is the thick black curve and each of the individual samples are shown in light grey. The mean force/width is 51.4945 mN/mm, it is shown in dashed red in the figure.

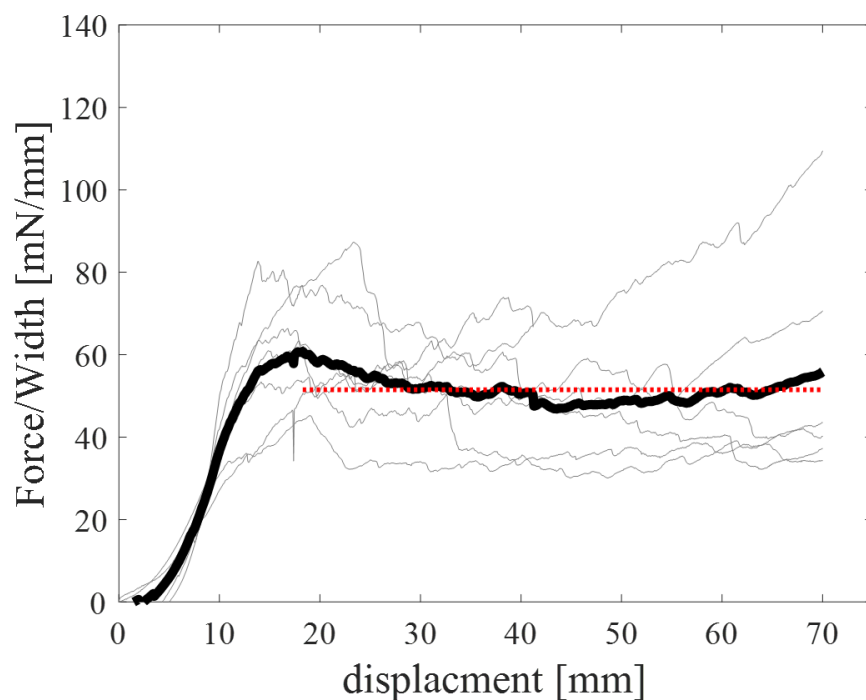


Figure 5.C1 Force/Width (mN/mm) as a function of the displacement (mm) for the peel test specimens. The mean Force/Width is 51.4945 mN/mm and is denoted by the red dotted line.

Computational fit

All the processes of the experiment are simulated to calibrate our mode I critical interface strength to the peel test data. The sensitivity of the system to variations in the critical interface strength to the peel test data. The sensitivity of the system to variations in the critical interface strength (σ_{max}) and variations in the mode I fracture energy (G_n^0) is investigated in Figure . No sensitivity of the Force/width to the mode II fracture energy (G_n^0) is found. This finding is in agreement with Ferrara and Pandolfi (2010), who found no sensitivity to mode I fracture energy in a numerical study of mode I peel tests of arterial tissue. The sensitivity of the force/width to the critical interface strength is explored in Figure where peel tests of various interface strengths are computed. A median filter is applied to the computed curves to eliminate noise caused by mesh. The mode I critical interface strength of ovine ascending aorta is calculated as $\sigma_{max} = 202kPa$.

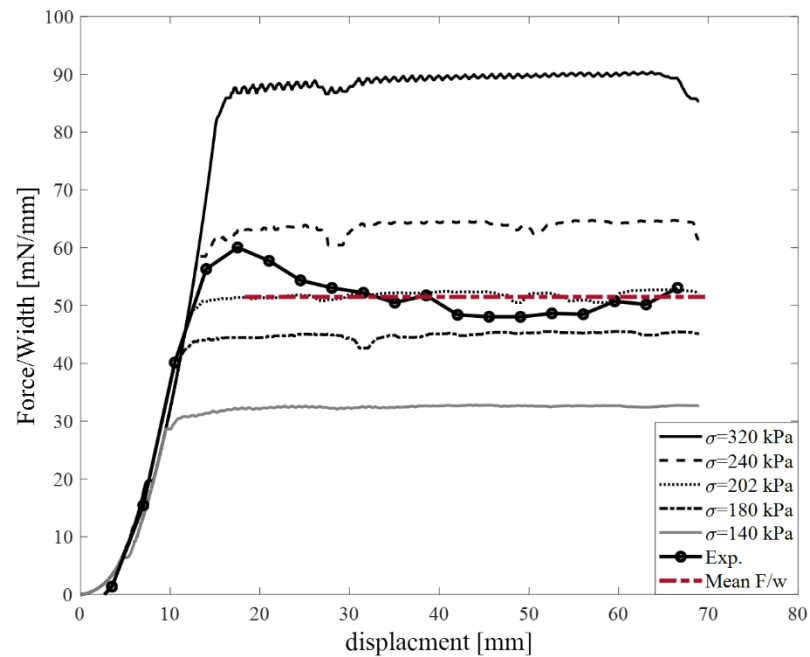


Figure 5.C2 Computed Force/width curves for several Mode I critical interface strengths. The mean force/width of the ascending ovine aorta undergoing a mode I peel is 51.49 mN/mm

The results of the peel test agree well with published literature. For example, the model presented in the current study with an interface strength of 140kPa calculates a nearly

identical mean force/width as seen in previous numerical studies of peel tests (29.03 mN/mm (present study) vs. 28.8 mN/mm (Sommer *et al.*, 2008; Ferrara and Pandolfi, 2010)). The differences in the mean experimental force/width may be partly explained by the difference in species, and anatomical location of the specimens. The mean force/width is in the region of other peel tests carried out on animals (51.49 mN/mm (present study) vs. 67.4 mN/mm (Noble *et al.*, 2016; Witzenburg *et al.*, 2017). Similarly to Ferrara *et al.* (Ferrara and Pandolfi, 2010), the mode I interface strength is found to be the primary determinant of the mean force/width and no significant influence of the fracture energy is found. Similar behaviour was also observed in the mesh convergence analysis (not here presented) where higher force/width and oscillations were observed with the coarser mesh and a reduction in force/width and oscillations was observed in the intermediate and finer meshes.

5.8 Appendix D: Mesh convergence

In this appendix we present the mesh convergence study carried out on the mesh used to calibrate the mode II interface strength and mode II fracture energy. The circumferential strain at initiation is shown as a function of the number of elements in the mesh. The only model parameter changed in each simulation was the mesh density. Mesh 3 is considered sufficiently accurate and was used for the calibration of the mode II interface strength and the mode II fracture energy. Mesh 3 contains an average of 8-9 nodes in the process zone throughout the simulation history.

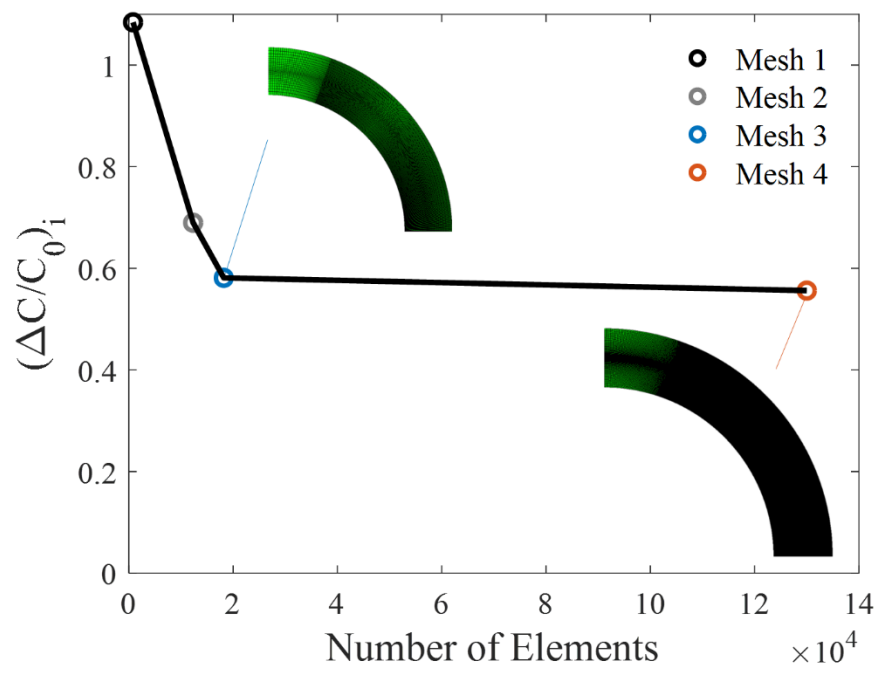


Figure 5.D1 Circumferential strain at initiation as a function of the number of elements in the mesh. Mesh 3 is the converged mesh.

5.9 Appendix E: Experimental Images



Figure 5.E1: Images of mode II crack propagation in 4 samples undergoing the SFRT. Red arrows approximately indicate the position of the crack tip. Fibrils formed during fibrillation are observed in the top left pane of images.

5.10 Appendix F: Viscoelasticity

In this appendix, viscoelastic material behaviour is considered, and the influence of including viscoelasticity on the calibration of the experimental results is also explored.

A two term Prony series is calculated according to previously published stress-relaxation data from Craiem *et al.* (Craiem *et al.*, 2008). Figure 5.F1(a) shows the Prony series fit to the stress-relaxation data for human arterial tissue. Figure 5.F1(b) shows the force over area curves as a function of the applied circumferential strain for three different strain rates, the mean experimental data of the SFRT is also presented.

A <2% decrease in final stress is computed between the physiological strain rate ($\frac{\Delta C}{C_0} =$

$800e - 3/s$) and the experimental strain rate ($\frac{\Delta\dot{C}}{C_0} = 6e - 3/s$). The experimental circumferential strain rate was chosen in order to allow for adequate frame rate capture during recording of the experiment.

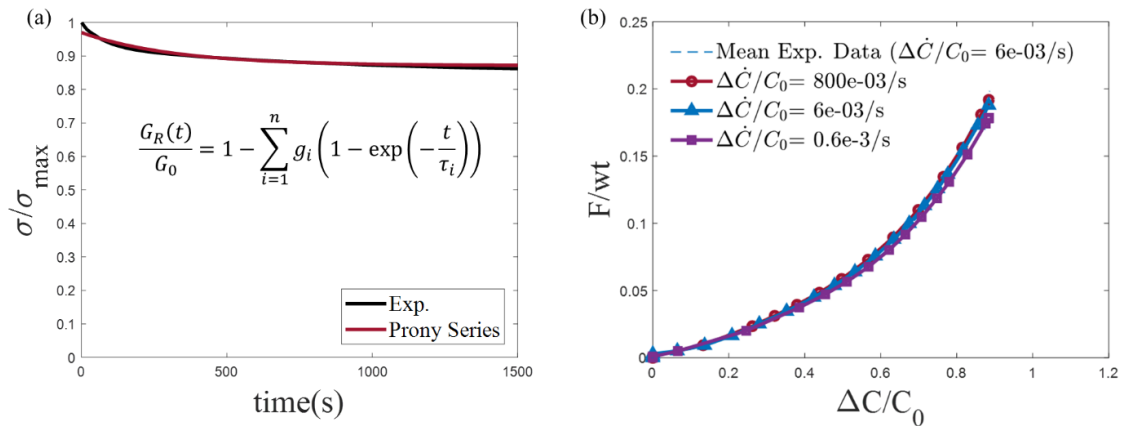


Figure 5.F1. (a) Stress relaxation data and computational model prediction of a two term prony series to data. (b) influence of physiological circumferential strain rate, experimental circumferential strain rate, and slow circumferential strain rate on the force/area. The mean experimental curve is also shown. Prony series parameters are as follows: $g_1 = 0.0256106$, $\tau_1 = 0.27891$, $g_2 = 0.12103$, $\tau_2 = 318.35$

5.11 Appendix G: The influence of friction on shear traction

In this appendix the influence of the coefficient of friction between the loading bar and the artery is explored. Figure 5.G1 shows the influence of the friction coefficient on the tangential traction at the crack tip. The influence of the friction coefficient on the tangential traction is shown to be minimal with only a $\sim 5\%$ increase in traction for a large friction coefficient of $\mu = 0.25$ compared to frictionless contact.

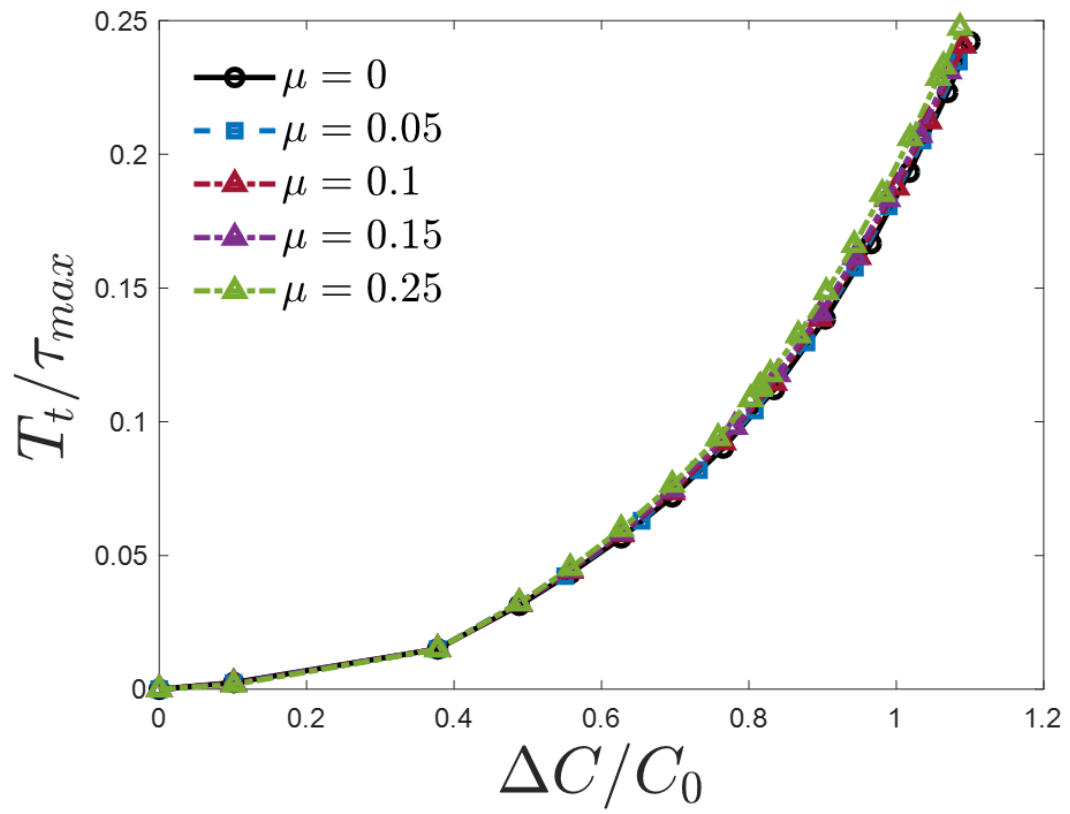


Figure 5.G1. Tangential traction at the crack tip as a function of the applied circumferential strain. 5 friction coefficients are shown.

Bibliography

- Abraham, P. A. et al. (1982) 'Marfan syndrome. Demonstration of abnormal elastin in aorta', *Journal of Clinical Investigation*. American Society for Clinical Investigation, 70(6), pp. 1245–1252. doi: 10.1172/JCI110723.
- Anderson, T. L. (2005) *Fracture Mechanics*. CRC Press. doi: 10.1201/9781420058215.
- Aun, R. (2013) 'Acute aortic dissection', in *Endovascular and Hybrid Therapies for Structural Heart and Aortic Disease*. Elsevier, pp. 74–89. doi: 10.1002/9781118504536.ch8.
- van Baardwijk, C. and Roach, M. R. (1987) 'Factors in the propagation of aortic dissections in canine thoracic aortas', *Journal of Biomechanics*. Elsevier, 20(1), pp. 67–73. doi: 10.1016/0021-9290(87)90268-5.
- Brandt, T. et al. (2001) 'Pathogenesis of cervical artery dissections: Association with connective tissue abnormalities', *Neurology*. Wolters Kluwer Health, Inc. on behalf of the American Academy of Neurology, 57(1), pp. 24–30. doi: 10.1212/WNL.57.1.24.
- Chikwe, J. et al. (2013) 'National outcomes in acute aortic dissection: Influence of surgeon and institutional volume on operative mortality', *Annals of Thoracic Surgery*. Elsevier, 95(5), pp. 1563–1569. doi: 10.1016/j.athoracsur.2013.02.039.
- Clough, R. E. and Nienaber, C. A. (2015) 'Management of acute aortic syndrome.', *Nature reviews. Cardiology*. Nature Publishing Group, a division of Macmillan Publishers Limited. All Rights Reserved., 12(2), pp. 103–14. doi: 10.1038/nrcardio.2014.203.
- Colli, A. et al. (2018) 'Acute DeBakey Type I aortic dissection without intimal tear in the arch: is total arch replacement the right choice?', *Interactive cardiovascular and thoracic surgery*, 26(1), pp. 84–90. doi: 10.1093/icvts/ivx229.
- Criado, F. J. (2011) 'Aortic dissection: a 250-year perspective.', *Texas Heart Institute journal / from the Texas Heart Institute of St. Luke's Episcopal Hospital, Texas Children's Hospital*, 38(6), pp. 694–700. Available at: <http://www.pubmedcentral.nih.gov/articlerender.fcgi?artid=3233335&tool=pmcentrez&rendertype=abstract> (Accessed: 5 January 2016).
- Dake, M. D. et al. (2013) 'DISSECT: a new mnemonic-based approach to the categorization of aortic dissection.', *European journal of vascular and endovascular surgery : the official journal of the European Society for Vascular Surgery*, 46(2), pp. 175–90. doi: 10.1016/j.ejvs.2013.04.029.
- Eshthardi, P. et al. (2010) 'Iatrogenic left main coronary artery dissection: Incidence, classification, management, and long-term follow-up', *American Heart Journal*, 159(6), pp. 1147–1153. doi: 10.1016/j.ahj.2010.03.012.
- Evangelista, A. et al. (2018) 'Insights from the international registry of acute aortic dissection: A 20-year experience of collaborative clinical research', *Circulation*. Lippincott Williams & Wilkins Hagerstown, MD, pp. 1846–1860. doi: 10.1161/CIRCULATIONAHA.117.031264.

- Fattori, R. et al. (2013) 'Interdisciplinary expert consensus document on management of type B aortic dissection.', *Journal of the American College of Cardiology*. *Journal of the American College of Cardiology*, 61(16), pp. 1661–78. doi: 10.1016/j.jacc.2012.11.072.
- Ferrara, A. and Pandolfi, A. (2010) 'A numerical study of arterial media dissection processes', in *International Journal of Fracture*. Springer Netherlands, pp. 21–33. doi: 10.1007/s10704-010-9480-y.
- Gasser, T. C. and Holzapfel, G. A. (2006) 'Modeling the propagation of arterial dissection', *European Journal of Mechanics - A/Solids*, 25(4), pp. 617–633. doi: 10.1016/j.euromechsol.2006.05.004.
- Gasser, T. C., Ogden, R. W. and Holzapfel, G. A. (2006) 'Hyperelastic modelling of arterial layers with distributed collagen fibre orientations.', *Journal of the Royal Society, Interface / the Royal Society*. The Royal Society, 3(6), pp. 15–35. doi: 10.1098/rsif.2005.0073.
- Hagan, P. G. et al. (2000) 'The International Registry of Acute Aortic Dissection (IRAD)', *The Journal of American Medical Association*. American Medical Association, 283(7), pp. 897–903. doi: 10.1001/jama.283.7.897.
- Haslach, H. W. et al. (2018) 'Fracture mechanics of shear crack propagation and dissection in the healthy bovine descending aortic media', *Acta Biomaterialia*. Elsevier, 68, pp. 53–66. doi: 10.1016/j.actbio.2017.12.027.
- Hirst, A. E., Johns, V. J. and Kime, S. W. (1958) 'Dissecting aneurysm of the aorta: A review of 505 cases', *Medicine (United States)*, pp. 217–279. doi: 10.1097/00005792-195809000-00003.
- Karthikesalingam, A. et al. (2010) 'The diagnosis and management of aortic dissection.', *Vascular and endovascular surgery*, 44(3), pp. 165–9. doi: 10.1177/1538574410362118.
- Larson, E. W. and Edwards, W. D. (1984) 'Risk factors for aortic dissection: A necropsy study of 161 cases', *The American Journal of Cardiology*, 53(6), pp. 849–855. doi: 10.1016/0002-9149(84)90418-1.
- Lemaire, S. A. and Russell, L. (2011) 'Epidemiology of thoracic aortic dissection', *Nature Reviews Cardiology*, pp. 103–113. doi: 10.1038/nrcardio.2010.187.
- Lui, R. C., Menkis, A. H. and McKenzie, F. N. (1992) 'Aortic dissection without intimal rupture: Diagnosis and management', *The Annals of Thoracic Surgery*, 53(5), pp. 886–888. doi: 10.1016/0003-4975(92)91460-Q.
- McGarry, J. P. et al. (2014) 'Potential-based and non-potential-based cohesive zone formulations under mixed-mode separation and over-closure. Part I: Theoretical analysis', *Journal of the Mechanics and Physics of Solids*, 63(1), pp. 336–362. doi: 10.1016/j.jmps.2013.08.020.
- McGarry, J. P. and McHugh, P. E. (2008) 'Modelling of in vitro chondrocyte detachment', *Journal of the Mechanics and Physics of Solids*. Pergamon, 56(4), pp. 1554–1565. doi: 10.1016/j.jmps.2007.08.001.

- Miller, D. C. et al. (1984) 'Independent determinants of operative mortality for patients with aortic dissections.', *Circulation*, 70(3 Pt 2), pp. 1153-64. Available at: <http://europepmc.org/abstract/med/6235061> (Accessed: 4 January 2016).
- Nakashima, Y., Shiokawa, Y. and Sueishi, K. (1990) 'Alterations of elastic architecture in human aortic dissecting aneurysm.', *Laboratory investigation; a journal of technical methods and pathology*, 62(6), pp. 751-60. Available at: <http://www.ncbi.nlm.nih.gov/pubmed/2359259> (Accessed: 2 February 2018).
- Noble, C. et al. (2016) 'Controlled peel testing of a model tissue for diseased aorta', *Journal of Biomechanics*, 49(15), pp. 3667-3675. doi: 10.1016/j.jbiomech.2016.09.040.
- Noble, C. et al. (2017) 'Simulation of arterial dissection by a penetrating external body using cohesive zone modelling', *Journal of the Mechanical Behavior of Biomedical Materials*, 71(Submitted), pp. 95-105. doi: 10.1016/j.jmbbm.2017.03.004.
- Nolan, D. R. et al. (2014) 'A robust anisotropic hyperelastic formulation for the modelling of soft tissue', *Journal of the Mechanical Behavior of Biomedical Materials*, 39, pp. 48-60. doi: 10.1016/j.jmbbm.2014.06.016.
- Nolan, D. R. and McGarry, J. P. (2016a) 'On the Compressibility of Arterial Tissue', *Annals of Biomedical Engineering*. Springer US, 44(4), pp. 993-1007. doi: 10.1007/s10439-015-1417-1.
- Nolan, D. R. and McGarry, J. P. (2016b) 'On the correct interpretation of measured force and calculation of material stress in biaxial tests', *Journal of the Mechanical Behavior of Biomedical Materials*. Elsevier, 53, pp. 187-199. doi: 10.1016/j.jmbbm.2015.08.019.
- Parry, G. and McGarry, P. (2012) 'An analytical solution for the stress state at stent-coating interfaces', *Journal of the Mechanical Behavior of Biomedical Materials*, 10, pp. 183-196. doi: 10.1016/j.jmbbm.2012.02.009.
- Sariola, H., Viljanen, T. and Luosto, R. (1986) 'Histological pattern and changes in extracellular matrix in aortic dissections', *Journal of Clinical Pathology*. BMJ Publishing Group, 39(10), pp. 1074-1081. doi: 10.1136/jcp.39.10.1074.
- Sommer, G. et al. (2008) 'Dissection properties of the human aortic media: an experimental study.', *Journal of biomechanical engineering*. American Society of Mechanical Engineers, 130(2), p. 021007. doi: 10.1115/1.2898733.
- Sommer, G. et al. (2016) 'Mechanical strength of aneurysmatic and dissected human thoracic aortas at different shear loading modes', *Journal of Biomechanics*, pp. 2374-2382. doi: 10.1016/j.jbiomech.2016.02.042.
- Tong, J. et al. (2011a) 'Dissection properties and mechanical strength of tissue components in human carotid bifurcations', *Annals of Biomedical Engineering*. Springer US, 39(6), pp. 1703-1719. doi: 10.1007/s10439-011-0264-y.
- Tong, J. et al. (2011b) 'Dissection Properties and Mechanical Strength of Tissue Components in Human Carotid Bifurcations', *Annals of Biomedical Engineering*, 39(6), pp. 1703-1719. doi: 10.1007/s10439-011-0264-y.

Trimarchi, S. et al. (2007) 'Acute abdominal aortic dissection: Insight from the International Registry of Acute Aortic Dissection (IRAD)', *Journal of Vascular Surgery*. Mosby, 46(5), pp. 913-919.e1. doi: 10.1016/J.JVS.2007.07.030.

Tsamis, A., Krawiec, J. T. and Vorp, D. A. (2013) 'Elastin and collagen fibre microstructure of the human aorta in ageing and disease: a review.', *Journal of the Royal Society, Interface / the Royal Society*, 10(83), p. 20121004. doi: 10.1098/rsif.2012.1004.

Ulbricht, D. et al. (2004) 'Cervical artery dissection: An atypical presentation with Ehlers-Danlos-like collagen pathology?', *Neurology*. Wolters Kluwer Health, Inc. on behalf of the American Academy of Neurology, 63(9), pp. 1708–1710. doi: 10.1212/01.WNL.0000142970.09454.30.

Wilson, S. K. and Hutchins, G. M. (1982) 'Aortic dissecting aneurysms. Causative factors in 204 subjects', *Archives of Pathology and Laboratory Medicine*, 106(4), pp. 175–180. Available at: <http://www.ncbi.nlm.nih.gov/pubmed/6895989> (Accessed: 18 January 2020).

Witzenburg, C. M. et al. (2017) 'Failure of the porcine ascending aorta: Multidirectional experiments and a unifying microstructural model', *Journal of Biomechanical Engineering*. American Society of Mechanical Engineers Digital Collection, 139(3). doi: 10.1115/1.4035264.

Yuan, S.-M. and Jing, H. (2011) 'Cystic medial necrosis: pathological findings and clinical implications', *Revista Brasileira de Cirurgia Cardiovascular*. *Revista Brasileira de Cirurgia Cardiovascular*, 26(1), pp. 107–115. doi: 10.1590/S0102-76382011000100019.

Chapter 6

6 VISCOPLASTIC COHESIVE ZONE MODELLING OF INTERFACIAL FIBRILLATION IN SOFT TISSUE

6.1 Introduction

6.1.1 General Background

Cohesive zone models are commonly used to model the delamination of an interface (Xu *et al.*, 1993; Camanho and Davila, 2002; Máirtín *et al.*, 2014; Dimitri *et al.*, 2015; Gallagher, Lamorinière and McGarry, 2018). CZMs can be formulated as continuous functions (Park, Paulino and Roesler, 2009; McGarry *et al.*, 2014; Dimitri *et al.*, 2015), or they may be expressed as piecewise functions (Camanho, Dávila and De Moura, 2003; Hanson, Bittencourt and Ingraffea, 2004). Interfacial fibrillation is a mechanism whereby delamination takes place by initiation, growth, extension, and ultimately fracture of fibrils between fracture surfaces (van den Bosch, Schreurs and Geers, 2007). Previously, standard cohesive zone models (CZMs) have been applied to model interfacial fibrillation in a variety of engineered materials including polymers, elastomers, paper, and plastics (Vossen *et al.*, 2014, 2016; Paggi and Reinoso, 2015). Van den Bosch *et al.*, adapting earlier work, proposed the use of a single relation between the opening displacement and the traction to account for large displacement problems, such as fibrillation (van den Bosch, Schreurs and Geers, 2006, 2007). This model was implemented by Vossen *et al.* as part of a multiscale modelling approach to describe the fibrillation micromechanics in a delaminating copper-rubber interface (Vossen *et al.*, 2014). In this approach idealised hyperelastic fibrils are explicitly

modelled as part of the multiscale modelling approach. The intrinsic adhesion between the fibrils and the copper is described by the previously developed standard cohesive zone model (van den Bosch, Schreurs and Geers, 2007). Another study examining fibrillar metal-elastomer interfaces explored the role of discrete fibrils within the fracture process zone (Vossen *et al.*, 2016). Several discrete hyperelastic elastomer fibrils were explicitly modelled without the use of a cohesive zone model. An anisotropic CZM for modelling fibrillar and crazing interfaces was proposed by Paggi & Reinoso (Paggi and Reinoso, 2015). The CZM was developed to describe the fracture of interfaces with a microstructure made of fibrils with statistically distributed in-plane and out-of-plane peeling orientations. The underlying CZM is based on the adhesion theory of an elastic tape (Kendall, 1975). In addition to fibrillation in engineered polymers, elastomers and composites, interfacial fibrillation has also been reported during fracture of biological materials such as hair (Kamath and Weigmann, 1982), skin (Arumugam, Naresh and Sanjeevi, 1994) and other collagenous tissues such as arterial tissue (Arumugam *et al.*, 1992; FitzGibbon and McGarry 2020). Cohesive zone modelling has been used previously to model fracture in biological tissues such as arteries (Gasser and Holzapfel, 2006; Noble *et al.*, 2017; Wang *et al.*, 2018), and cells (McGarry and McHugh, 2008), but toughening mechanism due to fibrillation have not been previously considered.

6.1.2 Examination of fibrillation during mode II delamination of arteries uncovered in recent experimental study (McGarry and FitzGibbon (2020))

The series of mode II fracture tests on arterial tissue presented in Chapter 5 (FitzGibbon and McGarry, 2020) demonstrates the rate of crack propagation is non uniform and that significant fibrillation occurs, both during initiation and propagation (see Figure 6.1). While a detailed description of the novel mode II soft tissue fracture methodology is beyond the scope of the current paper, the key evidence of fibrillation

and nonuniform crack propagation rate is outlined in Figure 6.1. A schematic of the experiment is shown in Figure 6.1(a). Briefly, an excised ring of aorta is placed on two circular loading bars. A radial notch is inserted to the side of the loading bars where high shear stress occurs. Displacement of loading bars (characterised by an effective circumferential strain $\Delta C/C_0$) to a critical level results in kinking of the crack with mode II initiation and propagation in the circumferential direction along a circumferential-axial plane. A J-integral analysis demonstrates that crack-kinking and mode II fracture occurs because collagen fibre alignment in front of the crack tip provides a significant toughening mechanism against mode I crack growth in the radial direction, through the thickness of the sample. Measured mode II crack propagation rates are shown as a function of the applied circumferential strain in Figure 6.1(b). Three characteristic regimes are observed; (i) initial slow crack growth with fibrillation (blue); (ii) fast crack growth over a long distance (red) without significant fibrillation; (iii) slow crack growth with significant fibrillation (green). Significant fibre formation is observed during the test (Figure 6.1(c)) and observed in the region of the crack tip following specimen removal from the test rig (Figure 6.1(c)). Fibrils are not simply elastically stretched between opposing crack surfaces; rather, they appeared to have undergone partial pull-out, such that removal of elastic strain energy does not result in significant fibril shortening and closure of crack surfaces. Finally, a standard cohesive zone model (CZM) that implements critical traction damage initiation, and exponential softening/damage evolution was used to simulate these mode II fracture tests (Figure 6.1(d-e)). The mode II fracture strength (τ_{max}) primarily governs crack initiation, whereas the mode II fracture energy (G_{II}) primarily governs the crack propagation rate. However, the use of a standard CZM is shown to compute an approximately uniform crack growth rate, providing only approximate predictions

of experimental measurements without capturing the three regimes of crack growth rate described above ($G_{II}=0.05$ N/mm captures only the slow growth rate at the start of the experiment, whereas $G_{II}=0.0005$ N/mm captures the fast crack growth rate in regime (ii), but not the slow crack growth in regimes (i) and (iii) (Figure 6.1(f)).

6.1.3 Structure and aims of the study

In the current study we aim to develop new CZM approaches to explore the relationship between fibrillation and the experimentally observed non-uniform crack propagation rates in arteries. In Section 6.2 we propose a new elastic fibrillation cohesive zone model (EF-CZM). Following initial damage evolution, this formulation incorporates elastic stretching and fracture of fibrils. This approach results in improved predictions compared to a standard exponential damage CZM, but it does not accurately capture experimentally measured non-uniform propagation rates in arteries. Furthermore, analysis of our experimental fracture surfaces suggests that fibrils undergo pull-out, in addition to elastic stretching, during propagation. Based on this observation we propose a novel visco-plastic CZM (VP-CZM) formulation to represent rate dependent fibril pull-out and associated dissipation during crack propagation. We demonstrate that the VP-CZM provides an improved prediction of non-uniform crack propagation during mode II dissection of arterial tissue.

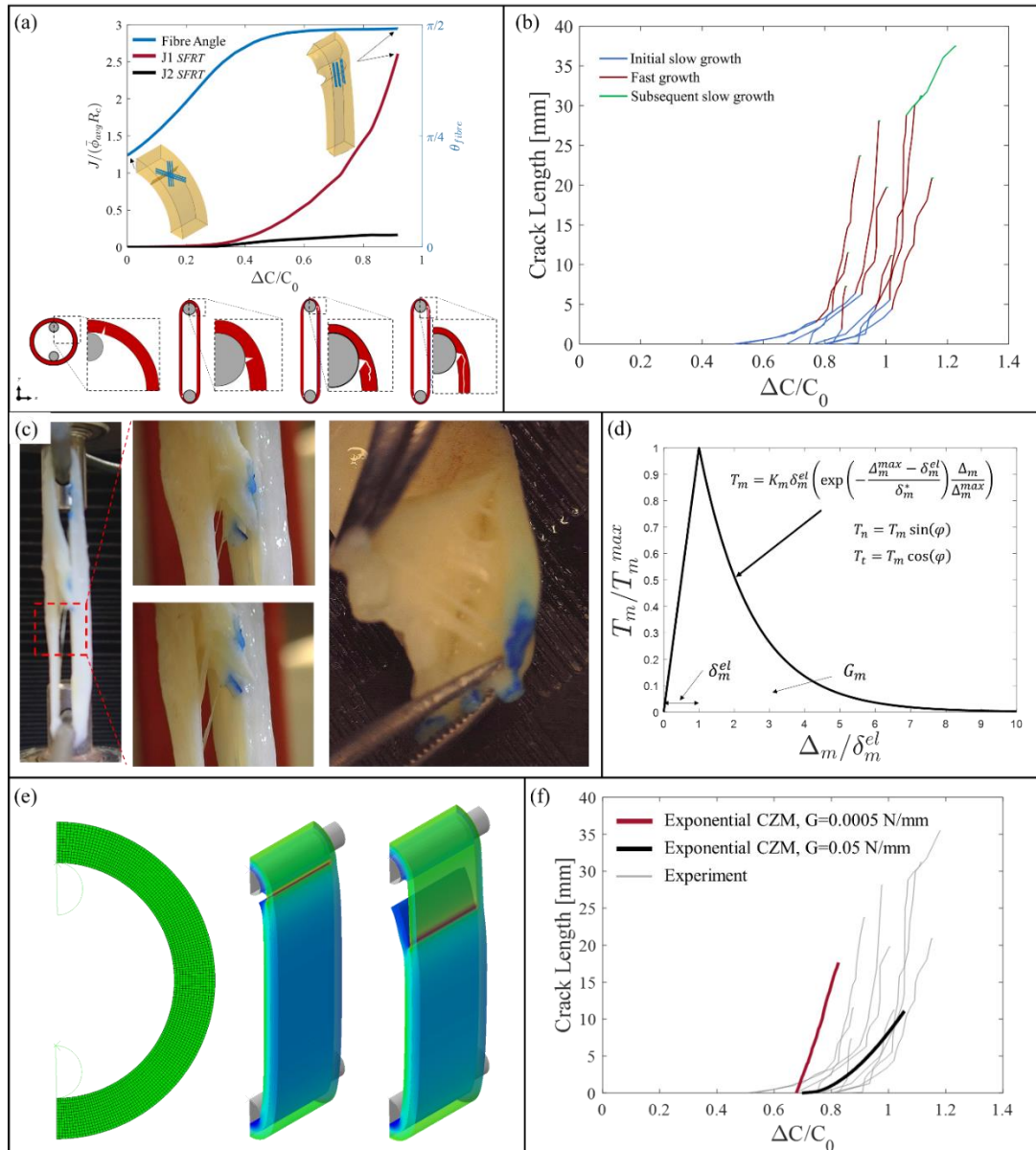


Figure 6.1. (a) J-Integral analysis of the novel mode II fracture experiment illustrating significant mode I toughening and fibre alignment behind the crack tip. (b) Measured crack length is shown as a function of the applied circumferential strain. Three characteristic regimes observed and are approximately indicated on the curves; (blue) initial crack growth is slow due to fibrillation; (red) crack growth velocity increases due to the rupture of fibres concentrating stresses at the crack tip; (green) crack growth slows due to fibrillation. (c) Experimental image showing fibrillation occurring, a large fibril is highlighted (red box). Images show detailed views of interfacial fibrillation. Experimental image of the ruptured aorta specimen showing significant permanent pull-out of fibrils; (d) Traction-separation response of the exponential CZM used previously; (e) image of the model in its undeformed configuration and two example contour plots showing crack propagation; (f) Crack growth predictions of the exponential CZM for two different mode II fracture energy (G_{II})

6.2 Elastic fibrillation cohesive zone model (EF-CZM)

In an effort to phenomenologically capture the fibril stretching between opposing crack flanks, we propose a new elastic fibrillation CZM (EF-CZM). As illustrated in Figure 6.2, this framework entails an initial intrinsic elastic region (shown in blue), followed by a standard exponential softening/damage region (yellow). Fibril formation is assumed to occur as part of the damage process, with fibrillation initiating when traction softens to a critical value ($T^{f_{init}}$). Fibrils are assumed to extend elastically (green) until they reach an ultimate fibril stress ($T^{f_{ult}}$), beyond which, fibril damage and softening initiates, ultimately leading to complete fibril rupture (red). Critical tractions associated with fibrillation initiation and ultimate rupture can be specified as a function of the mode mixity. As an example, Figure 6.2(b) illustrates a case of mode dependent fibrillation whereby fibrils extend to a higher traction under mode II loading than under Mode I loading. A full calibration of the model requires the specification of the following parameters for both mode I and mode II: interface strength (T_m^{max}), interface stiffness (K_m), fibril stiffness (K_f), fibril strength ($T_m^{f_{ult}}$), interface fracture energy prior to fibrillation (\hat{G}_m), and fibrillation fracture energy (G_m^d). The model also requires the specification of the mode dependence of the aforementioned parameters. In Section 6.1 we present full details of the EF-CZM formulation. In Section 6.2 we present rigorous parametric investigation of the model behaviour under mixed mode conditions. In Section 6.3 we explore the capability of the EF-CZM to predict the non-uniform crack propagation rates observed experimentally in our artery fracture experiments.

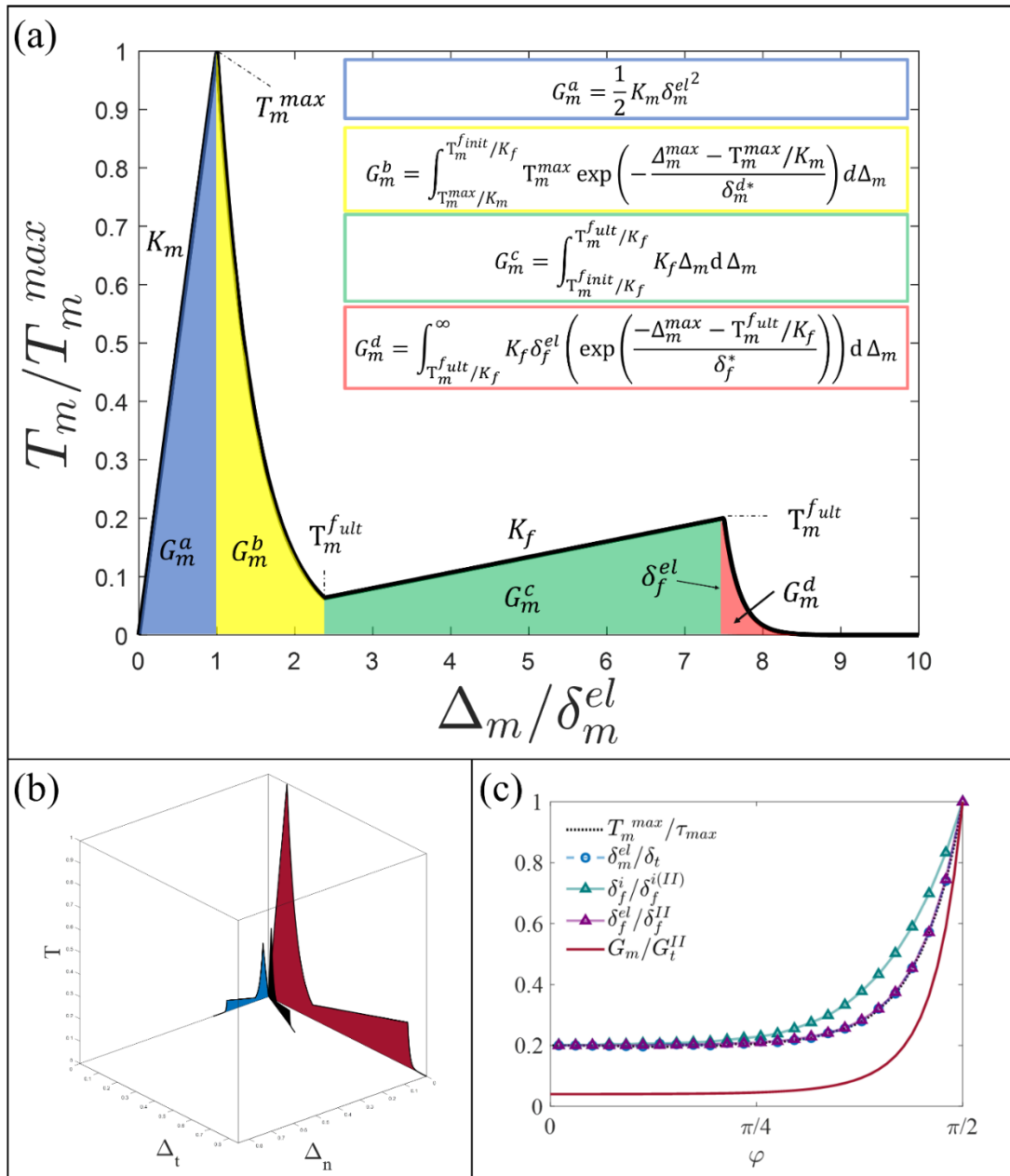


Figure 6.2. (a) Schematic of the EF-CZM undergoing a separation. K_f is the fibrillation stiffness, T_{m_f} is the fibrillation strength, and δ_f^{el} is the elastic limit of separation of the fibrillation regime. (b) 3D traction-separation schematic of the EF-CZM showing a mode II response (red), mixed mode response (black), and a mode I response (blue). (c) CZM parameters are shown as a function of mode angle. Interface strength, elastic limit, separation at fibrillation initiation, maximum fibril extension, and fracture energy are all shown.

6.2.1 EF-CZM formulation

For a given interface displacement vector $\mathbf{\Delta}$ with normal and tangential (shear) components Δ_n and Δ_t , respectively, the corresponding displacement magnitude is

given as $\Delta_m = (\Delta_n^2 + \Delta_t^2)^{1/2}$ and the mode angle is given as $\varphi = \tan^{-1}(\Delta_t/\Delta_n)$. The magnitude of the interface traction is expressed as a function of Δ_m and φ by the following formulation:

$$T_m(\Delta_m, \varphi) = \begin{cases} T_m^{max}(\varphi) \left(\exp\left(-\frac{K_m \Delta_m}{\delta_m^{d*}(\varphi)} \frac{\Delta_m}{\Delta_m^{max}}\right) \right) & , \Delta_m < T_m^{max}(\varphi)/K_m \\ & , T_m^{f_{init}}(\varphi)/K_f > \Delta_m \geq T_m^{max}(\varphi)/K_m \\ T_m^{f_{ult}}(\varphi) \left(\exp\left(-\frac{\Delta_m^{max} - T_m^{f_{ult}}(\varphi)/K_m}{\delta_m^{f*}(\varphi)} \frac{\Delta_m}{\Delta_m^{max}}\right) \right) & , K_f \Delta_m, T_m^{f_{init}}(\varphi)/K_f < \Delta_m \leq T_m^{f_{ult}}(\varphi)/K_f \delta_f^{el} \\ & , T_m^{f_{ult}}(\varphi)/K_f \leq \Delta_m \end{cases} \quad (6.1)$$

K_m is the intrinsic stiffness of an intact interface. In the current study we assume that K_m is mode-independent. $T_m^{max}(\varphi)$ is the specified mode-dependent interface strength; the corresponding displacement ($\delta_m^{el}(\varphi) = T_m^{max}(\varphi)/K_m$) represents the elastic limit of interface separation at the point of damage initiation. The mode-dependent parameter $\delta_m^{d*}(\varphi)$ governs the rate of softening in the initial $G_m^b(\varphi)$ damage region (yellow). Note that damage depends on the maximum separation throughout the displacement history, Δ_m^{max} , such that a reduction in interface separation during the damage region will directly result in elastic unloading. $T_m^{f_{init}}(\varphi)$ is the specified mode-dependent traction at which fibrillation initiates following initial damage and softening. K_f is the stiffness of a fibril, which is assumed to be mode-independent in the current implementation. $T_m^{f_{ult}}(\varphi)$ is the mode-dependent ultimate strength of a fibril, at which fibril damage initiates. By extension, the elastic limit of fibril extension is also mode-dependent ($\delta_m^{f_{ult}}(\varphi) = T_m^{f_{ult}}(\varphi)/K_f$). Finally, the mode-dependent parameter $\delta_m^{f*}(\varphi)$ governs the rate of softening in the G_m^d fibril damage/rupture region (red). The interface strength is defined as a function of the mode as follows:

$$\Gamma_m^{max}(\varphi) = \tau_{max} - \left(\frac{\tau_{max} - \sigma_{max}}{1 - \exp\left(-\frac{\pi}{2\Omega^T}\right)} \right) \left(1 - \exp\left(-\frac{\varphi}{\Omega^T}\right) \right) \quad (6.2)$$

where τ_{max} is the mode II interface strength, Ω^T sets the non-linearity of the transition from mode II to mode I, and σ_{max} is the mode I interface strength. The mode mixity of the initial interface damage parameter $\delta_m^*(\varphi)$ is obtained from

$$\delta_m^*(\varphi) = \frac{\hat{G}_m(\varphi)}{\Gamma_m^{max}(\varphi)} - \frac{\Gamma_m^{max}(\varphi)}{2K_m} \quad (6.3)$$

where $\hat{G}_m(\varphi) = G_m^a(\varphi) + G_m^b(\varphi)$ is the mode-dependent fracture energy prior to fibrillation, given as:

$$\hat{G}_m(\varphi) = \frac{1}{2} K_m \delta_m^{el}(\varphi)^2 + \int_{\Gamma_m^{max}(\varphi)/K_m}^{\Gamma_m^{finit}(\varphi)/K_f} \Gamma_m^{max}(\varphi) \exp\left(-\frac{\Delta_m^{max} - \delta_m^{el}}{\delta_m^{d*}}\right) d\Delta_m \quad (6.4)$$

We may specify the mode-dependence of $\hat{G}_m(\varphi)$ using the following function:

$$\hat{G}_m(\varphi) = G_t^0 - \left(\frac{G_t^0 - G_n^0}{1 - \exp\left(-\frac{\pi}{2\Omega^G}\right)} \right) \left(1 - \exp\left(-\frac{\varphi}{\Omega^G}\right) \right) \quad (6.5)$$

where G_t^0 is the mode II fracture energy prior to fibril formation and G_n^0 is the mode I fracture energy prior to fibril formation, and the parameter Ω^G sets the non-linearity of the transition from mode II to mode I. We specify the mode-dependence of $T_m^{fult}(\varphi)$ using the following function:

$$T_m^{fult}(\varphi) = \tau^{fult} - \left(\frac{\tau^{fult} - \sigma^{fult}}{1 - \exp\left(-\frac{\pi}{2}\right)} \right) \left(1 - \exp\left(-\frac{\varphi}{\Omega^{Tf}}\right) \right) \quad (6.6)$$

where τ^{fult} is the mode II fibril strength, σ^{fult} is the mode I fibril strength, and the parameter Ω^{Tf} sets the non-linearity of the transition from mode II to mode I. We may consider the mode dependence of the fibril fracture energy $\hat{G}_m^f(\varphi)$ where we define the fracture energy as the stored elastic energy of the fibril and the fibril damage energy:

$$\begin{aligned} \hat{G}_m^f(\varphi) = & \int_{T_m^{finit}(\varphi)/K_f}^{T_m^{fult}(\varphi)/K_f} K_f \Delta_m d \Delta_m \\ & + \int_{T_m^{fult}(\varphi)/K_f}^{\infty} K_f \delta_f^{el} \left(\exp\left(\frac{-\Delta_m^{max} - T_m^{fult}(\varphi)/K_f}{\delta_f^*}\right) \right) d \Delta_m \end{aligned} \quad (6.7)$$

or we may consider the mode dependence of the fibril fracture energy including only the fibril damage energy

$$\hat{G}_m^f(\varphi) = \int_{T_m^{fult}(\varphi)/K_f}^{\infty} K_f \delta_f^{el} \left(\exp\left(\frac{-\Delta_m^{max} - T_m^{fult}(\varphi)/K_f}{\delta_f^*}\right) \right) d \Delta_m \quad (6.8)$$

We specify the mode dependence of the fibril fracture energy $\hat{G}_m^f(\varphi)$ using the following function:

$$\hat{G}_m^f(\varphi) = G_t^d - \left(\frac{G_t^d - G_n^d}{1 - \exp\left(-\frac{\pi}{2}\right)} \right) \left(1 - \exp\left(-\frac{\varphi}{\Omega^{Gf}}\right) \right) \quad (6.9)$$

where G_t^d is the mode II fibril fracture energy, G_n^d is the mode I fibril fracture energy, and the parameter Ω^{Gf} sets the non-linearity of the transition from mode II to mode I.

Finally, we complete the description of the cohesive zone formulation by decomposing T_m into the normal and tangential components, T_n and T_t , respectively, such that

$$T_n = \begin{cases} K_{noc} \Delta_n, \Delta_n < 0 \\ T_m \sin(\varphi), \Delta_n \geq 0 \end{cases} \quad (6.10)$$

$$T_t = T_m \cos(\varphi) \quad (6.11)$$

where K_{noc} is the overclosure penalty stiffness.

The EF-CZM is implemented in the finite element solver Abaqus through a *User Defined Interface Subroutine (UINTER)*. The consistent tangent matrix is derived analytically from (6.1).

6.2.2 EF-CZM parametric investigation of mixed mode behaviour

Proportional loading path response:

Figure 6.3 we explore the mixed mode coupling of the CZM under proportional loading paths. Figure 6.3(A) shows the traction-separation response of the EF-CZM for the case of $\sigma_{max} = \tau_{max}$ and $G_n^0 = G_t^0$, such that a mode-independent traction-separation relationship is obtained. Figure 6.3

Figure 6.3(B) shows the fracture energy as a function of φ . In addition to the total energy, the individual energy contribution of each region (previously outlined in Figure 6.2) are also shown. Monotonic increases/decreases as a function of mode angle are obtained for all energy contributions. In Figure 6.3(C-F) we consider cases in which the degree of fibrillation is mode dependant. Figure 6.3(C) we consider the case in which mode dependence is chosen so that self-similar scaling of the traction-separation relationship is obtained as a function of mode-angle (i.e. the shape of each curve is similar, with highest tractions and fibrillation for pure mode II separations). Such self-similar scaling is achieved by prescribing mode-dependence of fibril

damage energy through equation (6.8). Fibrillation occurs at all mode-angles, which higher fibril tractions and stretching with increasing φ . The resultant mode-dependence of total fracture energy, including normal and tangential contributions, is shown in Figure 6.3(D). For the case shown in Figure 6.3(E-F) a different form of fibrillation mode dependence is shown. In this case, the mode-dependence of the *total* fibril energy is specified through equation (6.7). In this case, significant fibrillation is obtained only for mode angles close to mode II. For lower values of φ , close to mode I, from the point of fibril initiation the fibrils immediately enter the damage regime, with the result that stretching of fibrils at a constant stiffness is not computed. Again, the resultant mode-dependence of total fracture energy, including normal and tangential contributions, is shown in Figure 6.3(F). The three cases presented in Figure 6.3 merely serve to demonstrate the flexibility of the EF-CZM to represent a range of possible mode-dependent fibrillation regimes, while providing physically appropriate mode dependent traction-separation relationships and fracture energies.

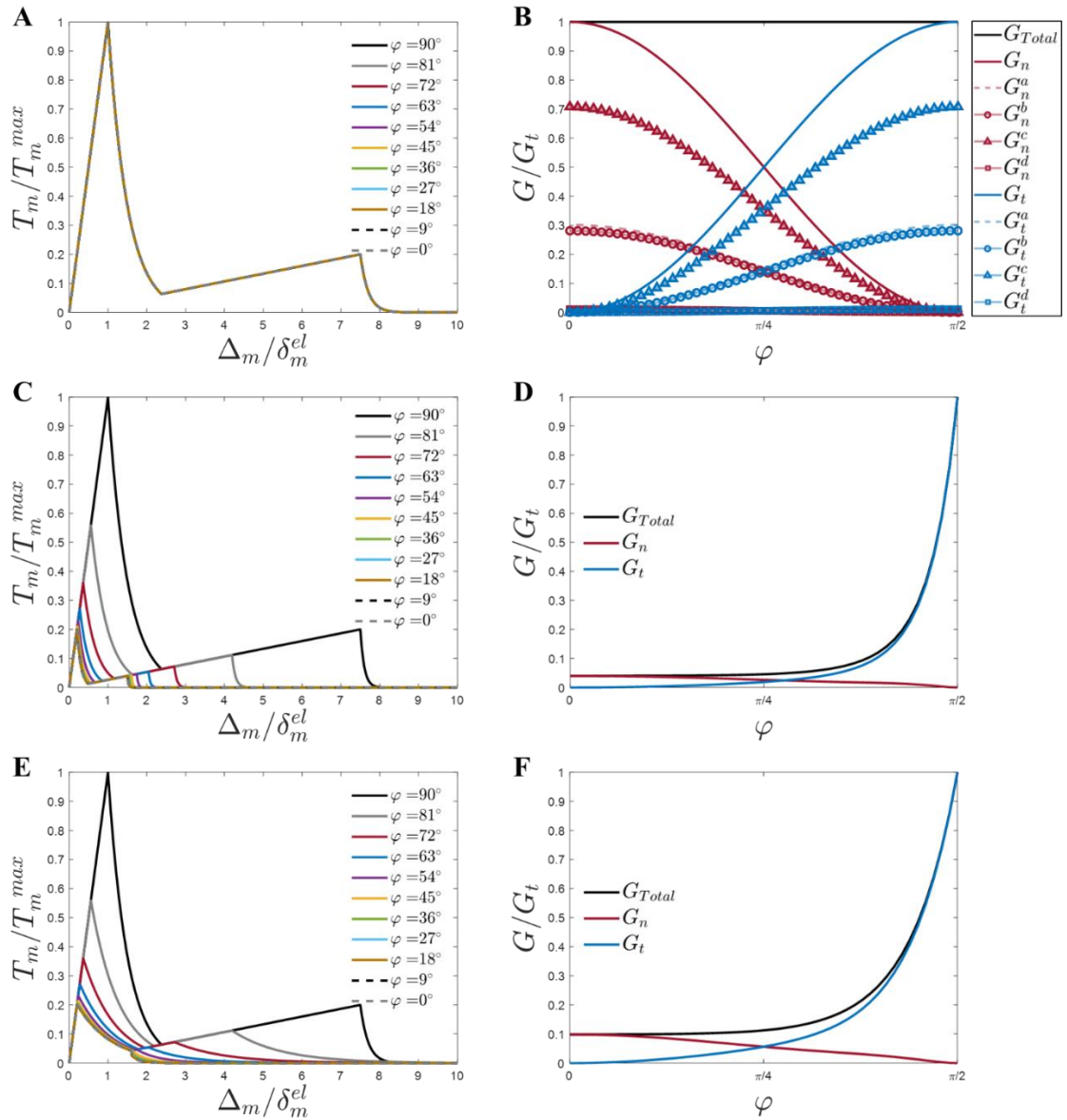


Figure 6.3. Response of EF-CZM to proportional loading paths with a constant mode angle φ . (A) Traction-separation relationship for the case of $\sigma_{max} = \tau_{max}$ and $G_n = G_t$. (B) Computed fracture energies corresponding to (A). Individual energy contributions of each region of the traction-separation curve (as illustrated in Figure 6.2) are also shown; (C) Traction-separation relationship for the case of $5\sigma_{max} = \tau_{max}$ and $G_n^0 = G_t^0 \left(\frac{\sigma_{max}}{\tau_{max}}\right)^2$ with mode dependence of fibril damage energy prescribed through equation (8); (D) Computed fracture energies corresponding to (C); (E) Traction-separation relationship for the case of $5\sigma_{max} = \tau_{max}$ and $G_n^0 = G_t^0 \left(\frac{\sigma_{max}}{\tau_{max}}\right)^2$ with mode dependence of fibril total energy prescribed through equation (7); (F) Computed fracture energies corresponding to (E).

Non-proportional loading path response: In this section the EF-CZM traction-separation response is examined in the case of a mode II separation to a specified finite value of Δ_t/δ_t , followed subsequently by complete normal separation, $\Delta_n = 0 \rightarrow \infty$. Computed traction-separation relationships for a range of such non-proportional mixed-mode paths are shown in Figure 6.4 for the following cases: (A-B) $\sigma_{max} = \tau_{max}, G_{n0} = G_{t0}$; (D-E) $5\sigma_{max} = \tau_{max}, G_{n0} = G_t^0 \left(\frac{\sigma_{max}}{\tau_{max}} \right)^2$. As shown in Figure 6.4(A), the occurrence of damage or fibrillation during the initial mode II separation depends on the prescribed value of Δ_t/δ_t . Traction-separation during the subsequent normal separation is shown in Figure 6.4(B). If a fibril is formed during initial mode II separation, elastic fibril stretching continues immediately during subsequent normal separation. On the other hand, if damage and fibril initiation does not occur during the initial mode II separation, then damage is computed during the initial phase of the subsequent normal separation, followed by fibril initiation and fibril stretching. The computed fracture energy as a function of the applied value of Δ_t^{max}/δ_t is shown in Figure 6.4(C). While the non-linear influence of fibril formation and fibril stretching is computed, the total energy is mode independent, as prescribed, and monotonic increases/decreases in the normal and tangential contributions are observed. Corresponding non-proportional loading path responses are shown in Figure 6.4(D-F) for the case of $5\sigma_{max} = \tau_{max}$ and $G_{n0} = G_t^0 \left(\frac{\sigma_{max}}{\tau_{max}} \right)^2$. Mode mixity of the total fracture energy is specified using equation (6.7). As shown in Figure 6.4(D,E), the occurrence of fibrillation during the initial mode II separation results in reduced elastic fibril deformation in the subsequent normal separation, with early onset of fibril damage and rupture. The total energy of separation is dominated by the mode II contribution during the initial phase of the loading path, as shown in Figure 6.4(F).

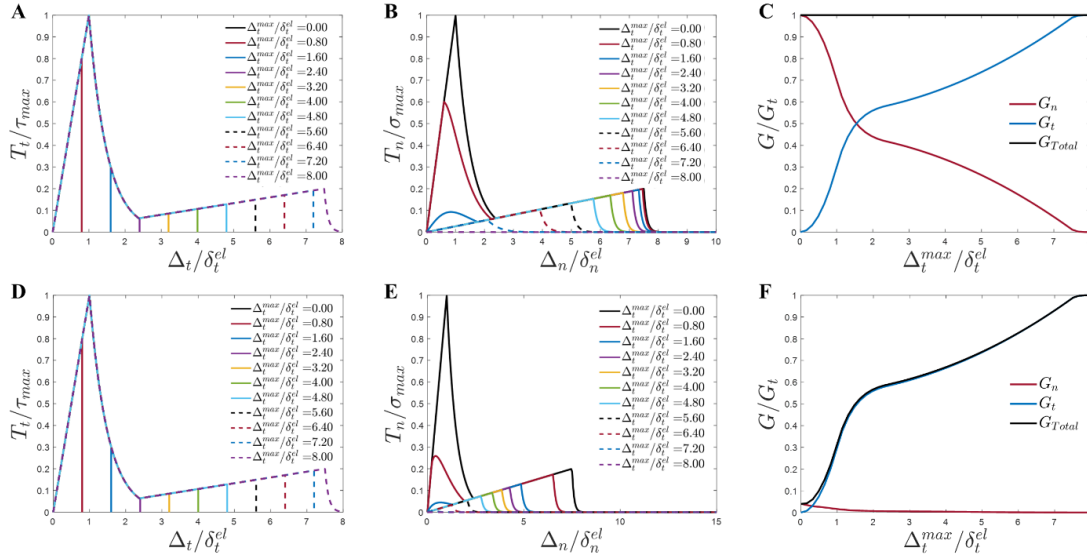


Figure 6.4: Traction-separation response of the EF-CZM to non-proportional loading paths in which an initial mode II separation up to a specified finite value of $\Delta_t^{max}/\delta_t^{el}$ is followed by a subsequent normal separation to ultimate rupture. (A-C) shows results for the case of $\sigma_{max} = \tau_{max}$ and $G_{n0} = G_{t0}$ in terms of, (A) tangential tractions, (B) normal tractions and (C) fracture energies. (D-F) shows results for the case of $5\sigma_{max} = \tau_{max}$ and $G_{n0} = G_t^0 \left(\frac{\sigma_{max}}{\tau_{max}}\right)^2$ in terms of, (D) tangential tractions, (E) normal tractions and (F) fracture energies.

Compliance of the EF-CZM with the requirement that instantaneous incremental dissipation is positive throughout a loading path is investigated in Figure 6.5. Instantaneous incremental dissipation is computed as $d\phi_i = 0.5(\underline{T}d\underline{\Delta} - \underline{\Delta}d\underline{T})$, in accordance with Cazes et al. (2009). Analyses are presented for all proportional and non-proportional loading paths considered in Figure 6.3 and Figure 6.4, respectively. For all parameter sets, analyses reveal that $d\phi_i \geq 0$ throughout all loading paths.

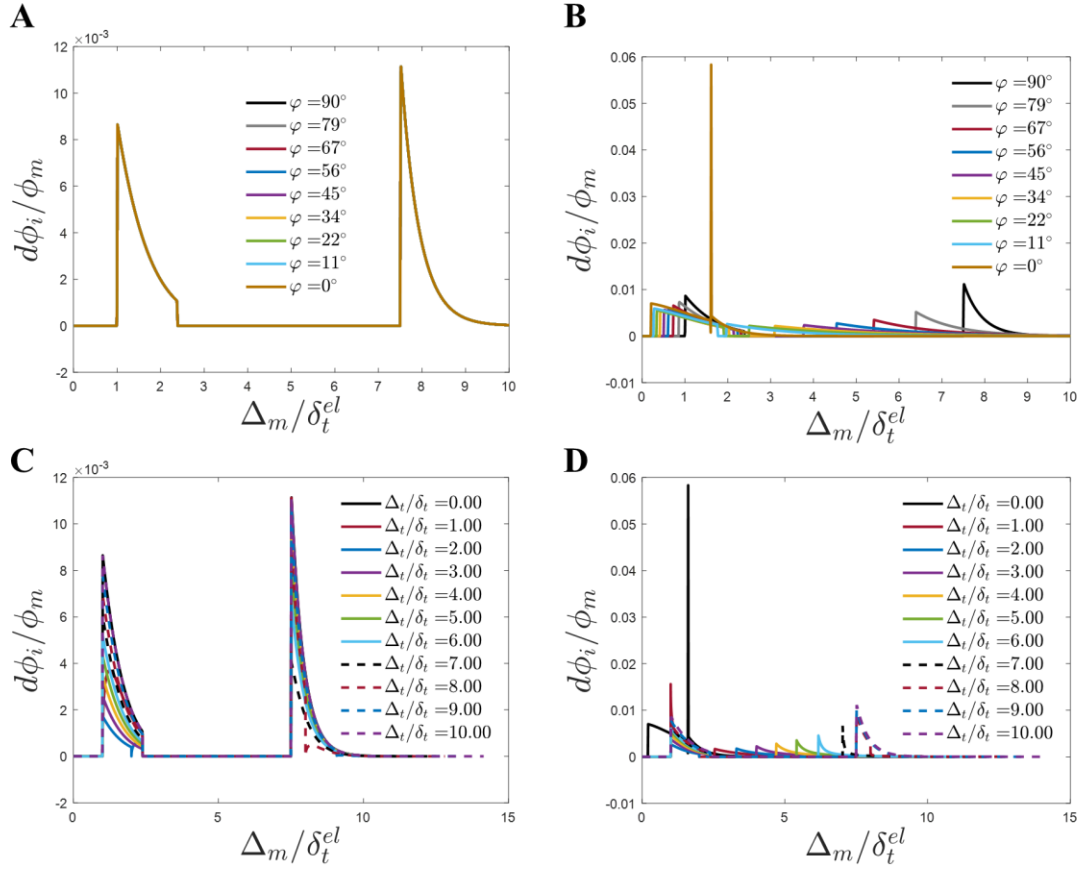


Figure 6.5. Instantaneous incremental dissipation ($d\phi_i = 0.5(Td\Delta - \Delta dT)$) during mixed mode loading paths. (A) Proportional loading paths for $\sigma_{max} = \tau_{max}$ and $G_{n0} = G_{t0}$; (B) Proportional loading paths for $5\sigma_{max} = \tau_{max}$ and $G_{n0} = G_t^0 \left(\frac{\sigma_{max}}{\tau_{max}}\right)^2$; (C) Non-proportional loading paths for $\sigma_{max} = \tau_{max}$ and $G_{n0} = G_{t0}$; (D) Non-proportional loading paths for $5\sigma_{max} = \tau_{max}$ and $G_{n0} = G_t^0 \left(\frac{\sigma_{max}}{\tau_{max}}\right)^2$.

Irreversible damage: The response of the EF-CZM to load-unload paths is explored in Figure 6.6. The response of the EF-CZM to mode I loading-unloading is shown in Figure 6.6(A). Two unloading paths are considered: one during the initial damage phase, and one during the final damage phase when the fibrils ultimate strength has been exceeded. In both cases the model imposes linear elastic unloading with the reduced modulus determined by the degree of damage. Negative values of Δ_n are prevented by an overclosure penalty. As shown in Figure 6.6(B), positive instantaneous incremental dissipation is computed throughout all loading-unloading

paths. The slightly more complex response of the model to mode II loading-unloading paths is shown in Figure 6.6(C). Tangential separation is increased such that the mode II strength is exceeded and initial damage occurs. The direction of interface separation is then reversed and elastic unloading occurs at a reduced damage modulus, passing through the undeformed position ($\Delta_t = 0$), and continuing to deform elastically ($\Delta_t < 0$) until the previously computed damage stress magnitude is again reached. At this point, damage and softening resumes until the point of fibril initiation. Elastic fibril stretching then occurs until the maximum value of tangential traction is reached and fibril damage initiates. The direction of separation is again reversed, and elastic fibril unloading-reloading occurs at a further reduced modulus, again until the reduced ultimate strength is reached and damage, and eventual fibril rupture, is computed. Positive instantaneous incremental dissipation is computed throughout this mode II loading-unloading path (Figure 6.6(D)).

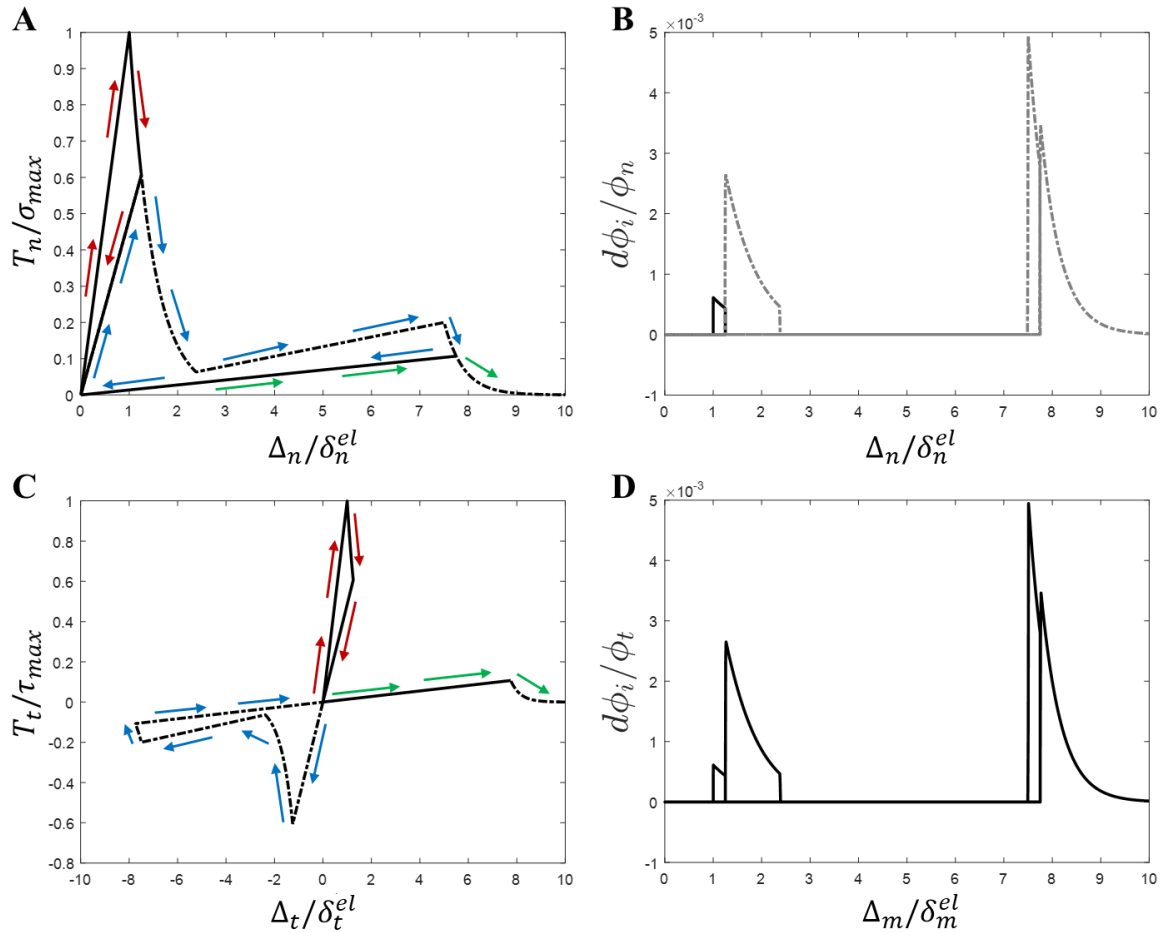


Figure 6.6. Exploration of loading-unloading paths in the normal direction (A) and tangential direction (C). Positive instantaneous incremental dissipation for the normal loading path (B) and for the tangential loading path (D).

6.2.3 Simulation of artery crack propagation experiment using EF-CZM

We next explore the ability of the EF-CZM to provide improved predictions (compared to a standard exponential damage CZM (recently implemented by FitzGibbon and McGarry (2020) and shown in Figure 6.1(D-F)). We focus specifically on the capability of the EF-CZM to predict the pattern of non-uniform crack propagation rate shown in Figure 6.1(F), i.e. initial slow crack propagation followed by fast crack propagation over a long distance, followed ultimately by slow crack propagation. A parametric investigation is performed to explore the influence of the fibril strength, the fibril fracture energy, and the maximum fibril extension on

computed crack propagation rates. In all simulations presented in Figure 6.7(A-C) it can be noted that the EF-CZM introduces a strong non-uniformity of crack propagation rate, with an initial slow crack rate followed by rapid crack growth, followed ultimately by slow crack growth. However, one significant limitation observed is that the formulation does not predict fast crack growth over a sufficiently long distance, and an alteration of model parameters does not facilitate an extension of this region. As shown in Figure 6.7(A), an increase in the ultimate fibrillation strength merely delays the initiation of the fast crack growth phase but does not extend it over a longer distance. Figure 6.7(B) shows that the predicted crack-propagation rates are not sensitive to the fibril fracture energy. Figure 6.7(C) shows that computed propagation rates are insensitive to the prescribed value of maximum fibril extension for values of $\delta_f^{el}/\delta_m^{el} \leq 75$. Increasing the value of maximum fibril extension merely delays the onset of fast crack growth and shortens the distance over which it occurs.

In summary, while the EF-CZM introduces highly non-uniform crack propagation, with slow crack growth predicted both before and after a phase of fast crack growth, the formulation is not capable of predicting a sufficiently long period of fast crack growth, compared to experimental observations. We suggest that this may be related to non-uniform fibrillation observed experimentally, with significantly lower fibrillation observed during fast crack growth. Therefore, in the following section we propose a visco-plastic cohesive zone formulation in which fibrillation is dependent on the rate of interface separation.

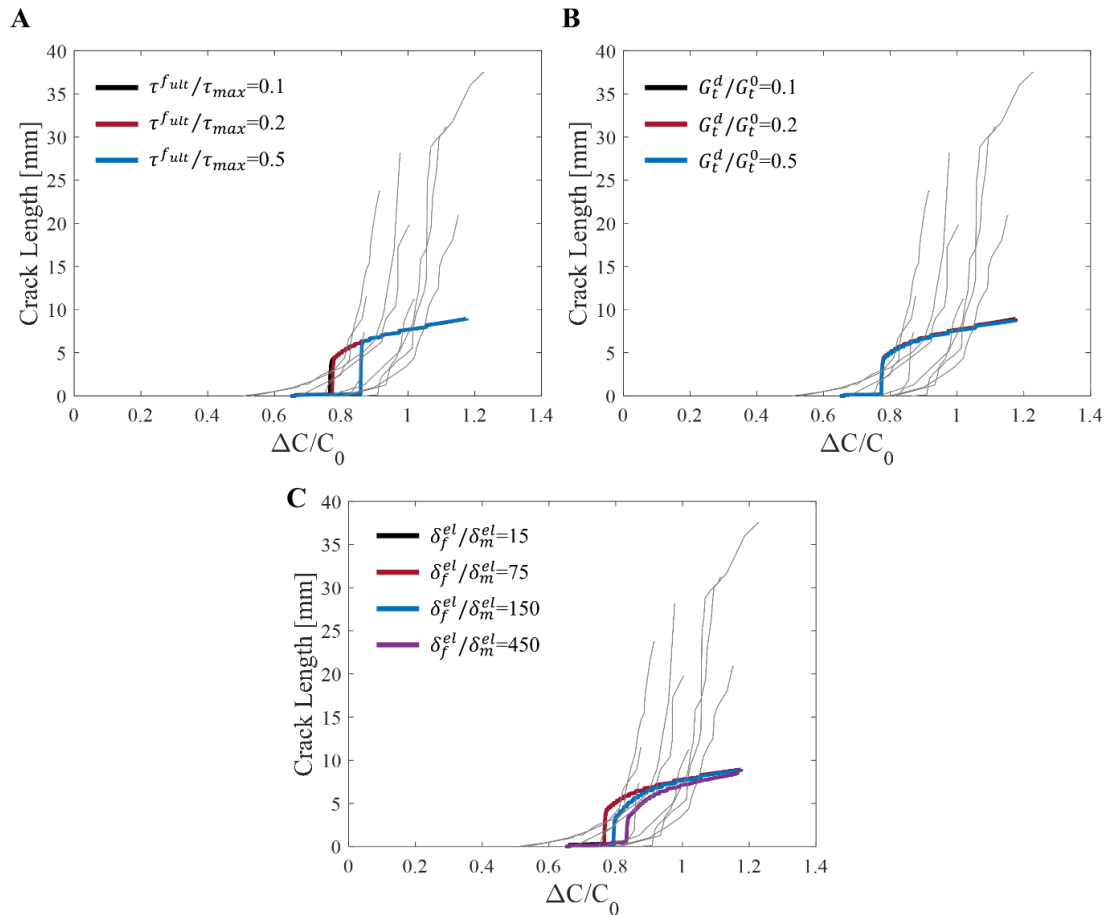


Figure 6.7. Elastic fibrillation EF-CZM predicted crack length vs strain curves. (A) Effect of ultimate fibril strength (τ^{fult}) on the predicted crack lengths. (B) Effect of fibril fracture energy (G_t^d) on predicted crack lengths. (C) Effect of maximum fibril extension (δ_f^{el}) on predicted crack lengths.

6.3 Visco-plastic cohesive zone model (VP-CZM)

As demonstrated in the previous section, the EF-CZM does not accurately capture the non-uniform crack propagation rates reported for mode II artery dissection in the experimental study presented in Chapter 5 (FitzGibbon and McGarry, 2020). Specifically, while the EF-CZM correctly predicts initial and ultimate slow crack growth, it does not predict fast crack growth over a sufficiently long distance. We next propose a visco-plastic mode for fibrillation during crack growth in arteries based on the following experimental observations from Chapter 5:

(i) fibrils do not merely deform elastically; unloading of the visible fibrils does not lead to fibril contraction and removal of the mode II separation between the fracture surfaces. Instead fibrils are observed to have undergone pull-out. Even fibrils near the crack-tip that have not ruptured and are attached to opposing fracture surfaces, are observed to have permanently “pulled-out” of the bulk material and do not exhibit any stored elastic strain energy (Figure 6.1(h)). We hypothesise that a plasticity mechanism should be used to capture the dissipative process of fibril pull-out and associated permanent fibril deformation.

(ii) Higher levels of fibrillation are observed during the initial and final phases of slow crack growth. This suggests a link between the rate of interface separation and fibrillation initiation. We hypothesise that a visco-plasticity mechanism can capture this phenomenon, whereby high rates of interface separation will delay the onset of plastic yielding (fibril pull-out) and result in higher fibril tractions so that the fibril ultimate strength is reached without significant plasticity (pull-out). Contrastingly, this hypothesis suggests that at slow interface separation rates fibrils will undergo early yield and significant plasticity (pull-out) before the ultimate fibril strength is reached. Essentially, a higher level of fibril plasticity (pull-out) is hypothesised to provide a significant dissipative mechanism, providing a link between non-uniform crack growth rates and non-uniform levels of fibrillation.

In Figure 6.8 we present a schematic of the proposed visco-plastic cohesive zone model (VP-CZM). A high interface separation-rate is shown in grey and a low interface separation-rate is shown in black. The initial regime of elastic deformation entails a linear increase in traction with increasing separation, characterised by the interface intrinsic elastic stiffness k_m . Plastic yielding and hardening are governed by

both the interface separation and separation-rate. When the ultimate stress (σ^{uts}) is reached an exponential damage phase initiates, resulting in ultimate interface rupture.

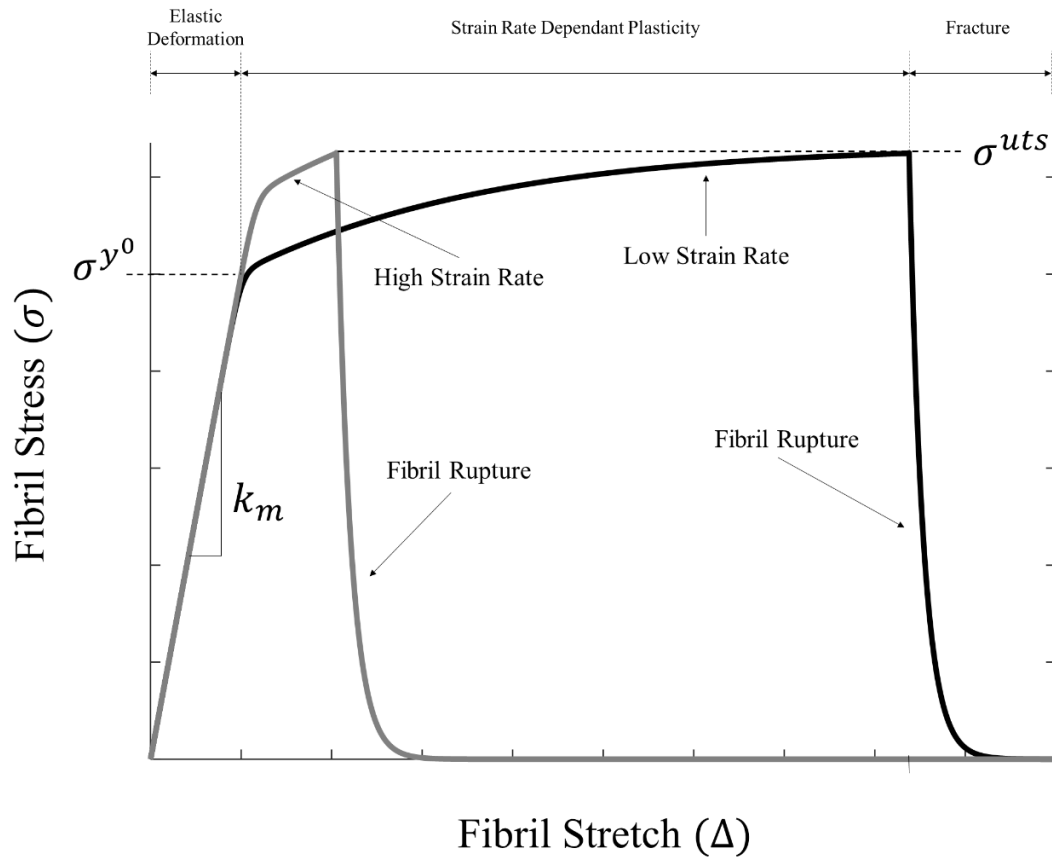


Figure 6.8. Schematic of the visco-plastic cohesive zone (VP-CZM) formulation

6.3.1 VP-CZM formulation

We propose a simple 1D elasto-visco-plastic formulation to describe elasto-plastic axial deformation of a fibril. For a given interface displacement vector Δ , the fibril axial deformation is given as the separation magnitude, Δ_m . To describe permanent fibril extension due to pull-out we perform an additive decomposition of Δ_m into an elastic recoverable separation, Δ_m^{el} , and an irrecoverable plastic (pull-out) separation, Δ_m^p (based on the approach of Cazes et al. (2010):

$$\frac{\Delta_m}{\delta_m^{el}} = \frac{\Delta_m^{el}}{\delta_m^{el}} + \frac{\Delta_m^p}{\delta_m^{el}} \quad (6.12)$$

where δ_m^{el} is a characteristic length. For convenience, and in keeping with standard plasticity notation, in the remainder of this section we refer to these non-dimensional fibril separations as effective fibril strains (elastic and plastic):

$$\frac{\Delta_m}{\delta_m^{el}} = \varepsilon = \varepsilon^{el} + \varepsilon^p \quad (6.13)$$

The axial fibril stress is obtained from the elastic effective fibril strain, such that

$$\sigma_f = k_m(\varepsilon - \varepsilon^p) \quad (6.14)$$

Strain-rate dependent visco-plasticity is implemented through the following relationship:

$$\dot{\varepsilon}^p = \dot{\varepsilon}_0 \left(\frac{\sigma_f}{\sigma_f^h(\varepsilon^p)} \right)^m \quad (6.15)$$

where $\dot{\varepsilon}^p$ is the effective fibril axial plastic strain rate and σ_f is the axial fibril stress. The parameter $\dot{\varepsilon}_0$ is a reference strain rate, m is the strain-rate hardening exponent, and $\sigma_f^h(\varepsilon^p)$ is the corresponding fibril yield stress (as a function of effective fibril axial plastic strain) at the reference strain-rate $\dot{\varepsilon}_0$. The form of $\sigma_f^h(\varepsilon^p)$ is specified through the following strain hardening law:

$$\sigma_f^h(\varepsilon^p) = \sigma_f^{y^0} + \left(\sigma_f^{y^\infty} - \sigma_f^{y^0} \right) \left(1 - \exp\left(\frac{-\varepsilon^p}{\varepsilon_n}\right) \right) \quad (6.16)$$

where $\sigma_f^{y^\infty}$ is the saturation yield stress, $\sigma_f^{y^0}$ is the initial yield stress, and ε_n is a hardening parameter. We assume a critical-stress failure initiation criterion, whereby

fibril rupture initiates when the fibril stress reaches a critical value; $\sigma_f = \sigma_f^{uts}$. Fibril rupture is described using a standard exponential damage formulation:

$$\sigma_f = \sigma_f^{uts} \exp\left(\frac{-\varepsilon^{max} - \varepsilon^{uts}}{\varepsilon_f^*}\right) \quad (6.17)$$

where ε^{uts} is the effective fibril axial strain at which σ_f^{uts} is reached, ε^{max} is the maximum strain reached, and the parameter ε_f^* governs the rate of damage/softening.

Numerical implementation:

Here we outline the numerical implementation of the visco-plastic fibrillation model. The total stress (σ_{f_i}) is expressed as the sum of the incremental increase in stress ($\Delta\sigma_f$) and the stress at the previous increment ($\sigma_{f_{i-1}}$):

$$\sigma_{f_i} = \sigma_{f_{i-1}} + \Delta\sigma_f \quad (6.18)$$

The incremental increase in stress is given as:

$$\Delta\sigma_f = k_m(\Delta\varepsilon - \Delta\varepsilon^p) \quad (6.19)$$

where $\Delta\varepsilon$ is the incremental total strain and $\Delta\varepsilon^p$ is the incremental change in plastic strain. The change in plastic strain ($\Delta\varepsilon^p$) is calculated through a Newton-Raphson scheme. The initial value/guess for $\Delta\varepsilon^p$ in the scheme is estimated using a rate tangent method. Briefly, the plastic strain increment is given as:

$$d\varepsilon^p = \frac{\frac{\partial \dot{\varepsilon}^p}{\partial \sigma_f} \Delta\varepsilon k_m \theta \Delta_{time} + \Delta_{time} \dot{\varepsilon}^p}{\frac{\partial \dot{\varepsilon}^p}{\partial \sigma_f} k_m \theta \Delta_{time} - \frac{\partial \dot{\varepsilon}^p}{\partial \sigma_f^h(\varepsilon^p)} d\sigma_f^h(\varepsilon^p) \theta \Delta_{time} + 1} \quad (6.20)$$

Where Δ_{time} is the current time increment, and θ determines the rate tangent solution method (a value of $\theta = 0.5$ is used (Crank–Nicolson method)).

The following expressions can be derived from equations (16)-(18)

$$\frac{\partial \dot{\varepsilon}^p}{\partial \sigma_f} = \dot{\varepsilon}_0 m \sigma_f^{(m-1)} \sigma_f^h (\varepsilon^p)^{-m} \quad (6.21)$$

$$\frac{\partial \dot{\varepsilon}^p}{\partial \sigma_f^h} = -\dot{\varepsilon}_0 m (\sigma_f \sigma_f^h (\varepsilon^p)^{-1})^m \sigma_f^h (\varepsilon^p)^{-1} \quad (6.22)$$

$$d\dot{\sigma}_f^h (\varepsilon^p) = \left(\frac{\sigma_f^\infty - \sigma_f^y}{\varepsilon_n} \right) \exp \left(\frac{-\varepsilon^p}{\varepsilon_n} \right) \quad (6.23)$$

Using the rate tangent solution as an initial guess, we can then iterate using a Newton-Raphson scheme using the following function:

$$f(x) = \Delta \varepsilon_p - (1 - \theta) \Delta_{time} \dot{\varepsilon} - \theta \Delta_{time} \dot{\varepsilon}_0 \left(\frac{\sigma_{f_{i-1}} + \Delta \sigma_f}{\sigma_f^h (\varepsilon^p)_{i-1} + \Delta \sigma_f} \right)^m \quad (6.24)$$

where i denotes the iteration number, and $i - 1$ is the previous iteration. $f'(x)$ is given as:

$$f'(x) = 1 - m\theta \Delta_{time} \dot{\varepsilon}_0 \left(\frac{\sigma_{f_{i-1}} + \Delta \sigma_{f_{i-1}}}{\sigma_f^h (\varepsilon^p)_{i-1}} \right)^{m-1} * \quad (6.25)$$

$$\left(\begin{array}{c} \sigma_f^h(\varepsilon^p)_{i-1}(-k_m) \\ \\ - \frac{\left(\frac{(\sigma_{f_{i-1}} + \Delta\sigma_f)(\sigma_f^\infty - \sigma_f^y)}{(-\varepsilon_n)} \exp\left(-\frac{\varepsilon_{i-1}^p + \Delta_{time}\Delta\varepsilon}{\varepsilon^n}\right) \right)}{\sigma_f^h(\varepsilon^p)_{i-1}^2} \end{array} \right)$$

and the updated increment of plastic strain is then given as:

$$\Delta\varepsilon^{p_{i+1}} = \Delta\varepsilon^p - \frac{f(x)}{f'(x)} \quad (6.26)$$

This formulation for axial elasto-visco-plastic fibril deformation is generalised within the framework of a CZM such that:

$$T_n = (\sigma_f) \sin(\varphi); \quad T_t = (\sigma_f) \cos(\varphi) \quad (6.27)$$

Mode-dependence of fibril visco-plasticity is specified through the following expressions for σ_f^y , σ_f^{uts} , and ε_f^* as a function of mode angle, φ :

$$\sigma_f^y(\varphi) = \tau^y - \left(\frac{\tau^y - \sigma^y}{1 - \exp\left(-\frac{\pi}{\Omega^y}\right)} \right) \left(1 - \exp\left(-\frac{\varphi}{\Omega^y}\right) \right) \quad (6.28)$$

where τ^y and σ^y are the values of initial yield stress under mode II and mode I loading, respectively, and the parameter Ω^y sets the non-linearity of the transition from mode II to mode I. Similarly, the mode-dependence of the ultimate strength of fibrils is given as:

$$\sigma_f^{uts}(\varphi) = \tau^{uts} - \left(\frac{\tau^{uts} - \sigma^{uts}}{1 - \exp\left(-\frac{\pi}{\Omega^{uts}}\right)} \right) \left(1 - \exp\left(-\frac{\varphi}{\Omega^{uts}}\right) \right) \quad (6.29)$$

where τ^{uts} and σ^{uts} are the values of initial yield stress under mode II and mode I loading, respectively, and the parameter Ω^{uts} sets the non-linearity of the transition from mode II to mode I. The description of the mode mixity of $\varepsilon_f^*(\varphi)$ is obtained from

$$\varepsilon_f^*(\varphi) = \frac{\hat{G}_m(\varphi)}{\sigma_f^{uts}(\varphi)} - \frac{\sigma_f^{uts}(\varphi)}{2K_m} \quad (6.30)$$

where $\hat{G}_m(\varphi)$ is the mode-dependent fibril fracture energy

$$\hat{G}_m(\varphi) = \int_{\varepsilon^{uts}}^{\infty} \sigma_f^{uts} \exp\left(\frac{-\varepsilon^{max} - \varepsilon^{uts}}{\varepsilon_f^*}\right) d\varepsilon \quad (6.31)$$

The mode dependence of the fibril fracture energy $\hat{G}_m(\varphi)$ is described using the following expression:

$$\hat{G}_m(\varphi) = G_t^d - \left(\frac{G_t^d - G_n^d}{1 - \exp\left(-\frac{\pi}{\Omega^{G^f}}\right)} \right) \left(1 - \exp\left(-\frac{\varphi}{\Omega^{G^f}}\right) \right) \quad (6.32)$$

where G_t^d is the fibril fracture energy in the tangential direction, G_n^d is the fibril fracture energy in the normal direction, and the parameter Ω^{G^f} sets the non-linearity of the transition from mode II to mode I. The VP-CZM is implemented in the finite element solver Abaqus through a *User Defined Interface Subroutine (UINTER)*. The consistent tangent matrix is derived estimated from (6.20).

6.3.2 Thermodynamic consideration in relation to a VP-CZM

From Gurtin (1979), the first and second principles of thermodynamics are expressed as:

$$\frac{de_s}{dt} = \underline{T}^s \frac{d[[\Delta]]}{dt} - [[q]] \underline{n} \quad (6.33)$$

$$\frac{ds_s}{dt} = -\frac{[[q]] \underline{n}}{H} + \frac{d(s_i)_s}{dt} \quad (6.34)$$

where e_s , s_s and $(s_i)_s$ are the surface densities of internal energy, entropy, and internal entropy, respectively. $[[\Delta]]$ represents the interface separation vector at the interface, \underline{T}^s is the stress vector defined over the discontinuity surface, $[[q]]$ is the heat flow jump, t is the time and H is the absolute temperature. The surface energy dissipated by the cohesive zone is then:

$$d\phi_s = Hd(s_i)_s \quad (6.35)$$

Using equations (6.33) and (6.34) one can obtain the following expression for the free surface energy:

$$\psi_s = e_s - Hs_s \quad (6.36)$$

This leads to the expression (originally derived by Cazes et al. (2010)) for an increment of dissipated energy, given as:

$$d\phi_s = \underline{T}^s d[[\Delta]] - d\psi_s - s_s dH \quad (6.37)$$

The total interface separation vector $[[\Delta]]$ is divided into elastic and plastic components.

$$[[\Delta]] = [[\Delta]]^{el} + [[\Delta]]^p \quad (6.38)$$

The free surface energy can trivially be defined as:

$$\psi_s = \frac{1}{2} \underline{T}^s d[[\Delta]]^{el} \quad (6.39)$$

Introducing equation (6.39) into equation (6.37), an expanded expression for an increment of dissipated energy is obtained, such that:

$$d\phi_s = \underline{T}^s d[[\Delta]]^p + \frac{1}{2} (\underline{T}^s d[[\Delta]]^{el} - [[\Delta]]^{el} d\underline{T}^s) \quad (6.40)$$

This can be rewritten in terms of the contribution of the evolution of the plastic interface separation $[[\Delta]]^p$ and of the elastic interface separation $[[\Delta]]^e$ as follows:

$$d\phi_s = d\phi_s^p + d\phi_s^{el} \quad (6.41)$$

Where the dissipated energy due to the plastic interface separation $[[\Delta]]^p$ is given as:

$$d\phi_s^p = \underline{T}^s d[[\Delta]]^p \quad (6.42)$$

and the dissipated energy due to the elastic interface separation $[[\Delta]]^{el}$ is given as:

$$d\phi_s^{el} = \frac{1}{2} (\underline{T}^s d[[\Delta]]^{el} - [[\Delta]]^{el} d\underline{T}^s) \quad (6.43)$$

The Clausius-Duhem inequality states that, in a thermodynamically allowable material, the dissipation is always positive. This requires the VP-CZM to exhibit instantaneous positive incremental dissipation over the entirety of a loading path. This leads to the following expression to estimate the thermodynamic legitimacy of the proposed model:

$$d\phi_s = \underline{T}^s d[[\Delta]]^p + \frac{1}{2} (\underline{T}^s d[[\Delta]]^{el} - [[\Delta]]^{el} d\underline{T}^s) \geq 0 \quad (6.44)$$

6.3.3 VP-CZM parametric investigation of mixed-mode behaviour

The VP-CZM is shown for a range of axial fibril strain rates ($\dot{\epsilon}$) in Figure 6.9. For high strain rates the VP-CZM behaviour is similar to a typical exponential-type model with negligible amounts of plasticity prior to reaching the ultimate strength. In contrast, for low strain rates the model predicts lower initial yielding, low hardening rates, and, consequently, high levels of plastic deformation prior to reaching the ultimate strength. This predicts that significantly higher levels of plastic deformation (fibril pull-out) and dissipation occur during low rates of interface separation.

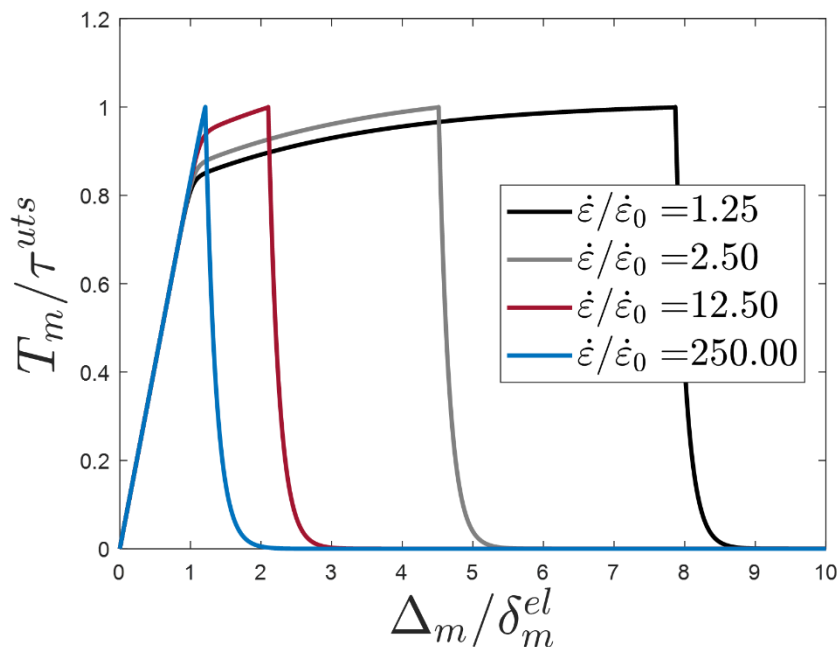


Figure 6.9. Traction as a function of separation for a range of strain rates. $\dot{\epsilon}_0$ is a VP-CZM parameter which controls the strain rate threshold. Fast strain rates exhibit negligible amounts of fibril pull-out, slow strain rates result in significant levels of fibril pull-out as indicated by the black curve.

Non-proportional loading path response: The mixed-mode behaviour of the VP-CZM is next explored by considering non-proportional loading paths subject to a range of strain rates for each path. The non-proportional loading paths consist of an initial mode II displacement to a prescribed value ($\Delta_t / \delta_t^{el} = 0 \rightarrow 10$) followed by complete

normal separation ($\Delta_n \rightarrow \infty$). We consider three cases in terms of imposed non-uniform strain rates: $\dot{\epsilon}_n = \dot{\epsilon}_t$; $\dot{\epsilon}_n > \dot{\epsilon}_t$; $\dot{\epsilon}_t > \dot{\epsilon}_n$. In Figure 6.10 we consider the case of mode-independent material parameters and we present computed traction separation relationships for the three aforementioned non-uniform strain rates ((A, D, G) Tangential components; (B, E, H) normal components; (C, F, I) magnitudes (effective fibril axial traction-separation relationship)). In all cases if significant plastic deformation occurs during the initial mode II separation, the computed level of plasticity (fibril pull-out) during subsequent normal separation is less pronounced. In terms of the effective axial fibril behaviour (traction-separation magnitude curves), transition from the mode II phase to the subsequent normal separation phase entails a temporary reduction in the strain-rate magnitude. This results in a reduction in the effective yield stress (in accordance with equation (6.15)) as normal separation increases, $\dot{\epsilon} \rightarrow \dot{\epsilon}_n$, and the final hardening curve prior to rupture depend on the value of $\dot{\epsilon}_n$. For example, in Figure 6.10(C) the hardening curve for the normal separation is lower than that for the initial mode II separation because $\dot{\epsilon}_t > \dot{\epsilon}_n$. In the case of the two highest prescribed values of initial mode II separation, fibril rupture initiates prior to the transition to normal separation.

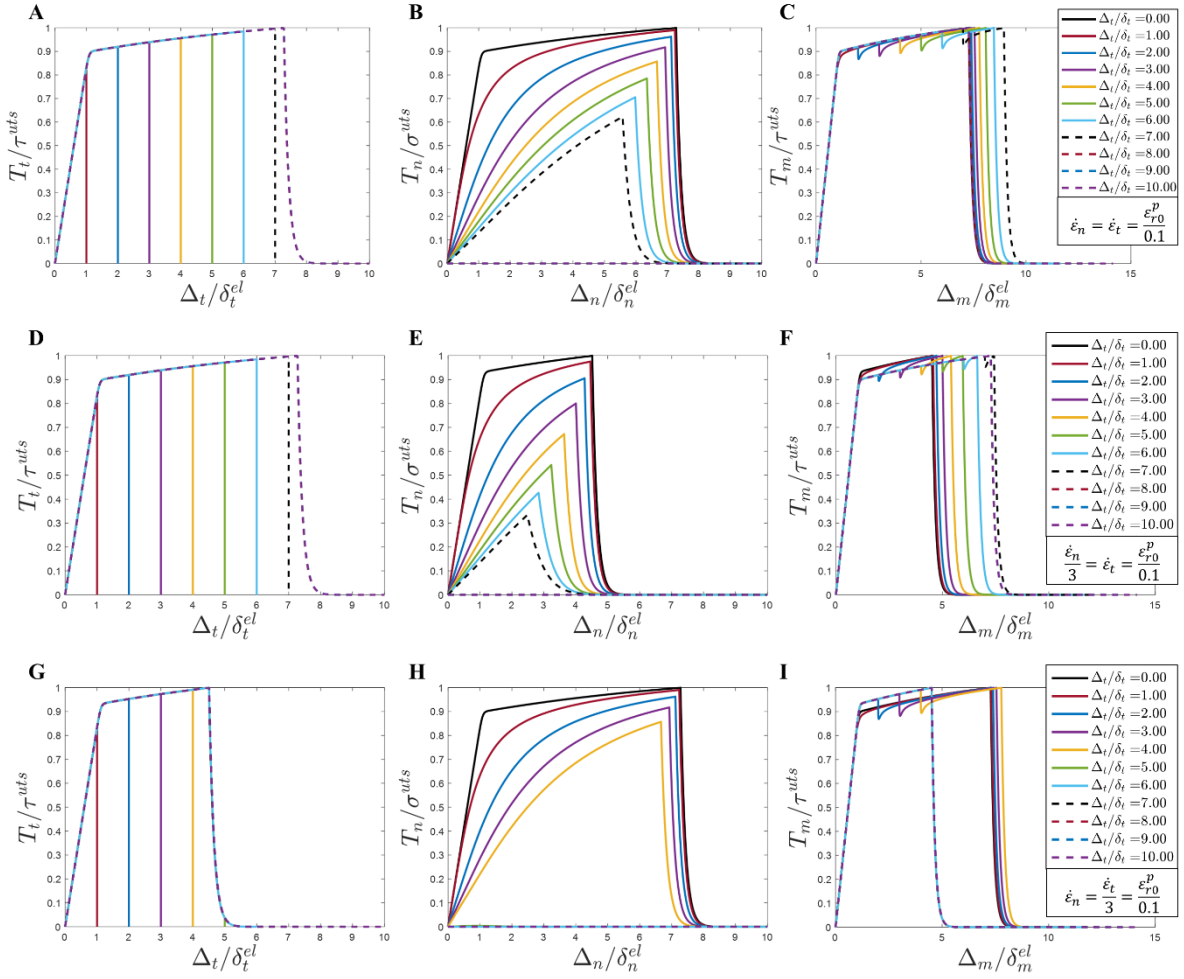


Figure 6.10. Normalised traction separation curves for the VP-CZM undergoing non-proportional loading paths in the case of $\dot{\epsilon}_n = \dot{\epsilon}_t = \dot{\epsilon}_0$ (A-C), $\dot{\epsilon}_n = 3\dot{\epsilon}_t = \dot{\epsilon}_0$ (D-F), $3\dot{\epsilon}_n = \dot{\epsilon}_t = \dot{\epsilon}_0$ (G-I). Other VP-CZM parameters are as follows: $k_m = 10\text{MPa}$, $\sigma_y = \tau_y$, $G_{n0} = G_{t0}$, $\sigma^{uts} = \tau^{uts}$, $\sigma^{uts} = 1.25\sigma^y$.

Proportional loading path response: The VP-CZM is now explored under proportional loading paths subject to a constant separation rate ($\dot{\epsilon}_m/\dot{\epsilon}_0 = 2.5$) for each path. Figure 6.11(A) confirms that the effective fibril axial traction-separation relationship is mode-independent when $\sigma_y = \tau_y$, $G_{n0} = G_{t0}$. Figure 6.11(B) shows the computed fracture energy is also mode-independent. The stored elastic energy is also shown in Figure 6.11(B). Tangential and normal components of the traction-separation relationships are shown in Figure 6.11(C,D). Corresponding relationships are shown in Figure 6.11(E-H) for the cases where the values of mode II yield stress and ultimate

strength are higher than the respective mode I values. The VP-CZM formulation produces consistent yield, hardening, and rupture behaviour for all mode angles. Furthermore, monotonic increases/decreases in the tangential/normal components of fracture energy are computed as a function of mode angle (Figure 6.11(F)). Normal and tangential traction components also exhibit consistent behaviour (Figure 6.11(G, H)).

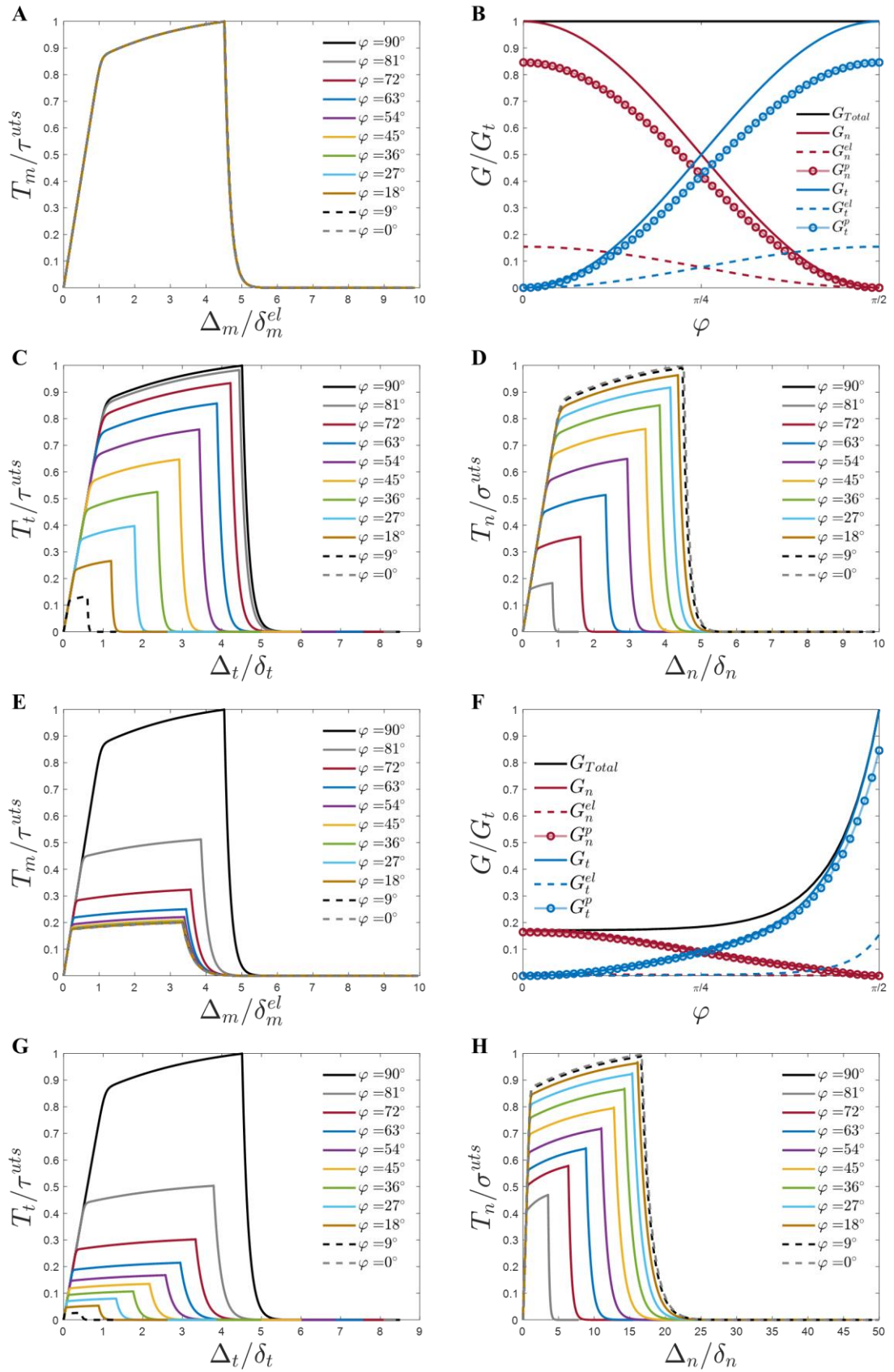


Figure 6.11. Traction separation response for the proportional loading paths subject to a constant separation rate ($\dot{\epsilon}_m/\epsilon_{r0}^p = 2.5$) for the VP-CZM with: (A-D): $\sigma_y =$

$\tau_y, G_{n0} = G_{t0}$, (E-H): $5\sigma_y = \tau_y, 5G_{n0} = G_{t0}$. In all cases $T_m^{uts} = 1.2(T_m^{y0})$. The calculated fracture energy is shown in the case of: (B) $\sigma_y = \tau_y, G_{n0} = G_{t0}$ and (F) $5\sigma_y = \tau_y, 5G_{n0} = G_{t0}$. The total fracture energy is shown as well as the individual energy contributions of the elastic recoverable energy (G^{el}) and the plastic irrecoverable (dissipated) energy (G^p).

The instantaneous incremental dissipation for the visco-plastic CZM is explored below in Figure 6.12 in the case of proportional loading (A, C, E) and non-proportional loading (D, D, F) in the case of $\sigma_y = \tau_y, G_n = G_t$ (A, B), $5\sigma_y = \tau_y, 5G_{n0} = G_{t0}$ (C, D), and $\sigma_y = 5\tau_y, G_{n0} = 5G_{t0}$ (E, F). Instantaneous incremental dissipation is positive throughout all loading scenarios explored; this satisfies the Clausium-Duhem inequality (equation (6.44)).

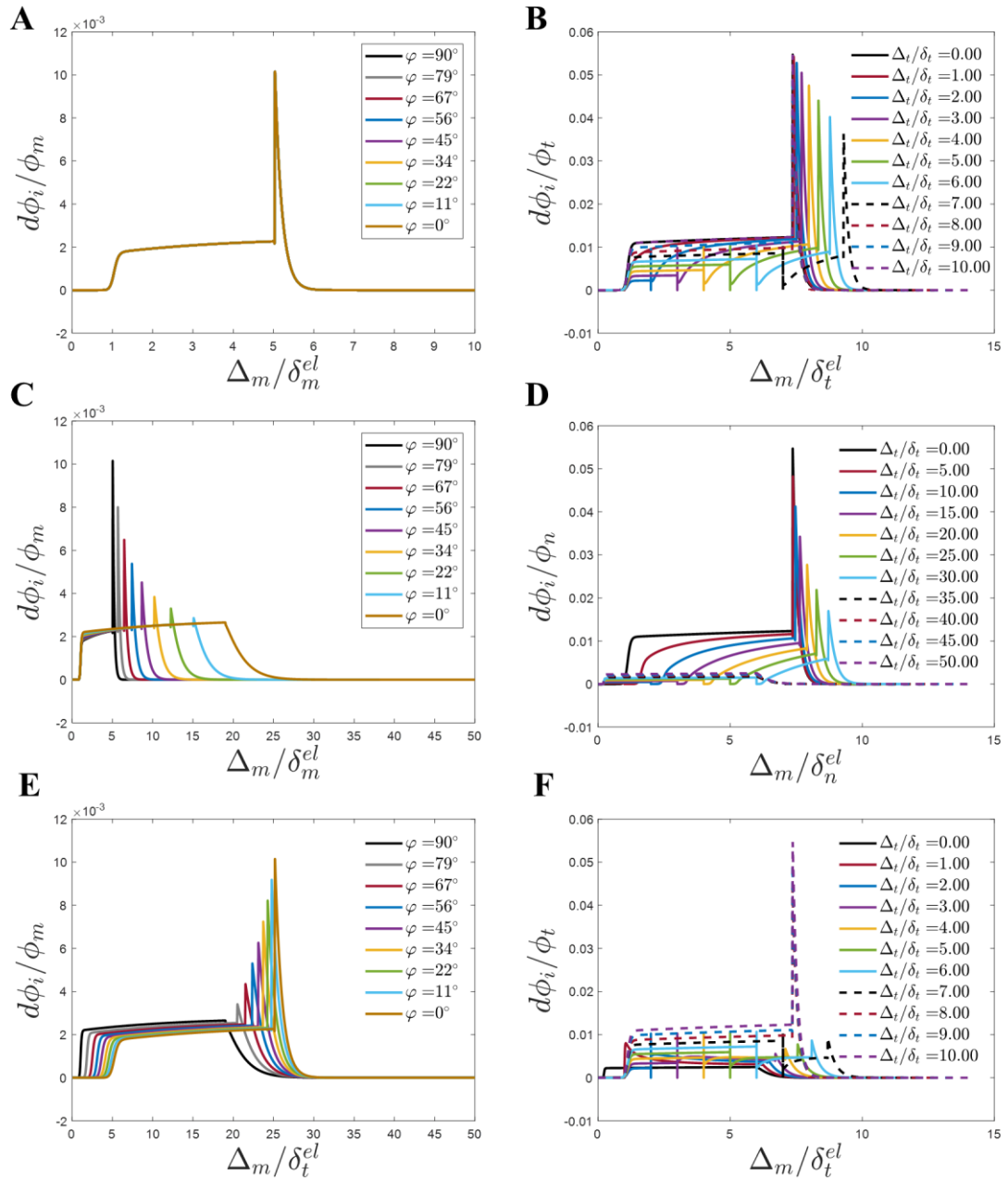


Figure 6.12. Demonstration of positive instantaneous incremental dissipation throughout loading history for the VP-CZM undergoing (A,C,E) Proportional loading and; (B,D,F) Non-proportional loading when; (A-B) $\sigma_y = \tau_y, G_{n0} = G_{t0}$ and; (C-D) $5\sigma_y = \tau_y, 5G_{n0} = G_{t0}$, and; (E-F) $\sigma_y = 5\tau_y, G_{n0} = 5G_{t0}$.

Irreversible damage and plastic deformation: The response of the VP-CZM to load-unload paths is explored in Figure 6.13. Figure 6.13(A) shows a mode I load-unload path (the path follows the red arrows, blue arrows, then green arrows). An illustration

of the fibrillation process is shown for a mode I load-unload scenario (i-viii). Collagen fibrils are initially embedded in the tissue matrix (i), upon stretching the fibrils stiffen and yield (ii-iii) with increasing interface separation. Fibrils then begin to plastically pull out of the tissue matrix (iv). Upon unloading, fibrils recover elastically (v) with significant permanent plastic pull-out (vi). Upon reloading, fibrils stretch elastically until yield is reached and begin to pull-out plastically until the point of rupture initiation (vii). Upon rupture, fibrils undergo total fibril pull-out or fibril damage (viii). The tangential traction-separation response to the same loading regime in mode II is shown in Figure 6.13(B) with positive instantaneous incremental dissipation demonstrated throughout (Figure 6.13 (C)). Figure 6.13(D) shows traction-separation curves for a range of mixed mode proportional loading for the load-unload regime outlined in (A). Figure 6.13(E) shows the tangential traction-separation response of mixed-mode proportional loading for the load-unload regime outlined in (B). Figure 6.13(D-E) demonstrate consistent behaviour with (A-B) in mixed mode scenarios.

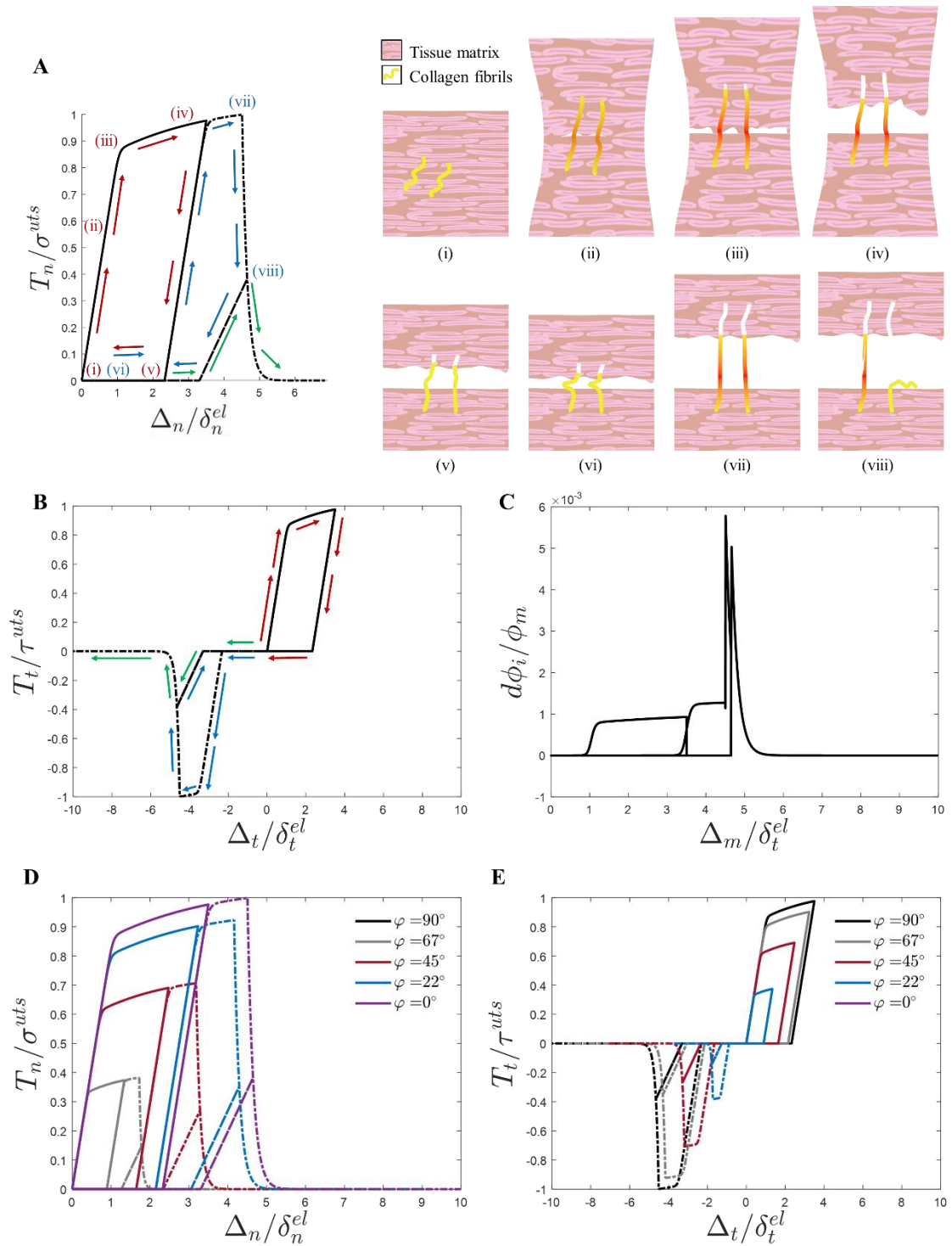


Figure 6.13. (A) Demonstration of permanent plastic deformation and fibril pull-out for a mode I loading-unloading scenario; (B) Demonstration of permanent plastic deformation and fibril pull-out for a mode II loading-unloading scenario following the arrows in order of (red, blue, green); (C) demonstration of positive instantaneous incremental energy dissipation; (D) Normal traction-separation curves in mixed mode loading unloading scenarios following the path outlined in (A); (E) Tangential traction-separation curves in mixed mode loading unloading scenarios following the path outlined in (B).

6.3.4 Simulation of artery crack propagation experiment using VP-CZM

In Figure 6.14 we assess the ability of the VP-CZM to predict non-uniform crack propagation rates in arteries. The model predictions are superimposed upon experimental results for Chapter 5 (presented in terms of measured crack length as a function of applied circumferential strain in the artery). Three values of $\dot{\epsilon}_0$ are presented ($\dot{\epsilon}_0 = 0.1$, $\dot{\epsilon}_0 = 0.01$, $\dot{\epsilon}_0 = 0.001$). Similar predictions are obtained in all cases. An initial phase of slow crack growth is computed, followed by a phase of fast crack growth over a long distance, followed by a phase of slower crack growth. Figure 6.13 (I) shows that significant plastic deformation (fibril pull-out) results in initially slow crack growth. During the fast crack growth phase, as the ultimate fibril strength is being reached without significant plasticity (Figure 6.13(II)) the effective VP-CZM behaviour in this region resembles a standard elastic-exponential damage formulation. Finally, after significant crack growth, plastic deformation re-emerges (Figure 6.13 (III)), resulting in a slowing of the rate of crack growth.

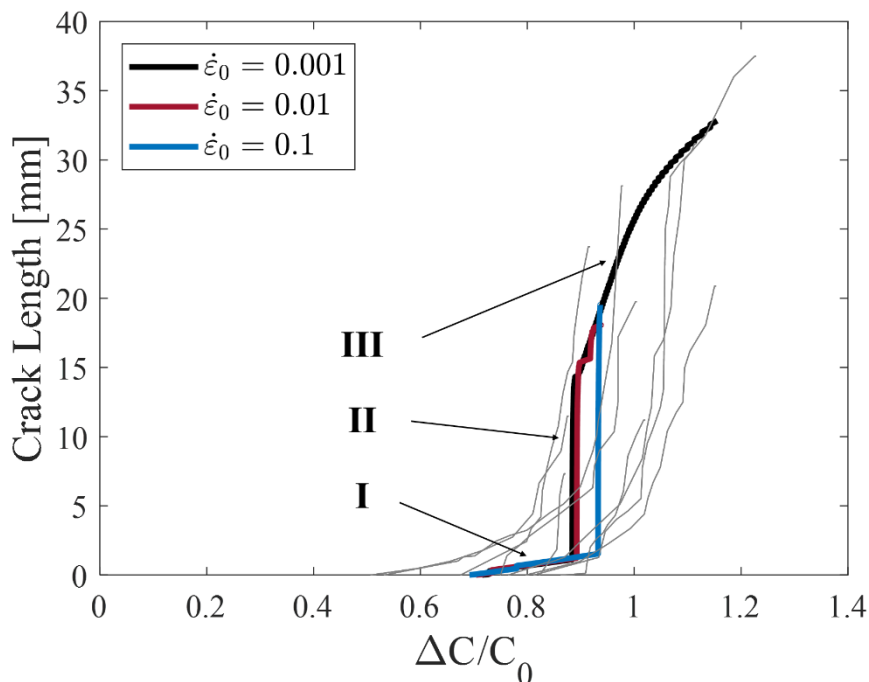


Figure 6.14: Predicted crack lengths superimposed over the experimentally measured crack lengths as a function of the circumferential strain for three values of $\dot{\epsilon}_0$ ($\dot{\epsilon}_0 = 0.1, \dot{\epsilon}_0 = 0.01, \dot{\epsilon}_0 = 0.001$).

Figure 6.15 shows the results of a finite element cohesive zone analysis of the experiments previously outlined in Chapter 5 of this thesis. Traction as a function of separation is shown for three phases along the cohesive interface throughout the simulation. Extensive plastic deformation is observed at phase I where the strain rate is lowest. Node A undergoes significant plastic deformation due to the slow strain rate, it is followed by Node B which undergoes the most plastic deformation, followed by nodes C and D which undergo little plastic deformation and no plastic deformation, respectively due to the increasing strain rate. Phase II shows three nodes (E-G), all of which undergo no plastic deformation as the strain rate results in rapid fracture. The final phase (III) shows three nodes (H-J) which increase from no plastic deformation to a moderate amount of plastic deformation as the strain rate begins to slow. These three phases mirror the trends observed in the experiment: a prolonged region of slow growth due to fibrillation (I), followed by a prolonged region of rapid crack growth (II), followed by a region of slow crack growth (III). This demonstrates the capability of the VP-CZM approach to generate a wide range of effective interface behaviours, resulting in non-uniform crack growth and a non-uniform prediction of plasticity (fibril pull-out).

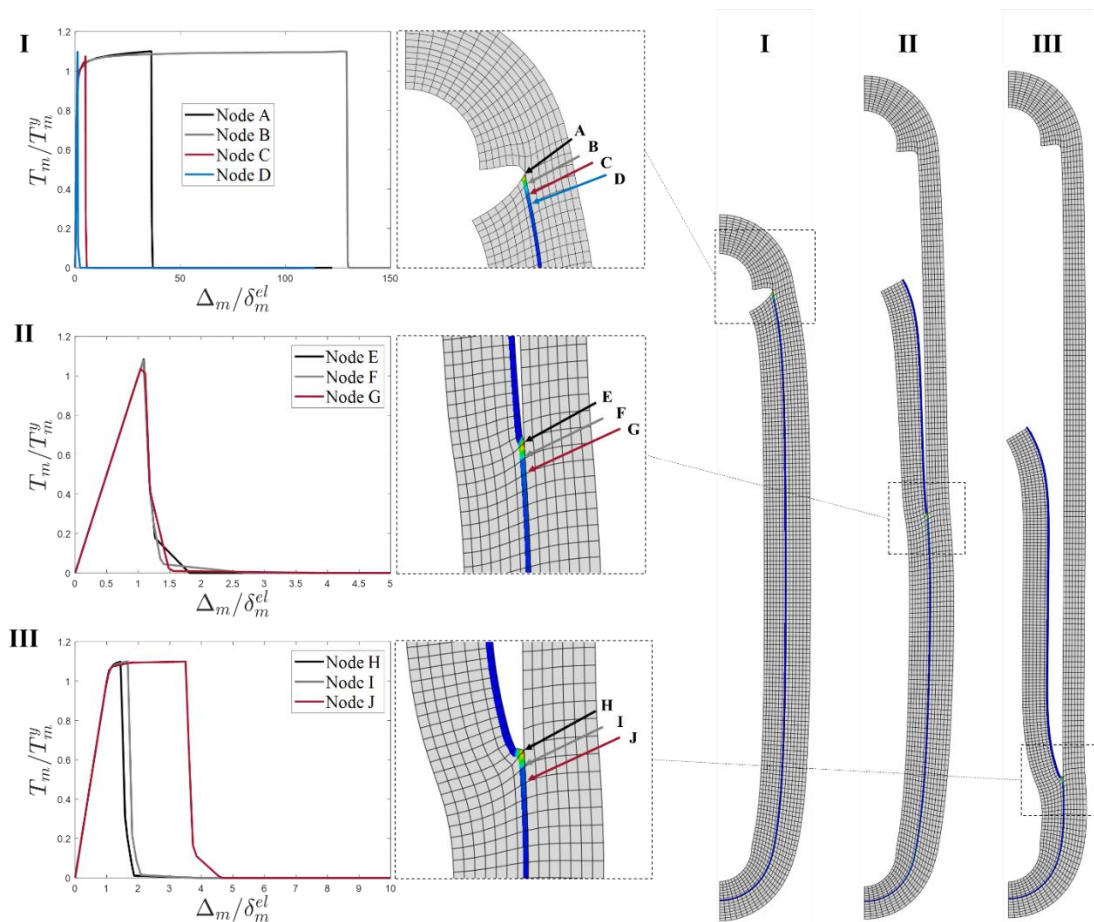


Figure 6.15. Normalised traction as a function of separation for three crack growth regimes selected along the cohesive zone interface. (I) Initial phase of crack growth: significant plasticity followed by rapid crack growth; (II) Rapid crack growth phase; (III) Final phase of increasing plasticity.

6.4 Concluding remarks

In the present study we propose two phenomenological CZM formulations to represent fibrillation during dissection of soft tissue. We first consider pure elastic fibrillation (EF-CZM). In this formulation fibrillation initiates during an initial phase of interface damage/softening. Fibrils then deform elastically until an ultimate strength is reached, followed by fibril rupture. Simulations reveal that such elastic fibrillation does not accurately predict the highly non-uniform crack propagation rates measured experimentally for arterial tissue. We then propose a phenomenological visco-plastic cohesive zone formulation for fibrillation (VP-CZM). This approach is motivated by

the experimental observation that fibrils undergo partial pull-out (in addition to elastic stretching) during dissection of arteries. Simulations reveal that this visco-plastic cohesive zone formulation provides a reasonable prediction of non-uniform crack propagation rates in arteries. Significant plasticity (representing fibril pull-out) during fracture initiation results in an initial slow phase of crack growth. The transition to fast crack growth is facilitated by the prediction of fibril rupture prior to extensive plasticity. The current implementation of fibril visco-plastic behaviour in a cohesive zone framework is limited to a phenomenological representation of axial fibril deformation and axial fibril pull-out. However, we provide extensive parametric exploration of the model behaviour under a range of mixed-mode loading paths, representing fibril reorientation in addition to fibril extension. We demonstrate that the formulation produces consistent behaviour for all loading paths and that positive incremental instantaneous dissipation is computed in all cases. The VP-CZM represents an advance on standard elastic-damage cohesive zone formulations. While the VP-CZM effectively produces such standard CZM behaviour at high interface separation rates, it predicts plastic deformation and energy dissipation (representing fibril pull-out) at low interface separation rates. The authors are not aware of a previous implementation of fibril visco-plastic behaviour in a CZM framework. In addition to the demonstrated application of artery dissection, the VP-CZM framework could be used to simulate the rate dependent fracture of collagen constructs (Arumugam *et al.*, 1992; Watton, Hill and Heil, 2004) and rate dependent fracture of skin. Furthermore, the consistent load-unload behaviour of the proposed framework facilitates the analysis of fatigue crack propagation under dynamic loading conditions (McCarthy, McGarry and Leen, 2014a, 2014b).

Bibliography

Arumugam, V. et al. (1992) 'Effect of strain rate on the fracture behaviour of collagen', *Journal of Materials Science*. Kluwer Academic Publishers, 27(10), pp. 2649–2652. doi: 10.1007/BF00540684.

Arumugam, V., Naresh, M. D. and Sanjeevi, R. (1994) 'Effect of strain rate on the fracture behaviour of skin', *Journal of Biosciences*. Springer India, 19(3), pp. 307–313. doi: 10.1007/BF02716820.

van den Bosch, M. J., Schreurs, P. J. G. and Geers, M. G. D. (2006) 'An improved description of the exponential Xu and Needleman cohesive zone law for mixed-mode decohesion', *Engineering Fracture Mechanics*. Pergamon, 73(9), pp. 1220–1234. doi: 10.1016/j.engfracmech.2005.12.006.

van den Bosch, M. J., Schreurs, P. J. G. and Geers, M. G. D. (2007) 'A cohesive zone model with a large displacement formulation accounting for interfacial fibrillation', *European Journal of Mechanics, A/Solids*. Elsevier Masson, 26(1), pp. 1–19. doi: 10.1016/j.euromechsol.2006.09.003.

Camanho, P. and Davila, C. G. (2002) 'Mixed-Mode Decoherence Finite Elements in for the Simulation Composite of Delamination Materials', Nasa, TM-2002-21(June), pp. 1–37. doi: 10.1177/002199803034505.

Camanho, P. P., Dávila, C. G. and De Moura, M. F. (2003) 'Numerical simulation of mixed-mode progressive delamination in composite materials', *Journal of Composite Materials*. SAGE Publications, 37(16), pp. 1415–1438. doi: 10.1177/0021998303034505.

Cazes, F. et al. (2009) 'A thermodynamic method for the construction of a cohesive law from a nonlocal damage model', *International Journal of Solids and Structures*. Pergamon, 46(6), pp. 1476–1490. doi: 10.1016/j.ijsolstr.2008.11.019.

Cazes, F. et al. (2010) 'A cohesive zone model which is energetically equivalent to a gradient-enhanced coupled damage-plasticity model', *European Journal of Mechanics, A/Solids*. Elsevier Masson, 29(6), pp. 976–989. doi: 10.1016/j.euromechsol.2009.11.003.

Dimitri, R. et al. (2015) 'Coupled cohesive zone models for mixed-mode fracture: A comparative study', *Engineering Fracture Mechanics*. Pergamon, 148, pp. 145–179. doi: 10.1016/j.engfracmech.2015.09.029.

FitzGibbon, B. and McGarry, P. (2020) 'Development of a novel test method to investigate mode II fracture and dissection of arteries'. engrXiv. doi: 10.31224/OSF.IO/D3JBR.

Gallagher, E. A., Lamorinière, S. and McGarry, P. (2018) 'Multi-axial damage and failure of medical grade carbon fibre reinforced PEEK laminates: Experimental testing and computational modelling', *Journal of the Mechanical Behavior of Biomedical Materials*. Elsevier, 82, pp. 154–167. doi: 10.1016/j.jmbbm.2018.03.015.

Gasser, T. C. and Holzapfel, G. A. (2006) 'Modeling the propagation of arterial dissection', *European Journal of Mechanics - A/Solids*, 25(4), pp. 617–633. doi: 10.1016/j.euromechsol.2006.05.004.

- Gurtin, M. E. (1979) ‘Thermodynamics and the cohesive zone in fracture’, *Zeitschrift für angewandte Mathematik und Physik ZAMP*. Birkhäuser-Verlag, 30(6), pp. 991–1003. doi: 10.1007/BF01590496.
- Hanson, J. H., Bittencourt, T. N. and Ingraffea, A. R. (2004) ‘Three-dimensional influence coefficient method for cohesive crack simulations’, *Engineering Fracture Mechanics*. Pergamon, 71(15), pp. 2109–2124. doi: 10.1016/j.engfracmech.2003.12.008.
- Kamath, Y. K. and Weigmann, H.-D. (1982) ‘Fractography of human hair’, *Journal of Applied Polymer Science*. John Wiley & Sons, Ltd, 27(10), pp. 3809–3833. doi: 10.1002/app.1982.070271016.
- Kendall, K. (1975) ‘Thin-film peeling—the elastic term’, *Journal of Physics D: Applied Physics*, 8(13), pp. 1449–1452. doi: 10.1088/0022-3727/8/13/005.
- Máirtín, É. Ó. et al. (2014) ‘Potential-based and non-potential-based cohesive zone formulations under mixed-mode separation and over-closure—Part II: Finite element applications’, *Journal of the Mechanics and Physics of Solids*. Pergamon, 63, pp. 363–385. doi: 10.1016/J.JMPS.2013.08.019.
- McCarthy, O. J., McGarry, J. P. and Leen, S. B. (2014a) ‘Micro-mechanical modelling of fretting fatigue crack initiation and wear in Ti-6Al-4V’, *International Journal of Fatigue*. Elsevier Ltd, 62, pp. 180–193. doi: 10.1016/j.ijfatigue.2013.04.019.
- McCarthy, O. J., McGarry, J. P. and Leen, S. B. (2014b) ‘The effect of grain orientation on fretting fatigue plasticity and life prediction’, *Tribology International*. Elsevier Ltd, 76, pp. 100–115. doi: 10.1016/j.triboint.2013.09.023.
- McGarry, J. P. et al. (2014) ‘Potential-based and non-potential-based cohesive zone formulations under mixed-mode separation and over-closure. Part I: Theoretical analysis’, *Journal of the Mechanics and Physics of Solids*, 63(1), pp. 336–362. doi: 10.1016/j.jmps.2013.08.020.
- McGarry, J. P. and McHugh, P. E. (2008) ‘Modelling of in vitro chondrocyte detachment’, *Journal of the Mechanics and Physics of Solids*. Pergamon, 56(4), pp. 1554–1565. doi: 10.1016/j.jmps.2007.08.001.
- Noble, C. et al. (2017) ‘Simulation of arterial dissection by a penetrating external body using cohesive zone modelling’, *Journal of the Mechanical Behavior of Biomedical Materials*, 71(Submitted), pp. 95–105. doi: 10.1016/j.jmbbm.2017.03.004.
- Paggi, M. and Reinoso, J. (2015) ‘An anisotropic large displacement cohesive zone model for fibrillar and crazing interfaces’, *International Journal of Solids and Structures*. Pergamon, 69–70, pp. 106–120. doi: 10.1016/j.ijsolstr.2015.04.042.
- Park, K., Paulino, G. H. and Roesler, J. R. (2009) ‘A unified potential-based cohesive model of mixed-mode fracture’, *Journal of the Mechanics and Physics of Solids*. Pergamon, 57(6), pp. 891–908. doi: 10.1016/j.jmps.2008.10.003.
- Vossen, B. G. et al. (2014) ‘Multi-scale modeling of delamination through fibrillation’, *Journal of the Mechanics and Physics of Solids*, 66(1), pp. 117–132. doi: 10.1016/j.jmps.2014.01.009.

Vossen, B. G. et al. (2016) 'High toughness fibrillating metal-elastomer interfaces: On the role of discrete fibrils within the fracture process zone', *Engineering Fracture Mechanics*, 164, pp. 93–105. doi: 10.1016/j.engfracmech.2016.05.019.

Wang, L. et al. (2018) 'Modelling peeling- and pressure-driven propagation of arterial dissection', *Journal of Engineering Mathematics*. Springer Netherlands, 109(1), pp. 227–238. doi: 10.1007/s10665-017-9948-0.

Watton, P. N., Hill, N. A. and Heil, M. (2004) 'A mathematical model for the growth of the abdominal aortic aneurysm.', *Biomechanics and modeling in mechanobiology*, 3(2), pp. 98–113. doi: 10.1007/s10237-004-0052-9.

Xu, X.-P. et al. (1993) 'Void nucleation by inclusion debonding in a crystal matrix', *Modelling and Simulation in Materials Science and Engineering*. IOP Publishing, 1(2), pp. 111–132. doi: 10.1088/0965-0393/1/2/001.

Chapter 7

7 A NUMERICAL INVESTIGATION OF THE INITIATION OF TYPE A AORTIC DISSECTION

7.1 Introduction:

Aortic dissection (AD) is a relatively rare but highly lethal disease. Population-based studies indicate incidences of 3.5 aortic dissections per 100,000-person years (Wang and Dake, 2006). One such study reports that 21% of patients died before admission, and, of those hospitalised, 22.7% died within the first 6 hours, 33.3% within the first 12 hours, 50% in the first 24 hours, and 68.2% within 48 hours (Mészáros *et al.*, 2000). Approximately two thirds (62.3%) of cases of AD initiate in the aortic arch, referred to as Stanford type A dissection (Hagan *et al.*, 2000). Stanford type B dissection refers to dissection initiating distal to the left subclavian artery. AD has been observed spreading to branching vessels in 41% of cases, most frequently to the brachiocephalic and carotid arteries (Mészáros *et al.*, 2000).

The underlying mechanics of AD are not well understood. It has been speculated that dissection occurs due to some intimal injury which causes an initial separation of the mural layers of the aorta (Criado, 2011). Delamination between the elastic lamellae of the media is observed (Gasser and Holzapfel, 2006). Propagation of the crack-front is not limited to the circumferential direction; rather, crack spiral-like crack propagation occurs in the circumferential-axial plane, referred to clinically as “spiral barber pole”

dissection (Fuster *et al.*, 2007). Cases in which the crack propagates in the radial direction through the artery wall are nearly always associated with pericardial effusion, leading to cardiac tamponade and death (Hagan *et al.*, 2000; Murai *et al.*, 2001).

Hypertension is the most common comorbidity associated with AD (Hagan *et al.*, 2000; Clough and Nienaber, 2015). Chronic hypertension is reported to increase the stiffness of the arterial wall through a pathological process of remodelling (Rorive and Carlier, 1983; Laurent, Boutouyrie and Lacolley, 2005; Arribas, Hinek and González, 2006; Greenwald, 2007). A study carried out on pigs with induced hypertension showed that it can lead to the creation of an intra-mural interface where the outer layer of the media becomes hypoxic due to restriction of blood flow to the vasa vasorum (Angouras, 2000). Hypertension also induces hypertrophy of the inner layer of the media (Henrichs *et al.*, 1980; Olivetti *et al.*, 1982; Owens, Rabinovitch and Schwartz, 2006). Hypertension, therefore, can lead to thickening of the inner layer of the media, arteriosclerosis of the outer layer of the media or of the entire vessel. The effect of such changes on the intramural mechanical stress state has not been previously examined.

During the cardiac cycle the aortic root undergoes significant deformation and displacement (Kozerke, Markus B. Scheidegger, *et al.*, 1999). A previous study suggests that forces acting on the aortic root throughout the cardiac cycle may play a role in initiation of AD (Emmott *et al.*, 2016). The effect of aortic root displacement on wall stress has been preliminarily examined through finite element modelling (Beller *et al.*, 2004, 2009). Such studies consider the circumferential and longitudinal stress in the wall as an indicator of AD potential. However, in the current study we argue that the interface traction along a circumferential-axial plane is a more

appropriate metric for examining AD as it pertains to inter-lamellar delamination. The effect anatomical deformation of the aortic root has on interfacial tractions has not yet been examined.

In the first part of this study (Section 7.2) we develop a realistic subject-specific aorta finite element model derived from a dual-ventricle MRI scan. We investigate if spontaneous dissection will occur under extreme hypertensive lumen blood pressure loading, or if significant reduction in interface strength must occur in order for dissection to initiate. Importantly, we also demonstrate that dissection initiation is a pure mode II fracture process, rather than a mixed mode or mode I process. In the second part of this study (section 7.3) we construct a parameterised idealised aorta model in order to assess the relative contribution for several anatomical and physiological factors to dissection risk. Such parametric analyses provide fundamental insight into the mechanics of stress localisation and delamination in the aorta. Overall, our detailed series of simulations suggest that variations in anatomical features and hypertensive loading will not result in a sufficient elevation of the stress state in the aorta wall to initiate dissection. Our results suggest that initiation of AD requires a significant reduction in the mode II fracture strength of the aortic wall, suggesting that dissection is preceded by structural and biomechanical remodelling.

7.2 Development of a realistic subject-specific model of aortic dissection

7.2.1.1 Construction of subject-specific mesh

In the current study we present construction of a subject-specific geometry of the aorta with spatially varying wall thickness. The model includes all major supra-aortic vasculature and major visceral branches. Lumen boundary points and the aortic centreline are extracted directly from MRI data using a bespoke MATLAB framework

using the GIBBON toolbox (Concannon *et al.*, no date; M Moerman, 2018a) (Figure 7.1(a)). A surface mesh of the main trunk of the aorta is created by sweeping the lumen boundary along the centreline (Figure 7.1(b)). The major branch vessels of the aorta are added to the surface mesh through a cut and extrusion process (Figure 7.1(c)). As shown in Figure 7.1(d), spatially varying wall thickness is accounted for by assigning all vertices with a wall thickness offset, based on reported values in human cadaveric experiments (Concannon *et al.*, 2020). A structured hexahedral mesh is created by offsetting the surface mesh through the wall thickness (e-f). Each element is assigned a local material orientation (g) and the aorta is modelled as a hyperelastic anisotropic fibre-reinforced material. Unless otherwise stated, the aorta is subject to a hypertensive lumen pressure of 300 mmHg. A cohesive zone model is applied to the medial interface of the aorta model (shown in Figure 7.1(f)), the normal interface strength calibrated from peel tests is $\sigma_{max} = 202 \text{ kPa}$ and the shear interface strength calibrated from shear fracture ring tests is $\tau_{max} = 1.6 \text{ MPa}$. A recently developed anisotropic bi-linear fibre-matrix hyperelastic formulation (Fereidoonzhad, O'Connor and McGarry, 2020) is used to simulate the aorta material behaviour. The ability of the calibrated constitutive law to predict the non-linear anisotropic behaviour of aortic tissue has been previously demonstrated by FitzGibbon and McGarry (2020) with best fit parameters reproduced in Figure 7.1(j-k).

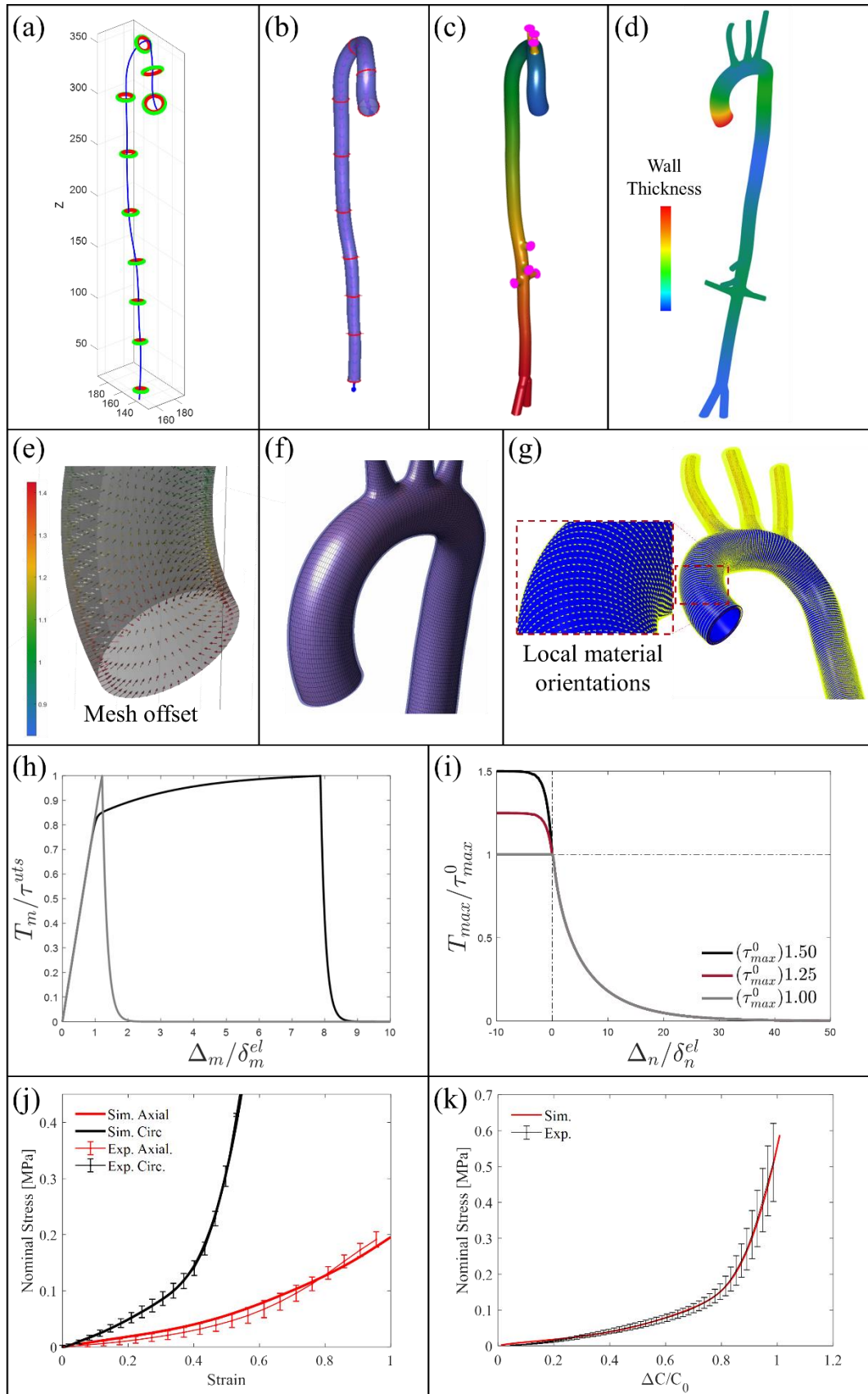


Figure 7.1. (a-g) Subject-specific aorta mesh creation process (a) Centreline and lumen boundary data extracted from dual-view MRI; (b) swept surface mesh along the

centreline of the main aortic trunk; (c) all major visceral and supra-aortic branch vessels are added to the surface mesh; (d) spatially varying wall thickness assigned to each vertex (e) surface mesh is offset by a spatially varying wall thickness resulting in a structured hexahedral mesh (f); Local material orientations assigned to each element (local circumferential direction shown in (g)). (h) CZM is applied to the medial interface of the aorta model; (i) overclosure hardening is an optional feature of the CZM; (j-k) material model calibrated to arterial tissue test data.

7.2.2 Key results for subject-specific aorta model dissection analysis

Figure 7.2 presents key results computed for the realistic subject-specific aorta model subjected to extreme hypertensive blood pressure loading of 300 mmHg. Figure 7.2(a) shows that the lumen blood pressure results in a compressive component of local radial stress throughout the aortic wall. This results in negative (compressive) normal tractions along the medial interface (Figure 7.2(b)). The cohesive zone formulation enforces a strong penalisation of overclosure, such that high negative pressure across the interface results in normal overclosure lower than 5 nanometres (Figure 7.2(c)). This result indicates that initiation of aortic delamination will be pure mode II, rather than mixed mode or mode I. Informed by this result, we examine the maximum local material shear stress in Figure 7.2(d). Shear stress concentrations are predicted near the ostia of the supra-aortic branch vessels and along the inner curve of the aortic arch (as shown by the rotated detail view in Figure 7.2(d)). In order to assess the risk of intramural delamination we examine the shear tractions at the medial interface in Figure 7.2(e). The predicted shear tractions produce similar trends to the max local material shear stress; high concentrations of shear traction are computed near the ostia of the supra-aortic branch vessels and the inner curve of the aortic arch (Figure 7.2(e)). Additionally, shear traction concentrations are computed near the ostia of the major visceral branch vessels (contour limits have been adjusted for detailed inset views to highlight regions of interest). Significant areas of localisation of shear traction are evident at the aortic root, along the arch, and in the descending thoracic aorta.

However, all computed maximum shear tractions are approximately two orders of magnitude lower than the experimentally measured mode II fracture strength ($\tau_{exp}=1.6$ MPa; FitzGibbon and McGarry, (2020)), suggesting that even extreme hypertensive loading will not initiate a dissection in healthy aortic tissue. In Figure 7.2(f) we present results for a series of simulations in which we investigate the influence of a reduced mode II fracture strength on dissection initiation. In the case of hypertensive blood pressure of $P=300$ mmHg, delamination initiation is not predicted even if the cohesive zone shear strength is reduced to a value of $\tau_{max}=0.08$ Mpa (i.e. 20 times lower than τ_{exp}). If τ_{max} is reduced to a value 100 times lower than τ_{exp} dissection is predicted to initiate at a lumen blood pressure of $P=72$ mmHg (i.e. approximately at a healthy diastolic blood pressure).

The results presented in Figure 7.2 indicate that extreme hypertensive lumen blood pressure loading will not result in dissection initiation in healthy aortic tissue (i.e. tissue with a mode II fracture strength of ~ 1.6 MPa, as measured experimentally). However, chronic hypertension is often associated with an inhibition of the vasa vasorum's vasodilator capacity resulting in intralamellar regions becoming hypoxic leading to the development of micro cracks, a credible antecedent of dissection (Heistad *et al.*, 1978; Marcus, 1985; Stefanadis *et al.*, 1995; Angouras, 2000). Therefore, chronic hypertension may lead to a gradual reduction in the fracture resistance of arterial tissue. Cystic medial degeneration may also lead to localised reduction in the fracture strength of the aortic wall, resulting in initiation of delamination (Carlson, Lillehei and Edwards, 1970). It is likely that some pathologies influence the fracture strength on a global scale, for example, connective tissue disorders significantly alter the inter-lamellar aortic microstructure through elastin deficiency (Marfan syndrome) and collagen deterioration (Ehler-Danlos syndrome)

(Brandt *et al.*, 2001; Ulbricht *et al.*, 2004). The incidence of arterial dissection is much higher in patients with connective tissue disorders such as Marfan syndrome and Ehler-Danlos syndrome (Abraham *et al.*, 1982; Nakashima, Shiokawa and Sueishi, 1990; Lemaire and Russell, 2011; Yuan and Jing, 2011). Further mode II testing of excised pathological tissue is required to establish the effect, if any, of such pathologies on mode II fracture strength.

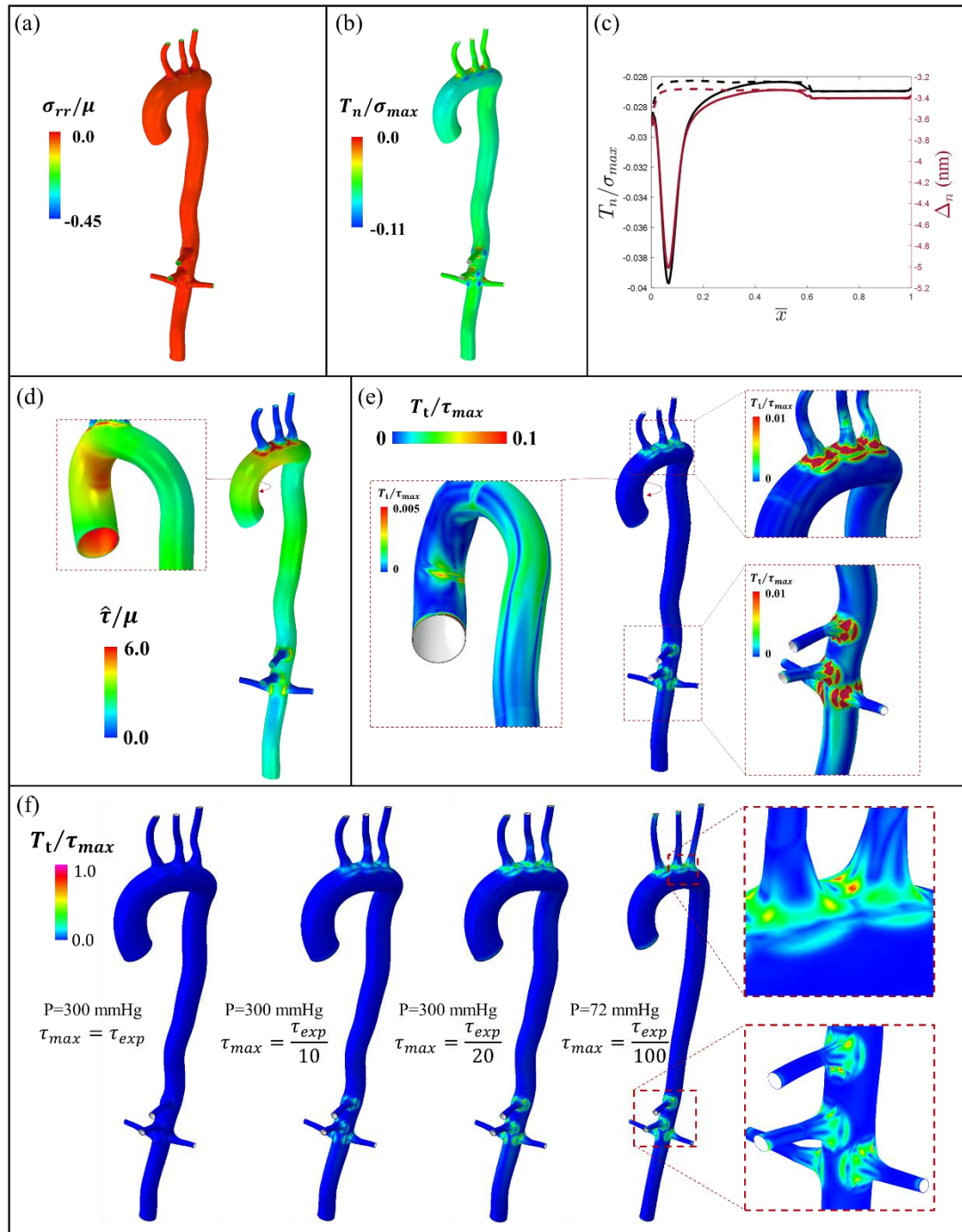


Figure 7.2. (a) contour plot of local radial compressive stress throughout the aorta under an applied pressure of 300 mmHg; (b) negative normal (compressive) tractions computed throughout the aorta under a pressure of 300 mmHg; (c) (left y-axis) normal traction along the inner and outer curve of the aorta as a function of normalised length (\bar{x}); (right y-axis) normal separation Δ_n as a function of normalised length (\bar{x}), heavy penalisation of overclosure is observed. (d) Maximum local material shear stress ($\hat{\tau}$) in the aorta subject to a lumen pressure of 300 mmHg; (e) Shear tractions in the medial interface in the aorta subject to a lumen pressure of 300 mmHg. Detail windows show limit-adjusted contours highlighting regions of elevated shear traction; (f) Contour plots of shear traction (T_t) for four values of mode II interface strength (τ_{max}). τ_{exp} is the experimentally measured mode II fracture strength (1.6 MPa). Delamination is

predicted to initiate if $T_t = \tau_{max}$. Applied lumen blood pressure (P) is indicated for all simulations.

7.3 Parametric investigation of the key factors that contribute to risk of vessel dissection

The results presented for the realistic subject-specific aorta model in Section 7.2 indicate that a significant reduction (100-fold) is required for spontaneous dissection initiation. In cases in which patients exhibit such reduced fracture strength of the aortic wall, additional anatomical features and physiological loading conditions may play an increased role in dissection risk. In the remainder of this study we perform a parametric assessment of the influence of a range of anatomical and physiological parameters on dissection risk, characterised by the computed shear traction distributions. Specifically, based on clinical evidence we investigate the following factors:

Material factors:

(i) Stiffness mismatch in the aortic wall in the radial direction. Chronic hypertension has been shown to induce hypoxic stiffening of the outer medial layer relative to the inner layer (Laurent, Boutouyrie and Lacolley, 2005; Laurent and Boutouyrie, 2015).

(ii) residual stress in the aorta wall. The opening angle of the aorta varies significantly as a function of aortic length, the influence of such heterogeneity of the residual stress field of the aorta on risk of dissection has not been previously quantified (Sokolis *et al.*, 2017).

Physiological factors:

(i) cranial (axial) displacement has been previously documented as the primary displacement direction of the aortic root (Kozerke, Markus B Scheidegger, *et al.*,

1999). The role this displacement plays on shear tractions in the aorta has not been identified¹.

(ii) cardiac cycle displacement. The influence of the multiple simultaneous aortic root loading modes on AD risk has not been quantified previously.

Anatomical factors:

(i) Aortic wall thickness is known to increase as a result of hypertrophic remodelling due to chronic hypertension (Laurent and Boutouyrie, 2015). Aortic wall thickness may also increase in the presence of diseases such as giant cell temporal arteritis (Corbett and Melms, 2003; Koster, Matteson and Warrington, 2018).

(ii) Aortic arch radius increases as does aortic length as the aorta ages (Redheuil *et al.*, 2011).

(iii) Branching vessels are frequently involved in aortic dissection (Lentini *et al.*, 2008) and may spontaneously dissect even without the presence of aortic dissection (Komiya *et al.*, 2001; Yoshida and Tobe, 2005).

The influence of all of the above factors on AD risk has not previously been quantified, either experimentally or computationally. Systematic analysis and insightful comparison of the above factors requires the construction of a regularised aorta model in which independent perturbation of a single parameter can be implemented. Additionally, parametric assessment of the influence of stiffness ratios through the aortic wall requires the implementation of linear material behaviour, rather than the complex anisotropic non-linear material behaviour used in our subject-specific model (Figure 7.2). In Section 7.3 we present the construction of a parameterised idealised

¹ A range of displacement modes were analysed (Figure 7.3 (e)), however, for brevity cranial and cardiac cycle displacements are presented as the two most dominant displacement modes.

aorta model and in Section 7.3.2 we present the key results of our extensive parametric investigations. Once again, it should be emphasised that the purpose of this component of our investigation is not to create a realistic representation of the aorta (this has already been attempted in Section 7.2 above). Rather, the purpose of this systematic analysis is to gain fundamental insight into the relative influence of key parameters on the vessel stress state and dissection risk.

7.3.1 Development of an idealised and parameterised model of the aorta

In order to systematically quantify the contribution of aortic anatomical features on dissection risk, we construct an idealised series of parameterised geometries of the ascending aorta, aortic arch, and descending aorta. Given the evidence that AD primarily occurs between the elastic lamellar layers of the media (Tam, Sapp and Roach, 1998; Gasser and Holzapfel, 2006), we assume the wall is a bi-layered composite; a cohesive zone model is applied at the interface between the two layers. Different material properties are assigned to each layer (Matsumoto and Hayashi, 1996b; Angouras, 2000) in order to explore the influence of stiffness mismatch on interface tractions and dissection. Although the parameterised geometry is highly idealised and neglects branching vessels, such a parameterisation is necessary to quantitatively parse the contribution of each material/anatomical factor to AD risk.

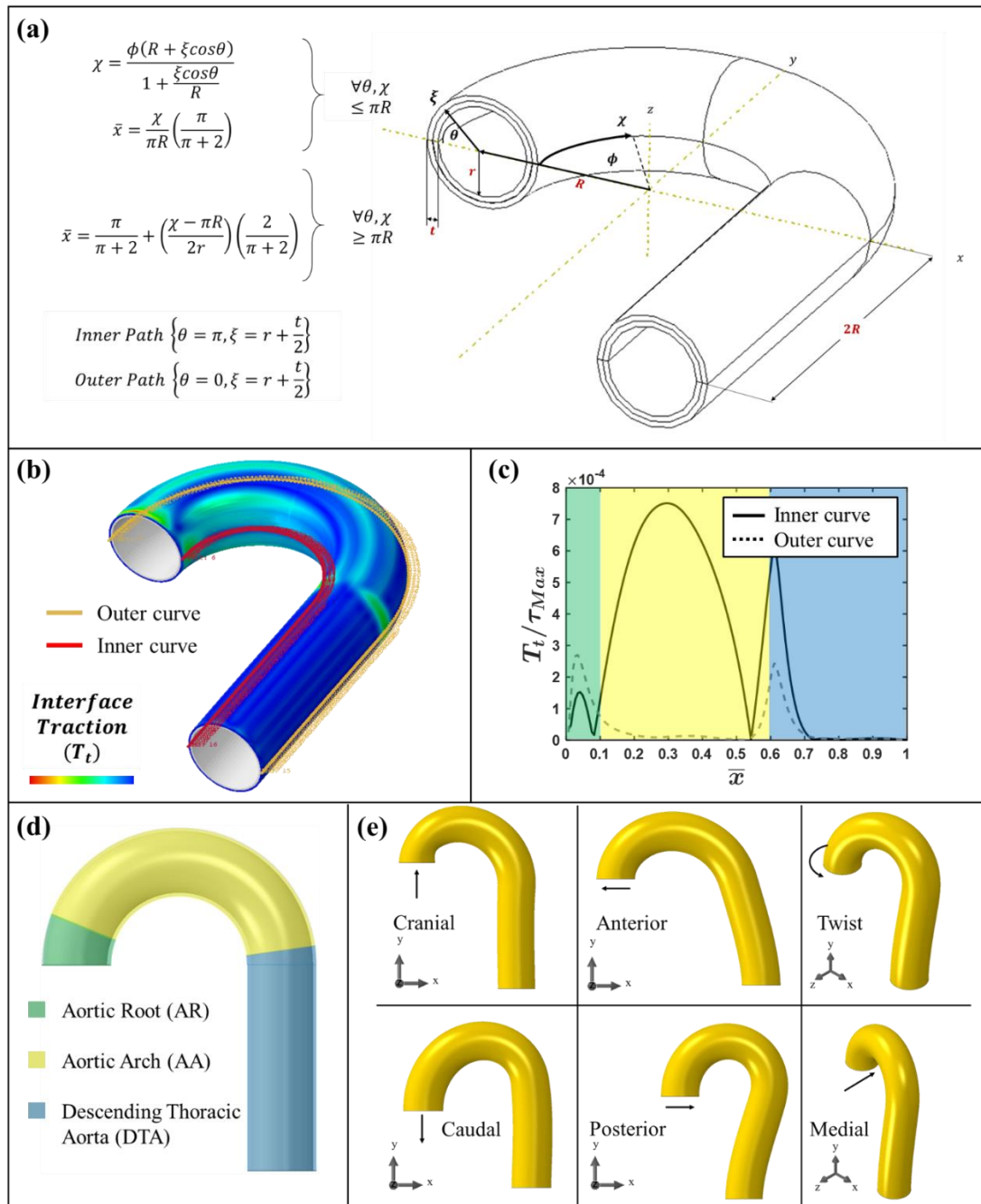


Figure 7.3. (a) Schematic representing the parameters in the model. The dimension $\chi(\phi, \theta, \xi)$ represents path length. \bar{x} is the normalised path length $\forall(\theta, \xi)$; (b) contour plot illustration of the inner curve and outer curve on a representative geometry with interface traction shown; (c) illustration of traction plot along the inner and outer curves. Three colour coded regions are shown in (d); (e) illustrations of loading modes explored in the present study.

Anatomical parameterisation of idealised aorta: Figure 7.3 shows a schematic of the parameterised model. An interface path coordinate is defined (χ) which is a function

of the angle ϕ , the local radial coordinate ξ , and the local circumferential angle θ , where the local system for $\chi \leq \pi R$ is distance R from the global origin. The interface path coordinate is then normalised to give the normalised path coordinate \bar{x} (referred to as *normalised aortic length*). This allows for the description of an interface path in terms of the aortic arch $\chi \leq \pi R, \forall(\theta, \xi)$ and the descending thoracic aorta $\chi \geq \pi R, \forall(\theta, \xi)$.

Path lines are chosen such that the ‘Inner’ path runs along the section of highest curvature of the arch and continues in that plane through the descending thoracic aorta ($\theta = \pi, \xi = r + t/2$) (see Figure 7.3(b)). Path data is normalized according to each model geometry. Traction is computed at the path lines and plot as a function of the normalised path length (\bar{x}), as seen in the example traction plot in Figure 7.3(c). For convenience, we approximately describe the normalised length in terms of its anatomical location: aortic root (AR) $\approx 0 \leq \bar{x} \leq 0.1$, aortic arch (AA) $\approx 0.1 \leq \bar{x} \leq 0.6$, descending thoracic aorta (DTA) $\approx 0.6 \leq \bar{x} < 1$, see Figure 7.3(c-d).

Parameters varied in the models are as follows: arch radius (aortic curvature) (R), wall thickness (t), wall stiffness (E), stiffness discrepancy in the layers (E_i, E_o), and inner and outer layer thickness (t_i, t_o). The inner lumen radius (r) does not change and the outer lumen radius (r_o) changes with the thickness. The value range of geometric parameters for arch geometries are selected based on CT scan data. Values of arch radii and wall thickness are chosen in physiological (Erbel and Eggebrecht, 2006), pathophysiological (Corbett and Melms, 2003; Koster, Matteson and Warrington, 2018), and non-physiological ranges. In order to parse the influence of material stiffness mismatch between the two layers of the vessel we assume quasi-linear elastic neo-hookean material behaviour (non-linear hyperelastic material behaviour does not

allow for the prescription of a constant stiffness ratio for a range of lumen pressures). Physiologically accurate non-linear anisotropic hyperelastic material behaviour is explored above in Section 7.2. Details of the cohesive zone formulation applied at the medial interface are presented in Section 7.2 above. Results of parametric studies are presented in terms of the following key non-dimensional groupings: t/r , R/r_o , E_i/E_o .

Physiological loading conditions and boundary conditions: Each model is created using a structured mesh of 8-noded quadrilateral first-order elements. To uncover the role of anatomical loading a variety of loading modes are investigated: caudal, cranial, anterior, posterior, mediolateral, and torsion (shown in Figure 7.3(e)). In order to accurately describe the physiological loading regime, displacement boundary conditions are based on ImageJ analysis of cine-MRI cardiac-cycle data (Schindelin *et al.*, 2015). Figure 7.4 shows an illustration of image analysis process in image J. Caudal-cranial motion and anterior-posterior motion is measured throughout the cardiac cycle at evenly spaced intervals. Extracted displacement data is normalised as a function of sinotubular junction (STJ) diameter and applied to the dimensions of the parameterised model as has been reported previously (Kozerke, Markus B. Scheidegger, *et al.*, 1999).

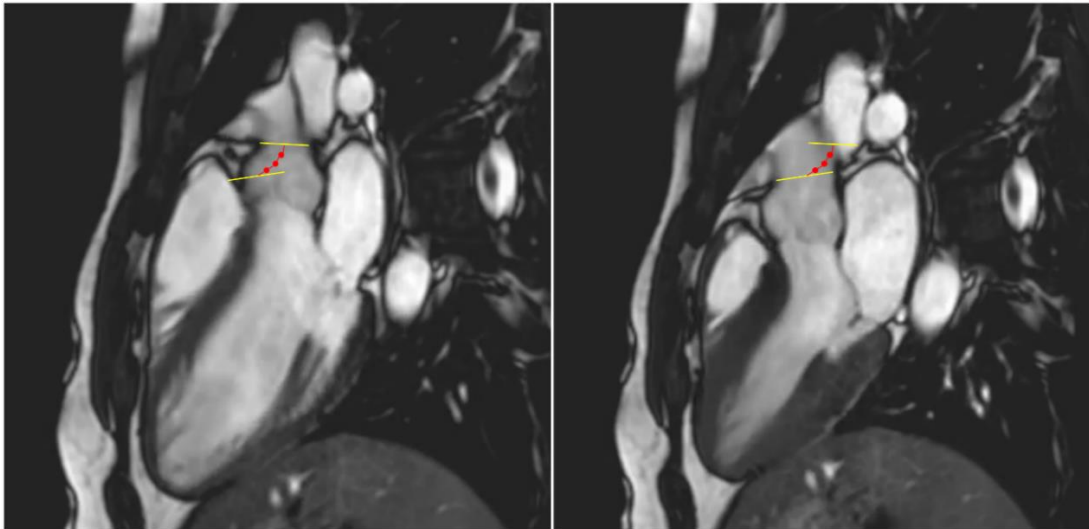


Figure 7.4. Cine MRI image analysis. Yellow lines are in the same position in both images, illustrating the displacement of the aortic root. Red lines and circles show an example of the path travelled by the aortic root.

Displacement boundary conditions are applied to the aortic root, while radial expansion due to applied lumen pressure is unconstrained. The aorta is constrained at the level of the mid-descending thoracic aorta, such that it remains planar with no axial displacement at this section (for $\bar{x} = 1.0, u_{zz} = 0 \forall \{\theta, \xi\}$), with only radial expansion and axial rotation being unconstrained at this section. In the case of applied loading due to cardiac movement, all transient displacements, rotations, and lumen pressures are applied at physiologically accurate magnitudes and time-scales.

Development of a new approach to implement residual stress in aorta wall: A novel methodology is developed to include spatially varying residual stress in the aorta. Aortic ring geometries are created to match the desired geometries of the aorta. An overview of the process is described in Figure 7.5. Opening angle (γ) of the human aorta has been described previously as a function of normalised aortic length (\bar{x}) (Sokolis *et al.*, 2017). Residual stress can be estimated in artery through reversing the stress-free open-angle configuration to a closed residually stressed position (shown in Figure 7.5(a)). We perform closing angle simulations for the range of measured

opening angles in the human aorta. The residual stress tensor is extracted as a function of radial coordinate (ξ) for each opening angle (local circumferential stress shown in Figure 7.5(a)). In order to apply the residual stress to the global aortic geometry, normalised aortic length (\bar{x}) and radial coordinate (ξ) are determined (Figure 7.5(b)). These dimensionless coordinates act as inputs to the residual stress tensor function (shown as the red lines in Figure 7.5(c)). The residual stress tensor is built using said inputs and transformed to the global coordinate system using the standard transformation shown in (d).

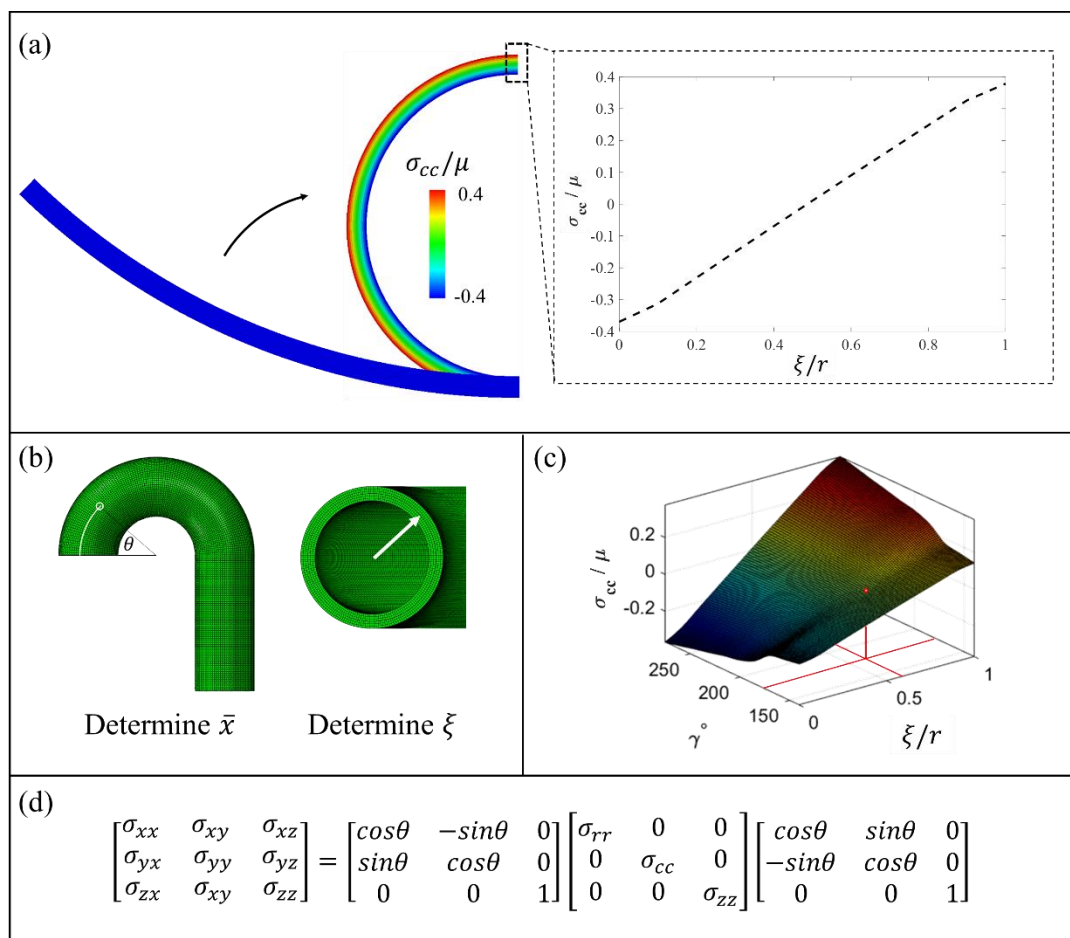


Figure 7.5. Overview of the residual stress methodology developed. (a) A series of opening-angle aortic ring geometries are closed and the local stress tensors are recorded as a function of radial coordinate (ξ); (b) For each integration point, the normalised aortic length (\bar{x}) is determined as well as the radial coordinate (ξ); γ (which corresponds to \bar{x}) and ξ are inputs to the residual stress function shown in (c); The local material residual stress tensor is then transformed into global coordinate (d).

Here we give a technical overview of the optimisation scheme: A MATLAB master function is developed which calls an objective function which calls and passes arguments to a python script. The python script opens the aortic ring model in Abaqus/CAE and updates the geometry, and any other model variables desired, based on the arguments from the objective function. The coordinates of the closed ring are imported using Matlab and the GIBBON toolbox to calculate the closed diameter and compare to the target diameter. Opening angle data of human aorta is evenly sampled at 10 points throughout the mean data-set for aortas aged over 60 years old (Sokolis *et al.*, 2017).

Finite element models of the open equilibrated configuration of the aortic rings are created using the opening angle and an initial guess at the curvature of the open configuration. The artery is modelled as a bilinear hyperelastic anisotropic fibre-reinforced material. Symmetry is assumed, as such, half the circumference is modelled. A methodology that allows for the closing of a ring from any specified initial opening angle is developed and implemented. The opened equilibrated state of the aortic specimen is closed, and the closed diameter is compared to the target diameter in an optimisation scheme. The initial guess at the curvature of the opened segment is updated iteratively until the solution converges. When convergence is achieved for the first opening angle, the process is repeated for the next opening angle in the loop. When the loop of opening angles is complete the master MATLAB function calls a Python post-processing script which loops through each output database of the converged closing simulations. A *user-defined material behaviour subroutine (UMAT)* is developed to construct a residual stress tensor for each element based on its normalised aortic length, and radial coordinate. The full process is

outlined in detail in the flowchart presented in Figure 7.6(a). The results of the closing angle simulations (Figure 7.6(b-c)) serve as input data to the user-defined subroutine.

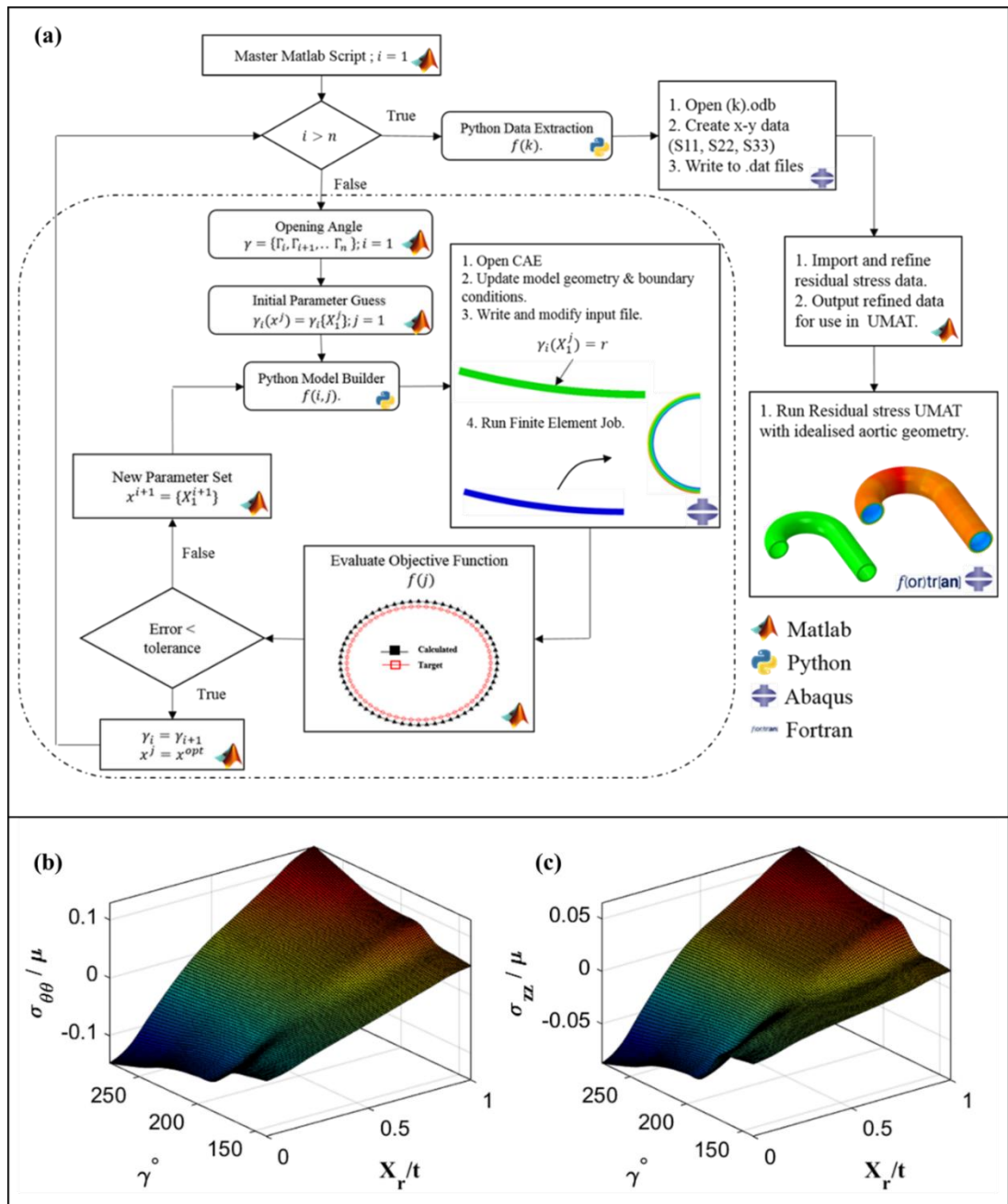


Figure 7.6. (a) Flowchart of the residual stress methodology; (b) circumferential stress as a function of opening angle γ and radial coordinate X_r/t ; (c) axial stress as a function of opening angle γ and radial coordinate X_r/t .

7.3.2 Results of parametric analysis of key factors in aorta shear tractions and dissection

Results of our parameteric investigation are presented in three sections: *Material factors*; *Physiological loading factors*; *Anatomical factors*. Despite the parameterised and idealised vessel geometry, it will be noted that the traction state in the vessel wall is quite complex, with significantly different patterns of traction being computed in the root region, the arch region and the descending thoracic aorta. We present a series of contour plots, in addition to traction distributions along several anatomical paths, in order to illustrate the key features of each parameteric investigation. Unless otherwise stated, the following idealised model parameters are implemented: $\frac{t}{r} =$

$$0.25, \frac{R}{r_0} = 3.0, \frac{E_i}{E_o} = 1.$$

7.3.2.1 The influence of aortic material parameters on interface traction distribution

Bi-layer stiffness mismatch: In cases of severe hypertension unequal stiffening of the layers of the media occurs through hypoxia of the outer media due to restriction of blood flow from the vasa vasorum (Angouras, 2000). Figure 7.7 shows that for an applied cranial displacement, calculated tractions are highest when the stiffness mismatch in the bi-layer interface is highest. For layers of equal stiffness the peak tractions occur at the start of the DTA, however, increase in stiffness mismatch results in peak tractions at the AR. This may bear clinical relevance as arteriosclerosis is associated with chronic hypertension, aging, diabetes, obesity, high cholesterol, and smoking (Mészáros *et al.*, 2000; Greenwald, 2007; Criado, 2011; Tsamis, Krawiec and Vorp, 2013). These findings suggest each of these risk factors (and any progenitor of arteriosclerosis) increase intramural tractions in the AR. While elevated intramural shear tractions contribute to the risk of dissection, in this case they are not sufficient to cause dissection.

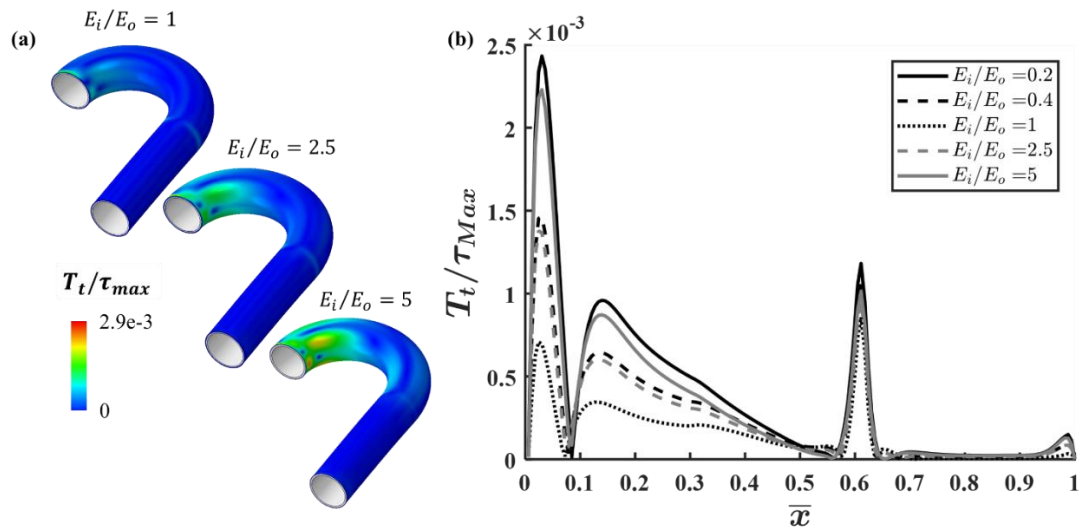


Figure 7.7. (a) T_t/τ_{max} contour plots for bi-layer stiffness mismatch for an applied cranial displacement $\bar{V}/R = 0.275$ and $t/r = 0.25$, $R/r_o = 3.0$; (b) T_t/τ_{max} vs \bar{x} for varying amounts of stiffness mismatch. Different parameter sets of E_i/E_o for a cranial displacement $\bar{V}/R = 0.275$ are investigated. $t/r = 0.25$, $R/r_o = 3.0$.

Residual stress: We next explore the influence of residual stress on AD risk. The opening angle of the human aorta has previously been measured and it has been shown that opening angle varies significantly as a function of aortic position (Sokolis *et al.*, 2017). The impact of such a heterogeneous residual stress state on AD risk has not been quantified previously. In Figure 7.8 we present the traction state of a residually stressed aorta and compare to a non-residually stressed aorta, both before and after the application of physiological loading conditions (systolic lumen pressure of 120 mmHg and cranial displacement of $\bar{V}/R \approx 0.2$). In the absence of physiological loading a highly heterogeneous distribution of residual circumferential stress is computed. However, the final stress state of the residually stressed aorta following the application of physiological loading is quite similar to that computed without the inclusion of residual stress. Essentially, heterogeneous residual stresses are approximately an order of magnitude lower than stresses generated by lumen pressure loading. The influence

of residual stress on AD risk is illustrated in Figure 7.8(b), showing computed shear traction along a path through the medial interface, both with and without inclusion of residual stress. While residual stress results in slight increases in peak tractions, computed values remain two orders of magnitude lower than the experimentally measured mode II interface strength (1.6 MPa).

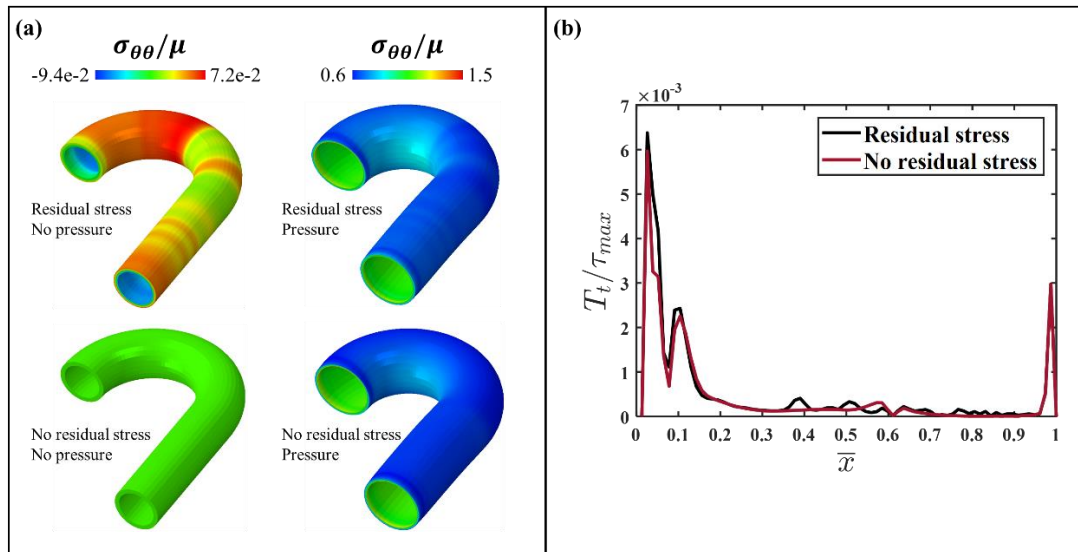


Figure 7.8. (a) Comparison of local circumferential stress distribution, both with and without inclusion of residual stress. Both zero applied loading and physiological applied loading (120 mmHg lumen pressure and $\bar{V}/R \approx 0.2$) are considered. (b) Computed shear traction along a path through the medial interface, both with and without inclusion of residual stress.

7.3.2.2 Influence of physiological and super-physiological loading on interface tractions

Here we examine the influence of a range of physiological boundary conditions on the AD risk. Although all of the loading modes listed in Figure 7.3(e) are examined, for brevity we focus on two predominant loading modes: cranial displacement and anterior displacement.

Anterior aortic root displacement: Figure 7.9(a) shows a series of contour plots demonstrating increasing traction with increasing applied anterior displacement at the

aortic root (\bar{V}/R). High traction concentrations are computed in the AR. Figure 7.9(b) shows shear traction as a function of \bar{x} for each recorded anterior displacement of the aortic root.

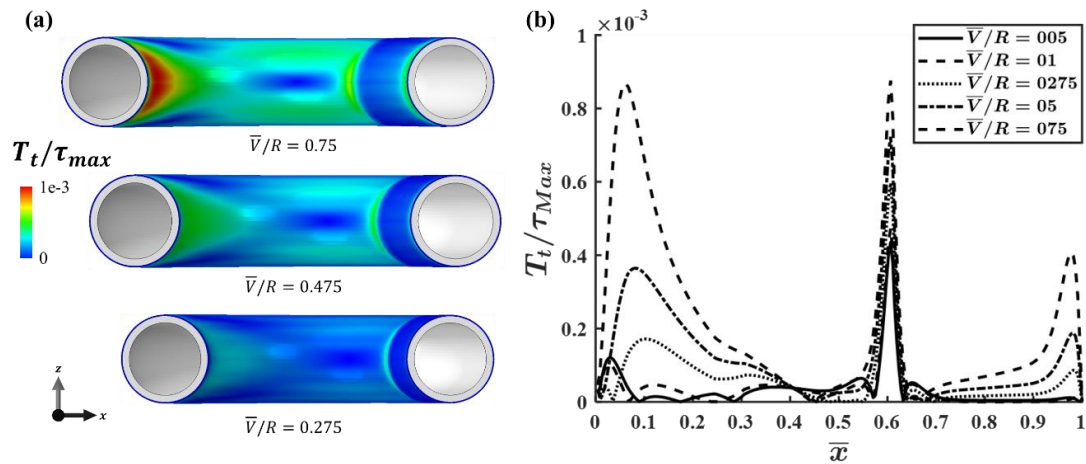


Figure 7.9. (a) T_t/τ_{Max} evolution with increasing anterior displacement (\bar{V}/R) and (b) T_t/τ_{Max} as a function of \bar{x} for an arch of $R/r_o = 3.0$, $t/r = 0.25$ for increasing anterior displacement.

Cranial aortic root displacement: As shown in Figure 7.10, simulations predict maximum tractions for highest values of cranial displacement. Average axial displacement of the aortic root has been observed to be $8.9 \pm 1.8\text{mm}$ (Kozerke, Markus B. Scheidegger, *et al.*, 1999), corresponding to $\bar{V}/R = 0.297 \pm 0.06$. Traction concentrations are computed in the AR, with similar concentrations computed at the start of the DTA. Increasing displacement has a near linear effect on the peak traction at $\bar{x} = 0.6$, whereas the effect in the AR is highly non-linear. The traction state in the DTA is insensitive to changes in displacement. This is not surprising as only 1.3% of AD are reported to initiate in the infrarenal aorta (Trimarchi *et al.*, 2007). These findings suggest that a possible reason for lower incidences of abdominal dissection may be the significantly lower intramural tractions present in the infrarenal aorta relative to the aortic arch.

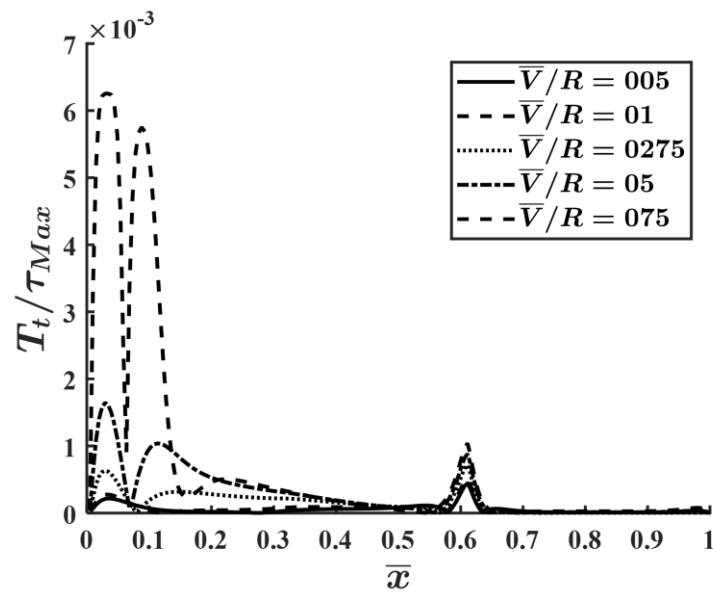


Figure 7.10: T_t/τ_{Max} on the inner curve vs. \bar{x} for the simulated range of values of cranial displacement ($\bar{V}_{CRANIAL}/R$) of an arch with parameters $R/r_o = 3.0, t/r = 0.25$.

Combined Caudal/Cranial, Anterior/Posterior displacement: Here we examine the influence of the full cardiac cycle on the risk of dissection. Figure 7.11(a) shows the contour plots of shear traction near the aortic root during key timepoints in the cardiac cycle where the tangential tractions are highest. As shown in Figure 7.11(a) at timepoint (a) (ventricular ejection) there is a small traction concentration near the aortic root on the inner curve and two larger concentrations in the centre of the arch ($\bar{x} = 0.3$) either side of the inner curve. Figure 7.11(b) reveals that, for timepoint (b) (maximum aortic systole), the peak shear stress tractions are increased in magnitude and area compared to the timepoint at which the aortic valve opens. This is the point in the cardiac cycle with the maximum calculated tractions.

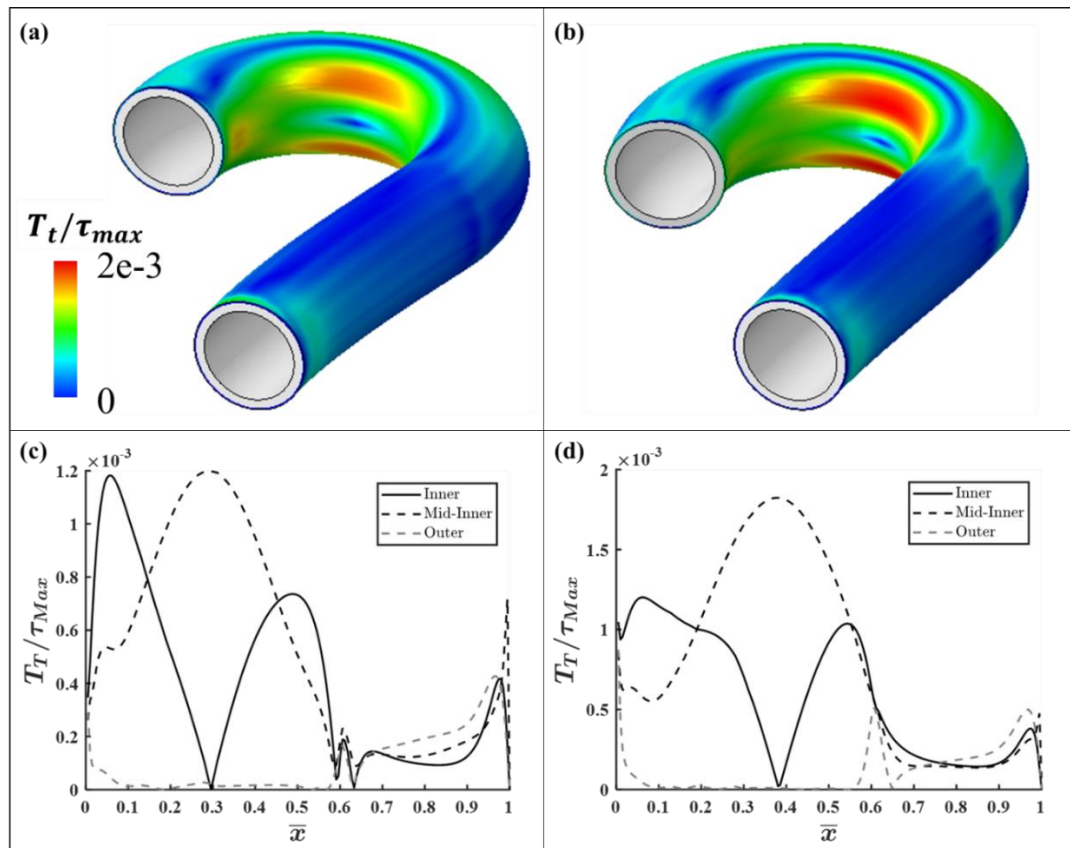


Figure 7.11. (a) T_t/τ_{Max} contour of the aortic arch during ventricular ejection with parameters $R/r_o = 3.0$, $t/r = 0.25$, $P_{Lumen} = 80mmHg$; (b) T_t/τ_{Max} contour of the aortic arch during max aortic systole ($P_{Lumen} = 120mmHg$); (c) T_t/τ_{Max} as a function of \bar{x} for simulation presented in (a) along the Inner, Outer and Mid-Inner curves ($\theta = \pi, \theta = 0, \theta = \pi/4$ respectively); (d) T_t/τ_{Max} as a function of \bar{x} for simulation presented in (b) along the Inner, Outer and Mid-Inner curves.

In Figure 7.12 we present a summary and comparison of the effect of each loading mode on AD risk in terms of computed shear traction (T_t/τ_{max}). A luminal pressure of 200 mmHg causes a peak in shear traction greater than any loading mode other than cranial displacement. Pressure loading does not result in traction concentrations in the AR but does in the DTA. Cranial causes the highest tractions, mainly in the AR. It can be seen from this figure that the stress state in the aorta is highly complex and that all physiological loading modes do not result in tractions that approach τ_{max} . The effects of disease on aortic root displacement has not been investigated in great detail in the literature, however one study has noted decreased axial displacement (caudal/cranial)

as a result of aortic valve regurgitation which in theory should reduce intramural traction (Kozerke, Markus B Scheidegger, *et al.*, 1999). The findings of this study, however, suggest that aortic root motion, both physiological and pathophysiological, does not produce sufficient traction to result in initiation of dissection.

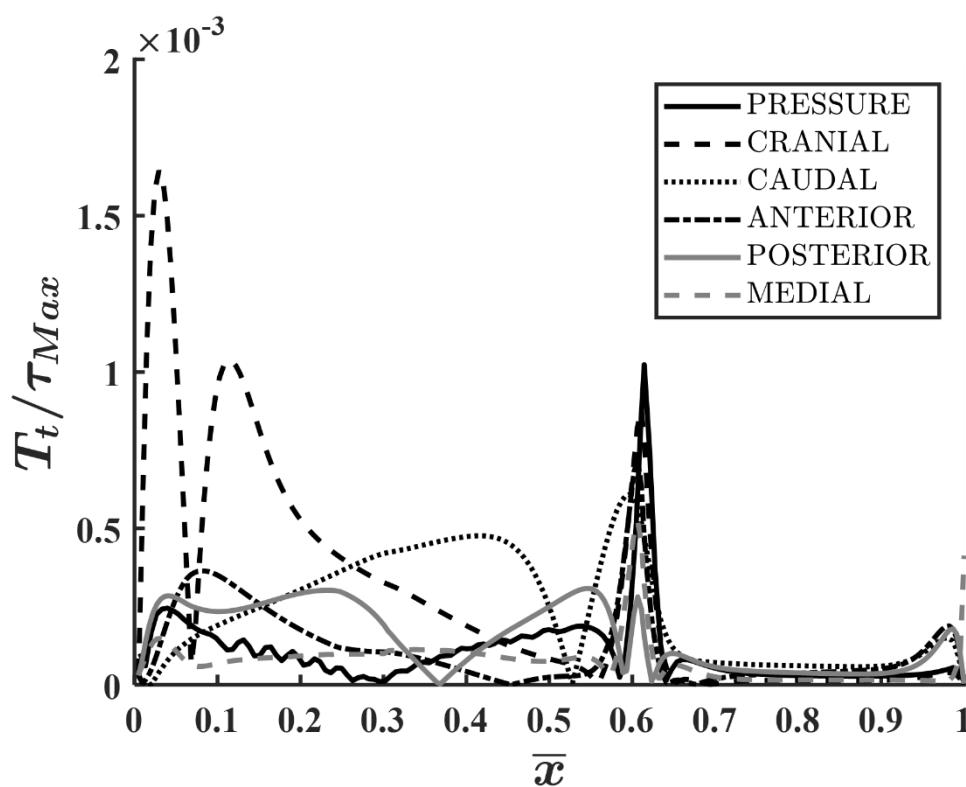


Figure 7.12: T_t/τ_{Max} as a function of \bar{x} along the inner path for an arch of $R/r = 0.3$, $t/r = 0.25$ for a displacement equal to $\bar{V}/R = 0.5$ for each loading mode, also included is a lumen pressure of 200mHg with no aortic root displacement.

7.3.2.3 Influence of geometric anatomical factors on interface tractions

Wall thickness: Increased wall thickness is a known result of chronic hypertension (Olivetti *et al.*, 1982; Owens, Rabinovitch and Schwartz, 2006) and also a known symptom of giant cell temporal arteritis (Corbett and Melms, 2003). Both, chronic

hypertension and giant cell arteritis are known risk factors of AD (Evans, O’Fallon and Hunder, 1995; Hagan *et al.*, 2000). These risk factors may be linked through some underlying mechanical basis, which we explore in Figure 7.13. The influence of aortic wall thickness on the shear traction in the inner and outer curve of the vessel is investigated by applying cranial displacement at the root of the arch. As shown in Figure 7.13, a higher value of wall thickness results in higher shear traction. The traction along the inner curve of the arch varies significantly, depending on the wall thickness. Peak tractions occurs along the inner curve at the centre of the arch ($\bar{x} \approx 0.3$) reaching a value of $T_t/\tau_{Max} = 7.5e-4$ when $t/r = 1$. The location of peak tractions aligns with the clinical observation that approximately two thirds of ADs occur in the ascending aorta and aortic arch (when $0.0 \leq \bar{x} \leq 0.6$) (Hagan *et al.*, 2000; Criado, 2011; Evangelista *et al.*, 2018). Additional traction localizations are computed at $\bar{x} = 0.6$ at the start of the DTA. Traction is near-zero in the DTA ($\bar{x} > 0.7$) regardless of wall thickness. Contour plots of shear traction distributions throughout the medial interface are shown in Figure 7.13(b) and Figure 7.13(c). Only half-wall thickness shown in order to expose the medial interface.

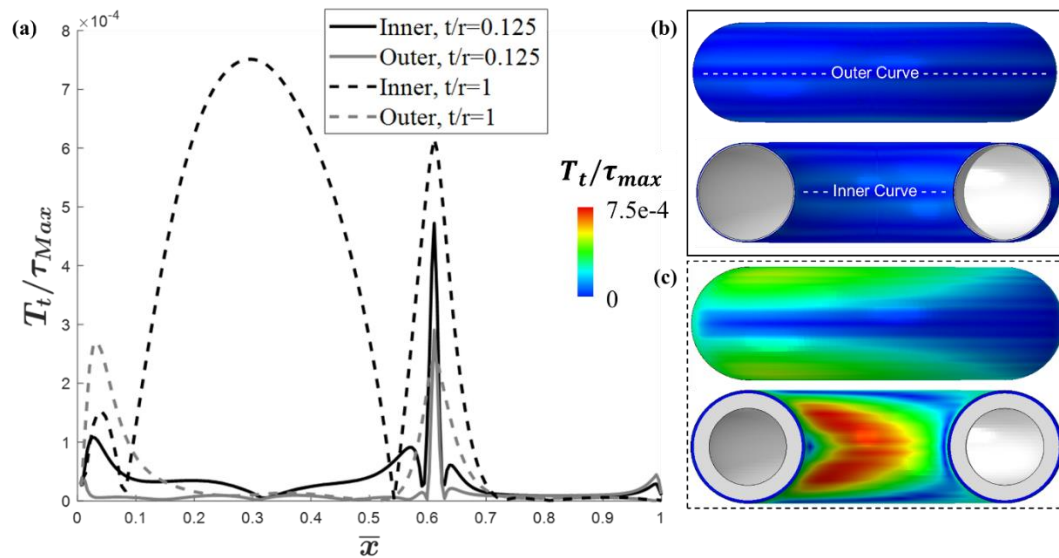


Figure 7.13. (a) Normalised shear traction (T_t/τ_{max}) as a function of normalised aortic length (\bar{x}) for an applied cranial displacement at the aortic root ($\bar{V}_{cranial}/R = 0.05$) for $t/r = 1$ and $t/r = 0.125$. Path data is taken from the Inner and outer curves. The contour plots (b) and (c) show the distribution of (T_t/τ_{Max}) on the interface for $t/r = 0.125$ and $t/r = 1$, respectively.

These findings suggest that wall thickness significantly influences the traction state in the aorta. However, even for extremely thick vessel walls computed tractions are significantly lower than the mode II strength of the aorta. As an example, even if the wall thickness is the same as the wall thickness in a severe case of giant cell temporal arteritis (Koster, Matteson and Warrington, 2018) ($t/r = 1$) and an applied physiological displacement results in tractions 1000 times smaller than the mode II strength of a healthy artery. Therefore, an increase in wall thickness alone, without a corresponding reduction in fracture strength will not result in spontaneous AD.

Arch radius: An increase in aortic arch radius occurs naturally with age. Similarly, an increase in aortic length occurs with age (Redheuil *et al.*, 2011). The influence of these anatomical changes on the AD risk has previously been investigated. As shown in Figure 7.14, a lower arch radius results in a higher traction at the medial interface.

Maximum tractions are computed in the configuration with the lowest arch radius ($R/r_o = 1.25$) with significant peaks predicted in the centre of the arch and at the DTA. Figure 7.14(b) shows the magnitude of the shear traction for each configuration of arch radius along the inner path of the aorta for an anterior displacement $\bar{V} = 0.15r_o$. Peak tractions are predicted in the centre of the arch along the inner curve.

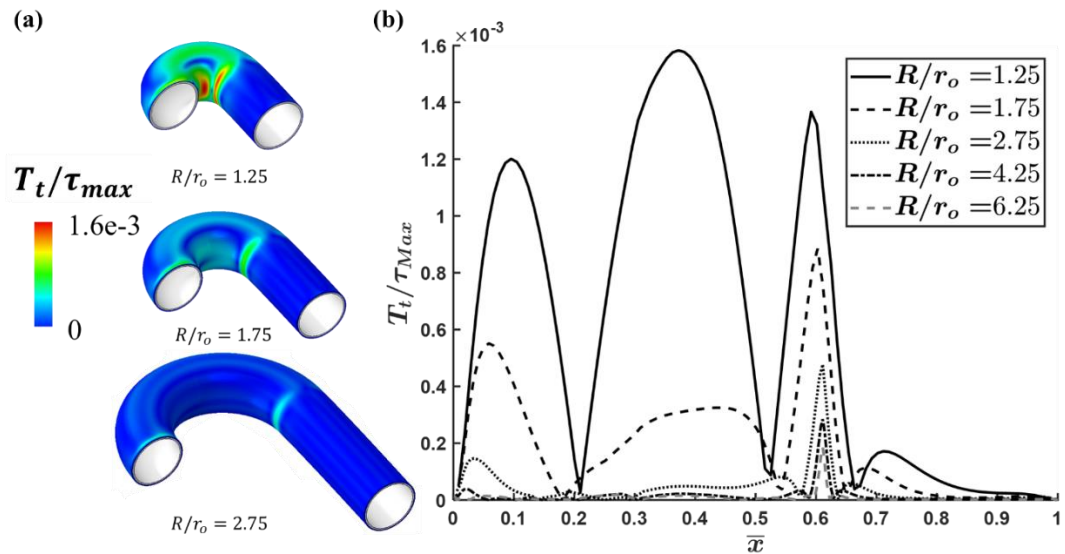


Figure 7.14. (a) Contour plot of normalised shear traction (T_t/τ_{Max}) for arch radius configurations $R/r_o = 1.25$, $R/r_o = 1.75$, and $R/r_o = 2.75$ for an applied anterior displacement $\bar{V} = 0.15r_o$; (b) T_t/τ_{Max} along the inner curve as a function of \bar{x} for each configuration of R/r_o where $t/r = 0.25$.

A known implication of the increase in radius of the aortic arch with age is a reduced risk of aortic transection following rapid deceleration (as typically experienced in road traffic accidents) (Azizzadeh *et al.*, 2009). The primary cause of transection in younger patients is generally purported to be due to the restraint (and consequent stress concentration) of the ligamentum arteriosum at the aortic isthmus (Benjamin and Roberts, 2012). The analyses presented in the current study suggest a secondary cause: the younger aorta, with a lower arch radius, is more prone to intramural delamination in blunt trauma due to higher interface tractions. Specifically, as shown in Figure 7.14, for the case of a low arch radius ($R/r_o = 1.25$) peak tractions of $T_t/\tau_{max} = 1.6 \times 10^{-3}$ occur in the aortic arch at $\bar{x} = 0.1$ and $\bar{x} = 0.4$. The current analysis suggests that the

increase of the radius of the aortic arch as part vessel remodelling with increasing age leads to a reduction in shear tractions along the medial interface, with a consequent reduction in AD risk. However, it should be noted age related pathophysiological remodelling of the vessel also entails an increase in vessel stiffness [9] and thickness [48], and both effects have been shown (Figure 7.7 and Figure 7.13, respectively) to increase shear tractions and AD risk.

Finally, and most importantly, it should be noted that even for the smallest arch radius simulated in Figure 7.14, the computed shear tractions along the medial interface are 3 orders of magnitude lower than the mode II strength of healthy tissue.

Branch vessels: In order to investigate the role of ostia and branching vessels, idealised geometries containing supra-aortic vessels are also created using the GIBBON toolbox in MATLAB (M Moerman, 2018b). The supra-aortic vessels represent the brachiocephalic, the left common carotid, and the left subclavian arteries (seen in Figure 7.15(a)). Figure 7.15 shows the effect of branching vessels on the shear traction distribution in the aortic arch under a luminal pressure load of 120mmHg. Significant traction concentrations are computed at the ostia of the brachiocephalic, the left common carotid, and the left subclavian arteries. The presence of supra-aortic vessels significantly increases the tractions in the arch. However, these tractions are approximately two orders of magnitude lower than the mode II fracture strength of healthy tissue and as such are insufficient to cause dissection.

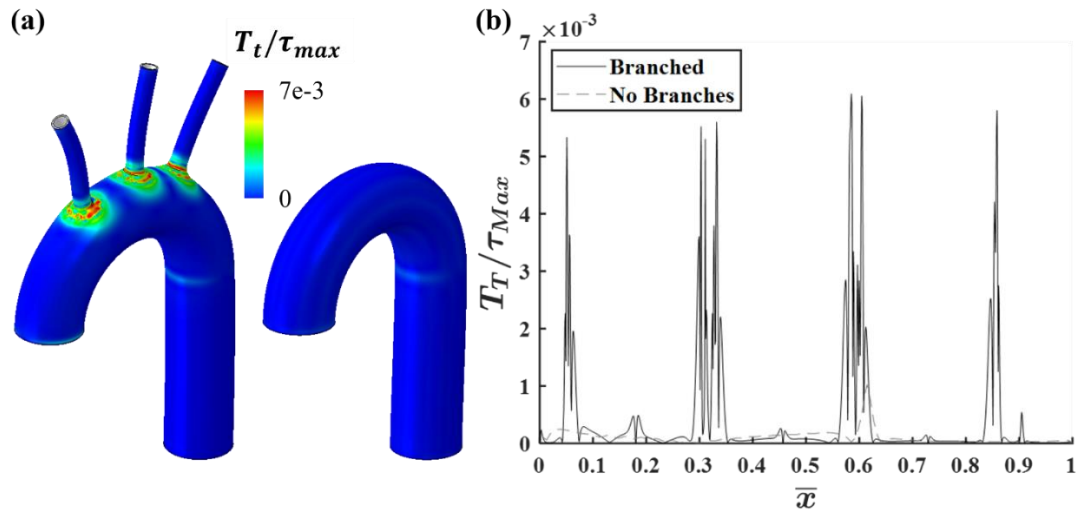


Figure 7.15. (a) Contour plot showing T_t/τ_{Max} of the aortic arch with and without supra-aortic branches for lumen pressurisation to 120mmHg; (b) T_t/τ_{max} vs \bar{x} along the outer curve of the aorta ($R/r = 3.0, t/r = 0.25$) with and without branches.

7.3.2.4 Will a dissection propagate a long distance if interface strength is reduced?

In order to further examine the conditions for spontaneous AD initiation and crack propagation, a series of simulations are performed using reduced values of mode II fracture strength along the medial interface, shown in Figure 7.16. Specifically, interface strengths that are 100, 1000, and 10000 times lower than the healthy value of $\tau_{exp}=1.6$ MPa are implemented. In all cases a physiological lumen pressure of 120 mmHg is applied and physiological ($\bar{V}/R = 0.5$) and super-physiological ($\bar{V}/R = 0.75$) cranial displacement are applied. Predicted regions of interface delamination are shown in Figure 7.16(a). In the case of a 100-fold reduction in fracture strength localised dissection is predicted at the AR only for the case of super-physiological cranial displacement. A 10000-fold reduction in interface strength must be implemented in order to computed extensive delamination throughout the entire region of the aortic arch. Simulations performed using the VP-CZM from Chapter 6 require a similar level of reduction in interface strength to predict corresponding patterns of dissection

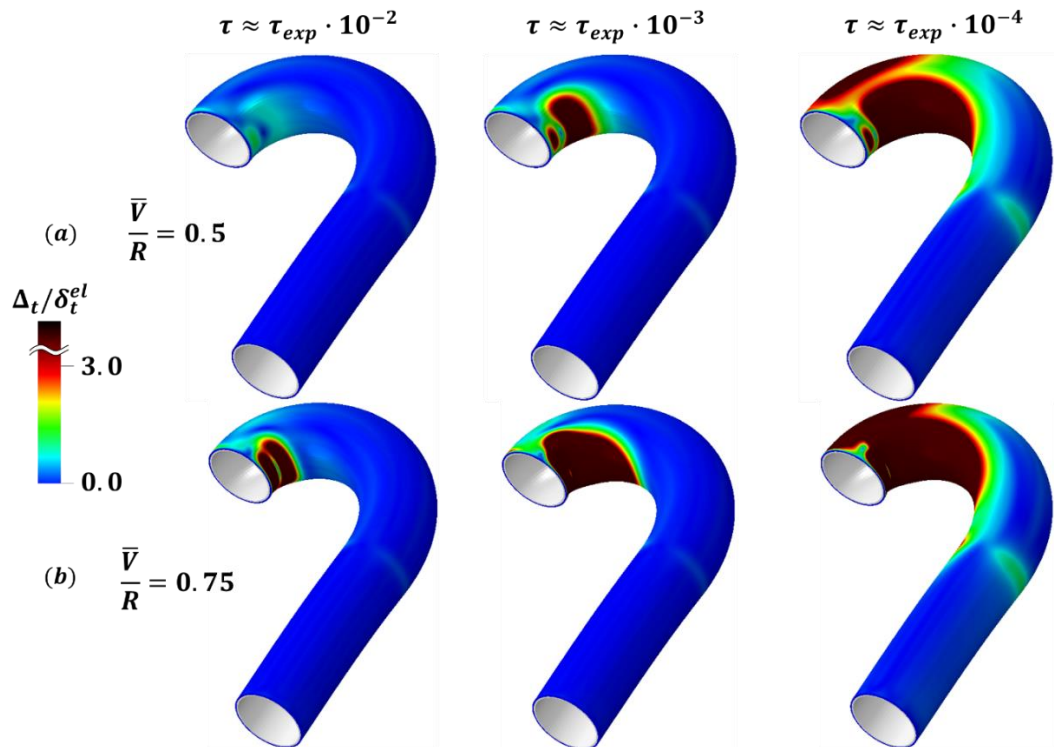


Figure 7.16. Computed regions of delamination (red + black contours) computed for three interface strengths, all of which are significantly (100,1000,10000 times) lower than the experimentally measured interface strength of a healthy intact aorta (τ_{exp}). A computed interface separation of $\Delta_t/\delta_t^{el} \geq 3$ indicates full damaged delamination. A physiological lumen pressure of 120 mmHg and a cranial displacement of the arch ($R/r = 3.0, t/r = 0.25$) are applied. (a) Interface delamination for a cranial displacement of $\bar{V}/R = 0.5$; (b) interface delamination for a cranial displacement of $\bar{V}/R = 0.75$.

7.4 Concluding remarks

Parametric investigations reveal that shear tractions along the medial interface are increased by the following factors: Increased stiffness mismatch in the vessel wall due to hypoxic stiffening of the outer media; increased wall thickness; decreased arch radius. Simulations also suggest that residual stress (as characterised by the vessel opening angle) does not significantly increase shear tractions along the medial interface. Significant concentrations of shear traction are computed near to branching vessels. Cranial movement of the AR during the cardiac cycle leads to higher values of tangential traction in comparison to anterior and caudal movements. However,

while all of the aforementioned parameters will result in increased interface tractions, it should be noted that even extreme pathophysiological loading, or pathological anatomical remodelling is shown to result in elevated shear tractions that are at least two orders of magnitude lower than the experimentally measured mode II shear strength of healthy aortic tissue. Simulations suggest that a 100-fold decrease in shear fracture strength is required to result in spontaneous dissection initiation at the AR, without extensive propagation. In order to simulate extensive propagation of a dissection throughout the arch (as reported clinically (Hagan *et al.*, 2000)) our simulations suggest that the mode II strength of the aorta must be reduced by a factor of 10^{-4} . This suggests that a significant phase change of the aortic tissue occurs prior to AD.

Pre-existing luminal injury or damage in the form of an intraluminal tear is not considered in the present study, nor is a pre-existing dissection with a patent false lumen. These are the subject of ongoing investigation and will be presented in a follow-on study.

7.5 Appendix A: Mesh Convergence

Here we present the mesh convergence study for the parameter study model. Convergence is achieved for the mesh with $\approx 93,000$ elements. All simulations are performed for these number of elements.

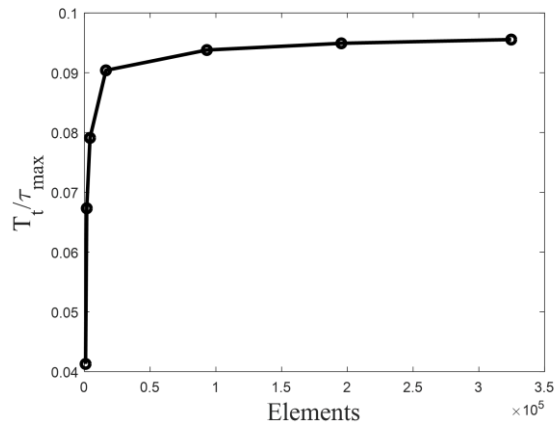


Figure 7.17: Variation of the normalised shear traction at $\bar{x} = 0.6$ verses the number of elements in the mesh.

Bibliography

- Abraham, P. A. et al. (1982) 'Marfan syndrome. Demonstration of abnormal elastin in aorta', *Journal of Clinical Investigation. American Society for Clinical Investigation*, 70(6), pp. 1245–1252. doi: 10.1172/JCI110723.
- Angouras, D. (2000) 'Effect of impaired vasa vasorum flow on the structure and mechanics of the thoracic aorta: implications for the pathogenesis of aortic dissection', *European Journal of Cardio-Thoracic Surgery*, 17(4), pp. 468–473. doi: 10.1016/S1010-7940(00)00382-1.
- Arribas, S. M., Hinek, A. and González, M. C. (2006) 'Elastic fibres and vascular structure in hypertension', *Pharmacology and Therapeutics*, 111(3), pp. 771–791. doi: 10.1016/j.pharmthera.2005.12.003.
- Azizzadeh, A. et al. (2009) 'Blunt traumatic aortic injury: Initial experience with endovascular repair', *Journal of Vascular Surgery. Mosby*, 49(6), pp. 1403–1408. doi: 10.1016/j.jvs.2009.02.234.
- Beller, C. J. et al. (2004) 'Role of Aortic Root Motion in the Pathogenesis of Aortic Dissection', *Circulation. American Heart Association, Inc.*, 109(6), pp. 763–769. doi: 10.1161/01.CIR.0000112569.27151.F7.
- Beller, C. J. et al. (2009) 'Finite element modeling of the thoracic aorta: including aortic root motion to evaluate the risk of aortic dissection', *Journal of Medical Engineering & Technology. Taylor & Francis*. Available at: <http://www.tandfonline.com/doi/abs/10.1080/03091900600687672> (Accessed: 14 January 2016).
- Benjamin, M. M. and Roberts, W. C. (2012) 'Fatal aortic rupture from nonpenetrating chest trauma.', *Proceedings (Baylor University. Medical Center). Baylor University Medical Center*, 25(2), pp. 121–3. doi: 10.1080/08998280.2012.11928805.
- Brandt, T. et al. (2001) 'Pathogenesis of cervical artery dissections: Association with connective tissue abnormalities', *Neurology. Wolters Kluwer Health, Inc. on behalf of the American Academy of Neurology*, 57(1), pp. 24–30. doi: 10.1212/WNL.57.1.24.
- Carlson, R. G., Lillehei, C. W. and Edwards, J. E. (1970) 'Cystic medial necrosis of the ascending aorta in relation to age and hypertension', *The American Journal of Cardiology. Elsevier*, 25(4), pp. 411–415. doi: 10.1016/0002-9149(70)90006-8.
- Clough, R. E. and Nienaber, C. A. (2015) 'Management of acute aortic syndrome.', *Nature reviews. Cardiology. Nature Publishing Group, a division of Macmillan Publishers Limited. All Rights Reserved.*, 12(2), pp. 103–14. doi: 10.1038/nrcardio.2014.203.
- Concannon, J. et al. (2020) 'Quantification of the regional bioarchitecture in the human aorta', *Journal of Anatomy. John Wiley & Sons, Ltd*, 236(1), pp. 142–155. doi: 10.1111/joa.13076.
- Concannon, J. et al. (no date) 'Development of an MRI/FEA framework for Analysis of Subject-Specific Aortic Compliance: Part I - Development of a dual-VENC 4D

- Flow MRI Protocol for Measurement of Heterogeneous non-linear vessel Deformation'. engrXiv. doi: 10.31224/OSF.IO/SPZGD.
- Corbett, J. J. and Melms, A. (2003) 'Giant Cell Arteritis and Polymyalgia Rheumatica', in *Neurological Disorders: Course and Treatment: Second Edition*. NIH Public Access, pp. 475–479. doi: 10.1016/B978-012125831-3/50234-3.
- Criado, F. J. (2011) 'Aortic dissection: a 250-year perspective.', *Texas Heart Institute journal / from the Texas Heart Institute of St. Luke's Episcopal Hospital, Texas Children's Hospital*, 38(6), pp. 694–700. Available at: <http://www.pubmedcentral.nih.gov/articlerender.fcgi?artid=3233335&tool=pmcentre&rendertype=abstract> (Accessed: 5 January 2016).
- Emmott, A. et al. (2016) 'Biomechanics of the Ascending Thoracic Aorta: A Clinical Perspective on Engineering Data.', *The Canadian journal of cardiology*, 32(1), pp. 35–47. doi: 10.1016/j.cjca.2015.10.015.
- Erbel, R. and Eggebrecht, H. (2006) 'Aortic dimensions and the risk of dissection.', *Heart (British Cardiac Society)*, 92(1), pp. 137–42. doi: 10.1136/hrt.2004.055111.
- Evangelista, A. et al. (2018) 'Insights from the international registry of acute aortic dissection: A 20-year experience of collaborative clinical research', *Circulation*. Lippincott Williams & Wilkins Hagerstown, MD, pp. 1846–1860. doi: 10.1161/CIRCULATIONAHA.117.031264.
- Evans, J. M., O'Fallon, W. M. and Hunder, G. G. (1995) 'Increased incidence of aortic aneurysm and dissection in giant cell (temporal) arteritis: A population-based study', *Annals of Internal Medicine*. American College of Physicians, 122(7), pp. 502–507. doi: 10.7326/0003-4819-122-7-199504010-00004.
- Fereidoonzehad, B., O'Connor, C. and McGarry, P. (2020) 'A new anisotropic soft tissue model for elimination of unphysical auxetic behaviour', *Journal of Biomechanics*. engrXiv. doi: 10.31224/OSF.IO/G6DSE.
- FitzGibbon, B. and McGarry, P. (2020) 'Development of a novel test method to investigate mode II fracture and dissection of arteries'. engrXiv. doi: 10.31224/OSF.IO/D3JBR.
- Fuster, V. et al. (2007) *Hurst's the heart*. McGraw Hill Professional.
- Gasser, T. C. and Holzapfel, G. A. (2006) 'Modeling the propagation of arterial dissection', *European Journal of Mechanics, A/Solids*, 25(4), pp. 617–633. doi: 10.1016/j.euromechsol.2006.05.004.
- Greenwald, S. E. (2007) 'Ageing of the conduit arteries', *Journal of Pathology*. John Wiley & Sons, Ltd., pp. 157–172. doi: 10.1002/path.2101.
- Hagan, P. G. et al. (2000) 'The International Registry of Acute Aortic Dissection (IRAD)', *The Journal of American Medical Association*. American Medical Association, 283(7), pp. 897–903. doi: 10.1001/jama.283.7.897.
- Heistad, D. D. et al. (1978) 'Regulation of blood flow to the aortic media in dogs', *Journal of Clinical Investigation*. American Society for Clinical Investigation, 62(1), pp. 133–140. doi: 10.1172/JCI109097.

- Henrichs, K. J. et al. (1980) 'Is arterial media hypertrophy in spontaneously hypertensive rats a consequence of or a cause for hypertension?', *Clinical Science*, 59 Suppl 6, pp. 331s-333s. Available at: <http://www.ncbi.nlm.nih.gov/pubmed/7449279> (Accessed: 21 June 2017).
- Komiyama, M. et al. (2001) 'High Incidence of Arterial Dissection Associated With Left Vertebral Artery of Aortic Origin.', *Neurologia medico-chirurgica. The Japan Neurosurgical Society*, 41(1), pp. 8–12. doi: 10.2176/nmc.41.8.
- Koster, M. J., Matteson, E. L. and Warrington, K. J. (2018) 'Large-vessel giant cell arteritis: diagnosis, monitoring and management', *Rheumatology. Narnia*, 57(suppl_2), pp. ii32–ii42. doi: 10.1093/rheumatology/kex424.
- Kozerke, S., Scheidegger, Markus B., et al. (1999) 'Heart motion adapted cine phase-contrast flow measurements through the aortic valve', *Magnetic Resonance in Medicine. John Wiley & Sons, Ltd*, 42(5), pp. 970–978. doi: 10.1002/(SICI)1522-2594(199911)42:5<970::AID-MRM18>3.0.CO;2-I.
- Kozerke, S., Scheidegger, Markus B, et al. (1999) 'Heart motion adapted cine phase-contrast flow measurements through the aortic valve', *Magnetic Resonance in Medicine*, 42(5), pp. 970–978. doi: 10.1002/(SICI)1522-2594(199911)42:5<970::AID-MRM18>3.0.CO;2-I.
- Laurent, S. and Boutouyrie, P. (2015) 'The Structural Factor of Hypertension: Large and Small Artery Alterations', *Circulation Research. American Heart Association, Inc.*, pp. 1007–1021. doi: 10.1161/CIRCRESAHA.116.303596.
- Laurent, S., Boutouyrie, P. and Lacolley, P. (2005) 'Structural and genetic bases of arterial stiffness', *Hypertension. American Heart Association, Inc.*, pp. 1050–1055. doi: 10.1161/01.HYP.0000164580.39991.3d.
- Lemaire, S. A. and Russell, L. (2011) 'Epidemiology of thoracic aortic dissection', *Nature Reviews Cardiology*, pp. 103–113. doi: 10.1038/nrcardio.2010.187.
- Lentini, S. et al. (2008) 'Type A aortic dissection involving the carotid arteries: carotid stenting during open aortic arch surgery', *Interactive CardioVascular and Thoracic Surgery. Oxford University Press (OUP)*, 8(1), pp. 157–159. doi: 10.1510/icvts.2008.186023.
- M Moerman, K. (2018a) 'GIBBON: The Geometry and Image-Based Bioengineering add-On', *The Journal of Open Source Software*, 3(22), p. 506. doi: 10.21105/joss.00506.
- M Moerman, K. (2018b) 'GIBBON: The Geometry and Image-Based Bioengineering add-On', *The Journal of Open Source Software*, 3(22), p. 506. doi: 10.21105/joss.00506.
- Marcus, M. L. (1985) 'Effects of chronic hypertension on vasa vasorum in the thoracic aorta', *Cardiovascular Research. Oxford University Press*, 19(12), pp. 777–781. doi: 10.1093/cvr/19.12.777.
- Matsumoto, T. and Hayashi, K. (1996) 'Stress and strain distribution in hypertensive and normotensive rat aorta considering residual strain', *J Biomech Eng. American Society of Mechanical Engineers*, 118(1), pp. 62–73. doi: 10.1115/1.2795947.

- Mészáros, I. et al. (2000) 'Epidemiology and clinicopathology of aortic dissection: A population- based longitudinal study over 27 years', *Chest*. Elsevier, 117(5), pp. 1271–1278. doi: 10.1378/chest.117.5.1271.
- Murai, T. et al. (2001) 'Sudden death due to cardiovascular disorders: a review of the studies on the medico-legal cases in Tokyo', *The Keio Journal of Medicine*, 50(3), pp. 175–181. doi: 10.2302/kjm.50.175.
- Nakashima, Y., Shiokawa, Y. and Sueishi, K. (1990) 'Alterations of elastic architecture in human aortic dissecting aneurysm.', *Laboratory investigation; a journal of technical methods and pathology*, 62(6), pp. 751–60. Available at: <http://www.ncbi.nlm.nih.gov/pubmed/2359259> (Accessed: 2 February 2018).
- Olivetti, G. et al. (1982) 'Quantitative structural changes of the rat thoracic aorta in early spontaneous hypertension. Tissue composition, and hypertrophy and hyperplasia of smooth muscle cells', *Circulation Research*. American Heart Association, Inc., 51(1), pp. 19–26. doi: 10.1161/01.RES.51.1.19.
- Owens, G. K., Rabinovitch, P. S. and Schwartz, S. M. (2006) 'Smooth muscle cell hypertrophy versus hyperplasia in hypertension.', *Proceedings of the National Academy of Sciences*. National Academy of Sciences, 78(12), pp. 7759–7763. doi: 10.1073/pnas.78.12.7759.
- Redheuil, A. et al. (2011) 'Age-Related Changes in Aortic Arch Geometry', *Journal of the American College of Cardiology*. NIH Public Access, 58(12), pp. 1262–1270. doi: 10.1016/j.jacc.2011.06.012.
- Rorive, G. L. and Carlier, P. G. (1983) 'Hypertension and the arterial wall.', *Acta Clinica Belgica*, 38(6), pp. 353–359. Available at: <http://www.ncbi.nlm.nih.gov/pubmed/7036052> (Accessed: 21 June 2017).
- Schindelin, J. et al. (2015) 'The ImageJ ecosystem: An open platform for biomedical image analysis', *Molecular Reproduction and Development*, 82(7–8), pp. 518–529. doi: 10.1002/mrd.22489.
- Sokolis, D. P. et al. (2017) 'Regional distribution of circumferential residual strains in the human aorta according to age and gender', *Journal of the Mechanical Behavior of Biomedical Materials*. Elsevier, 67, pp. 87–100. doi: 10.1016/j.jmbbm.2016.12.003.
- Stefanadis, C. et al. (1995) 'Effect of Vasa Vasorum Flow on Structure and Function of the Aorta in Experimental Animals', *Circulation*, 91(10).
- Tam, A. S., Sapp, M. C. and Roach, M. R. (1998) 'The effect of tear depth on the propagation of aortic dissections in isolated porcine thoracic aorta.', *Journal of biomechanics*, 31(7), pp. 673–6. Available at: <http://www.ncbi.nlm.nih.gov/pubmed/9796691> (Accessed: 18 July 2019).
- Trimarchi, S. et al. (2007) 'Acute abdominal aortic dissection: Insight from the International Registry of Acute Aortic Dissection (IRAD)', *Journal of Vascular Surgery*. Mosby, 46(5), pp. 913-919.e1. doi: 10.1016/J.JVS.2007.07.030.
- Tsamis, A., Krawiec, J. T. and Vorp, D. A. (2013) 'Elastin and collagen fibre microstructure of the human aorta in ageing and disease: a review.', *Journal of the*

Royal Society, *Interface / the Royal Society*, 10(83), p. 20121004. doi: 10.1098/rsif.2012.1004.

Ulbricht, D. et al. (2004) 'Cervical artery dissection: An atypical presentation with Ehlers-Danlos-like collagen pathology?', *Neurology*. Wolters Kluwer Health, Inc. on behalf of the American Academy of Neurology, 63(9), pp. 1708–1710. doi: 10.1212/01.WNL.0000142970.09454.30.

Wang, D. S. and Dake, M. D. (2006) 'Endovascular therapy for aortic dissection', in *Thoracic Aortic Diseases*. Springer Berlin Heidelberg, pp. 189–198. doi: 10.1007/3-540-38309-3_19.

Yoshida, K. and Tobe, S. (2005) 'Dissection and rupture of the left subclavian artery presenting as hemothorax in a patient with von Recklinghausen's disease', *Japanese Journal of Thoracic and Cardiovascular Surgery*. Japanese Association for Thoracic Surgery, 53(2), pp. 117–119. doi: 10.1007/s11748-005-0014-x.

Yuan, S.-M. and Jing, H. (2011) 'Cystic medial necrosis: pathological findings and clinical implications', *Revista Brasileira de Cirurgia Cardiovascular*. *Revista Brasileira de Cirurgia Cardiovascular*, 26(1), pp. 107–115. doi: 10.1590/S0102-76382011000100019.

Chapter 8

8 A NUMERICAL INVESTIGATION OF THE PROPAGATION OF DISSECTION

8.1 Introduction

The progression and pathogenesis of aortic dissection (AD) is relatively poorly understood compared to other cardiovascular diseases (Vilacosta *et al.*, 2010; Criado, 2011). For example, several clinical studies suggest that AD occurs as a result of initial damage to the intima, with such damage referred to in clinical literature as an “intimal tear” or “entry tear” (Larson and Edwards, 1984; Criado, 2011; Lemaire and Russell, 2011; Kim *et al.*, 2014). However, a number of clinical studies report AD without an intimal tear (Lui, Menkis and McKenzie, 1992; Eichelberger, 1994; Utoh *et al.*, 1997; Colli *et al.*, 2018). Conversely, an intimal tear may present without extensive AD, indicating early arrest of tear propagation (Svensson *et al.*, 1999). AD is typically characterised in the clinical literature as the occurrence of a true and false lumen separated by an intraluminal septum (Hasleton and Leonard, 1979; Sayer *et al.*, 2008; Nienaber *et al.*, 2010; Huang *et al.*, 2015). The end point of the false lumen is typically used to indicate the extent of the AD, which may be as short as 1 cm from the original entry tear (Svensson *et al.*, 1999) or as long as the entire aorta and iliac vessels (>1 m) (Dotter, Roberts and Steinberg, no date; Hagan *et al.*, 2000; Dake *et al.*, 2013; Qiao, Yin and Chu, 2015; Gambardella *et al.*, 2017). In recent years there have been a myriad of numerical studies examining the fluid dynamics of AD, and more recently, studies examining AD from a fluid-structure interaction standpoint (Cheng *et al.*, 2013, 2014; Alimohammadi *et al.*, 2015; Doyle and Norman, 2016; Ryzhakov, Soudah and

Dialami, 2019; Bäumlner *et al.*, 2020; Xiong *et al.*, 2020; Zorrilla, Soudah and Rossi, 2020). Many of these studies explore subject matter such as the effect of bypassing the false lumen on fluid flow using a bypass graft (Qiao, Yin and Chu, 2015); development of patient-specific models (Alimohammadi *et al.*, 2015; Xiong *et al.*, 2020); and analysis of intraluminal septum rigidity (Bonfanti *et al.*, 2018). However, to the authors knowledge, no study to date has examined the risk of false lumen propagation from a fracture mechanics standpoint.

In the present study we investigate AD risk due to a range of pre-existing injuries. In the first section of the study we investigate if an intraluminal tear (radial notch) will result in extensive AD under physiological and super-physiological lumen blood pressure. Cohesive zone analysis (CZM) is used to assess AD propagation. Finite element cohesive zone analyses suggest propagation of an intimal tear is not predicted for pressures less than $P=275$ mmHg in a healthy aorta. In the second section of the study we investigate if extensive AD will occur due to the presence of a pre-existing intraluminal septum and a patent false lumen. Computational fluid dynamics (CFD) analyses are performed to compute pressure loading on the intraluminal septum, and AD risk is again assessed using a CZM analysis. The results of the combined fluid dynamics and finite element cohesive zone analyses suggest extensive propagation of a false lumen is not predicted at a slightly hypertensive systolic pressure of 140 mmHg in a healthy aorta. Even in extreme hypertensive loading conditions AD propagation is arrested due to blunting of the crack tip and an increase in the mode angle towards mode II. The results of this study suggest an intimal tear will not develop into a false lumen in a healthy normotensive aorta.

8.2 Examination of an artery with an intraluminal tear

Methods and model construction: In this section we examine the risk of dissection propagation in an artery with a pre-existing intraluminal tear in the form of a radial notch Figure 8.1(a) shows an illustration of the intraluminal tear highlighted in red on the arterial geometry. In order to assess the risk of the intraluminal tear propagating under a luminal pressure load a cohesive zone is defined in the circumferential plane around the intraluminal tear, as shown by the red surface in Figure 8.1(b).

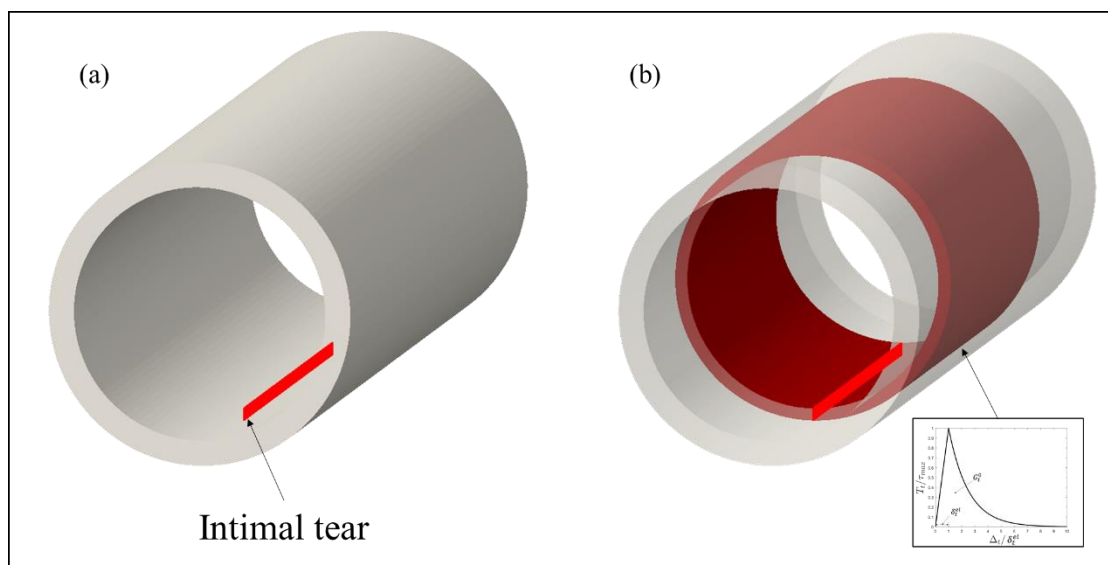


Figure 8.1. (a) illustration of the intraluminal tear in the artery is shown in (a). (b) shows the surface of the cohesive zone model.

The cohesive zone model (CZM) is comprised of an initial intrinsic elastic modulus followed by damage initiation and exponential reduction in the strength of the interface until total rupture occurs. A full description of the CZM is presented in Chapter 4. The cohesive zone model parameters are those previously calibrated from peel tests ($\sigma^{max} = 0.2$ MPa) and shear fracture ring tests ($\tau^{max} = 1.6$ MPa) (Chapter 5).

Hyperelastic anisotropic fibre-reinforced material behaviour is prescribed to the artery model according to the bilinear fibre model proposed by Fereidoonzhad et al.

(Fereidoonzhad, O'Connor and McGarry, 2020). Material parameters are as described in Chapter 5 (Table 5.2).

In order to determine an upper limit of allowable lumen pressure a super-physiological blood pressure of 500 mmHg is applied in the lumen. A 10% axial stretch is applied to the artery prior to lumen pressurisation.

Results: Figure 8.2(a) shows the max principal stress in the aorta at a lumen pressure of 500 mmHg. Crack growth is shown as a function of the lumen pressure in Figure 8.2(b). The crack initiates at a pressure of 275 mmHg and continues to propagate with increasing applied pressure. The final crack growth is ≈ 5.75 mm at a pressure of 500 mmHg. No crack propagation is recorded at lumen pressures below 275 mmHg. The crack initiates and propagates in a pure mode II due to compressive tractions at the medial interface caused by the hypertensive blood pressure. The super-physiological pressures cause the aorta to enter a buckling mode prior to any crack propagation, as seen in Figure 8.2(c).

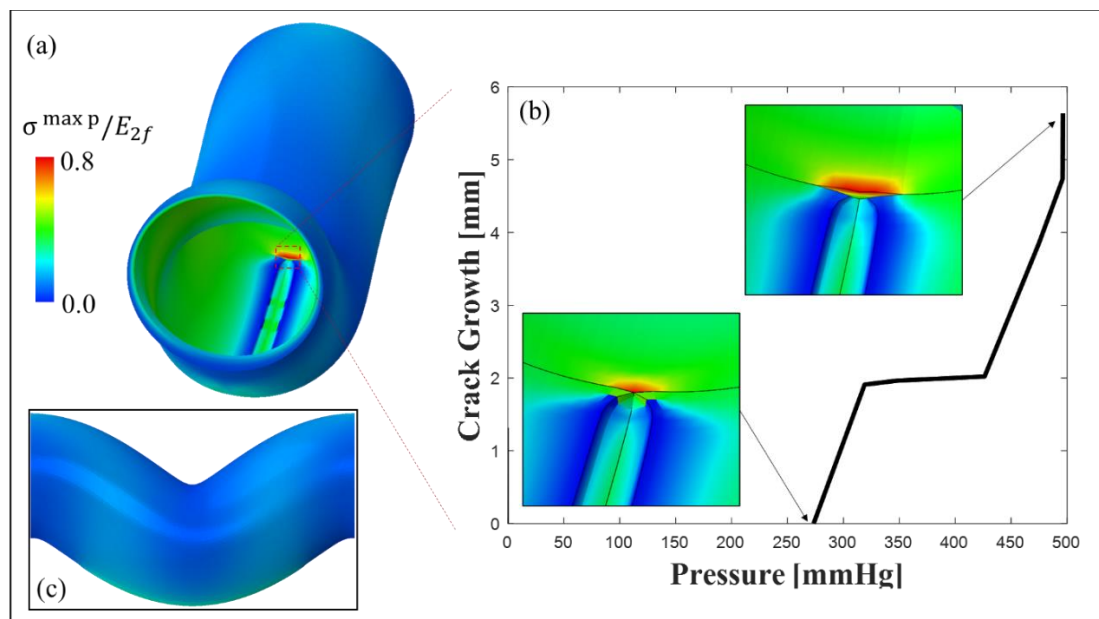


Figure 8.2. (a) Max principal stress in the aorta subject to 500 mmHg of lumen pressure; (b) Computed crack length as a function of pressure in the aorta with an intraluminal tear; (c) Side view of the aorta in a buckling mode subject to 500 mmHg

of lumen pressure.

Here we examine the influence of interface strength on pressure required to propagate the intraluminal tear. A 500 mmHg lumen pressure load is applied to aorta with decreasing interface strengths. Figure 8.3 shows the interface strength as a function of the lumen pressure at the point of intraluminal tear propagation. $\tau^{max}/\tau^{exp} = 1$ indicates the interface strength is the experimentally recorded value of $\tau^{max} = 1.6$ MPa. As shown, a 50% reduction in interface strength will lead to an intimal tear propagation under a typical hypertensive blood pressure load of $P \approx 190$ mmHg. A further reduction in interface strength ($\tau^{max}/\tau^{exp} = 0.25$) results in tear propagation in the normotensive blood pressure range. The highest recorded blood pressure in humans is 480/350 mmHg during heavy-resistance exercise (MacDougall *et al.*, 1985), these are referred to here as super-physiological. Our results seem to suggest under such blood pressure conditions an intimal tear is likely to propagate in a mode II in a healthy artery.

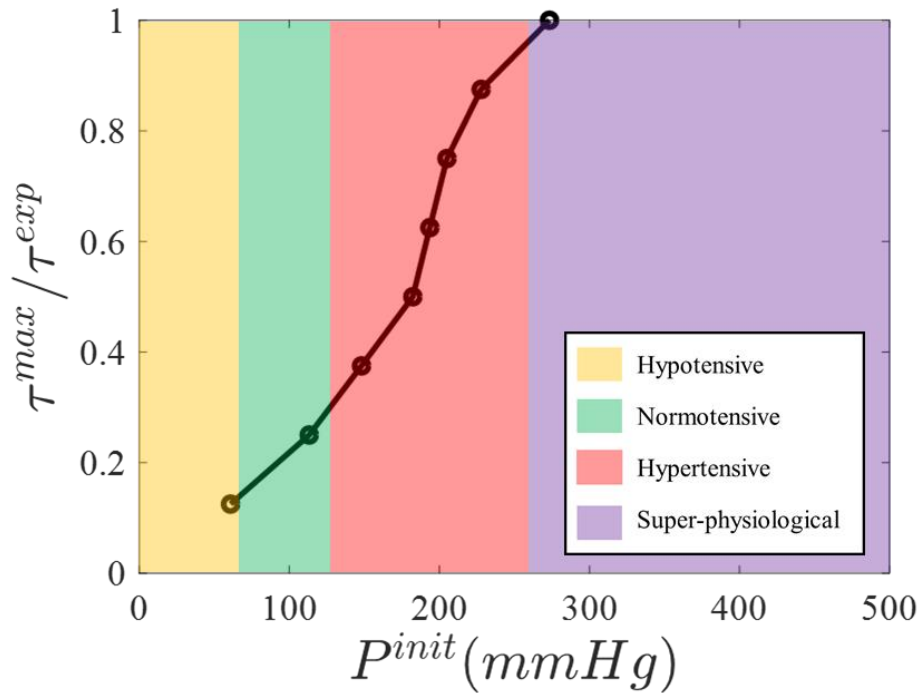


Figure 8.3. Interface strength (τ^{max}) as a function of pressure at crack propagation (P^{init}). Four regions of blood pressure are shown: hypotensive, normotensive, hypertensive, and super-physiological.

8.3 Examination of a dissected artery with a patent false lumen

Methods and model construction: In this section we explore the risk of a false lumen propagating further in an artery with a pre-existing patent false lumen, as shown in Figure 8.4(c). We begin our investigation by exploring the fluid flow and pressure in the dissected artery. The flow profile prescribed at the inlet is described by the analytical field

$$\frac{V(x, y)}{V_0} = 1 - \left(\frac{x^2}{r^2}\right) - \left(\frac{y^2}{r^2}\right) \quad (8.1)$$

which forms the elliptic paraboloid shown in Figure 8.4(a,c), V_0 is the max prescribed velocity. A zero-velocity (no-slip) condition is imposed at the wall for the fluid. Flow amplitudes are prescribed at physiologically accurate timepoints (shown in Figure 8.4(b)). The velocity amplitude is cycled for ten seconds in order to develop converged flow conditions. A fluid pressure condition is prescribed at the outlet such that pressure

ramps to a normotensive systolic blood pressure of $P=120$ mmHg prior to fluid velocity cycling.

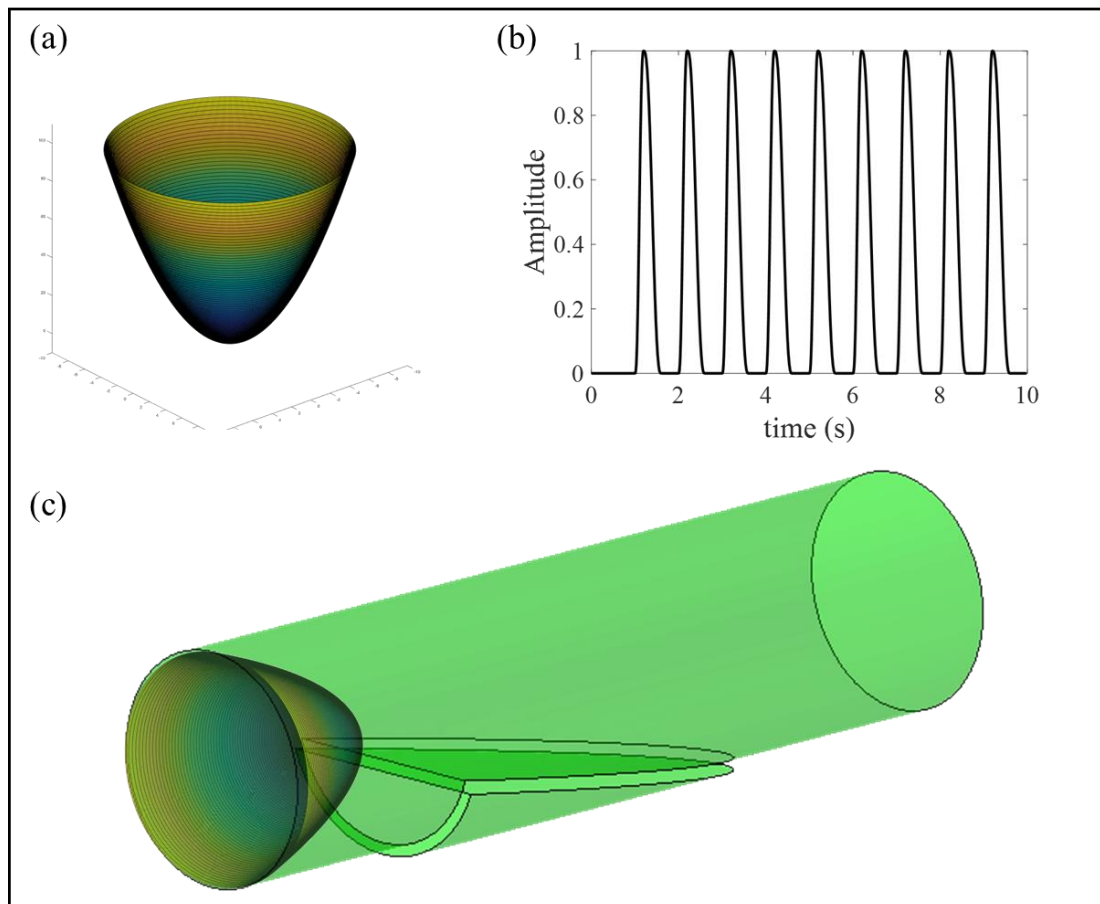


Figure 8.4. (a) paraboloid flow profile defined at the inlet; (b) Flow velocity amplitude; (c) Illustration of the dissected geometry with the paraboloid flow profile. The intraluminal septum is shown.

The fluid flow is assumed to be incompressible with a constant viscosity coefficient.

The fluid flow can be described using with the Navier-Stokes equations:

Conservation of mass:

$$\frac{D\rho}{Dt} + \rho(\nabla \cdot \mathbf{V}) = 0 \quad (8.2)$$

Where ρ is the density of the fluid and \mathbf{V} is velocity. The gradient operator gives:

$$\nabla = \mathbf{i} \frac{\partial}{\partial x} + \mathbf{j} \frac{\partial}{\partial y} + \mathbf{k} \frac{\partial}{\partial z} \quad (8.3)$$

Assuming constant density and incompressible flow yields the following:

$$\frac{D\rho}{Dt} = 0 \rightarrow \nabla \cdot \mathbf{V} = \frac{\partial u}{\partial x} + \frac{\partial v}{\partial y} + \frac{\partial w}{\partial z} = 0 \quad (8.4)$$

Conservation of momentum:

$$\rho \left(\frac{DV}{Dt} \right) = \rho \cdot g - \nabla p + \frac{\partial}{\partial x_i} \left[\mu \left(\frac{\partial v_i}{\partial x_j} \right) + \delta_{ij} \lambda \nabla \cdot V \right] \quad (8.5)$$

Assuming fluid incompressibility and a constant viscosity coefficient μ leads to the Navier-Stokes equations for an incompressible fluid in three-dimensional flow:

$$\rho \left(\frac{DV}{Dt} \right) = \rho g - \nabla p + \mu \nabla^2 V \quad (8.6)$$

The density of blood is $\rho=1060$ (kg/m³), the blood is assumed to be a non-Newtonian fluid in the present study with a dynamic viscosity of $\mu=2.78 \times 10^{-3}$ (Pa.s).

Pressure data is extracted from the CFD simulation and applied to a solid finite element cohesive zone model to assess the risk of a false lumen propagating (Figure 8.5).

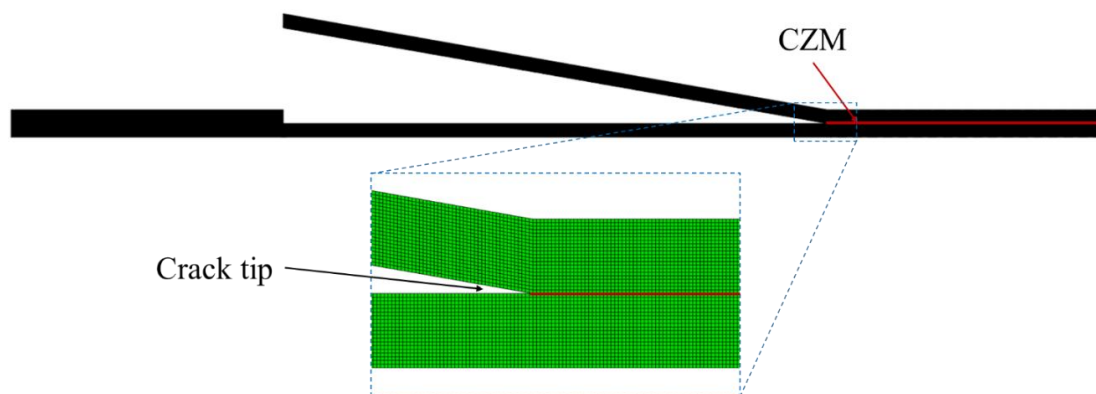


Figure 8.5. Image of the finite element cohesive zone model with the CZM highlighted in red. Detailed view of the crack tip, mesh, and CZM are shown in the detail view.

Results: In Figure 8.6 we examine the flow-field in the dissected aorta with an intraluminal septum and patent false lumen with peak inlet velocities at systole. Flow

velocity streamlines are shown in the lumen in Figure 8.6. Velocity is shown in the axial direction of the aorta. Maximum velocity occurs above the intraluminal septum and minimum velocities occur in the false lumen.

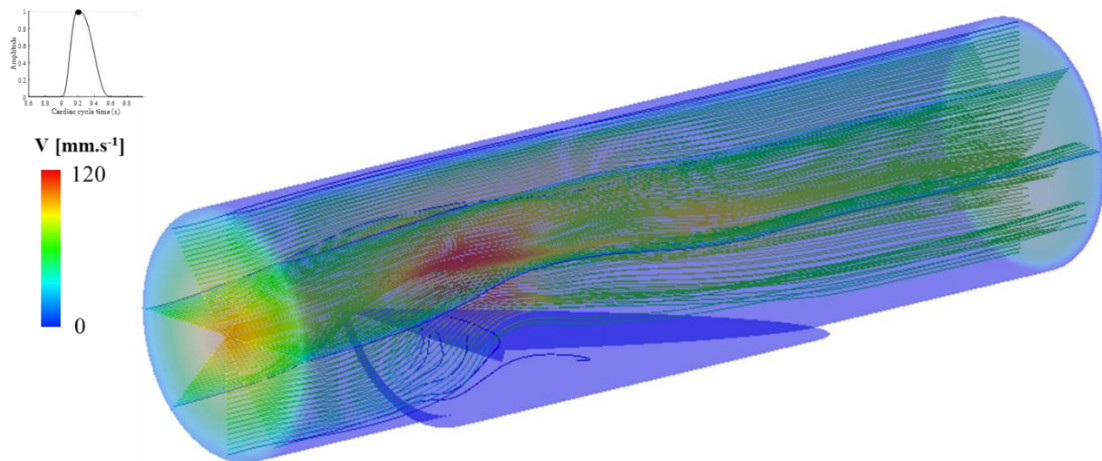


Figure 8.6: Velocity magnitude (mm.s^{-1}) streamline plot of the dissected geometry.

In Figure 8.7 we examine the pressure (P) and velocity (V) profiles through a plane in the middle of the aorta at peak systole. As expected, there is zero fluid velocity at the wall and the flow is parabolic. As shown in the fluid velocity contour plot in Figure 8.7(a), stagnant blood ($V \sim 0$ mmHg) is computed in the false lumen. Such stagnation is likely to result in false lumen thrombosis (Lip and Gibbs, 1999; Lowe, 2003; del Zoppo, 2008; Watson, Shantsila and Lip, 2009). Complete thrombosis of the false lumen is commonly reported clinically (Akutsu *et al.*, 2004; Sayer *et al.*, 2008; Dake *et al.*, 2013). Maximum flow velocity is computed above the intraluminal septum. As shown in the fluid pressure contour plot in Figure 8.7, at peak systole a pressure gradient of ~ 2 mmHg is computed across the intraluminal septum with peak pressures in the aorta occurring in the false lumen. This occurs due to the false lumen creating a stagnation point for the accumulation of low velocity blood flow, resulting in a pressure increase relative to the true lumen.

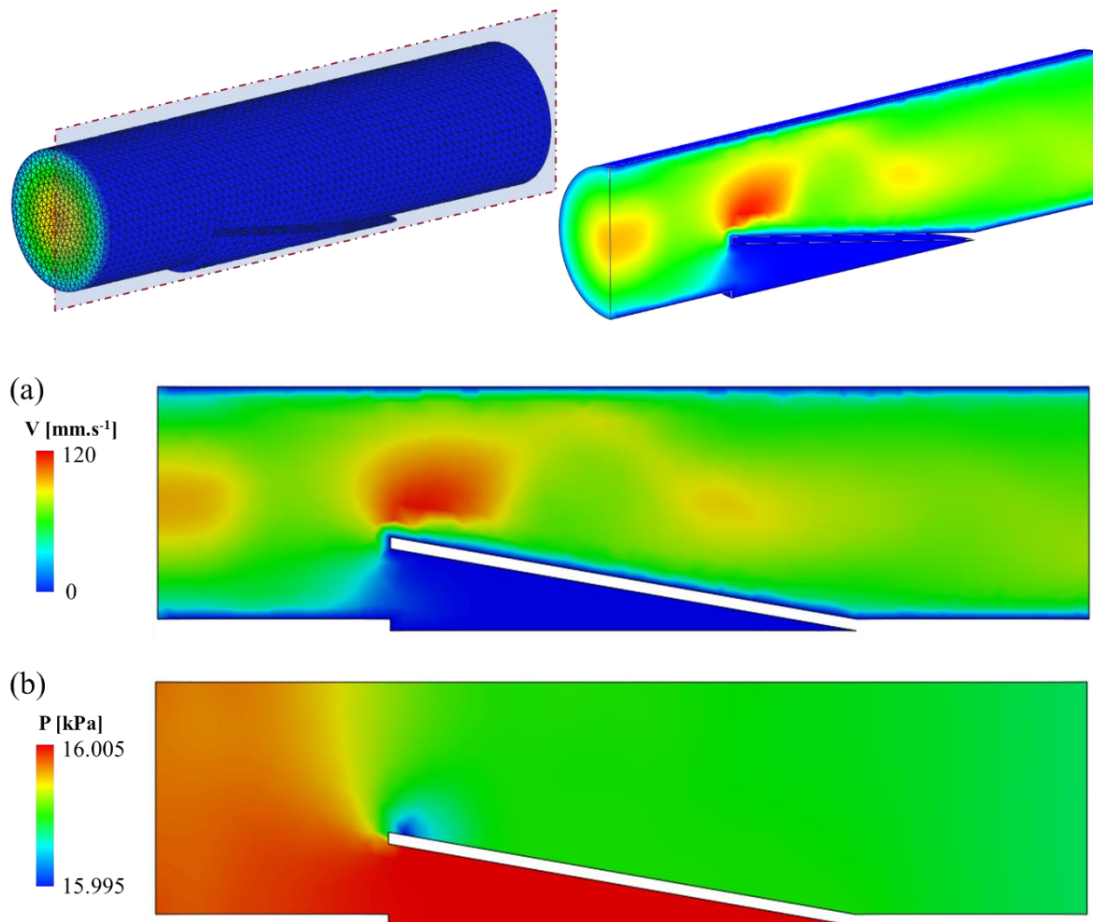


Figure 8.7. (a) Velocity magnitude ($\text{mm}\cdot\text{s}^{-1}$) contour plot; (b) Pressure (kPa) contour plot taken at a section midway through the artery.

Previous studies have suggested that increased pulse pressure may result in the propagation of a false lumen (Rajagopal, Bridges and Rajagopal, 2007). In order to assess the effects of elevated false lumen pressure on the risk of false lumen propagation, pressure data is extracted from the fluid domain and applied to the solid domain. Figure 8.8(a) shows a cut-view of the aorta at a lumen pressure of 140 mmHg immediately prior to false lumen propagation. (b) shows the aorta at ~ 160 mmHg. As shown in Figure 8.8(c) crack length is computed as a function of applied mean pressure. The false lumen is not predicted to propagate extensively at a pressure of ~ 140 mmHg with the crack growing approximately 0.15 mm after a pressurisation to 300 mmHg.

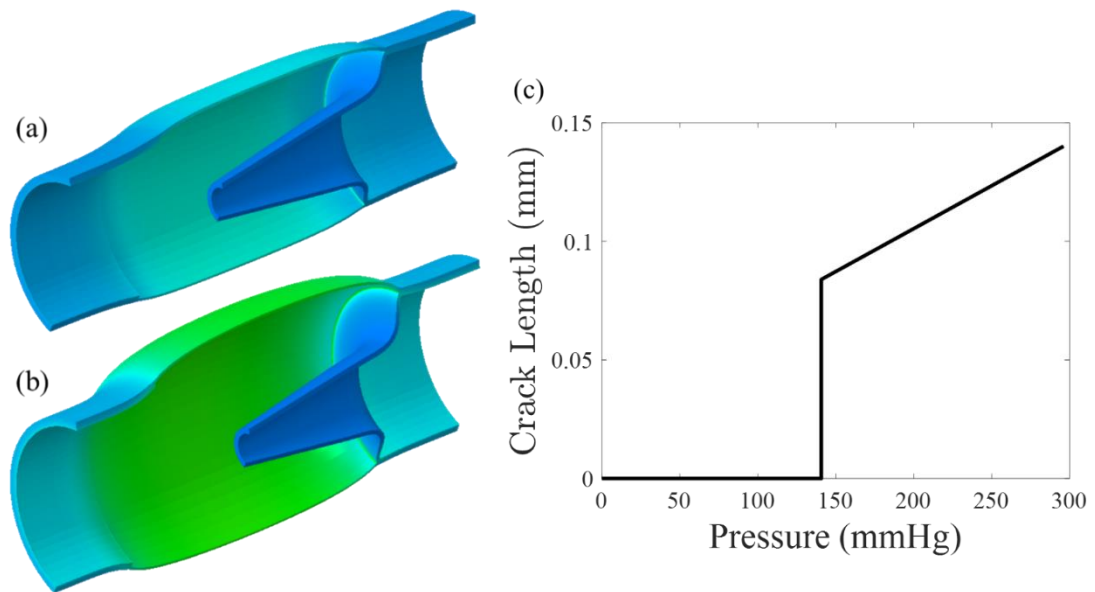


Figure 8.8. Crack length as a function of pressure. Crack growth is calculated to occur at 140 mmHg.

Figure 8.9 explores crack arrest due to blunting of the crack tip. Figure 8.9(a-c) show the progression of the simulation as the pressure is increased. Figure 8.9(d) shows the mode mixity at the crack tip as a function of the mean lumen pressure. The crack tip is clearly shown to be in a mixed mode, rather than pure mode I or mode II. While earlier chapters demonstrate that initiation of AD is a pure mode II process, the simulations presented in Figure 8.9 suggests that the eventual formation of a false lumen, following mode II initiation, will result in mixed mode conditions at the crack-tip. A form of toughening of the crack tip is also evident in (d) as the mode angle at the crack tip increases (tending towards mode II propagation) with increasing pressure. As the mode II strength has been shown to be eight times higher than mode I strength (Chapter 5), such an increase in the mode angle with increasing pressure will be accompanied by a significant increase fracture resistance. Such a toughening mechanism is incorporated into our model through our calibrated mixed-mode CZM formulation (Chapter 4 & 6). Both the VP-CZM (Chapter 6) and E-CZM (Chapter 4) predict crack propagation arrest due to this toughening mechanism.

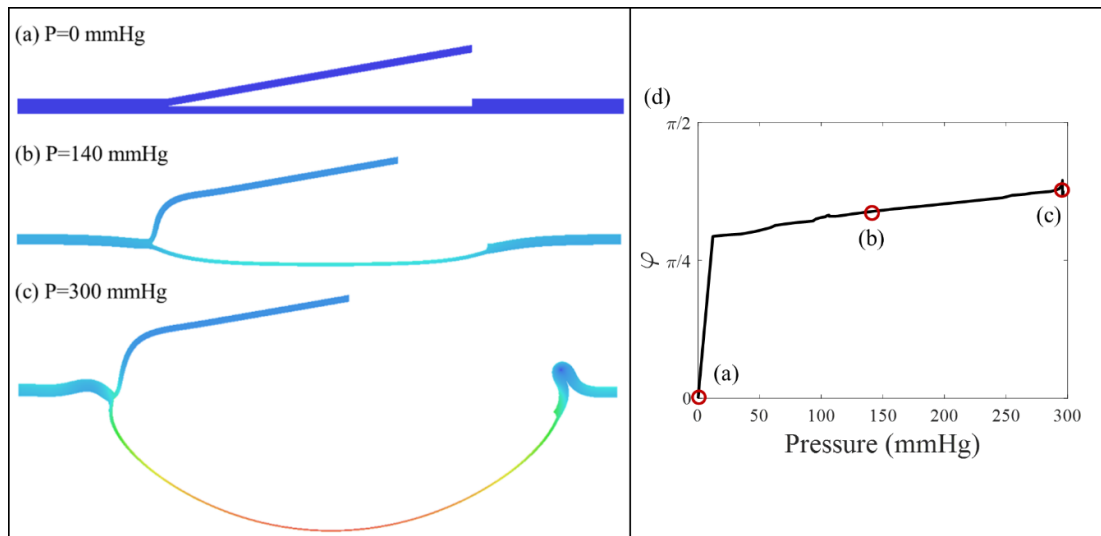


Figure 8.9. Images show blunting of the crack tip. Mode at the crack tip is shown as a function of the lumen pressure.

8.4 Conclusions

In the present study we examine the risk of dissection in an artery with a range of pre-existing injuries. In the first section of the study we examine the risk of dissection in an artery with an intraluminal tear (radial notch). Finite element cohesive zone analyses suggest propagation of an intimal tear is not predicted for pressures less than $P=275$ mmHg in a healthy aorta. In Chapter 7 we demonstrate that, in the absence of damage or significant artery wall remodelling and reduction of fracture strength, physiological super-physiological loading will not result in AD initiation. The results of the current chapter show that even in the presence of significant damage to the artery wall (i.e. a radially aligned notch) super-physiological loading is required to initiate AD in healthy tissue. Furthermore, simulations suggest that even if AD is initiated at the notch, extensive propagation will not occur.

In the second section of the study, we examine the risk of dissection in an artery with a pre-existing intraluminal septum and a patent false lumen. Computational fluid

dynamics (CFD) analyses are performed, and pressure data is extracted and applied to a solid fracture model. The results of the combined fluid dynamics and finite element cohesive zone analyses suggest extensive propagation of a false lumen is not predicted at a slightly hypertensive systolic pressure of 140 mmHg in a healthy aorta. Even in extreme hypertensive loading conditions AD propagation is arrested due to blunting of the crack tip and an increase in the mode angle towards mode II. The results of this study suggest an intimal tear will not develop into a false lumen in a healthy normotensive aorta. Moreover, we show that false lumen propagation under such conditions is a mixed mode process. Earlier chapters of this thesis demonstrate that AD initiation is a mode II process. However, simulations presented in the current chapter suggest that if a false lumen subsequently develops, mixed mode loading occurs at the crack tip. This highlights the importance of a full calibration of a CZM formulation, using both mode II experiments (i.e. the SRFT developed in Chapter 5) and peel tests (also presented in Appendix C, Chapter 5). The results of this study suggest an intimal tear will not develop into a false lumen in a healthy normotensive aorta. Simulations also suggest that hypertensive conditions will result in an increase in mode angle (towards mode II) at the false lumen crack tip. This provides a significant toughening mechanism against AD, given that our earlier experiments reveal that the mode II fracture strength of an artery is eight times higher than the mode I strength.

Bibliography

- Akutsu, K. et al. (2004) 'Effects of the patent false lumen on the long-term outcome of type B acute aortic dissection.', *European journal of cardio-thoracic surgery : official journal of the European Association for Cardio-thoracic Surgery*, 26(2), pp. 359–66. doi: 10.1016/j.ejcts.2004.03.026.
- Alimohammadi, M. et al. (2015) 'Aortic dissection simulation models for clinical support: fluid-structure interaction vs. rigid wall models.', *Biomedical engineering online*. BioMed Central, 14(1), p. 34. doi: 10.1186/s12938-015-0032-6.
- Bäumler, K. et al. (2020) 'Fluid–structure interaction simulations of patient-specific aortic dissection', *Biomechanics and Modeling in Mechanobiology*. Springer Berlin Heidelberg, pp. 1–22. doi: 10.1007/s10237-020-01294-8.
- Bonfanti, M. et al. (2018) 'A simplified method to account for wall motion in patient-specific blood flow simulations of aortic dissection: Comparison with fluid-structure interaction', *Medical Engineering & Physics*. Elsevier, 58, pp. 72–79. doi: 10.1016/J.MEDENGGPHY.2018.04.014.
- Cheng, Z. et al. (2013) 'Initial findings and potential applicability of computational simulation of the aorta in acute type B dissection.', *Journal of vascular surgery*, 57(2 Suppl), pp. 35S–43S. doi: 10.1016/j.jvs.2012.07.061.
- Cheng, Z. et al. (2014) 'Predicting flow in aortic dissection: comparison of computational model with PC-MRI velocity measurements.', *Medical engineering & physics*. Elsevier Ltd, 36(9), pp. 1176–84. doi: 10.1016/j.medengphy.2014.07.006.
- Colli, A. et al. (2018) 'Acute DeBakey Type I aortic dissection without intimal tear in the arch: is total arch replacement the right choice?', *Interactive cardiovascular and thoracic surgery*, 26(1), pp. 84–90. doi: 10.1093/icvts/ivx229.
- Criado, F. J. (2011) 'Aortic dissection: a 250-year perspective.', *Texas Heart Institute journal / from the Texas Heart Institute of St. Luke's Episcopal Hospital, Texas Children's Hospital*, 38(6), pp. 694–700. Available at: <http://www.pubmedcentral.nih.gov/articlerender.fcgi?artid=3233335&tool=pmcentrez&rendertype=abstract> (Accessed: 5 January 2016).
- Dake, M. D. et al. (2013) 'DISSECT: a new mnemonic-based approach to the categorization of aortic dissection.', *European journal of vascular and endovascular surgery : the official journal of the European Society for Vascular Surgery*, 46(2), pp. 175–90. doi: 10.1016/j.ejvs.2013.04.029.
- Dotter, C. T., Roberts, D. J. and Steinberg, I. (no date) Aortic Length: Angiocardigraphic Measurements. Available at: <http://ahajournals.org> (Accessed: 13 July 2020).
- Doyle, B. J. and Norman, P. E. (2016) 'Computational Biomechanics in Thoracic Aortic Dissection: Today's Approaches and Tomorrow's Opportunities.', *Annals of biomedical engineering*, 44(1), pp. 71–83. doi: 10.1007/s10439-015-1366-8.
- Eichelberger, J. P. (1994) 'Aortic Dissection Without Intimal Tear: Case Report and Findings on Transesophageal Echocardiography', *Journal of the American Society of Echocardiography. J Am Soc Echocardiogr*, 7(1), pp. 82–86. doi: 10.1016/S0894-7317(14)80423-9.

- Fereidoonzhad, B., O'Connor, C. and McGarry, P. (2020) 'A new anisotropic soft tissue model for elimination of unphysical auxetic behaviour', *Journal of Biomechanics*. engrXiv. doi: 10.31224/OSF.IO/G6DSE.
- Gambardella, I. et al. (2017) 'Surgical Outcomes of Chronic Descending Dissections: Type I Versus III DeBakey', *Annals of thoracic surgery*, 104(2 PG-593–598), pp. 593–598. doi: <https://dx.doi.org/10.1016/j.athoracsur.2016.10.056>.
- Hagan, P. G. et al. (2000) 'The International Registry of Acute Aortic Dissection (IRAD)', *The Journal of American Medical Association*. American Medical Association, 283(7), pp. 897–903. doi: 10.1001/jama.283.7.897.
- Hasleton, P. S. and Leonard, J. C. (1979) 'Dissecting aortic aneurysms: a clinicopathological study. II. Histopathology of the aorta.', *The Quarterly journal of medicine*, 48(189), pp. 63–76. Available at: <http://www.ncbi.nlm.nih.gov/pubmed/482592> (Accessed: 15 February 2020).
- Huang, X. et al. (2015) 'Endovascular repair of Stanford B aortic dissection using two stent grafts with different sizes', *Journal of Vascular Surgery*, 62(1), pp. 43–48. doi: 10.1016/j.jvs.2015.02.022.
- Kim, J. B. et al. (2014) 'Outcomes of acute retrograde type a aortic dissection with an entry tear in descending aorta', *Circulation*, 130(11), pp. S39–S44. doi: 10.1161/CIRCULATIONAHA.113.007839.
- Larson, E. W. and Edwards, W. D. (1984) 'Risk factors for aortic dissection: A necropsy study of 161 cases', *The American Journal of Cardiology*, 53(6), pp. 849–855. doi: 10.1016/0002-9149(84)90418-1.
- Lemaire, S. A. and Russell, L. (2011) 'Epidemiology of thoracic aortic dissection', *Nature Reviews Cardiology*, pp. 103–113. doi: 10.1038/nrcardio.2010.187.
- Lip, G. Y. H. and Gibbs, C. R. (1999) 'Does heart failure confer a hypercoagulable state? Virchow's triad revisited', *Journal of the American College of Cardiology*. Elsevier Inc., pp. 1424–1426. doi: 10.1016/S0735-1097(99)00033-9.
- Lowe, G. D. O. (2003) 'Virchow's triad revisited: Abnormal flow', in *Pathophysiology of Haemostasis and Thrombosis*, pp. 455–457. doi: 10.1159/000083845.
- Lui, R. C., Menkis, A. H. and McKenzie, F. N. (1992) 'Aortic dissection without intimal rupture: Diagnosis and management', *The Annals of Thoracic Surgery*, 53(5), pp. 886–888. doi: 10.1016/0003-4975(92)91460-Q.
- MacDougall, J. D. et al. (1985) 'Arterial blood pressure response to heavy resistance exercise', *Journal of Applied Physiology*, 58(3), pp. 785–790. doi: 10.1152/jappl.1985.58.3.785.
- Narloch, J. A. and Brandstater, M. E. (1995) 'Influence of breathing technique on arterial blood pressure during heavy weight lifting', *Archives of Physical Medicine and Rehabilitation*. W.B. Saunders, 76(5), pp. 457–462. doi: 10.1016/S0003-9993(95)80578-8.
- Nienaber, C. A. et al. (2010) 'Strategies for subacute/chronic type B aortic dissection: the Investigation Of Stent Grafts in Patients with type B Aortic Dissection (INSTEAD)

trial 1-year outcome.’, *The Journal of thoracic and cardiovascular surgery*, 140(6 Suppl), pp. S101-8; discussion S142-S146. doi: 10.1016/j.jtcvs.2010.07.026.

Qiao, A., Yin, W. and Chu, B. (2015) ‘Numerical simulation of fluid–structure interaction in bypassed DeBakey III aortic dissection’, *Computer Methods in Biomechanics and Biomedical Engineering*. Taylor & Francis, 18(11), pp. 1173–1180. doi: 10.1080/10255842.2014.881806.

Rajagopal, K., Bridges, C. and Rajagopal, K. R. (2007) ‘Towards an understanding of the mechanics underlying aortic dissection.’, *Biomechanics and modeling in mechanobiology*, 6(5), pp. 345–59. doi: 10.1007/s10237-006-0069-3.

Ryzhakov, P., Soudah, E. and Dialami, N. (2019) ‘Computational modeling of the fluid flow and the flexible intimal flap in type B aortic dissection via a monolithic arbitrary Lagrangian/Eulerian fluid-structure interaction model’, *International Journal for Numerical Methods in Biomedical Engineering*. John Wiley & Sons, Ltd, 35(11). doi: 10.1002/cnm.3239.

Sayer, D. et al. (2008) ‘Aortic morphology following endovascular repair of acute and chronic type B aortic dissection: implications for management.’, *European journal of vascular and endovascular surgery : the official journal of the European Society for Vascular Surgery*, 36(5), pp. 522–9. doi: 10.1016/j.ejvs.2008.06.023.

Svensson, L. G. et al. (1999) *Intimal Tear Without Hematoma An Important Variant of Aortic Dissection That Can Elude Current Imaging Techniques*. Available at: <http://www.circulationaha.org> (Accessed: 13 July 2020).

Utoh, J. et al. (1997) ‘Acute aortic dissection without intimal tear.’, *The Journal of cardiovascular surgery*, 38(4), pp. 419–20. Available at: <http://www.ncbi.nlm.nih.gov/pubmed/9267356> (Accessed: 18 July 2019).

Vilacosta, I. et al. (2010) ‘Acute aortic syndrome: a new look at an old conundrum’, *pmj.bmj.com*. Available at: <https://pmj.bmj.com/content/86/1011/52.short> (Accessed: 15 February 2020).

Watson, T., Shantsila, E. and Lip, G. Y. (2009) ‘Mechanisms of thrombogenesis in atrial fibrillation: Virchow’s triad revisited’, *The Lancet*. Elsevier, pp. 155–166. doi: 10.1016/S0140-6736(09)60040-4.

Xiong, Z. et al. (2020) ‘A computational fluid dynamics analysis of a patient with acute non-A-non-B aortic dissection after type I hybrid arch repair’, *Medical Engineering & Physics*. Elsevier. doi: 10.1016/J.MEDENGGPHY.2019.10.019.

del Zoppo, G. J. (2008) ‘Virchow’s triad: the vascular basis of cerebral injury.’, *Reviews in neurological diseases*. NIH Public Access, 5 Suppl 1(Suppl 1), pp. S12-21. Available at: <http://www.ncbi.nlm.nih.gov/pubmed/18645567> (Accessed: 13 July 2020).

Zorrilla, R., Soudah, E. and Rossi, R. (2020) ‘Computational modeling of the fluid flow in type B aortic dissection using a modified finite element embedded formulation’, *Biomechanics and Modeling in Mechanobiology*. Springer Berlin Heidelberg, pp. 1–19. doi: 10.1007/s10237-020-01291-x.

Chapter 9

9 CONCLUDING REMARKS & FUTURE PERSPECTIVES

9.1 Summary of Key Contributions

This section outlines the key contributions of this thesis to the field of biomechanics.

Chapter 4:

- Two mixed mode cohesive zone models are proposed, in which interfacial stiffness (K_m) and the fracture energy (G_m) are uncoupled.
- A novel form of “overclosure hardening” is presented, whereby the shear interface strength is augmented as a function of negative normal traction.
- Anomalous behaviour of the Abaqus exponential damage model is highlighted where damage evolution is specified according to energy.

Chapter 5:

- A novel experimental method to robustly and repeatably generate mode II crack initiation and propagation in arteries is proposed and validated.
- A fracture toughening mechanism resisting radial crack growth due to collagen fibre alignment in the circumferential-axial plane behind the crack tip is uncovered.
- The mode II fracture strength of the aorta along the circumferential-axial plane is shown to be eight times higher than the corresponding mode I strength determined from a standard peel test.

- Mode II crack propagation rates recorded from shear fracture ring test experiments are presented.
- The mode II fracture energy is calibrated based on the measurements of crack propagation rates.
- It is shown that lap-shear testing of arterial tissue results in mixed mode fracture, rather than pure mode II.

Chapter 6:

- Evidence of interfacial fibrillation in arterial tissue undergoing mode II fracture is presented.
- A novel elastic fibrillation cohesive zone model is developed where fibrils form during the damage process and cause a secondary damage region in the traction-separation response. The model is implemented in Abaqus through a user-defined surface interaction subroutine (UINTER).
- A novel physically motivated viscoplastic cohesive zone model is developed where the rate of strain hardening is dependent on the strain rate. The model is implemented in a user-defined surface interaction subroutine (UINTER).
- It is shown that non-linear crack growth trends observed in interfacial fibrillation can be predicted using the novel viscoplastic cohesive zone model.

Chapter 7:

- A framework for the generation of a realistic dual-vent MRI-derived subject-specific aorta finite element model to assess the risk of dissection using cohesive zone analysis is developed.
- It is demonstrated that initiation of aortic dissection is a mode II fracture process, rather than a mixed mode or mode I.

- The results of the subject-specific finite element cohesive zone analysis suggest aortic dissection will not occur unless there is a 100-fold decrease in interface strength.
- It is shown that anatomical features, material factors, and displacement of the aortic root do not play a significant role in the initiation of aortic dissection.
- A novel method for the inclusion of residual stress in the aorta is developed and implemented in Abaqus through a user-defined material behaviour subroutine (UMAT).

Chapter 8:

- Finite element cohesive zone analyses suggest propagation of an intimal tear is only predicted for extremely hypertensive pressures (≥ 275 mmHg) in a healthy aorta.
- Extensive Propagation of a false lumen is not predicted at a slightly hypertensive blood pressure of (140 mmHg). Even in extreme hypertensive loading conditions AD propagation is arrested due to blunting of the crack tip and an increase in the mode angle towards mode II.
- The results of this study suggest an intimal tear will not develop into a false lumen in a healthy normotensive aorta.

9.2 Future Perspectives

The work presented in this thesis has addressed several key topics in relation to aortic dissection and the fracture mechanics of arterial tissue. These contributions have implications for related areas in biomechanics, design of medical devices, and clinicians. This section provides a discussion of future perspectives.

In chapter 4 we propose two novel cohesive zone formulations including a novel overclosure hardening method. Future studies could examine the effects of a variable compressive displacement coupled with a shear displacement applied to an interface implementing overclosure hardening. The effects of a variable shear interface strength due to variable overclosure hardening should be analogous to a separation of varying mode angle. However, this would need to be confirmed with parametric investigations examining the fracture energy, interface strength, and traction-separation response. The impact of a proportional traction load and non-proportional traction load could also be examined, as is seen in McGarry *et al.* (2014).

In Chapter 5 it is demonstrated that lap shear tests performed by Sommer *et al.* and Witzenburg *et al.* do not result in a mode II fracture (Sommer *et al.*, 2016; Witzenburg *et al.*, 2017). Therefore, studies using mode II values calibrated from mixed mode experiments should be revisited using correct shear interface strength properties (Witzenburg *et al.*, 2017; Gültekin *et al.*, 2019). The use of in-depth computational analysis of soft tissue anisotropic fracture mechanics to guide experimental design sets a new paradigm for development of insightful experimental analysis of soft tissue. In fact, we argue that this approach to soft tissue fracture mechanics is of fundamental importance, given that fracture mechanics testing of soft tissue must be developed within the constraints inherent in anatomical specimen geometries and local fibre arrangements. Future studies should design experiments using computational analysis.

The fibre alignment observed at the crack tip in soft collagenous tissues, such as arterial tissue, has been shown to resist crack propagation in the direction of the crack tip (Bircher *et al.*, 2019). Future studies may examine the role of collagen fibre alignment through collagen knockout experiments on arterial tissue similar to those seen in Schriefl *et al.* (2015) and Noble *et al.* (2016). Future studies may apply the shear fracture ring test methodology to other tubular/cylindrical tissues. Rupture patterns observed bear resemblance to experiments by Haslach *et al.* (2011,2015,2018). Future studies should carry out further imaging of the rupture surface. Accurate calibration of the shear interface strength was due, in part, to the accuracy of the material constitutive behaviour implemented (Fereidoonzhad, O'Connor and McGarry, 2020). The use of an anisotropic material law (Holzapfel, Gasser and Ogden, 2000; Gasser, Ogden and Holzapfel, 2006; Nolan *et al.*, 2014) leads to unphysical auxetic behaviour and significantly over-predicts stresses in regions of localised large strains, such as those seen in arterial fracture mechanics. Future studies dealing with large strain problems should implement constitutive laws: (i) without exponentially stiffening behaviour and, (ii) that allow for the control of unphysical auxetic behaviour.

Chapter 6 demonstrates that the proposed viscoplastic cohesive zone model is capable of predicting crack growth trends observed in interfacial fibrillation. Future studies may implement a more complex form of hardening based on more experimental data. Future experimental studies and data may also inform the development of a less phenomenological fibrillation initiation criteria.

Chapter 7 clearly demonstrates that initiation of dissection must be a mode II fracture process, this is in agreement with the recently published study from Gültekin *et al.* (2019). Future studies examining the mode II initiation of aortic dissection should use

mode II properties calibrated from pure mode II experiments. Dissection is not predicted to propagate unless the interface strength is reduced 100-fold, this is also in agreement with Gültekin et al. (2019) who assume a ~100 fold reduction in fracture energy to propagate a dissection. Wang et al. assumes an interface strength of 3 kPa (2017), and 0.3 kPa (2018) which is approximately 500 and 5000 times weaker (respectively) than that of healthy aorta. Future studies should aim to determine the effects of disease on interface strength in the aorta.

Finally, in Chapter 8 analyses of a pre-existing intimal tear, and false lumen are presented. Future studies should attempt to propagate a false lumen experimentally, similar to the experiments of Chen et al. (2016). Future studies may also attempt to propagate an intimal tear experimentally.

Bibliography

Bircher, K. et al. (2019) ‘Tear resistance of soft collagenous tissues’, *Nature Communications*. Nature Publishing Group, 10(1), pp. 1–13. doi: 10.1038/s41467-019-08723-y.

Chen, H. Y. et al. (2016) ‘Editor’s Choice – Fluid–Structure Interaction Simulations of Aortic Dissection with Bench Validation’, *European Journal of Vascular and Endovascular Surgery*, 52(5), pp. 589–595. doi: 10.1016/j.ejvs.2016.07.006.

Fereidoonzhad, B., O’Connor, C. and McGarry, P. (2020) ‘A new anisotropic soft tissue model for elimination of unphysical auxetic behaviour’, *Journal of Biomechanics*. engrXiv. doi: 10.31224/OSF.IO/G6DSE.

Gasser, T. C., Ogden, R. W. and Holzapfel, G. A. (2006) ‘Hyperelastic modelling of arterial layers with distributed collagen fibre orientations.’, *Journal of the Royal Society, Interface / the Royal Society*. The Royal Society, 3(6), pp. 15–35. doi: 10.1098/rsif.2005.0073.

Gültekin, O. et al. (2019) ‘Computational modeling of progressive damage and rupture in fibrous biological tissues: application to aortic dissection’, *Biomechanics and Modeling in Mechanobiology*. Springer Berlin Heidelberg, 18(6), pp. 1607–1628. doi: 10.1007/s10237-019-01164-y.

Haslach, H. W. et al. (2015) ‘Crack Propagation and Its Shear Mechanisms in the Bovine Descending Aorta.’, *Cardiovascular engineering and technology*, 6(4), pp. 501–18. doi: 10.1007/s13239-015-0245-7.

Haslach, H. W. et al. (2018) ‘Fracture mechanics of shear crack propagation and dissection in the healthy bovine descending aortic media’, *Acta Biomaterialia*. Elsevier, 68, pp. 53–66. doi: 10.1016/j.actbio.2017.12.027.

Haslach, H. W., Riley, P. and Molotsky, A. (2011) ‘The Influence of Medial Substructures on Rupture in Bovine Aortas’, *Cardiovascular Engineering and Technology*. Springer US, 2(4), pp. 372–387. doi: 10.1007/s13239-011-0056-4.

Holzapfel, G. A., Gasser, T. C. and Ogden, R. W. (2000) ‘A new constitutive framework for arterial wall mechanics and a comparative study of material models’, *Journal of Elasticity*. Kluwer Academic Publishers, 61(1–3), pp. 1–48. doi: 10.1023/A:1010835316564.

McGarry, J. P. et al. (2014) ‘Potential-based and non-potential-based cohesive zone formulations under mixed-mode separation and over-closure. Part I: Theoretical analysis’, *Journal of the Mechanics and Physics of Solids*, 63(1), pp. 336–362. doi: 10.1016/j.jmps.2013.08.020.

Noble, C. et al. (2016) ‘Controlled peel testing of a model tissue for diseased aorta’, *Journal of Biomechanics*, 49(15), pp. 3667–3675. doi: 10.1016/j.jbiomech.2016.09.040.

Nolan, D. R. et al. (2014) ‘A robust anisotropic hyperelastic formulation for the modelling of soft tissue’, *Journal of the Mechanical Behavior of Biomedical Materials*, 39, pp. 48–60. doi: 10.1016/j.jmbbm.2014.06.016.

Schriebl, A. J. et al. (2015) ‘Selective enzymatic removal of elastin and collagen from human abdominal aortas: Uniaxial mechanical response and constitutive modeling’, *Acta Biomaterialia*. Elsevier Ltd, 17, pp. 125–136. doi: 10.1016/j.actbio.2015.01.003.

Sommer, G. et al. (2016) ‘Mechanical strength of aneurysmatic and dissected human thoracic aortas at different shear loading modes’, *Journal of Biomechanics*, pp. 2374–2382. doi: 10.1016/j.jbiomech.2016.02.042.

Wang, L. et al. (2017) ‘Propagation of dissection in a residually-stressed artery model’, *Biomechanics and Modeling in Mechanobiology*. Springer Berlin Heidelberg, 16(1), pp. 139–149. doi: 10.1007/s10237-016-0806-1.

Wang, L. et al. (2018) ‘Modelling peeling- and pressure-driven propagation of arterial dissection’, *Journal of Engineering Mathematics*. Springer Netherlands, 109(1), pp. 227–238. doi: 10.1007/s10665-017-9948-0.

Witzenburg, C. M. et al. (2017) ‘Failure of the porcine ascending aorta: Multidirectional experiments and a unifying microstructural model’, *Journal of Biomechanical Engineering*. American Society of Mechanical Engineers Digital Collection, 139(3). doi: 10.1115/1.4035264.

APPENDIX A

10 DEVELOPED CODE: SUBROUTINES, AND OPTIMISATION SCHEMES

The following is a presentation and brief description of select code written in MATLAB, Python, and FORTRAN used for each technical chapter.

Chapters (4 & 6): The following MATLAB code is used in the development and analysis of new cohesive zone models. It contains a master script and a function that acts analogous to a UINTER subroutine. This coding framework also facilitates the analysis of the Abaqus inbuilt cohesive zone behaviours. This framework facilitated the extensive cohesive zone development in Chapter 4 and Chapter 6. “Plot” states have been omitted for brevity.

```

% PARAMETER STUDY FOR NEW CZM
% MIXED MODE SCENARIOS - Proportional loading
theta=linspace(0,0,4);
% theta=[0 , pi/8, pi/2];
shear=cos(theta)*1.0;
normal=sin(theta)*1.0;

% Control Parameters
% -----
%elasticBias--> switch to 1 if initial elastic slope is very high
elasticBias=0;
% unload--> 1 = load halfway - unload - load all the way //
0=monotonic loading
unload=0;
rev1=-1; rev2=-1; % change shear direction after unloading set to -
1.
% pctLoad --> if unload =1 // amount to load before unloading.
1=full loading
% pctLoad=[0.45 0.525];
pctLoad=[0.25 0.5];
% form --> 1 = linear // 2 = exponential // 3 = squared exponential
formSet=2;

% Fibrillation --> 1 = Add Fibrillation // 0 - No Fibrillation
fibrillation=0;
% plasticity --> 1 = Add Plasticity // 0 - No Plasticity
plasticity=0;
% If using plasticity set areaFraction to 1 to add curves
areaFraction=0;
% Add viscoplasticity? --> 1 = yes // 0 = no viscoplasticity
viscoplasticity=1;

% Add old viscoplasticity? --> 1 = yes // 0 = no viscoplasticity
viscoplasticity_old=0;
plotOn=1;
plotAbaqus=0;
dInit=0; % 0 for same as G // 1 for abaqus
resolution=1000;
% -----
% CZM parameters
tno=1.;
tto=1.;
km=10.0;
% gno=20e-3;
gto=100e-3;
gno=gto*(tno/tto);
% gno=gto*(tno/tto).^2;

delt=tto/km;
deln=tno/km;
xi0=pi/16;

% Elastic Fibrillation parameters
% ff1a=5;
% ff2=10;
% dft=0.75;

% Plastic Fibrillation Parameters
ff1a=1.0;

```

```

ff1b=1.2;
ff2=0.25;
dft=0.5;

eta=[0.0,0.25,0.5,0.75,1.0];

% Viscoplasticity parameters -----
% epsilon p zero (affects spread of rates)
% smaller=less sensitive to change in rate (sensitivity parameter)
epr0= 4.0e-3;
% strain rate hardening exponent 'm'
m=20;
% epsilon ^n (similar to initial hardening slope) smaller=stiffer
% how quickly you reach the plateau
en=0.25;
% theta - to set backward euler or forard
xtheta=1.0;

% yield stress
sy0=tto;
% saturation stress at infinity
tinf=sy0*ff1b;
% Srain rate
strainRate=([4.005e-3 5.005e-3 6.e-3 8.e-3 10.e-3 14.e-3 20.e-3 0.04
0.4]);
% strainRate=linspace(4.e-3,0.5,10);
strainRateN=0.01;
strainRateT=[epr0.*1.25 epr0.*2.5 epr0.*12.50 epr0.*250];
strainRateM=0.01;

%Abaqus linear parameters
lno=9;
lto=3;
% Abaqus exponential parameter alpha
a=10;

% prevent plasticity being active with fibrillation
if plasticity==1
    % Parameters 'fibrillation' and 'plasticity' are mutually
exclusive
    fibrillation=0;
end

% begin loop through different proportional separations
for k=1:length(theta)
    if k<=length(co)
        ck=k;
    else
        ck=k-length(co);
    end

    propStruct.form=formSet;
    propStruct.km=km;
    propStruct.a=a;
    propStruct.fibrillation=fibrillation;
    propStruct.plasticity=plasticity;
    propStruct.areaFraction=areaFraction;
    propStruct.viscoplasticity=viscoplasticity;
    propStruct.viscoplasticity_old=viscoplasticity_old;
    propStruct.ff1a=ff1a;

```

```

propStruct.ff1b=ff1b;
propStruct.ff2=ff2;
propStruct.dft=dft;
propStruct.eta=eta(1);
propStruct.tno=tno;
propStruct.tto=tto;
propStruct.gno=gno;
propStruct.gto=gto;
propStruct.lno=lno;
propStruct.lto=lto;
propStruct.xi0=xi0;
propStruct.epr0=epr0;
propStruct.m=m;
propStruct.sy0=sy0;
propStruct.tinf=tinf;
propStruct.en=en;
propStruct.xtheta=xtheta;
propStruct.strainRate=strainRate(1);
propStruct.strainRateN=strainRateN;
propStruct.strainRateT=strainRateT(k);
propStruct.strainRateM=strainRateM;

switch elasticBias
    case 1
        UN=[linspace(0,(normal(k)/10),resolution/2)
            linspace((normal(k)/10),normal(k),resolution/2)'];
        UT=[linspace(0,(shear(k)/10),resolution/2)
            linspace((shear(k)/10),shear(k),resolution/2)'];
        UT=UT+(linspace(0,1,length(UT))*1e-9).*max(UT);
        UN=UN+(linspace(0,1,length(UN))*1e-9).*max(UN);
    case 0
        UN=linspace(0,normal(k),resolution)';
        UT=linspace(0,shear(k),resolution)';
end
if theta(k)<0
    UT=UT.*1;
end
mixmode(k).mode=round(rad2deg(theta(k)));
switch unload
    case 2
        unSep=[UN*(pctLoad(1));flipud(pctLoad(1)*UN); ...
            UN*(pctLoad(2));flipud(pctLoad(2)*UN);UN];
        utSep=[UT*(pctLoad(1));flipud(pctLoad(1)*UT); ...
            UT*(pctLoad(2)).*rev1 ;flipud(pctLoad(2)*UT).*rev2
;UT.*rev2];
        mixmode(k).sep=[unSep utSep];
    case 1
        unSep=[UN*(pctLoad(1));flipud(pctLoad(1)*UN);UN];
        utSep=[UT*(pctLoad(1));flipud(pctLoad(1)*UT);UT.*rev1];
        mixmode(k).sep=[unSep utSep];

    case 0
        mixmode(k).sep=[UN UT];
end
clear newCZM_mag
for h=1:length(mixmode(k).sep(:,1))
    mixmode(k).Un(h)=(mixmode(k).sep(h,1));
    mixmode(k).Ut(h)=(mixmode(k).sep(h,2));

outputStruct(:,h)=newCZM_mag(mixmode(k).sep(h,:),h,dInit,propS
truct);

```

```

end
% extract data from the output struct
mixmode(k).Tn=extractfield(outputStruct,'tn');
mixmode(k).Tno=extractfield(outputStruct,'tno');
mixmode(k).Tt=extractfield(outputStruct,'tt');
mixmode(k).Tto=extractfield(outputStruct,'tto');
mixmode(k).Tm=extractfield(outputStruct,'tm');

mixmode(k).Tme=extractfield(outputStruct,'tme');

mixmode(k).Un=extractfield(outputStruct,'un');
mixmode(k).Ut=extractfield(outputStruct,'ut');
mixmode(k).Um=extractfield(outputStruct,'um');
mixmode(k).Umo=extractfield(outputStruct,'umo');

mixmode(k).mode=mean(extractfield(outputStruct,'mode'));
mixmode(k).gmcheck=mean(extractfield(outputStruct,'gmcheck'));
mixmode(k).lmstar=extractfield(outputStruct,'lmstar');
if propStruct.form==2 || propStruct.form==3
    mixmode(k).psi=extractfield(outputStruct,'psi');
end
if areaFraction==true
    mixmode(k).Tm1=extractfield(outputStruct,'tm1');
    mixmode(k).Tm2=extractfield(outputStruct,'tm2');
    mixmode(k).dsfm=extractfield(outputStruct,'dsfm');
    mixmode(k).tmefi=extractfield(outputStruct,'tmefi');
    mixmode(k).tmefm=extractfield(outputStruct,'tmefm');
    mixmode(k).umef=extractfield(outputStruct,'umef');
    mixmode(k).kfp=extractfield(outputStruct,'kfp');
end
if viscoplasticity==true
    mixmode(k).ept=extractfield(outputStruct,'ept');
end
if(fibrillation==true)
    mixmode(k).fi=extractfield(outputStruct,'fi');
    [fi(k),fi_ind(k)]=max(mixmode(k).fi);
end
% find maximum values for T and U
[mixmode(k).TnMax,I]=max(mixmode(k).Tn);
[mixmode(k).TtMax,J]=max(mixmode(k).Tt);
[mixmode(k).TmMax,Kk]=max(mixmode(k).Tm);
mixmode(k).UnBar=mixmode(k).Un(I);
mixmode(k).UtBar=mixmode(k).Ut(J);
mixmode(k).UmBar=mixmode(k).Um(Kk);
mixmode(k).UnMax=max(mixmode(k).Un);
mixmode(k).UtMax=max(mixmode(k).Ut);
mixmode(k).UmMax=max(mixmode(k).Um);
mode(k)=theta(k);
TnMax(k)=mixmode(k).TnMax;
TtMax(k)=mixmode(k).TtMax;
TmMax(k)=mixmode(k).TmMax;

UnMax(k)=mixmode(k).UnMax;
UtMax(k)=mixmode(k).UtMax;
UmMax(k)=mixmode(k).UmMax;
tol=(mixmode(k).Um(end)/resolution);
% current energy calculations
if unload==1 || unload==2
    % index to find where the reload curve joins back up with
the

```

```

    % original traction curve
    if unload==1
        restOfCurve=find(abs(mixmode(k).Um-
(mixmode(k).Um(end)*pctLoad(1)))<tol,1,'last');
        elseif unload==2
            restOfCurve=find(abs(mixmode(k).Um-
(mixmode(k).Um(end)*pctLoad(2)))<tol,1,'last');
        end

figure();plot(mixmode(k).Un(restOfCurve:end),mixmode(k).Tn(restOfCurve:end))

    mixmode(k).Tn_Gcalc=[mixmode(k).Tn(1:resolution-1)
mixmode(k).Tn(restOfCurve:end)];
    mixmode(k).Un_Gcalc=[mixmode(k).Un(1:resolution-1)
mixmode(k).Un(restOfCurve:end)];
    mixmode(k).Tt_Gcalc=[mixmode(k).Tt(1:resolution-1)
mixmode(k).Tt(restOfCurve:end)];
    mixmode(k).Ut_Gcalc=[mixmode(k).Ut(1:resolution-1)
mixmode(k).Ut(restOfCurve:end)];
    mixmode(k).Tm_Gcalc=[mixmode(k).Tm(1:resolution-1)
mixmode(k).Tm(restOfCurve:end)];
    mixmode(k).Um_Gcalc=[mixmode(k).Um(1:resolution-1)
mixmode(k).Um(restOfCurve:end)];
    %
mixmode(k).Gn_s2=ones(1,length(mixmode(k).sep(:,1))*(2/3));
    for g=1:length(mixmode(k).Tn_Gcalc)-1

mixmode(k).Gn(g)=trapz(mixmode(k).Un_Gcalc(1:g+1),mixmode(k).Tn_Gcalc(1:g+1));

mixmode(k).Gt(g)=trapz(mixmode(k).Ut_Gcalc(1:g+1),mixmode(k).Tt_Gcalc(1:g+1));

mixmode(k).Gm(g)=trapz(mixmode(k).Um_Gcalc(1:g+1),mixmode(k).Tm_Gcalc(1:g+1));

        end
        elseif unload==0
            for ggg=2:length(mixmode(k).sep(:,1))

mixmode(k).Gn(ggg)=trapz(mixmode(k).Un(1:ggg),mixmode(k).Tn(1:ggg));

mixmode(k).Gt(ggg)=trapz(mixmode(k).Ut(1:ggg),mixmode(k).Tt(1:ggg));

mixmode(k).Gm(ggg)=trapz(mixmode(k).Um(1:ggg),mixmode(k).Tm(1:ggg));
            end
        end

        for gg=2:length(mixmode(k).sep(:,1))

mixmode(k).Gn_el(gg)=0.5*(mixmode(k).Un(gg))*(mixmode(k).Tn(gg));

mixmode(k).Gt_el(gg)=0.5*(mixmode(k).Ut(gg))*(mixmode(k).Tt(gg));

mixmode(k).Gm_el(gg)=0.5*(mixmode(k).Um(gg))*(mixmode(k).Tm(gg));
        end

    Gn(k)=mixmode(k).Gn(end);
    Gt(k)=mixmode(k).Gt(end);
    Gm(k)=mixmode(k).Gm(end);

```

```

    if(viscoplasticity==true)
        % Decompose the Normal and Tangential total plastic strain

mixmode(k).eptN=mixmode(k).ept.*sin(atan2(mixmode(k).Un,mixmode(k).Ut));

mixmode(k).eptT=mixmode(k).ept.*cos(atan2(mixmode(k).Un,mixmode(k).Ut));

        % Calculate the Elastic Strain
mixmode(k).UmEl=mixmode(k).Um-mixmode(k).ept;
mixmode(k).UnEl=mixmode(k).Un-mixmode(k).eptN;
mixmode(k).UtEl=mixmode(k).Ut-mixmode(k).eptT;
        % Find the intrinsic elastic energy
mixmode(k).GmEl=(mixmode(k).UmEl.*mixmode(k).Tm).*0.5;
mixmode(k).GnEl=(mixmode(k).UnEl.*mixmode(k).Tn).*0.5;
mixmode(k).GtEl=(mixmode(k).UtEl.*mixmode(k).Tt).*0.5;

GnEl(k)=max(mixmode(k).GnEl);
GtEl(k)=max(mixmode(k).GtEl);
GmEl(k)=max(mixmode(k).GmEl);

GnP(k)=Gn(k)-GnEl(k);
GtP(k)=Gt(k)-GtEl(k);
GmP(k)=Gm(k)-GmEl(k);
    end

    if(fibrillation==true)
        [aa,bb]=uniquetol(mixmode(k).Umo);
%         ind_g0_end=find(abs(mixmode(k).Um-
(min(aa)))<tol,1,'last');

        [minValue,ind_g0_end] = min(abs(mixmode(k).Um-min(aa)));
ume_true(k)=mixmode(k).Um(ind_g0_end);

%         ume_true(k)=mixmode(k).Um(ind_g0_end);

        ind_g1_end=fi_ind(k);
%         ind_g2_end=find(abs(mixmode(k).Um-
(max(aa)))<tol,1,'last');

        [minValue,ind_g2_end] = min(abs(mixmode(k).Um-max(aa)));
ume_fibril(k)=mixmode(k).Um(ind_g2_end);

gn_0(k)=trapz(mixmode(k).Un(1:ind_g0_end),mixmode(k).Tn(1:ind_g0_end));

gt_0(k)=trapz(mixmode(k).Ut(1:ind_g0_end),mixmode(k).Tt(1:ind_g0_end));

gm_0(k)=trapz(mixmode(k).Um(1:ind_g0_end),mixmode(k).Tm(1:ind_g0_end));

gn_1(k)=trapz(mixmode(k).Un(1:ind_g1_end),mixmode(k).Tn(1:ind_g1_end))-gn_0(k);

gt_1(k)=trapz(mixmode(k).Ut(1:ind_g1_end),mixmode(k).Tt(1:ind_g1_end))-gt_0(k);

```

```

gm_1(k)=trapz(mixmode(k).Um(1:ind_g1_end),mixmode(k).Tm(1:ind_g1_end
))-gm_0(k);

gn_2(k)=trapz(mixmode(k).Un(1:ind_g2_end),mixmode(k).Tn(1:ind_g2_end
))-gn_1(k);

gt_2(k)=trapz(mixmode(k).Ut(1:ind_g2_end),mixmode(k).Tt(1:ind_g2_end
))-gt_1(k);

gm_2(k)=trapz(mixmode(k).Um(1:ind_g2_end),mixmode(k).Tm(1:ind_g2_end
))-gm_1(k);

gn_3(k)=trapz(mixmode(k).Un(ind_g2_end:end),mixmode(k).Tn(ind_g2_end
:end));

gt_3(k)=trapz(mixmode(k).Ut(ind_g2_end:end),mixmode(k).Tt(ind_g2_end
:end));

gm_3(k)=trapz(mixmode(k).Um(ind_g2_end:end),mixmode(k).Tm(ind_g2_end
:end));
end

gmcheck(k)=mixmode(k).gmcheck(end);
Gsum(k)=mixmode(k).Gt(end)+mixmode(k).Gn(end);
Umo(k)=mean(mixmode(k).Umo);
TmMax(k)=mixmode(k).TmMax;
lmstar(k)=mean(mixmode(k).lmstar);
tto_sim(k)=mean(mixmode(k).Tto);

% Instantaneous incremental dissipation (dPhi) (Cazes et al.
2009)

diffUt=diff(mixmode(k).Ut);
diffTt=diff(mixmode(k).Tt);

diffUn=diff(mixmode(k).Un);
diffTn=diff(mixmode(k).Tn);

if(viscoplasticity==true)

diffUnEl=diff(mixmode(k).UnEl);
diffUtEl=diff(mixmode(k).UtEl);
diffUmEl=diff(mixmode(k).UmEl);

diffeptN=diff(mixmode(k).eptN);
diffeptT=diff(mixmode(k).eptT);

diffPhise=((mixmode(k).Tn(2:end).*diffUnEl)+(mixmode(k).Tt(2:end).*
diffUtEl))...
-
((diffTn.*mixmode(k).UnEl(2:end))+(diffTt.*mixmode(k).UtEl(2:end)))
.*0.5;

diffPhisp=((mixmode(k).Tn(2:end).*diffeptN)+(mixmode(k).Tt(2:end).*d
iffeptT));

```

```

        diffPhi=diffPhise+diffPhisp;
    else

diffPhi=(( (mixmode(k).Tn(2:end).*diffUn)+(mixmode(k).Tt(2:end).*diff
Ut))...
-
((diffTn.*mixmode(k).Un(2:end))+(diffTt.*mixmode(k).Ut(2:end)))).*0.
5;

    end

%% Non-proportional loading paths
resolution=1000;
% -----
plotOn=1;
formSet=2;           % 0 - linear // 1 - exponential // 2 -
squared exponential // 3 abaqus disp exp. softening
dInit=0;             % 0 for same as G // 1 for modified abaqus
plotAbaqus=0;
% Fibrillation --> 1 = Add Fibrillation // 0 - No Fibrillation
fibrillation=0;
% Pseudoplasticity?
plasticity=0;
% Area fraction eta?
areaFraction=0;
% Viscoplasticity_old?
viscoplasticity_old=0;
% Viscoplasticity
viscoplasticity=1;
% -----
% CZM parameters
tno=0.2;
tto=1.0;
km=10.0;
% gno=20e-3;
gto=100e-3;
% gno=gto.*(tno/tto).^2;
gno=gto.*(tno/tto);
% gno=gto;

%Abaqus linear parameters
lno=9;
lto=3;
% Abaqus exponential parameter alpha
a=10;
delt=tto/km;
deln=tno/km;
xi0=pi/16;
lmstar=5;
deltaT=linspace(0,1.0,11);
deltaN=linspace(1.0,1.0,length(deltaT));

M2M1switch=1; %1=m2 the m1 // 0=m1 then m2
% Fibrillation parameters
ff1a=1.0;
ff1b=1.2;
ff2=0.25;
dft=0.35;

```

```

% Elastic Fibrillation parameters
% ff1a=5;
% ff2=0.5;
% dft=0.75;
eta=[0.0,0.25,0.5,0.75,1.0];

% Viscoplasticity parameters -----
% epsilon p zero (affects spread of rates)
% smaller=less sensitive to change in rate (sensitivity parameter)
epr0=0.004;
% strain rate hardening exponent 'm'
m=30.0;
% epsilon ^n (similar to initial hardening slope) smaller=stiffer
% how quickly you reach the plateau
en=0.75;
% theta - to set backward euler or forard
xtheta=1.0;
% yield stress
sy0=tto;
% saturation stress at infinity
tinf=sy0*ff1b;
% Srain rate
strainRate=[4.005e-3 8.e-3 0.04 0.4]);
strainRateN=epr0/0.1;
strainRateT=epr0/0.1;
strainRateM=epr0/0.1;

for g=1:length(deltaT)

    propStruct.form=formSet;
    propStruct.km=km;
    propStruct.a=a;
    propStruct.fibrillation=fibrillation;
    propStruct.plasticity=plasticity;
    propStruct.areaFraction=areaFraction;
    propStruct.viscoplasticity=viscoplasticity;
    propStruct.viscoplasticity_old=viscoplasticity_old;
    propStruct.ff1a=ff1a;
    propStruct.ff1b=ff1b;
    propStruct.ff2=ff2;
    propStruct.dft=dft;
    propStruct.eta=eta(1);
    propStruct.tno=tno;
    propStruct.tto=tto;
    propStruct.gno=gno;
    propStruct.gto=gto;
    propStruct.lno=lno;
    propStruct.lto=lto;
    propStruct.xi0=xi0;

    propStruct.epr0=epr0;
    propStruct.m=m;
    propStruct.sy0=sy0;
    propStruct.tinf=tinf;
    propStruct.en=en;
    propStruct.xtheta=xtheta;
    propStruct.strainRate=strainRate(1);
    propStruct.strainRateN=strainRateN(1);
    propStruct.strainRateT=strainRateT(1);
    propStruct.strainRateM=strainRateM(1);

```

```

loopLength=1;
% begin loop through different constant mixed mode separations
for k=1:loopLength

    if M2M1switch==1 % m2 then m1
        UN=[linspace(0,0,resolution)
linspace(0,deltaN(g),resolution)]';
        UT=[linspace(0,deltaT(g),resolution)
linspace(deltaT(g),deltaT(g),resolution)]';
    elseif M2M1switch==0 % m1 then m2
        UT=[linspace(0,0,resolution)
linspace(0,deltaT(g),resolution)]';
        UN=[linspace(0,deltaN(g),resolution)
linspace(deltaN(g),deltaN(g),resolution)]';
    end

    M2M1(g).sep=[UN UT];
    clear newCZM_mag;
    for h=1:length(UN)
        M2M1(g).Un(h)=UN(h);
        M2M1(g).Ut(h)=UT(h);

outputStruct(:,h)=newCZM_mag(M2M1(g).sep(h,:),h,dInit,propStruct);
    end

% extract data from the output struct
M2M1(g).Tn=extractfield(outputStruct,'tn');
M2M1(g).Tt=extractfield(outputStruct,'tt');
M2M1(g).Tm=extractfield(outputStruct,'tm');
M2M1(g).tme=extractfield(outputStruct,'tme');

M2M1(g).Un=extractfield(outputStruct,'un');
M2M1(g).Ut=extractfield(outputStruct,'ut');
M2M1(g).Um=extractfield(outputStruct,'um');
M2M1(g).UmMax=extractfield(outputStruct,'umMax');
M2M1(g).Umo=extractfield(outputStruct,'umo');
%     ume(g)=M2M1(g).Umo;
M2M1(g).mode=(extractfield(outputStruct,'mode'));
M2M1(g).meanmode=mean(extractfield(outputStruct,'mode'));
M2M1(g).gmcheck=mean(extractfield(outputStruct,'gmcheck'));
M2M1(g).lmstar=mean(extractfield(outputStruct,'lmstar'));

if(viscoplasticity==true)
    M2M1(g).dtime=(extractfield(outputStruct,'dtime'));
    M2M1(g).dun=(extractfield(outputStruct,'dun'));
    M2M1(g).dut=(extractfield(outputStruct,'dut'));
    M2M1(g).dum=(extractfield(outputStruct,'dum'));
    M2M1(g).ept=(extractfield(outputStruct,'ept'));
end

lmstar1(g)=M2M1(g).lmstar;
% find maximum values for T and U
[M2M1(g).TnMax,I]=max(M2M1(g).Tn);
[M2M1(g).TtMax,J]=max(M2M1(g).Tt);
[M2M1(g).TmMax,Kk]=max(M2M1(g).Tm);
M2M1(g).UnBar=M2M1(g).Un(I);
M2M1(g).UtBar=M2M1(g).Ut(J);
M2M1(g).UmBar=M2M1(g).Um(Kk);
M2M1(g).Gn=trapz(M2M1(g).Un,M2M1(g).Tn);
M2M1(g).Gt=trapz(M2M1(g).Ut,M2M1(g).Tt);
M2M1(g).Gm=trapz(M2M1(g).Um,M2M1(g).Tm);

```

```

Gn(g)=M2M1(g).Gn;
Gt(g)=M2M1(g).Gt;
Gm(g)=M2M1(g).Gm;
Gsum(g)=M2M1(g).Gt+M2M1(g).Gn;
UtBar(g)=M2M1(g).UtBar;
UtMax(g)=max(UT);
UnMax(g)=max(UN);
UnMin(g)=min(UN);
UnEnd(g)=UN(end);
UnBar(g)=M2M1(g).UnBar;
TtMax(g)=M2M1(g).TtMax;
TnMax(g)=M2M1(g).TnMax;
TmMax(g)=M2M1(g).TmMax;
mode=M2M1(g).mode;
tme=M2M1(g).tme;

% Instantaneous incremental dissipation (dPhi) (Cazes et al.
2009)
diffUt=diff(M2M1(g).Ut);
diffTt=diff(M2M1(g).Tt);

diffUn=diff(M2M1(g).Un);
diffTn=diff(M2M1(g).Tn);

if(viscoplasticity==true)
    % Decompose the Normal and Tangential total plastic
strain
M2M1(g).eptN=M2M1(g).ept.*sin(atan2(M2M1(g).Un,M2M1(g).Ut));
M2M1(g).eptT=M2M1(g).ept.*cos(atan2(M2M1(g).Un,M2M1(g).Ut));
    % Calculate the Elastic Strain
M2M1(g).UmEl=M2M1(g).Um-M2M1(g).ept;
M2M1(g).UnEl=M2M1(g).Un-M2M1(g).eptN;
M2M1(g).UtEl=M2M1(g).Ut-M2M1(g).eptT;

diffUnEl=diff(M2M1(g).UnEl);
diffUtEl=diff(M2M1(g).UtEl);
diffUmEl=diff(M2M1(g).UmEl);

diffeptN=diff(M2M1(g).eptN);
diffeptT=diff(M2M1(g).eptT);
    % Find the intrinsic elastic energy
M2M1(g).GmEl=(M2M1(g).UmEl.*M2M1(g).Tm).*0.5;
M2M1(g).GnEl=(M2M1(g).UnEl.*M2M1(g).Tn).*0.5;
M2M1(g).GtEl=(M2M1(g).UtEl.*M2M1(g).Tt).*0.5;

GnEl(g)=max(M2M1(g).GnEl);
GtEl(g)=max(M2M1(g).GtEl);
GmEl(g)=max(M2M1(g).GmEl);

GnP(g)=Gn(g)-GnEl(g);
GtP(g)=Gt(g)-GtEl(g);
GmP(g)=Gm(g)-GmEl(g);

diffPhise=((M2M1(g).Tn(2:end).*diffUnEl)+(M2M1(g).Tt(2:end).*diffUt
El))...
-
((diffTn.*M2M1(g).UnEl(2:end))+(diffTt.*M2M1(g).UtEl(2:end)))...
).*0.5;

```

```

diffPhisp=((M2M1(g).Tn(2:end).*diffeptN)+(M2M1(g).Tt(2:end).*diffept
T));

        diffPhi=diffPhise+diffPhisp;
    else

diffPhi=(( (M2M1(g).Tn(2:end).*diffUn)+(M2M1(g).Tt(2:end).*diffUt))..
.
-
((diffTn.*M2M1(g).Un(2:end))+(diffTt.*M2M1(g).Ut(2:end))))*.0.5;

        end

function
[outputStruct]=newCZM_mag(separationVector,inc,dInit,propStruct)

persistent umMax fibril plastic eps_p stresso sn
delta_plastic_strain sdv1 umCrit eps epsCrit epto...
    sighto epdotto xum xun xut sdvUnload umCrit2 flag1
if inc==1
    umMax=0;
    fibril=0;
    plastic=0;
    %    try
    %    clear stresso eps epsCrit sn delta_plastic_strain sdv1
eps eps_p
    %    end
    eps_p=0;
    eps=0;
    sdv1=0;
    stresso=[];
    eps=0;
    epsCrit=0;
    sn=0;
    delta_plastic_strain=0;
    sdvUnload=0;
    umCrit2=100;
    flag1=0;
end
% disp(['----- inc=' sprintf('%2.0f',inc)])
format long
tno=propStruct.tno;
tto=propStruct.tto;
gno=propStruct.gno;
gto=propStruct.gto;
% delta m star for linear formulation
lno=propStruct.lno;
lto=propStruct.lto;
form=propStruct.form;
fibrillation=propStruct.fibrillation;
plasticity=propStruct.plasticity;
areaFraction=propStruct.areaFraction;
viscoplasticity_old=propStruct.viscoplasticity_old;
viscoplasticity=propStruct.viscoplasticity;

if(areaFraction==true)
    eta=propStruct.eta;
else
    eta=0;
end

```

```

ff1a=propStruct.ff1a;
ff1b=propStruct.ff1b;
ff2=propStruct.ff2;
dft=propStruct.dft;

% exponential parameter for abaqus exponential softening
a=propStruct.a;
xi0=propStruct.xi0;
km=propStruct.km;
knoc=km*10.0;

% viscoplastic parameters
epr0=propStruct.epr0;
m=propStruct.m;
tinf=propStruct.tinf;
en=propStruct.en;
xtheta=propStruct.xtheta;
strainRate=propStruct.strainRate;
strainRateN=propStruct.strainRateN;
strainRateT=propStruct.strainRateT;
strainRateM=propStruct.strainRateM;

tft=tto/ff1a;
tfn=tno/ff1a;
kf=tft/dft;
dfn=tfn/kf;
deln=tno/km;
delt=tto/km;

if(fibril==1)
    tto=tft;
    tno=tfn;
    delt=dft;
    deln=dfn;
    km=kf;
    gno=tfn*dfn/2+gno/ff1a/ff2;
    gto=tft*dft/2+gto/ff1a/ff2;
end

if(plasticity==true)
    kfpCur=0;
    dsfm=0;
    tmefi=0;
    tmefm=0;
    umef=0;
end

un=separationVector(:,1);
ut=separationVector(:,2);

% calculate the magnitude of the separation Vector
if un>=0
    um=sqrt(un^2+ut^2);
    %calculate mode mixity based on input separation vector
    xi=atan2(un,abs(ut));
else
    um=sqrt(ut^2);
    %if in overclosure treat as a pure mode II
    xi=atan2(0,abs(ut));
end

```

```

% Overclosure hardening
if un<0.0
    tn=un*knoc;
%     tto=tto + tto*(fflb-1.0)*(1-exp(((tn.*1.0e+6/tno)/km)));
end

% define the initiation criteria // yield surface

kap1=((tto-tno)/km)/(1-exp(-(pi/2)/ xi0 ));
switch dInit
    case 0
        ume=(tto/km)-kap1*(1-exp(-xi/xi0));
    case 1
        ume=deln*sqrt(1/(sin(xi)^2+(deln/delt)^2*cos(xi)^2));
end
% check if um>umMax
if sqrt(um^2)>umMax
    umMax=sqrt(um^2);
end

tme=ume*km;
% description of how G changes as a fn of xi
gtohat=gto-(0.5*tto*delt);
gnohat=gno-(0.5*tno*deln);
kap=(gtohat-gnohat)/(1-exp(-(pi/2)/xi0));
gmhat=gtohat-kap*(1-exp(-xi/xi0));
gm=gmhat+(1/2)*tme*ume;

% Fibrillation traction at start
tfit=max([tto tno])*ffla;
% Fibrillation traction at end
tfft=max([tto tno])*fflb;
% platic fibrillation stiffness
kfp=(tfft-tfit)/dft;
tmefi=km*ume*ffla;
% mixed mode fibrillation max traction
tmefm=km*ume*fflb;
% Max fibrillation displacement
umef=(tmefm-tmefi)/kfp;

sy0=km*ume;
sinf=sy0*fflb;
fi=0;
%% calculate magnitude of the traction based on
% tme=km*ume*(1-eta);
tme=km*ume;
% tme2=km*ume*eta;
switch form
    case 1 % linear form
        lmstar=(2*gm/tme);
    case 2 % exponential softening
        lmstar=gm/tme-ume/2;
    case 3 % squared exponential softening
        lmstar=(2*gm/(tme*sqrt(pi)))-(ume/sqrt(pi));
    case 4
        kap=(lto-lno)/(1-exp(-(pi/2)/xi0));
        lmstar=lto-kap*(1-exp(-xi/xi0));
end

% mixed mode Fibrillation energy reduction factor

```

```

dsfm=lmstar*ff1b*ff2;

if (umMax<ume)
    tm1=km*um*(1-eta);
    tm2=km*um*eta;
    psi=0;
    if form==4
        tn=km*un;
        tt=km*ut;
    end
else
    switch form
        case 1 % linear form
            if umMax<lmstar
                tm=(-tme/(lmstar-ume))*umMax+(tme*lmstar)/(lmstar-
ume)*um/umMax;
            else
                tm=0;
            end
        case 2 % exponential softening
            psi=exp(-((umMax-ume)/lmstar))*(um/umMax);
            tm1=tme*(psi)*(1-eta);
            tm2=0;
        case 3 % squared exponential softening
            psi=exp(-((umMax-ume)/lmstar)^2)*(um/umMax);
            tm1=tme*psi;
            tm2=0;
        case 4 % abaqus exponential softening (displacement based)
            D=1-(ume/umMax)*(1-((1-exp(-a*((umMax-ume)/(lmstar-
ume))))/(1-exp(-a)))));
            if um<lmstar
                tm=km*um*(1-D);
                tn=km*un*(1-D);
                tt=km*ut*(1-D);
            else
                tm=0;
                tn=0;
                tt=0;
            end
        end
    end

    if (fibrillation==true)
        if (fibril==0)
            if (tm1<=(kf*um) && um/umMax==1)
                tm1=kf*um;
                fibril=1;
                fi=um; % fibril initiation
            end
        end
    end

    if (plasticity==true)
        if (areaFraction==true)
            if plastic==0
                Fibrillation regime
                tm2=(kfp*umMax+tme*fi)*eta;
                plastic=1;% set new traction calculations to
            end
            if plastic==1
                if umMax<=umef %if disp is below the final plastic
                    fibrillation displacement

```



```

                                % Begin newton-raphsoin iterations and loop until
deltadep
                                tol=1.e-12;
                                while (deltadep>=tol)
                                    % keep track of the current iteration
                                    iter=iter+1;

                                    dsn=((sinf-sy0)-sn)*1/en;
                                    % Yield term
                                    xterm=(trstress-(km*delta_plastic_strain)-sn-sy0);

                                    phi=((epr0/sy0^m)*xterm^m);
                                    dphidp=(-km*(epr0/sy0^m)*m*xterm^(m-1));
                                    dphidr=(-1.*(epr0/sy0^m)*m*xterm^(m-1));
                                    deltadep=( phi-
(delta_plastic_strain/dtime))/((1/dtime)-dphidp-dsn*dphidr));
                                    delta_plastic_strain=delta_plastic_strain+deltadep;
                                    % Strain hardening
                                    sn=sn0+dsn*delta_plastic_strain;

                                end
                            end
                        end

                    if (inc==1)
                        delta_elastic_strain=delta_strain-delta_plastic_strain ;
                        dstress=km*delta_elastic_strain;
                        stress=dstress;
                    else
                        delta_elastic_strain=delta_strain-delta_plastic_strain ;
                        dstress=km*delta_elastic_strain;
                        stress=stress+dstress;

                    end
                    stresso(inc)=stress;

                    delta_elastic_strain_out=delta_elastic_strain;
                    depo=delta_plastic_strain;
                    shout=sn;
                    dsho=dsn;
                    dstresso=dstress;

                    tm1=stresso(inc);
                    % If threshold stress is exceeded enter softening regime

                    if tm1>=tmefm
                        if sdv1==0
                            umCrit=um;
                            epsCrit=eps(inc);
                            sdv1=1;
                        end
                        tm1=tmefm*exp(-(((eps_i-epsCrit)/(dsfm/cl))));
                    end

                    tm2=0;

                end
            %% New viscoplasticity law

            if(viscoplasticity==true)
                q1=1.0000000000000000;
            end
        end
    end
end

```

```

q2=2.0000000000000000;
xum(inc)=um;
xun(inc)=un;
xut(inc)=ut;

%      convert current um into current strain increment eps_i
cl=1;
eps_i=um/cl;
eps(inc)=eps_i;

% Assumed constant strain rate so dstrani is constant

if (inc==1)
    % Initialise stress
    delta_strain=eps(inc);
    epto=0;
    ept=epto;
    stresso(inc)=0.0;
    dum=xum(inc);
    dun=xun(inc);
    dut=xut(inc);

    if(dun==0)
        dtime=dut./strainRateT;
    elseif(dut==0)
        dtime=dun./strainRateN;
    elseif(dun~=0 && dut~=0)
        dtime=dum./strainRateM;
    end

    sigt=km*um;
    sight=0;
    sighto=sight;
    epdott=0;
    epdotto(inc)=epdott;
else
    sigt=stresso(inc-1);
    ept=epto;
    sight=sighto;
    epdott=epdotto(inc-1);
    dstrani=eps(inc)-eps(inc-1);
    delta_strain = dstrani;
    dum=xum(inc)-xum(inc-1);
    dun=xun(inc)-xun(inc-1);
    dut=xut(inc)-xut(inc-1);

    if(dun==0)
        dtime=abs(dut./strainRateT);
    elseif(dut==0)
        dtime=abs(dun./strainRateN);
    elseif(dun~=0 && dut~=0)
        dtime=abs(dum./strainRateM);
    else
        dtime=abs(dun./strainRateN);
        if(dtime==0)
            dtime=abs(dut./strainRateT);
        end
    end
    strainRate=dum./dtime;
    td=xtheta*dtime;

```

```

        % Calculate rate tangent solution as initial guess for
newton raphson
    % scheme
    if(sight==0)
        deprds=0;
        deprdsh=0;
    else
        deprds=epr0*m*sigt^(m-1.0)*sight^(-m);
        deprdsh=-epr0*m*(sigt*sight^-1.0)^m*sight^-1.0;
    end
    dshr=(sinf-sy0)/en*exp(-ept/en);
    depssp=(deprds*dum*km*td+dttime*epdott)*...
        (deprds*km*td-deprdsh*dshr*td+1.0)^-1.0;

    % Newton raphson control parameters
    tol=1.0e-7;
    minIter=5;
    maxIter=1.0e+4;
    res=999;
    deps=depssp;
    deps1=0;
    iter=0;

    if(sdv1~=1)
        if(dum>0)
            while ((res>=tol) || (iter<=minIter))
                deps=deps1;
                iter=iter+1;
                if(iter>=maxIter)
                    break
                end
                dsignr=km*(dum-deps);
                dsighnr=sy0+(sinf-sy0)*(1.0-exp(-
(ept+dttime*deps)/en))-sight;
                sighnr=sy0+(sinf-sy0)*(1.0-exp(-
(ept+dttime*deps)/en));
                ff=deps-(q1-xtheta)*dttime*epdott-
xtheta*dttime*epr0*...
                    ((sigt+dsignr)/(sight+dsighnr))^m;
                term1=(sighnr*(-q1*km)-(sigt+dsignr)*(sinf-
sy0)/(-q1*en)...
                    *exp(-(ept+dttime*deps)/en))/(sighnr^q2);
                term2=m*xtheta*dttime*epr0*((sigt+dsignr)/sighnr)^(m-q1);
                gradff=q1-term2*term1;
                deps1=deps-ff/gradff;
                if(iter==1)
                    res=999;
                else
                    res=abs((deps1-deps)/deps);
                end
            end
        else
            deps1=0;
        end
    end

    depssp=deps1;
    if(um>0)
        epdott=depssp/dttime;
        if(isnan(epdott))

```

```

        epdott=0;
    end
else
    epdott=0;
end

ept=ept+depsp;
sight=sy0+(sinf-sy0)*(q1-exp(-ept/en));
dsig=km*(dum-depsp);

if (sdvUnload~=1)
    sigt=sigt+dsig;
elseif (sdvUnload==1)
    if (um<(ept))
        sigt=0;
    else
        sigt=sigt+dsig;
    end
end

if (sigt<0)
    sigt=0;
    sdvUnload=1;
end

epdotto(inc)=epdott;
epto=ept;
stresso(inc)=sigt;
tm1=sigt;
sighto=sight;

end

tol=0.001;

if (tm1>=tme fm-tol)

    if sdv1==0
        umCrit=um;
        epsCrit=eps(inc);
        sdv1=1;
    end
end

if (sdv1==1)
    if (xum(inc)<xum(inc-1))
        tm1=(tme fm*exp(-((umMax-umCrit)/(dsfm))))/(umMax-
ept))*(um-ept);
        if (tm1<=0)
            tm1=0;
            sdvUnload=2;
            if (flag1==0)
                umCrit2=um;
                flag1=1;
            end
        end
    else
        if (sdvUnload~=2)
            tm1=tme fm*exp(-((umMax-umCrit)/(dsfm)));
        else

```

```

        if (um<ept)
            tm1=0;
        elseif (um<umMax)
            tm1=(tmefm*exp(-(((umMax-
umCrit)/(dsfm))))/(umMax-ept))*(um-ept);
        else
            tm1=tmefm*exp(-(((umMax-umCrit)/(dsfm))));
        end
    end
end
end

    tm2=0;

    stresso(inc)=tm1;
end

tm=tm1+tm2;
if form ~=4
    if un>=0.0
        tn=tm*sin(xi);
    else
        tn=un*knoc;
    end

    tt=tm*cos(xi);

end

if (ut<0)
    tt=tt*-1;
end

%% output section
outputStruct.tn=tn;
outputStruct.tt=tt;
outputStruct.tm=tm;
outputStruct.tm1=tm1;
outputStruct.tm2=tm2;
if (fibrillation==true)
    outputStruct.fi=fi;
end
if (areaFraction==true)
    outputStruct.kfp=kfp;
    outputStruct.umef=umef;
    outputStruct.tmeffi=tmeffi;
    outputStruct.tmefm=tmefm;
    outputStruct.dsfm=dsfm;
end
if (viscoplasticity==true)
    outputStruct.dtime=dtime;
    outputStruct.dun=dun;
    outputStruct.dut=dut;
    outputStruct.dum=dum;
    outputStruct.ept=ept;
    outputStruct.strainRate=strainRate;
    outputStruct.strainRateN=strainRateN;
    outputStruct.strainRateT=strainRateT;
end
if (viscoplasticity_old==true)

```

```

        outputStruct.delta_strain=delta_strain;
        outputStruct.delta_elastic_strain=delta_elastic_strain;
        outputStruct.delta_plastic_strain=delta_plastic_strain;
        outputStruct.eps=eps(inc);
        outputStruct.eps_y=eps_y;
        outputStruct.cl=cl;
end
outputStruct.tno=tno;
outputStruct.tto=tto;
outputStruct.tme=tme;
outputStruct.un=un;
outputStruct.ut=ut;
outputStruct.um=um;
outputStruct.umMax=umMax;
outputStruct.umo=ume;
outputStruct.gmcheck=gm;
outputStruct.mode=xi;
outputStruct.lmstar=lmstar;
if form==2 || form==3
    outputStruct.psi=psi;
else
    outputStruct.psi=0;
end
end
end

```

The following UINTER files were developed in Chapter 4 and used throughout the thesis. 2D & 3D UINTERs are presented for the exponential softening model presented in Chapter 4.

2D Exponential Cohesive Zone Model UINTER:

```

subroutine uinter(stress,ddsddr,amki,amski,flux,ddfddt,ddsddt,
1   ddfddr,statev,sed,sfd,spd,svd,scd,pnewdt,rdisp,drdisp,
2   temp,dtemp,predef,dpred,time,dtime,freqr,ciname,slname,
3   msname,props,coords,alocaldir,drot,area,chrlngth,node,ndir,
4   nstatv,npred,nprops,mcrd,kstep,kinc,kit,linper,lopenclse,
5   lstate,lspi,lprint)
c
include 'aba_param.inc'
c
dimension stress(ndir),ddsddr(ndir,ndir),flux(2),ddfddt(2,2),
$   ddsddt(ndir,2),ddfddr(2,ndir),statev(nstatv),rdisp(ndir),
$   drdisp(ndir),temp(2),dtemp(2),predef(2,npred),dpred(2,npred),
$   time(2),props(nprops),coords(mcrd),alocaldir(3,3),
$   drot(2,2),amki(ndir,ndir),amski(ndir,ndir)
character*80 ciname,slname,msname
c
real*8 q2,q1,tno,tto,gno,gto
real*8 km,zeta,knoc,un,ut,dun,dut
real*8 um,xi,xio,deln,delt,ue
real*8 ephi,expi,kap,gm,kap1,ume
real*8 ummax,tme,lms,tm

```

```

real*8 j11,j12,j21,j22,tt,tn
real*8 q0,viscN,viscT, uta
real*8 pi,dviscN,dviscT
logical writeOn
c ! Set writeOn to true or false if debugging for printed statements to .dat
file
writeOn=.false.
      q2=2.d0
      q1=1.d0
      q0=0.d0
      pi=4.d0*atan(1.d0)
c
c! -----
-
c  Uinter developed by Brian FitzGibbon - National University of Ireland, Galway
c  email:      brian.fitzgibbon@nuigalway.ie
c  FitzGibbon, B., & McGarry, P. (2020, July 10).
c  Development of a novel test method to investigate
c  mode II fracture and dissection of arteries.
c  https://doi.org/10.31224/osf.io/d3jbr
c! -----
-
c
c!  interface strengths in mode I and mode II
      tno=props(1)
      tto=props(2)
c!  fracture energy in mode I and mode II
      gno=props(3)
      gto=props(4)
c!  initial elastic stiffness
      km=props(5)
c!  overclosure penalty stiffness (a good starting point is km*10 or 100)
      knoc=props(6)
c!  optional viscosity term (This model works best without viscosity i.e
zeta=0.0)
      zeta=props(7)
c!  ocf - overclosure hardening factor (eg ocf=1.5 means tto will scale to
tto*1.5)
      ocf=props(8)
c!  kocs - overclosure hardening sensitivity factor (how quickly ocf scales)
      kocs=props(9)
c
      un=rdisp(1)*-1.
      ut=rdisp(2)
      dun=drdisp(1)*-1.
      dut=drdisp(2)
c
c      ! Optional "overclosure hardening"
      if(un.lt.q0)then
          tn=un*knoc
c!  ocf is the overclosure factor (eg ocf=1.5 means tto will scale to
tto*1.5)
c!  kocs is the sensitivity
          tto=tto+tto*(ocf-q1)*(q1-exp(((tn*kocs/tno)/km)))
          end if
c
      deln=tno/km
      delt=tto/km
c
      viscN=(zeta*tno*dun/(dtime*deln))
      viscT=(zeta*tto*dut/(dtime*delt))
c
      dviscN=zeta*tno/deln/dtime
      dviscT=zeta*tto/delt/dtime
c
c!  xio is the shaping parameter that describes gm as a function of xi

```

```

xio=pi/16.0
c
if(un.gt.q0)then
  um=sqrt((un*un)+(ut*ut))
else
  um=abs(ut)
end if
c
if (kinc.eq.1)then
  statev(7)=um
end if
c
c! calculate mode mixity
if(um.eq.q0)then
  xi=0.0
  ephi=1.0
else if(un.le.q0)then
  xi=0.0
  ephi=1.0
else if(ut.eq.q0)then
  xi=pi/2.0
  ephi=exp(-xi/xio)
else
  xi=abs(atan(un/abs(ut)))
  ephi=exp(-xi/xio)
end if
c
expi=q1-exp(-(pi/2.0)/xio)
c! describe how gm changes as a fn of mode (xi)
kap=(gto-gno)/(expi)
gm=gto-kap*(q1-ephi)
c! define the initiation criteria
kap1=((tto-tno)/km)/(1.0-exp(-(pi/2.0)/xi0))
c! ume is the separation magnitude at the elastic limit
if(un.gt.q0)then
  ume=(tto/km)-kap1*(1.0-ephi)
else
  ume=delt
end if
c
c! update ummax if necessary
if (um.gt.statev(7)) then
  statev(7)=um
end if

c! magnitude of the traction at the elastic limit
tme=km*ume
c! parameter lms shapes the damage curve
lms=(gm/(km*ume))+(ume/2.0)
c
c!----- ELASTIC REGION
c
if (statev(7).lt.ume) then

  statev(9)=-1
  statev(10)=tme
  tm=km*um
  dtmddelm=km
c
c!----- DAMAGE REGION

else if (statev(7).ge.ume) then
c
  tm=ume*km*exp(-(statev(7)-ume)/lms)*um/statev(7)
  dtmddelm=-km*ume/lms*exp((-statev(7)-ume)/lms)
c

```

```

statev(9)=1
c
  if (abs((tm-statev(10))).gt.(tme*0.2))then
c! Prevent Abaqus from skipping the damage curve
  pnewdt=0.1
    if (writeOn) then
      write(6,*)'*** PnewDT=0.1 ***'
    end if
  end if
c
statev(10)=tm

  if((UM/STATEV(7)).LT.Q1)then
c! Handle "unloading during damage" scenarios
  dtmddelm=km*(exp(-(statev(7)-ume)/lms)*um/statev(7))
  end if

end if

c
c!----- JACOBIAN DECOMPOSITION
c
  DTNDUN1=((UN/UM)*(UN/UM))*DTMDDELM
  DTNDUN2=((UM*UM)-(UN*UN))/(UM*UM*UM)*tm
  DTNDUN=DTNDUN1+DTNDUN2

  J11=DTNDUN
c
  DTTDUT1=((UT/UM)*(UT/UM))*DTMDDELM
  DTTDUT2=((UM*UM)-(UT*UT))/(UM*UM*UM)*TM
  DTTDUT=DTTDUT1+DTTDUT2

  J22=DTTDUT
c
  DTNDUT1=((UT/UM)*(UN/UM))*DTMDDELM
  DTNDUT2=((-(UT*UN))/(UM*UM*UM))*TM
  DTNDUT=(DTNDUT1+DTNDUT2)

  J12=DTNDUT
c
  DTTDUN1=((UN/UM)*(UT/UM))*DTMDDELM
  DTTDUN2=((-(UN*UT))/(UM*UM*UM))*TM
  DTTDUN=(DTTDUN1+DTTDUN2)

  J21=DTTDUN
c
c!-----
c
  tn=tm*sin(xi)+viscN
  tt=tm*cos(xi)+viscT
c
  if (un .lt. q0) then ! penalise overclosure through the knoc penalty
stiffness
  tn=un*knoc
  j11=knoc
end if
c
  if (ut .le. q0) then
  tt=tt * -q1
end if
c
  if(kinc.eq.0)then
  tn=q0
  tt=q0
  j11=q0
  j12=q0
  j21=q0

```

```

        j22=q0
    end if
c
    ddsddr(1,1)=j11+dviscN
    ddsddr(1,2)=j12
    ddsddr(2,1)=j21
    ddsddr(2,2)=j22+dviscT
c
    stress(1)=tn*-q1
    stress(2)=tt
c
    statev(1)=tn
    statev(2)=tt
    statev(3)=tm
    statev(4)=un
    statev(5)=ut
    statev(6)=sqrt((un*un)+(ut*ut))
c! statev(7) is the max separation achieved (defined in the code above)
    statev(8)=xi ! The separation based mode
c! statev(9) is a damage flag.
c
    if(writeOn)then
        write(6,*)'lms=',lms
        write(6,*)'tno=',tno
        write(6,*)'ddsddr(1,1)=' ,ddsddr(1,1)
        write(6,*)'ddsddr(1,2)=' ,ddsddr(1,2)
        write(6,*)'ddsddr(2,1)=' ,ddsddr(2,1)
        write(6,*)'ddsddr(2,2)=' ,ddsddr(2,2)
    end if

    return
end

```

3D Exponential Cohesive Zone Model UINTER:

```
subroutine uinter(stress,ddsddr,amki,amski,flux,ddfddt,ddsddt,
1 ddfddr,statev,sed,sfd,spd,svd,scd,pnewdt,rdisp,drdisp,
2 temp,dtemp,predef,dpred,time,dtime,freqr,ciname,slname,
3 msname,props,coords,alocaldir,drot,area,chrlngh,node,ndir,
4 nstatv,npred,nprops,mcrd,kstep,kinc,kit,linper,lopclose,
5 lstate,lsdi,lprint)
c
c   include 'aba_param.inc'
c
c   dimension stress(ndir),ddsddr(ndir,ndir),flux(2),ddfddt(2,2),
$   ddsddt(ndir,2),ddfddr(2,ndir),statev(nstatv),rdisp(ndir),
$   drdisp(ndir),temp(2),dtemp(2),predef(2,npred),dpred(2,npred),
$   time(2),props(nprops),coords(mcrd),alocaldir(3,3),
$   drot(2,2),amki(ndir,ndir),amski(ndir,ndir)
character*80 ciname,slname,msname
c
c   real*8 q2,q1,tno,tto,gno,gto
c   real*8 us,uv,ts,tv,cdx,su, sqs
c   real*8 st, usq, uvq, uml, cx, dus, duv
c   real*8 km,zeta,knoc,un,ut,dun,dut
c   real*8 um,xi,xio,ln,lt,ue,dnt
c   real*8 ephi,expi,kap,gm,kap1,ume
c   real*8 ummax,tme,lms,tm
c   real*8 j11,j12,j21,j22,tt,tn
c   real*8 q0,viscN,viscT, uta
c   real*8 pi,dviscN,dviscT
c   logical writeOn, delamOn
c   ! LOGICAL, SAVE :: doOnce
c   writeOn=.false.
c   delamOn=.false.
c   q2=2.d0
c   q1=1.d0
c   q0=0.d0
c   pi=4.d0*atan(1.d0)
c
c
c! -----
c
c   Uinter developed by Brian FitzGibbon - National University of Ireland, Galway
c   email: brian.fitzgibbon@nuigalway.ie
c   Citation:
c   FitzGibbon, B., & McGarry, P. (2020, July 10).
c   Development of a novel test method to investigate
c   mode II fracture and dissection of arteries.
c   https://doi.org/10.31224/osf.io/d3jbr
c! -----
c
c'   !interface strengths in mode i and mode ii
c   tno=props(1)
c   tto=props(2)
c'   !work of separation in mode i and mode ii
c   gno=props(3)
c   gto=props(4)
c'   !initial elastic stiffness
c   km=props(5)
c'   overclosure penalty stiffness
c   knoc=props(6)
c   zeta=props(7)
c!   ocf - overclosure hardening factor
```

```

ocf=props(8)
c! kocs - overclosure hardening sensitivity factor
kocs=props(9)
c
un=rdisp(1)*-1.
us=rdisp(2)
uv=rdisp(3)
ut=sqrt(us*us+uv*uv)
dun=drdisp(1)*-1.
dus=drdisp(2)
duv=drdisp(3)
dut=sqrt(dus*dus+duv*duv)

c      ! Optional "overclosure hardening"
      if(un.lt.q0)then
          tn=un*knoc
c!      ocf is the overclosure factor (eg ocf=1.5 means tto will scale to
tto*1.5)
c!      kocs is the sensitivity
          tto=tto+tto*(ocf-q1)*(q1-exp(((tn*kocs/tno)/km)))
          end if

      ln=tno/km
      lt=tto/km
      ue=lt-ln
      viscN=zeta*tno*dun/dtime /ln
      viscT=zeta*tto*dut/dtime /lt
      dviscN=zeta*tno/dtime/ln
      dviscT=zeta*tto/dtime/lt

c
c' xio is the shaping parameter that describes gm as a function of xi
xio=pi/2.0
c
      if(un.gt.q0)then
          um=sqrt((un*un)+(ut*ut))
      else
          um=abs(ut)
      end if

c
      if (kinc.eq.1)then
          statev(7)=um
      end if

c
c' !calculate mode mixity
      if(um.eq.q0)then
          xi=0.0
          ephi=1.0
      else if(un.le.q0)then
          xi=0.0
          ephi=1.0
      else if(ut.eq.q0)then
          xi=pi/2.0
          ephi=exp(-xi/xio)
      else
          xi=abs(atan(un/abs(ut)))
          ephi=exp(-xi/xio)
      end if

c
      expi=q1-exp(-(pi/2.0)/xio)
c ' !describe how gm changes as a fn of xi
      kap=(gto-gno)/(expi)
      gm=gto-kap*(q1-ephi)
c ' !define the initiation criteria
      kap1=((tto-tno)/km)/(1.0-exp(-(pi/2.0)/xi0))
c' ! ume is the separation magnitude at the elastic limit
      if(un.gt.q0)then

```

```

        ume=(tto/km)-kap1*(1.0-ePhi)
    else
        ume=lt
    end if
c
    dnt=(un**2/ut**2)+1.0
c
c' !update ummax if necessary
    if (um.gt.statev(7)) then
        statev(7)=um
    end if
c' !magnitude of the traction at the elastic limit
    tme=km*ume
c' !parameter lms is based on the integral of tm from ume to um
    lms=(gm/(km*ume))+(ume/2.0)
c
c-----
c
    if (statev(7).lt.ume) then
        tm=km*um
        statev(13)=tme
c' ! dtndun note:: if un is positive then knoc=km
!-----
! new jacobian for 3d - elastic region
!-----
        if(un.le.q0)then
            j11=knoc
        else
            j11=km+dviscN
        end if
        j12=q0
        j13=q0
        j21=q0
        j22=km+dviscT
        j23=q0
        j31=q0
        j32=q0
        j33=km+dviscT
c
    else if (statev(7).ge.ume) then ! softening regime
c
        tm=ume * km * exp(-(statev(7) - ume) / lms) * um / statev(7)
c
        if (abs((tm-statev(13))).gt.(tme*0.2))then
            pnewdt=0.1
            if (writeOn) then
                write(6,*)'NODE=',NODE
                write(6,*)'*** PnewDT=0.1 ***'
                write(6,*)'tmNew-tmOld=',abs((tm-statev(13)))
                write(6,*)'Dtime=',dtime
            end if
        end if
c
        statev(13)=tm
c
c
        usq=sqrt(un ** 2 + us ** 2 + uv ** 2)
        uvq=sqrt(un ** 2 + us ** 2 + ut ** 2)
        sqs=sqrt(us ** 2 + ut ** 2)
        su=1 + un ** 2 / (us ** 2 + uv ** 2)
        uml=(lt - ln) * (0.1D1 - exp(-atan2(un, sqrt(us ** 2 + ut ** 2
&)) / xio))
        st=1 + un ** 2 / (us ** 2 + ut ** 2)
        cx=lt - (lt - ln) / exPI * (0.1D1 - exp(-atan2(un, sqs) /
&xio))
        cdx=uvq - lt + (lt - ln) / exPI * (0.1D1 - exp(-atan2(un, sqs

```

&) / xio))

! new jacobian for 3d - debonding region

```
j11=-km * (lt - ln) / exPI / ut / su / xio * ePhi * exp(-(-ume  
& + usq) / lms) * un / usq + km * ume * (-un / usq + (lt - ln) /  
& exPI / ut / su / xio * ePhi) / lms + (-ume + usq) / lms ** 2 * (-  
&kap / ut / su / xio * ePhi / km / ume + gm / km / ume ** 2 * (lt  
&- ln) / exPI / ut / su / xio * ePhi + (lt - ln) / exPI / ut /  
&su / xio * ePhi / 0.2D1)) * exp(-(-ume + usq) / lms) * un / usq +  
&km * ume * exp(-(-ume + usq) / lms) / usq - km * ume * exp(-(-ume  
&+ usq) / lms) * un ** 2 * (un ** 2 + us ** 2 + uv ** 2) **  
&(-0.3D1 / 0.2D1) +dviscN
```

```
j12=km * (lt - ln) / exPI * (us ** 2 + uv ** 2) ** (-0.3D1 / 0  
&.2D1) * us * un ** 2 / su / xio * ePhi * exp(-(-ume + usq) / lms)  
&/ usq + km * ume * (-0.1D1 / usq * us - (lt - ln) / exPI * (us  
&** 2 + uv ** 2) ** (-0.3D1 / 0.2D1) * us * un / su / xio * ePhi) /  
&lms + (-ume + usq) / lms ** 2 * (kap * (us ** 2 + uv ** 2) ** (-0  
&.3D1 / 0.2D1) * us * un / su / xio * ePhi / km / ume - gm / km /  
&ume ** 2 * (lt - ln) / exPI * (us ** 2 + uv ** 2) ** (-0.3D1 / 0.  
&2D1) * us * un / su / xio * ePhi - (lt - ln) / exPI * (us ** 2 +  
&uv ** 2) ** (-0.3D1 / 0.2D1) * us * un / su / xio * ePhi / 0.2D1)  
&) * exp(-(-ume + usq) / lms) * un / usq - km * ume * exp(-(-ume +  
&usq) / lms) * un * (un ** 2 + us ** 2 + uv ** 2) ** (-0.3D1 / 0.2D  
&1) * us
```

```
j13= km * (lt - ln) / exPI * (us ** 2 + uv ** 2) ** (-0.3D1 / 0  
&.2D1) * uv * un ** 2 / su / xio * ePhi * exp(-(-ume + usq) / lms)  
&/ usq + km * ume * (-0.1D1 / usq * uv - (lt - ln) / exPI * (us  
&** 2 + uv ** 2) ** (-0.3D1 / 0.2D1) * uv * un / su / xio * ePhi) /  
&lms + (-ume + usq) / lms ** 2 * (kap * (us ** 2 + uv ** 2) ** (-0  
&.3D1 / 0.2D1) * uv * un / su / xio * ePhi / km / ume - gm / km /  
&ume ** 2 * (lt - ln) / exPI * (us ** 2 + uv ** 2) ** (-0.3D1 / 0.  
&2D1) * uv * un / su / xio * ePhi - (lt - ln) / exPI * (us ** 2 +  
&uv ** 2) ** (-0.3D1 / 0.2D1) * uv * un / su / xio * ePhi / 0.2D1)  
&) * exp(-(-ume + usq) / lms) * un / usq - km * ume * exp(-(-ume +  
&usq) / lms) * un * (un ** 2 + us ** 2 + uv ** 2) ** (-0.3D1 / 0.2D  
&1) * uv
```

```
j21=- (lt - ln) / exPI / st / xio * exp(-atan2(un, sqrt(us ** 2  
& + ut ** 2)) / xio) * km * exp(-(uvq - lt + (lt - ln) / exPI *  
&(0.1D1 - exp(-atan2(un, sqrt(us ** 2 + ut ** 2)) / xio))) / lms) /  
&uvq * us / ut + (lt - (lt - ln) / exPI * (0.1D1 - exp(-atan2(  
&un, sqrt(us ** 2 + ut ** 2)) / xio))) * km * (-0.1D1 / uvq * un +  
&(lt - ln) / exPI * (us ** 2 + ut ** 2) ** (-0.1D1 / 0.2D1) / st  
&/ xio * exp(-atan2(un, sqrt(us ** 2 + ut ** 2)) / xio)) / lms + (  
&uvq - lt + (lt - ln) / exPI * (0.1D1 - exp(-atan2(un, sqrt(us **  
&2 + ut ** 2)) / xio))) / lms ** 2 * (-kap / ut / su / xio * ePhi  
&/ km / ume + gm / km / ume ** 2 * (lt - ln) / exPI / ut / su /  
&xio * ePhi + (lt - ln) / exPI / ut / su / xio * ePhi / 0.2D1)) *  
&exp(-(uvq - lt + (lt - ln) / exPI * (0.1D1 - exp(-atan2(un, sqrt  
&(us ** 2 + ut ** 2)) / xio))) / lms) * sqrt(us ** 2 + ut ** 2) /  
&uvq * us / ut - (lt - (lt - ln) / exPI * (0.1D1 - exp(-atan2(un  
&, sqrt(us ** 2 + ut ** 2)) / xio))) * km * exp(-(uvq - lt + (lt  
&- ln) / exPI * (0.1D1 - exp(-atan2(un, sqrt(us ** 2 + ut ** 2)) /  
&xio))) / lms) * sqrt(us ** 2 + ut ** 2) * (un ** 2 + us ** 2 + ut  
&** 2) ** (-0.3D1 / 0.2D1) * us / ut * un
```

```
j22= (lt - ln) / exPI / (us ** 2 + ut ** 2) * us ** 2 * un / st  
& / xio * exp(-atan2(un, sqs) / xio) * km * exp(-cdx / lms) / uvq /  
&ut + cx * km * (-0.1D1 / uvq * us - (lt - ln) / exPI * (us **  
&2 + ut ** 2) ** (-0.3D1 / 0.2D1) * us * un / st / xio * exp(-atan2  
&(un, sqs) / xio)) / lms + cdx / lms ** 2 * (kap * (us ** 2 + uv **  
&2) ** (-0.3D1 / 0.2D1) * us * un / su / xio * ePhi / km / ume -  
&gm / km / ume ** 2 * (lt - ln) / exPI * (us ** 2 + uv ** 2) ** (-
```

```

&0.3D1 / 0.2D1) * us * un / su / xio * ePhi - (lt - ln) / exPI *
&(us ** 2 + uv ** 2) ** (-0.3D1 / 0.2D1) * us * un / su / xio * ePhi
&/ 0.2D1)) * exp(-cdx / lms) * sqs / uvq * us / ut + cx * km * exp
&(-cdx / lms) / sqs / uvq * us ** 2 / ut - cx * km * exp(-cdx / lms
&) * sqs * (un ** 2 + us ** 2 + ut ** 2) ** (-0.3D1 / 0.2D1) * us
&** 2 / ut + cx * km * exp(-cdx / lms) * sqs / uvq / ut - cx * km *
&exp(-cdx / lms) * sqs / uvq * us ** 2 * (us ** 2 + uv ** 2) ** (-
&0.3D1 / 0.2D1)+dviscT

```

```

j23= (lt - ln) / exPI / (us ** 2 + ut ** 2) * us ** 2 * un / st
&/ xio * exp(-atan2(un, sqs) / xio) * km * exp(-cdx / lms) / uvq /
&ut + cx * km * (-0.1D1 / uvq * us - (lt - ln) / exPI * (us **
&2 + ut ** 2) ** (-0.3D1 / 0.2D1) * us * un / st / xio * exp(-atan2
&(un, sqs) / xio)) / lms + cdx / lms ** 2 * (kap * (us ** 2 + uv **
&2) ** (-0.3D1 / 0.2D1) * us * un / su / xio * ePhi / km / ume - gm
&/ km / ume ** 2 * (lt - ln) / exPI * (us ** 2 + uv ** 2) ** (-
&0.3D1 / 0.2D1) * us * un / su / xio * ePhi - (lt - ln) / exPI *
&(us ** 2 + uv ** 2) ** (-0.3D1 / 0.2D1) * us * un / su / xio * ePhi
&/ 0.2D1)) * exp(-cdx / lms) * sqs / uvq * us / ut + cx * km * exp
&(-cdx / lms) / sqs / uvq * us ** 2 / ut - cx * km * exp(-cdx / lms
&) * sqs * (un ** 2 + us ** 2 + ut ** 2) ** (-0.3D1 / 0.2D1) * us
&** 2 / ut + cx * km * exp(-cdx / lms) * sqs / uvq / ut - cx * km *
&exp(-cdx / lms) * sqs / uvq * us ** 2 * (us ** 2 + uv ** 2) ** (-
&0.3D1 / 0.2D1)

```

```

j31= -(lt - ln) / exPI / st / xio * exp(-atan2(un, sqs) / xio)
&* km * exp(-cdx / lms) / uvq * uv / ut + cx * km * (-0.1D1 / uvq
&* un + (lt - ln) / exPI / sqs / st / xio * exp(-atan2(un, sqs) /
&xio)) / lms + cdx / lms ** 2 * (-kap / ut / su / xio * ePhi / km
&/ ume + gm / km / ume ** 2 * (lt - ln) / exPI / ut / su / xio *
&ePhi + (lt - ln) / exPI / ut / su / xio * ePhi / 0.2D1)) * exp(-
&cdx / lms) * sqs / uvq * uv / ut - cx * km * exp(-cdx / lms) * sqs
&* (un ** 2 + us ** 2 + ut ** 2) ** (-0.3D1 / 0.2D1) * uv / ut *
&un

```

```

j32= (lt - ln) / exPI / (us ** 2 + ut ** 2) * us * un / st / xio
&* exp(-atan2(un, sqs) / xio) * km * exp(-cdx / lms) / uvq * uv /
&ut + cx * km * (-0.1D1 / uvq * us - (lt - ln) / exPI * (us **
&2 + ut ** 2) ** (-0.3D1 / 0.2D1) * us * un / st / xio * exp(-atan2
&(un, sqs) / xio)) / lms + cdx / lms ** 2 * (kap * (us ** 2 + uv **
&2) ** (-0.3D1 / 0.2D1) * us * un / su / xio * ePhi / km / ume -
&gm / km / ume ** 2 * (lt - ln) / exPI * (us ** 2 + uv ** 2) ** (-
&0.3D1 / 0.2D1) * us * un / su / xio * ePhi - (lt - ln) / exPI *
&(us ** 2 + uv ** 2) ** (-0.3D1 / 0.2D1) * us * un / su / xio * ePhi
&/ 0.2D1)) * exp(-cdx / lms) * sqs / uvq * uv / ut + cx * km * exp
&(-cdx / lms) / sqs / uvq * uv / ut * us - cx * km * exp(-cdx / lms
&) * sqs * (un ** 2 + us ** 2 + ut ** 2) ** (-0.3D1 / 0.2D1) * uv
&/ ut * us - cx * km * exp(-cdx / lms) * sqs / uvq * uv * (us ** 2
&+ uv ** 2) ** (-0.3D1 / 0.2D1) * us

```

```

j33= cx * km * cdx / lms ** 2 * (kap * (us ** 2 + uv ** 2) ** (-0
&.3D1 / 0.2D1) * uv * un / su / xio * ePhi / km / ume - gm / km /
&ume ** 2 * (lt - ln) / exPI * (us ** 2 + uv ** 2) ** (-0.3D1 / 0.
&2D1) * uv * un / su / xio * ePhi - (lt - ln) / exPI * (us ** 2 +
&uv ** 2) ** (-0.3D1 / 0.2D1) * uv * un / su / xio * ePhi / 0.2D1)
&* exp(-cdx / lms) * sqs / uvq * uv / ut + cx * km * exp(-cdx / lms
&) * sqs / uvq / ut - cx * km * exp(-cdx / lms) * sqs / uvq * uv *
&* 2 * (us ** 2 + uv ** 2) ** (-0.3D1 / 0.2D1) + dviscT

```

```

if(un.le.q0)then
  j11=knoc+dviscN
else if(ut.le.q0)then
  j21=q0
  j22=q0
  j23=q0

```

```

        j32=q0
        j33=q0
    end if
c'
    end if

c
    tn=tm*sin(xi)+viscN
    tt=tm*cos(xi)+viscT
    if(un.le.q0)then
        tn=un*knoc+viscN
        j11=knoc+dviscN
    end if
    if(ut.eq.q0)then
        ts=q0
        tv=q0
    else
        ts=tt*(us/ut)
        tv=tt*(uv/ut)
    end if

c
    ddsddr(1,1)=j11
    ddsddr(1,2)=j12
    ddsddr(1,3)=j12
    ddsddr(2,1)=j21
    ddsddr(2,2)=j22
    ddsddr(2,3)=j23
    ddsddr(3,1)=j31
    ddsddr(3,2)=j32
    ddsddr(3,3)=j33

c
    stress(1)=tn*-q1
    stress(2)=ts
    stress(3)=tv

c
    statev(1)=tn
    statev(2)=tt
    statev(3)=ts
    statev(4)=tv
    statev(5)=tm
    statev(6)=un
c! statev(7) is the max displacement achieved
    statev(8)=ut
    statev(9)=us
    statev(10)=uv
    statev(11)=um
    statev(12)=xi

c
    return
end

```

The following UINTER contains the elastic fibrillation CZM formulation presented in Chapter 6. A 2D form is presented here.

Chapter 6: Elastic Fibrillation Cohesive Zone Model (EF-CZM) UINTER:

```

subroutine uinter(stress,ddsddr,amki,amski,flux,ddfddt,ddsddt,
1   ddfddr,statev,sed,sfd,spd,svd,scd,pnewdt,rdisp,drdisp,
2   temp,dtemp,predef,dpred,time,dtime,freqr,ciname,slname,
3   msname,props,coords,alocaldir,drot,area,chrlngth,node,ndir,
4   nstatv,npred,nprops,mcrd,kstep,kinc,kit,linper,lopenclse,
5   lstate,lsvi,lprint)
c
include 'aba_param.inc'
c
dimension stress(ndir),ddsddr(ndir,ndir),flux(2),ddfddt(2,2),
$   ddsddt(ndir,2),ddfddr(2,ndir),statev(nstatv),rdisp(ndir),
$   drdisp(ndir),temp(2),dtemp(2),predef(2,npred),dpred(2,npred),
$   time(2),props(nprops),coords(mcrd),alocaldir(3,3),
$   drot(2,2),amki(ndir,ndir),amski(ndir,ndir)
character*80 ciname,slname,msname
c
real*8 q2,q1,tno,tto,gno,gto
real*8 km,zeta,knoc,un,ut,dun,dut
real*8 um,xi,xio,ln,lt,ue,dnt
real*8 ephi,expi,kap,gm,kap1,ume
real*8 ummax,tme,lms,tm
real*8 j11,j12,j21,j22,tt,tn
real*8 q0,viscN,viscT,uta
real*8 pi,dviscN,dviscT
real*8 ff1,ff2,dft,tft,tfn,kf,dfn
logical writeOn, delamOn
writeOn=.true.
delamOn=.true.
    if (writeOn) then
        write(6,*),' _____ '
    end if
c'! -----
    q2=2.d0
    q1=1.d0
    q0=0.d0
    pi=4.d0*atan(1.d0)
c
c' !interface strengths in mode i and mode ii
    tno=props(1)
    tto=props(2)
c' !work of separation in mode i and mode ii
    gno=props(3)
    gto=props(4)
c' !initial elastic stiffness
    km=props(5)
c' overclosure penalty stiffness
    knoc=props(6)
    zeta=props(7)
    ff1=props(8)
    ff2=props(9)
    dft=props(10)
c
    tft=tto/ff1
    tfn=tno/ff1
    kf=tft/dft
    dfn=tfn/kf
c
un=rdisp(1)*-1.

```

```

ut=rdisp(2)
dun=drdisp(1)*-1.
dut=drdisp(2)
ln=tno/km
lt=tto/km
ue=lt-ln
viscN=(zeta*tno*dun/(dtime*ln))
viscT=(zeta*tto*dut/(dtime*lt))
c
dviscN=zeta*tno/ln/dtime
dviscT=zeta*tto/lt/dtime
c
c   reset parameters if fibrillation started in previous increment
c   if(int(statev(11)).eq.int(1))then
c       tto=tft
c       tno=tfn
c       lt=dft
c       ln=dfn
c       km=kf
c       gno=tfn*dfn/2+gno/ff1/ff2
c       gto=tft*dft/2+gto/ff1/ff2
c   end if

c' xio is the shaping parameter that describes gm as a function of xi
xio=pi/2.0
c
if(un.gt.q0)then
um=sqrt((un*un)+(ut*ut))
else
um=abs(ut)
end if
c
if (kinc.eq.1)then
statev(7)=um
statev(11)=-1
end if
c' !calculate mode mixity
if(um.eq.q0)then
xi=0.0
ephi=1.0
else if(un.le.q0)then
xi=0.0
ephi=1.0
else if(ut.eq.q0)then
xi=pi/2.0
ephi=exp(-xi/xio)
else
xi=abs(atan(un/abs(ut)))
ephi=exp(-xi/xio)
end if
c
expi=q1-exp(-(pi/2.0)/xio)
c ' !describe how gm changes as a fn of xi
kap=(gto-gno)/(expi)
gm=gto-kap*(q1-ephi)
c ' !define the initiation criteria
kap1=((tto-tno)/km)/(1.0-exp(-(pi/2.0)/xi0))
c' ! ume is the separation magnitude at the elastic limit
if(un.gt.q0)then
ume=(tto/km)-kap1*(1.0-ePhi)
else
ume=lt
end if
c
dnt=(un**2/ut**2)+1.0
c' !update ummax if necessary

```

```

        if (um.gt.statev(7)) then
            statev(7)=um
        end if
c' !magnitude of the traction at the elastic limit
tme=km*ume
c' !parameter lms is based on the integral of tm from ume to um
lms=(gm/(km*ume))-(ume/2.0)
c
c----- ELASTIC REGION
c
        if (statev(7).lt.ume) then
            statev(9)=-1
            statev(10)=tme
            tm=km*um
c' ! dtndun note:: if un is positive then knoc=km
            if(un.le.q0)then
                j11=knoc
                j12=q0
                j21=q0
                j22=km
            else
c' dtndun
                j11 =km
                j12 =q0
                j21 = q0
                j22 =km
                end if
c----- DAMAGE REGION
        else if (statev(7).ge.ume) then ! softening regime
c
            tm=ume * km * exp(-(statev(7) - ume) / lms) * um / statev(7)
c
            statev(9)=1
            if (abs((tm-statev(10))).gt.(tme*0.2))then
                pnewdt=0.1
                if (writeOn) then
                    write(6,*)'NODE=',NODE
                    write(6,*)'*** PnewDT=0.1 ***'
                    write(6,*)'tmNew-tmOld=',abs((tm-statev(10)))
                    write(6,*)'Dtime=',dtime
                end if
            end if
c
c first fibrillation increment (non extra cutback implemented for now)
c
            IF(int(statev(11)).eq.int(-1)) THEN
                IF (tm.lt.kf*um) THEN
                    tm=kf*um
                    j11 =kf
                    j12 =q0
                    j21 = q0
                    j22 =kf
                    statev(10)=tme
                    statev(11)=1
                END IF
            END IF
c
            statev(10)=tm
            delamOn=.true.
c
            IF((UM/STATEV(7)).LT.Q1)THEN
                J11= km * ( exp(-(statev(7) - ume) / lms) * um / statev(7))
                J12=Q0
                J21=Q0
                J22= km * ( exp(-(statev(7) - ume) / lms) * um / statev(7))

```

```

ELSE IF((UM/STATEV(7)).GE.Q1)THEN
c' ! dtndun
if (ut.eq.q0)then
j11=q0
j12=q0
j21=q0
j22=q0
else if (un.le.q0)then
j11= knoc
j12=q0
j21=q0
j22=-km * ume * exp(-(-ume + um) / lms) * ut ** 2 / um ** 2 / lms
$ + km * ume * exp(-(-ume + um) / lms) / um - km * ume * exp(-(-ume
$ + um) / lms) * ut ** 2 * (ut ** 2) ** (-0.3D1 / 0.2D1)
else
c'! dtndun
j11=-km * (lt - ln) / exPI / ut / dnt / xio * ePhi * exp(-(-ume
$ + um) / lms) * un / um + km * ume * (- (un / um + (lt - ln) /
$ exPI / ut / dnt / xio * ePhi) / lms + (-ume + um) / lms ** 2 * (-kap
$ / ut / dnt / xio * ePhi / km / ume + gm / km / ume ** 2 * (lt -
$ ln) / exPI / ut / dnt / xio * ePhi + (lt - ln) / exPI / ut /
$ dnt / xio * ePhi / 0.2D1)) * exp(-(-ume + um) / lms) * un / um + km
$ * ume * exp(-(-ume + um) / lms) / um - km * ume * exp(-(-ume + um
$ ) / lms) * un ** 2 * (un ** 2 + ut ** 2) ** (-0.3D1 / 0.2D1)
c ' ! dtndut
j12=km * (lt - ln) / exPI * un ** 2 / ut ** 2 / dnt / xio *
$ ePhi * exp(-(-ume + um) / lms) / um + km * ume * (- (0.1D1 / um * ut
$ - (lt - ln) / exPI * un / ut ** 2 / dnt / xio * ePhi) / lms + (-
$ ume + um) / lms ** 2 * (kap * un / ut ** 2 / dnt / xio * ePhi / km
$ / ume - gm / km / ume ** 2 * (lt - ln) / exPI * un / ut ** 2 /
$ dnt / xio * ePhi - (lt - ln) / exPI * un / ut ** 2 / dnt / xio *
$ ePhi / 0.2D1)) * exp(-(-ume + um) / lms) * un / um - km * ume *
$ exp(-(-ume + um) / lms) * un * (un ** 2 + ut ** 2) ** (-0.3D1 / 0.2
$ D1) * ut
c' ! dttdun
j21=-km * (lt - ln) / exPI / dnt / xio * ePhi * exp(-(-ume +
$ um) / lms) / um + km * ume * (- (un / um + (lt - ln) / exPI / ut /
$ dnt / xio * ePhi) / lms + (-ume + um) / lms ** 2 * (-kap / ut /
$ dnt / xio * ePhi / km / ume + gm / km / ume ** 2 * (lt - ln) /
$ exPI / ut / dnt / xio * ePhi + (lt - ln) / exPI / ut / dnt / xio *
$ ePhi / 0.2D1)) * exp(-(-ume + um) / lms) * ut / um - km * ume *
$ exp(-(-ume + um) / lms) * ut * (un ** 2 + ut ** 2) ** (-0.3D1 / 0.2
$ D1) * un
c' ! dttdut
j22=km * (lt - ln) / exPI * un / ut / dnt / xio * ePhi * exp(-
$ (-ume + um) / lms) / um + km * ume * (- (ut / um - (lt - ln) /
$ exPI * un / ut ** 2 / dnt / xio * ePhi) / lms + (-ume + um) / lms **
$ 2 * (kap * un / ut ** 2 / dnt / xio * ePhi / km / ume - gm / km /
$ ume ** 2 * (lt - ln) / exPI * un / ut ** 2 / dnt / xio * ePhi -
$ (lt - ln) / exPI * un / ut ** 2 / dnt / xio * ePhi / 0.2D1)) *
$ exp(-(-ume + um) / lms) * ut / um + km * ume * exp(-(-ume + um) /
$ lms) / um - km * ume * exp(-(-ume + um) / lms) * ut ** 2 * (un **
$ 2 + ut ** 2) ** (-0.3D1 / 0.2D1)
c
end if
end if
END IF
c
tn=tm*sin(xi)+viscN
tt=tm*cos(xi)+viscT
c
if (un .lt. q0) then ! penalise overclosure through the knoc penalty
stiffness
tn=un*knoc
j11=knoC

```

```

end if
c
if (ut .le. q0) then
  tt=tt * -q1
end if
c
if(kinc.eq.0)then
  tn=q0
  tt=q0
  j11=q0
  j12=q0
  j21=q0
  j22=q0
end if
c
if(un.lt.q0)then
  ddsddr(1,1)=j11
else
  ddsddr(1,1)=j11+dviscN
end if
ddsddr(1,2)=j12
ddsddr(2,1)=j21
ddsddr(2,2)=j22 + dviscT
c
stress(1)=tn*-q1
stress(2)=tt
c
statev(1)=tn
statev(2)=tt
statev(3)=tm
statev(4)=un
statev(5)=ut
statev(6)=sqrt((un*un)+(ut*ut))
statev(8)=xi
c
return
end

```

The following UINTER contains the viscoplastic cohesive zone formulation presented in Chapter 6. A 2D form is presented here.

Chapter 6: Viscoplastic Cohesive Zone Model (VP-CZM) UINTER:

```

subroutine uinter(stress,ddsddr,amki,amski,flux,ddfddt,ddsddt,
1   ddfddr,statev,sed,sfd,spd,svd,scd,pnewdt,rdisp,drdisp,
2   temp,dtemp,predef,dpred,time,dtime,freqr,ciname,slname,
3   msname,props,coords,alocaldir,drot,area,chrlngth,node,ndir,
4   nstatv,npred,nprops,mcrd,kstep,kinc,kit,linper,lopenclse,
5   lstate,lsgi,lprint)
c
include 'aba_param.inc'
c
dimension stress(ndir),ddsddr(ndir,ndir),flux(2),ddfddt(2,2),
$   ddsddt(ndir,2),ddfddr(2,ndir),statev(nstatv),rdisp(ndir),
$   drdisp(ndir),temp(2),dtemp(2),predef(2,npred),dpred(2,npred),
$   time(2),props(nprops),coords(mcrd),alocaldir(3,3),
$   drot(2,2),amki(ndir,ndir),amski(ndir,ndir)
character*80 ciname,slname,msname
c
real*8 q2,q1,tno,tto,gno,gto
real*8 km,zeta,knoc,un,ut,dun,dut
real*8 um,xi,xio,ln,lt,ue,dnt
real*8 ephi,expi,kap,gm,kap1,ume
real*8 ummax,tme,lms,tm,tm1,tm2
real*8 J11,J12,J21,J22,tt,tn
real*8 epr0,m,en,xstress,dsn,dep,sn,trstress,fy,sn0
real*8 sight,ept,sigt,epdott,dsig,depsp,dshr,deprdsh,deprds
    real*8 q0,viscN,viscT, uta,td,xdepsp
real*8 pi,dviscN,dviscT,dTm,cl
real*8 ff2,dft,tft,tfn,kf,dfn
real*8 ff1a,ff1b,dsfm,tfft,tfit,umef,tmefm,tmefi,xrt,xlp
logical write0n, delam0n

    ! if(node.eq.1060)then
    !   write0n=.true.
    ! end if
delam0n=.true.
if (write0n) then
    write(6,*), '_____ '
end if
c
q2=2.d0
q1=1.d0
q0=0.d0
pi=4.d0*atan(1.d0)
c
c' !interface strengths in mode i and mode ii
tno=props(1)
tto=props(2)
c' !work of separation in mode i and mode ii
gno=props(3)
gto=props(4)
c' !initial elastic stiffness
km=props(5)
c' overclosure penalty stiffness
knoc=props(6)
zeta=props(7)
c' Plasticity parameters
ff1a=props(8) ! strength reduction parameter a
ff1b=props(9) ! strength reduction parameter b
ff2=props(10) ! fibrillation energy reduction parameter

```

```

c'      Rate related parameters
      epr0=props(11) ! epsilon p zero
      m=props(12) ! strain rate hardening exponent
      en=props(13) ! epsilon^n similar to initial hardening slope
(smaller=stiffer)

      tfit=tto*ff1a
      tfft=tto*ff1b
      sy0=tto
      sinf=sy0*ff1b
      theta=1.0 !      theta= 1//forward euler
      un=rdisp(1)*-1.
      ut=rdisp(2)
      dun=drdisp(1)*-1.
      dut=drdisp(2)
      dum=sqrt((dun*dun)+(dut*dut))
      statev(16)=dum/dtime
      ln=tno/km
      lt=tto/km
      ue=lt-ln
      viscN=(zeta*tno*dun/(dtime*ln))
      viscT=(zeta*tto*dut/(dtime*lt))

c
      dviscN=zeta*tno/ln/dtime
      dviscT=zeta*tto/lt/dtime

c
c'      xio is the shaping parameter that describes gm as a function of xi
      xio=pi/2.0

c
      if(un.gt.q0)then
        um=sqrt((un*un)+(ut*ut))
      else
        um=abs(ut)
      end if

      if (kinc.eq.1)then
        statev(25)=um
        statev(7)=um
        statev(28)=um
        statev(29)=q0
        statev(9)=-1
        statev(12)=q0
        statev(14)=q0
        statev(27)=q0
        statev(18)=q0
        statev(11)=q0
        tm=q0
      end if

c
c'      !calculate mode mixity
      if(um.eq.q0)then
        xi=0.0
        ephi=1.0
      else if(un.le.q0)then
        xi=0.0
        ephi=1.0
      else if(ut.eq.q0)then
        xi=pi/2.0
        ephi=exp(-xi/xio)
      else
        xi=abs(atan(un/abs(ut)))
        ephi=exp(-xi/xio)
      end if

c
      expi=q1-exp(-(pi/2.0)/xio)
c ' !describe how gm changes as a fn of xi

```

```

kap=(gto-gno)/(expi)
gm=gto-kap*(q1-ephi)
c' !define the initiation criteria
kap1=((tto-tno)/km)/(1.0-exp(-(pi/2.0)/xi0))
c' ! ume is the separation magnitude at the elastic limit
if(un.gt.q0)then
    ume=(tto/km)-kap1*(1.0-ePhi)
else
    ume=lt
end if

c
dnt=(un**2/ut**2)+1.0

c
c' !update ummax if necessary
if(um.gt.statev(28))then
    statev(28)=um
end if

c' !magnitude of the traction at the elastic limit
tme=km*ume

c
c' More plasticity parameters
dft=0.5d0
tfit=tto*ff1a
tfft=tto*ff1b
kfp=(tfft-tfit)/dft
tmefi=km*ume*ff1a ! initial plastic traction
tmefm=km*ume*ff1b ! final plastic traction
umef=(tmefm-tmefi)/kfp

c
c' !parameter lms is based on the integral of tm from ume to um
lms=(gm/(km*ume))-(ume/2.0)
dsfm=lms*ff1b*ff2

c
dsn=q1/en*(sinf-sy0)

c
statev(22)=dum
umCrit=100.d0
if(un.lt.q0)then
    if(writeOn)then
        write(6,*)'overclosing'
    end if
end if

if((statev(7)-um).gt.q0)then
    statev(22)=statev(22)*-q1
end if
statev(26)=statev(22)+statev(26)

if(kinc.eq.1)then
    statev(7)=um
    statev(9)=-1
    statev(10)=tmefm
    statev(17)=q0
    statev(19)=dum
    statev(20)=dut
    statev(21)=dun
    statev(26)=q0
    statev(27)=dum
    sigt=km*statev(27)
    if(dum.eq.q0)then
        sigt=q0
    end if
    statev(12)=sigt
    tm=statev(12)

```

```

    ept=q0 !total plastic strain
    statev(13)=ept

    epdott=q0
    statev(14)=epdott

    depsp=q0

    sight=q0
    statev(15)=sight
else
if(writeOn)then
    write(6,*)'1091 statev(9)=' ,statev(9)
end if
c'    Assign variables from state variables
    sigt=statev(12)
    ept=statev(13)
    epdott=statev(14)
    sight=statev(15)

    td=theta*dtime
    if(sight.eq.q0)then
        deprds=q0
        deprdsh=q0
    else
        deprds=epr0*m*sigt**(m-q1)*sight**(-m)
        deprdsh=-epr0*m*(sigt*sight**(-q1))**m*sight**-q1
    end if

    dshr=(sinf-sy0)/en*exp(-ept/en)
    depsp=(deprds*statev(22)*km*td+dtime*epdott)*(deprds*km*td-
$deprdsh*dshr*td+q1)**-q1

    tol=1.0e-7
    minIter=5
    maxIter=1.0e+4
    res=999
    deps=depsp
    iter=0

if(um.ge.statev(7))then
    if(statev(9).ne.3)then
        do while ((res.ge.tol).or.(iter.le.minIter))
            deps=deps1
            iter=iter+1
            if(iter.ge.maxIter)then
                exit
            end if
            dsignr=km*(statev(22)-deps)
            dsighnr=sy0+(sinf-sy0)*(q1-exp(-(ept+dtime*deps)/en))-sight
            sighnr=sy0+(sinf-sy0)*(q1-exp(-(ept+dtime*deps)/en))
            ff=deps-(q1-theta)*dtime*epdott-theta*dtime*epr0*
$((sigt+dsignr)/(sight+dsighnr))**m
            term1=(sighnr*(-q1*km)-(sigt+dsignr)*(sinf-sy0)/(-q1*en)
$*exp(-(ept+dtime*deps)/en))/(sighnr**q2)
            term2=m*theta*dtime*epr0*((sigt+dsignr)/sighnr)**(m-q1)
            gradff=q1-term2*term1
            deps1=deps-ff/gradff
            if(iter.eq.1)then
                res=999
            else
                res=abs((deps1-deps)/deps)
            end if
        end do
    end if
end do

```

```

        if(iter.ge.maxIter)then
            pnewdt=0.1
        end if

    end if
end if

    depsp=deps1

    if(depsp.gt.dum)then
        if(writeOn)then
            write(6,*)'depsp === dum'
            depsp=dum
        end if

    end if

    if (um.ge.statev(7)) then
        xdepsp=depsp* um/statev(26)
    else
        xdepsp=q0
        depsp=q0
    end if

    if(statev(22).lt.q0)then
        depsp=q0
    end if

    epdott=depsp/dtime

c**
    ept=ept+xdepsp

    if(ept.gt.statev(28))then
        ept=statev(28)
        ! pnewdt=0.1
        if(writeOn)then
            write(6,*)'ept>umMax!'
        end if
    end if

    sight=sy0+(sinf-sy0)*(q1-exp(-ept/en))

    sigt=km*(um-ept)
    statev(12)=sigt
    tm=sigt
    statev(13)=ept
    statev(29)=depsp
    statev(14)=epdott
    statev(15)=sight
    statev(17)=statev(7)-ept

    statev(20)=statev(20)+dut
    statev(21)=statev(21)+dun

end if

c
    if((statev(13).ge.1.e-20).and.(statev(9).eq.-1))then
        statev(9)=1
    end if

    if (statev(22).ne.q0)then
        DTMDDELm=km*(q1-(ept/um))
    else
        DTMDDELm=km
    end if

```

```

if (um.lt.statev(7)) then
  dtmddelm=km
end if
c----- SOFTENING REGIME
  if(statev(12).ge.tmefm)then
    if(kinc.gt.1)then
      if(statev(9).ne.3)then
        statev(9)=3
        statev(11)=um
        statev(18)=tm
      end if
    end if
  end if
  if(statev(9).eq.3)then
    umCrit=statev(11)
    tm=tmefm*exp(-(statev(28)-umCrit)/dsfm)
    dtmddelm=-tmefm/dsfm*exp(-(statev(28)-umCrit)/dsfm)
  end if

  if(um.lt.statev(7))then
    dtmddelm=km
  end if

c
c'   If threshold stress is exceeded enter softening regime
c
c'                                     Assign the critical um
c-----

DTNDUN1=((UN/UM)*(UN/UM))*DTMDDELM
DTNDUN2=((UM*UM)-(UN*UN))/(UM*UM*UM)*tm
DTNDUN=DTNDUN1+DTNDUN2

J11=DTNDUN
! J11=km
c
DTTDUT1=((UT/UM)*(UT/UM))*DTMDDELM
DTTDUT2=((UM*UM)-(UT*UT))/(UM*UM*UM)*TM
DTTDUT=DTTDUT1+DTTDUT2

J22=DTTDUT
! J22=km
c
DTNDUT1=((UT/UM)*(UN/UM))*DTMDDELM
DTNDUT2=((-(UT*UN))/(UM*UM*UM))*TM
DTNDUT=(DTNDUT1+DTNDUT2)

! J12=q0
J12=DTNDUT

c
DTTDUN1=((UN/UM)*(UT/UM))*DTMDDELM
DTTDUN2=((-(UN*UT))/(UM*UM*UM))*TM
DTTDUN=(DTTDUN1+DTTDUN2)

! J21=q0
J21=DTTDUN
! J21=DTNDUT

c-----
statev(7)=um
statev(19)=statev(19)+statev(27)
statev(12)=tm
tn=tm*sin(xi)+viscN
tt=tm*cos(xi)+viscT
c

```

```

if (statev(9).eq.3) then
  if (abs((tm-statev(10))).gt.(tmefm*0.05))then
    pnewdt=0.1
  end if
  statev(10)=tm
end if
c
  if (un .lt. q0) then ! penalise overclosure through the knoc penalty
stiffness
  tn=un*knoc
  j11=knoc
end if
c
  if (ut .le. q0) then
  tt=tt * -q1
end if
c
  if(isnan(J11))then
    J11=q0
  end if
  if(isnan(J12))then
    J12=q0
  end if
  if(isnan(J21))then
    J21=q0
  end if
  if(isnan(J22))then
    J22=q0
  end if

  if(un.lt.q0)then
    ddsddr(1,1)=J11
  else
    ddsddr(1,1)=J11 + dviscN
  end if
  ddsddr(1,2)=J12
  ddsddr(2,1)=J21
  ddsddr(2,2)=J22 + dviscT

  stress(1)=tn*-q1
  stress(2)=tt
c
  statev(1)=tn
  statev(2)=tt
  statev(3)=tm
  statev(4)=un
  statev(5)=ut
  statev(6)=sqrt((un*un)+(ut*ut))
  statev(8)=xi
c
  return
end

```

Chapter 7: The following Python script is used to generate the parameterised idealised aorta presented in Chapter 7. The script receives user input to direct the parameter being perturbed. Optionality to automatically upload files to a server (HPC for example) using SFTP protocol is included.

```
1. from abaqus import *
2. from abaqusConstants import *
3. from numpy import linspace
4. from textRepr import prettyPrint
5. from random import*
6. import part
7. import material
8. import section
9. import assembly
10. import step
11. import interaction
12. import load
13. import mesh
14. import optimization
15. import job
16. import sketch
17. import visualization
18. import connectorBehavior
19. import os
20. import sys
21. import fileinput
22. sys.path.append('C:\\Python27\\Lib\\site-packages')
23. # import paramiko
24. ##
25. fields=(('Arch_Radius','0'),('Wall_Thickness','0'),('Stiffness','0'),('stiffne
ss mismatch','0'),('Layer_Thickness','0'))
26. ArchRadius, WallThickness, Stiffness,LayerStiffness,LayerThickness= (getInputs
(fields=fields,label='Enter 1 in ONE of the boxes below',
27. dialogTitle='What Parameter are you varying?'))
28.
29. SIGMA=[1E-02,5E-03,1E-03,1E-04,1E-05]
30. signame=['1E-2','5E-3','1E-3','1E-4','1E-5']
31. o=0
32. elementsize=0.6
33. SIGM,DELN,DELT,SIGT,ZETA = SIGMA[o],0.3,0.3,SIGMA[o],SIGMA[o]*1E-02
34.
35. if float(ArchRadius)==1.0 and (float(WallThickness)+float(Stiffness)+float(Lay
erStiffness)+float(LayerThickness)==0.0):
36.     print('Varying Arch Radius')
37.     partname='ArchR_SIG'+str(signame[o])+ '_'
38.     arcl = [12.5,17.5,27.5,42.5,62.5]
39.     tube = [2*arcl[0],2*arcl[1],2*arcl[2],2*arcl[3],2*arcl[4]]
40.     rout = [10.0,10.0,10.0,10.0,10.0]
41.     rin = [8.0,8.0,8.0,8.0,8.0]
42.     LE=[0.5,0.5,0.5,0.5,0.5]
43. elif float(WallThickness)==1.0 and (float(ArchRadius)+float(Stiffness)+float(L
ayerStiffness)+float(LayerThickness)==0.0):
44.     print('Varying Wall Thickness')
45.     partname='WallThick_SIG'+str(signame[o])+ '_'
46.     arcl = [30.0,30.0,30.0,30.0,30.0]
47.     tube = [2*arcl[0],2*arcl[1],2*arcl[2],2*arcl[3],2*arcl[4]]
```

```

48.     rout = [9.0,10.0,12.0,14.0,16.0]
49.     rin = [8.0,8.0,8.0,8.0,8.0]
50.     LE=[0.5,0.5,0.5,0.5,0.5]
51.     elif float(Stiffness)==1.0 and (float(ArchRadius)+float(WallThickness)+float(L
ayerStiffness)+float(LayerThickness)==0.0):
52.         print('Varying Stiffness')
53.         partname='Stiffness_SIG'+str(signame[o])+ '_'
54.         arcl = [30.0,30.0,30.0,30.0,30.0]
55.         tube = [2*arcl[0],2*arcl[1],2*arcl[2],2*arcl[3],2*arcl[4]]
56.         rout = [10.0,10.0,10.0,10.0,10.0]
57.         rin = [8.0,8.0,8.0,8.0,8.0]
58.         LE=[0.1,0.2,0.5,1.25,2.5]
59.     elif float(LayerStiffness)==1.0 and (float(ArchRadius)+float(WallThickness)+fl
oat(Stiffness)+float(LayerThickness)==0.0):
60.         print('Varying Layer Stiffness')
61.         partname='stiffness_mismatch_SIG'+str(signame[o])+ '_'
62.         arcl = [30.0,30.0,30.0,30.0,30.0]
63.         tube = [2*arcl[0],2*arcl[1],2*arcl[2],2*arcl[3],2*arcl[4]]
64.         rout = [10.0,10.0,10.0,10.0,10.0]
65.         rin = [8.0,8.0,8.0,8.0,8.0]
66.         LE=[0.5,0.5,0.5,1.25,2.5]
67.     elif float(LayerThickness)==1.0 and (float(ArchRadius)+float(WallThickness)+fl
oat(Stiffness)+float(LayerStiffness)==0.0):
68.         print('Varying Layer Thickness')
69.         partname='Layer_thickness_SIG'+str(signame[o])+ '_'
70.         arcl = [30.0,30.0,30.0,30.0,30.0]
71.         tube = [2*arcl[0],2*arcl[1],2*arcl[2],2*arcl[3],2*arcl[4]]
72.         rout = [10.0,10.0,10.0,10.0,10.0]
73.         rin = [8.0,8.0,8.0,8.0,8.0]
74.         LE=[0.5,0.5,0.5,0.5,0.5]
75.         thick=[0.25,0.375,0.5,0.625,0.75]
76.     else:
77.         raise ValueError('More than one parameter selected')
78.         # print('More than one parameter selected')
79.
80.     ##
81.
82.     diastolic=0.0106657912
83.     systolic=0.0159986868
84.     fields1=(('Torsion', '0'),('Caudal', '0'),('Cranial', '0'),('Anterior', '0'),('Pos
terior', '0'))
85.     Torsion, Caudal, Cranial, Anterior, Posterior= (getInputs(fields=fields1,label
='Enter 1 in ONE of the boxes below',dialogTitle='What Mode of Loading?'))
86.     torque=0.785398
87.     caudal=-30.0
88.     cranial=30.0
89.     anterior=-30.0
90.     posterior=30.0
91.     modelName='Model-1'
92.
93.     jobname=partname
94.     cutbacks=10.0
95.     ##
96.     ##### Create Step 1 - Pressure
97.     mdb.models[modelName].StaticStep(name='Step-1', previous='Initial',
98.         maxNumInc=100000, initialInc=0.25, minInc=1e-11, maxInc=0.5, nlgeom=ON)
99.     mdb.models[modelName].steps['Step-
100.     1'].control.setValues(allowPropagation=OFF,
101.         resetDefaultValues=OFF, timeIncrementation=(4.0, 8.0, 9.0, 16.0, 10.0, 4.0
,
102.         12.0, cutbacks, 6.0, 3.0, 50.0))
103.     ##### Create Step 2 - Torque
104.     mdb.models[modelName].StaticStep(name='Step-2', previous='Step-1',
105.         maxNumInc=100000, initialInc=0.05, minInc=1e-11, maxInc=0.1, nlgeom=ON)
106.     mdb.models[modelName].steps['Step-
2'].control.setValues(allowPropagation=OFF,

```

```

106.     resetDefaultValues=OFF, timeIncrementation=(4.0, 8.0, 9.0, 16.0, 10.0, 4.0
    ,
107.     12.0, cutbacks, 6.0, 3.0, 50.0))
108. ## Create Field Output and History Output
109. try:
110.     mdb.models[modelname].fieldOutputRequests['F-Output-
111.     1'].setValues(variables=(
112.         'S', 'LE', 'U', 'RF', 'COORD'))
113.     mdb.models[modelname].historyOutputRequests['H-Output-
114.     1'].setValues(variables=(
115.         'ALLIE', 'ALLKE', 'ALLSE', 'ETOTAL'))
116. except:
117.     print('!!!!!!!!!!!!!!!!!!!!!!!!!!!!!!!!!!!!!!!!!!!!!!!!!!!!!!!!!!!!!!!!!!!!!!
118.     !!!!!!!!!!!!!!!!!!!!!!!!!!!!!!!!!!!!!!!!!!!!!!!!!!!!!!!!!!!!!!!!!!!!!!!')
119.     print('_____no field output created_____')
120.     print('!!!!!!!!!!!!!!!!!!!!!!!!!!!!!!!!!!!!!!!!!!!!!!!!!!!!!!!!!!!!!!!!!!!!!!
121.     !!!!!!!!!!!!!!!!!!!!!!!!!!!!!!!!!!!!!!!!!!!!!!!!!!!!!!!!!!!!!!!!!!!!!!!')
122. # for i in xrange(len(arcl)):
123. #####
124. #####
125. ##### LOOP STARTS #####
126. #####
127. #####
128. for i in range(0,2):
129. # i=2
130. ##### Create Material
131. material='LE'+str(i)
132. mdb.models[modelname].Material(name=material)
133. mdb.models[modelname].materials[material].Elastic(table=((LE[i], 0.45), ))
134.
135. ##### Create Section
136. mdb.models[modelname].HomogeneousSolidSection(name=material, material=mate
137. rial, thickness=None)
138. tol=arcl[i]/(20.0*arcl[i])
139. s = mdb.models[modelname].ConstrainedSketch(name='__sweep__', sheetSize=20
140. 0.0)
141. g, v, d, c = s.geometry, s.vertices, s.dimensions, s.constraints
142. ## Arc length (R) goes here
143. s.ArcByCenterEnds(center=(0.0, 0.0), point1=(arcl[i], 0.0), point2=(-
144. arcl[i], 0.0), direction=COUNTERCLOCKWISE)
145. ## Line length (tube) goes here
146. s.Line(point1=(arcl[i], 0.0), point2=(arcl[i], -tube[i]))
147. s1 = mdb.models[modelname].ConstrainedSketch(name='__profile__', sheetSize
148. =200.0, transform=(1.0, -1.22464679914735e-16, 0.0, -0.0, 0.0, 1.0, -
149. 1.22464679914735e-16, -1.0, -0.0, -25.0, 3.06161699786838e-15, 0.0))
150. g1, v1, d1, c1 = s1.geometry, s1.vertices, s1.dimensions, s1.constraints
151. ## Define the circular profile of the arch, inner diameter and outer diame
152. ter
153. s1.CircleByCenterPerimeter(center=(0.0, 0.0), point1=(rin[i], 0.0))
154. s1.CoincidentConstraint(entity1=v1[0], entity2=g1[2], addUndoState=False)
155.
156. if float(LayerThickness)==1.0 and (float(ArchRadius)+float(WallThickness)+
157. float(Stiffness)+float(LayerStiffness)==0.0):
158.     s1.CircleByCenterPerimeter(center=(0.0, 0.0), point1=(rin[i]+(rout[i]-
159. rin[i])*thick[i], 0.0))
160. else:
161.     s1.CircleByCenterPerimeter(center=(0.0, 0.0), point1=(rin[i]+(rout[i]-
162. rin[i])/2, 0.0))
163. ## Define the part name
164. partnamei=partname+str(i)
165. p = mdb.models[modelname].Part(name=partnamei, dimensionality=THREE_D, typ
166. e=DEFORMABLE_BODY)
167. p.BaseSolidSweep(sketch=s1, path=s)
168. ## Define the job name
169. jobnamei=partnamei

```

```

152.     ## Create Datum Planes
153.     p.DatumPlaneByPrincipalPlane(principalPlane=XYPLANE, offset=0.0)
154.     p.DatumPlaneByPrincipalPlane(principalPlane=YZPLANE, offset=0.0)
155.     p.DatumPlaneByPrincipalPlane(principalPlane=XZPLANE, offset=0.0)
156.     d1 = p.datums
157.     ## Create Principal Axes
158.     p = mdb.models[modelname].parts[partnamei]
159.     p.DatumAxisByPrincipalAxis(principalAxis=ZAXIS)
160.     p = mdb.models[modelname].parts[partnamei]
161.     p.DatumAxisByPrincipalAxis(principalAxis=XAXIS)
162.     p = mdb.models[modelname].parts[partnamei]
163.     p.DatumAxisByPrincipalAxis(principalAxis=YAXIS)
164.     ## Create Set for Part
165.     p = mdb.models[modelname].parts[partnamei]
166.     c = p.cells
167.     region = p.Set(cells=c, name='Set-1')
168.     ## Assign Section
169.     p = mdb.models[modelname].parts[partnamei]
170.     p.SectionAssignment(region=region, sectionName=material, offset=0.0, offsetType=MIDDLE_SURFACE, offsetField='', thicknessAssignment=FROM_SECTION)
171.     ## Place Instance in The assembly
172.     a = mdb.models[modelname].rootAssembly
173.     p = mdb.models[modelname].parts[partnamei]
174.     a.Instance(name=partnamei, part=p, dependent=ON)
175.     ## Partition the Geometry
176.     p = mdb.models[modelname].parts[partnamei]
177.     c = p.cells
178.     p.PartitionCellByPlaneThreePoints(cells=c, point1=(arcl[i],0.0,0.0), point2=(-arcl[i],0.0,0.0), point3=(-arcl[i],-arcl[i],0.0))
179.     p = mdb.models[modelname].parts[partnamei]
180.     c = p.cells
181.     p.PartitionCellByPlaneThreePoints(cells=c, point1=(0.0,0.0,arcl[i]), point2=(0.0,0.0,-arcl[i]), point3=(arcl[i],0.0,-arcl[i]))
182.     p = mdb.models[modelname].parts[partnamei]
183.     c = p.cells
184.     p.PartitionCellByPlaneThreePoints(cells=c, point1=(0.0,0.0,arcl[i]), point2=(0.0,0.0,-arcl[i]), point3=(0.0,arcl[i],-arcl[i]))
185.     ## create cylindrical coordinate systems
186.     # root
187.     a.DatumCsysByThreePoints(name='root'+str(i), coordSysType=CYLINDRICAL, origin=(-arcl[i], 0.0, 0.0), point1=(-arcl[i],0.0,rin[i]), point2=(-arcl[i]+rin[i],0.0,0.0))
188.     #dia
189.     a.DatumCsysByThreePoints(name='dia'+str(i), coordSysType=CYLINDRICAL, origin=(arcl[i], -tube[i], 0.0), point1=(arcl[i], -tube[i], rin[i]), point2=(arcl[i]+rin[i], -tube[i], 0.0))
190.     ## Assign Element Type
191.     p = mdb.models[modelname].parts[partnamei]
192.     elemType1 = mesh.ElemType(elemCode=C3D8R, elemLibrary=STANDARD, kinematicSplit=AVERAGE_STRAIN, secondOrderAccuracy=OFF, hourglassControl=ENHANCED, distortionControl=DEFAULT)
193.     elemType2 = mesh.ElemType(elemCode=C3D8R, elemLibrary=STANDARD, kinematicSplit=AVERAGE_STRAIN, secondOrderAccuracy=OFF, hourglassControl=ENHANCED, distortionControl=DEFAULT)
194.     p = mdb.models[modelname].parts[partnamei]
195.     c = p.sets['Set-1']
196.     p.setElementType(regions=c, elemTypes=(elemType1,elemType2))
197.     ## Assign Mesh controls and Mesh The Part
198.     ## Seed the edges
199.     p = mdb.models[modelname].parts[partnamei]
200.     seedededge=p.edges.getClosest(coordinates=((-arcl[i]-((rout[i]-rin[i])/2-rin[i]+tol,0.0,(0.0)),(-arcl[i]+((rout[i]-rin[i])/2+rin[i]-tol),0.0,(0.0))),)
201.     p.seedPart(size=(elementsiz+((2.5*i)/arcl[i])), deviationFactor=0.1, minSizeFactor=0.1)
202.     edges= []

```

```

205.     for key in seededge:
206.         edges.append(seededge[key][0])
207.         p.seedEdgeByNumber(edges=edges,number=2)
208.         # Less seed for the lower tube
209.         # topseed=p.edges.getClosest(coordinates=(((-
arcl[i],0.0,rin[i]+0.25*(rout[i]-rin[i])+tol),(-arcl[i],0.0,-rin[i]-
0.25*(rout[i]-rin[i])))))
210.         # topseeds =[]
211.         # for key in topseed:
212.             # topseeds.append(topseed[key][0])
213.             # p.seedEdgeByNumber(edges=topseeds,number=25)
214.             # tubeedges=p.edges.getByBoundingBox(xMin=0.0,yMin=-2*tube[i],zMin=-
2*arcl[i],xMax=2*arcl[i],yMax=-tol,zMax=2*arcl[i])
215.             # p.seedEdgeBySize(edges=tubeedges,size=elementsSize)
216.             # p.seedEdgeByNumber(edges=tubeedges,number=25)
217.             p.generateMesh()
218.             ## Find all lumen faces and include the outer ones
219.             a = mdb.models[modelname].rootAssembly
220.             s1 = a.instances[partnamei].faces
221.             oneface=s1.getClosest(coordinates=((-arcl[i]-sqrt((rout[i]**2)/2-
(tol)),(tol),(sqrt((rout[i]**2)/2+(tol))),),),)
222.             r=oneface[0][0]
223.             t=r.getFacesByFaceAngle(20.0)
224.             a.Surface(side1Faces=t, name='Inner'+str(i))
225.
226.             #####
227.             ##### Create Second part #####
228.             #####
229.             if float(LayerStiffness)==1.0 and (float(ArchRadius)+float(WallThickness)+
float(Stiffness)==0.0):
230.                 material='OuterMedia'+str(i)
231.                 mdb.models[modelname].Material(name=material)
232.                 mdb.models[modelname].materials[material].Elastic(table=((LE[-i-
1], 0.45), ))
233.                 ##### Create Section
234.                 mdb.models[modelname].HomogeneousSolidSection(name=material, material=
material, thickness=None)
235.             else: print('Layers will have equal stiffness')
236.             s = mdb.models[modelname].ConstrainedSketch(name='__sweep__1', sheetSize=2
00.0)
237.             g, v, d, c = s.geometry, s.vertices, s.dimensions, s.constraints
238.             ## Arc length (R) goes here
239.             s.ArcByCenterEnds(center=(0.0, 0.0), point1=(arcl[i], 0.0), point2=(-
arcl[i], 0.0), direction=COUNTERCLOCKWISE)
240.             ## Line length (tube) goes here
241.             s.Line(point1=(arcl[i], 0.0), point2=(arcl[i], -tube[i]))
242.             s1 = mdb.models[modelname].ConstrainedSketch(name='__profile__1', sheetSiz
e=200.0, transform=(1.0, -1.22464679914735e-16, 0.0, -0.0, 0.0, 1.0, -
1.22464679914735e-16, -1.0, -0.0, -25.0, 3.06161699786838e-15, 0.0))
243.             g1, v1, d1, c1 = s1.geometry, s1.vertices, s1.dimensions, s1.constraints
244.             ## Define the circular profile of the arch, inner diameter and outer diame
ter
245.             if float(LayerThickness)==1.0 and (float(ArchRadius)+float(WallThickness)+
float(Stiffness)+float(LayerStiffness)==0.0):
246.                 s1.CircleByCenterPerimeter(center=(0.0, 0.0), point1=(rin[i]+((rout[i]
-rin[i])*thick[i]), 0.0))
247.             else:
248.                 print('Layers will have equal thickness')
249.                 s1.CircleByCenterPerimeter(center=(0.0, 0.0), point1=(rin[i]+((rout[i]
-rin[i])/2), 0.0))
250.                 s1.CoincidentConstraint(entity1=v1[0], entity2=g1[2], addUndoState=False)
251.                 s1.CircleByCenterPerimeter(center=(0.0, 0.0), point1=(rout[i], 0.0))

```

```

252.     ## Define the part name
253.     pouter=partnamei+'_outer'
254.     p = mdb.models[modelname].Part(name=pouter, dimensionality=THREE_D, type=D
EFORMABLE_BODY)
255.     p.BaseSolidSweep(sketch=s1, path=s)
256.     ## Define the job name
257.     jobnamei=pouter
258.     ## Create Datum Planes
259.     p.DatumPlaneByPrincipalPlane(principalPlane=XYPLANE, offset=0.0)
260.     p.DatumPlaneByPrincipalPlane(principalPlane=YZPLANE, offset=0.0)
261.     p.DatumPlaneByPrincipalPlane(principalPlane=XZPLANE, offset=0.0)
262.     d1 = p.datums
263.     ## Create Principal Axes
264.     p = mdb.models[modelname].parts[pouter]
265.     p.DatumAxisByPrincipalAxis(principalAxis=ZAXIS)
266.     p = mdb.models[modelname].parts[pouter]
267.     p.DatumAxisByPrincipalAxis(principalAxis=XAXIS)
268.     p = mdb.models[modelname].parts[pouter]
269.     p.DatumAxisByPrincipalAxis(principalAxis=YAXIS)
270.     ## Create Set for Part
271.     p = mdb.models[modelname].parts[pouter]
272.     c = p.cells
273.     region = p.Set(cells=c, name='Set-1')
274.     ## Assign Section
275.     p = mdb.models[modelname].parts[pouter]
276.     p.SectionAssignment(region=region, sectionName=material, offset=0.0, offse
tType=MIDDLE_SURFACE, offsetField='', thicknessAssignment=FROM_SECTION)
277.     ## Place Instance in The assembly
278.     a = mdb.models[modelname].rootAssembly
279.     p = mdb.models[modelname].parts[pouter]
280.     a.Instance(name=pouter, part=p, dependent=ON)
281.     ## Partition the Geometry
282.     p = mdb.models[modelname].parts[pouter]
283.     c = p.cells
284.     p.PartitionCellByPlaneThreePoints(cells=c,point1=(arcl[i],0.0,0.0), point2
=(-arcl[i],0.0,0.0), point3=(-arcl[i],-arcl[i],0.0))
285.     p = mdb.models[modelname].parts[pouter]
286.     c = p.cells
287.     p.PartitionCellByPlaneThreePoints(cells=c,point1=(0.0,0.0,arcl[i]), point2
=(0.0,0.0,-arcl[i]), point3=(arcl[i],0.0,-arcl[i]))
288.     p = mdb.models[modelname].parts[pouter]
289.     c = p.cells
290.     p.PartitionCellByPlaneThreePoints(cells=c,point1=(0.0,0.0,arcl[i]), point2
=(0.0,0.0,-arcl[i]), point3=(0.0,arcl[i],-arcl[i]))
291.     ## Find all lumen faces and exclude the outer ones
292.     a = mdb.models[modelname].rootAssembly
293.     s1 = a.instances[pouter].faces
294.     oneface=s1.getClosest(coordinates=((-arcl[i]-
sqrt((rin[i]**2)/2+(tol)),(tol),(sqrt((rin[i]**2)/2+(tol))))),),)
295.     r=oneface[0][0]
296.     t=r.getFacesByFaceAngle(20.0)
297.     a.Surface(side1Faces=t, name='Outer'+str(i))
298.     ## Assign Element Type
299.     p = mdb.models[modelname].parts[pouter]
300.     elemType1 = mesh.ElemType(elemCode=C3D8R, elemLibrary=STANDARD, kinematicS
plit=AVERAGE_STRAIN, secondOrderAccuracy=OFF, hourglassControl=ENHANCED, disto
rtionControl=DEFAULT)
301.     elemType2 = mesh.ElemType(elemCode=C3D8R, elemLibrary=STANDARD, kinematicS
plit=AVERAGE_STRAIN, secondOrderAccuracy=OFF, hourglassControl=ENHANCED, disto
rtionControl=DEFAULT)
302.     p = mdb.models[modelname].parts[pouter]
303.     c = p.sets['Set-1']
304.     p.setElementType(regions=c, elemTypes=(elemType1,elemType2))
305.     ## Assign Mesh controls and Mesh The Part
306.     ## Seed the edges
307.     p = mdb.models[modelname].parts[pouter]

```

```

308.     p.seedPart(size=(elementsize+((2.5*i)/arcl[i])), deviationFactor=0.1, minS
sizeFactor=0.1)
309.     seedededge=p.edges.getClosest(coordinates=(((-arcl[i]-rout[i]+0.25*(rout[i]-
rin[i]),0.0,0.0),(-arcl[i]+rout[i]-0.25*(rout[i]-rin[i]),0.0,0.0))))
310.     edges= []
311.     for key in seedededge:
312.         edges.append(seedededge[key][0])
313.     # p.seedEdgeBySize(edges=edges,size=elementsize*0.5)
314.     # Less seed for the lower tube
315.     # topseed=p.edges.getClosest(coordinates=(((-arcl[i],0.0,rout[i]),(-
arcl[i],0.0,-rout[i]))))
316.     # topseeds =[]
317.     # for key in topseed:
318.         # topseeds.append(topseed[key][0])
319.     p.seedEdgeByNumber(edges=edges,number=2)
320.     # p.seedEdgeByNumber(edges=topseeds,number=25)
321.     # tubeedges=p.edges.getByBoundingBox(xMin=0.0,yMin=-2*tube[i],zMin=-
2*arcl[i],xMax=2*arcl[i],yMax=-tol,zMax=2*arcl[i])
322.     # p.seedEdgeByNumber(edges=tubeedges,number=25)
323.     # p.seedEdgeBySize(edges=tubeedges,size=elementsize)
324.     p.generateMesh()
325.     #####
#####
326.     ##### WORK IN THE ASSEMBLY #####
#####
327.     #####
#####
328.     ## ----- ARCH NODE SETS OUTER -----
329.     allnodes mdb.models['Model-1'].parts[pointer].nodes
330.     arch=[]
331.     archlabel=[]
332.     posZ=[]
333.     posZset=[]
334.     negZ=[]
335.     k=0
336.     j=0
337.     # Find all nodes in the upper left quadrant
338.     for eachnode in allnodes:
339.         coords=allnodes[k].coordinates
340.         if not (coords[1]<=0.0 or coords[0]>=0.0):
341.             arch.append(allnodes[k])
342.             archlabel.append(allnodes[k].label)
343.             k=k+1
344.         else:
345.             k=k+1
346.     # Split those nodes into positive and negative
347.     for everynode in arch:
348.         coords=arch[j].coordinates
349.         if (coords[2]>=0.0):
350.             posZ.append(arch[j].label)
351.         elif(coords[2]<=0.0):
352.             negZ.append(arch[j].label)
353.         j=j+1
354.     p = mdb.models[modelname].parts[pointer]
355.     p.SetFromNodeLabels(name='Arch'+str(i), nodeLabels=archlabel)
356.     p.SetFromNodeLabels(name='posZ'+str(i), nodeLabels=posZ)
357.     p.SetFromNodeLabels(name='negZ'+str(i), nodeLabels=negZ)
358.     ## ----- ARCH NODE SETS INNER -----
359.     allnodes=mdb.models['Model-1'].parts[partnamei].nodes
360.     archinner=[]
361.     archlabelinner=[]
362.     posZinner=[]
363.     posZsetinner=[]
364.     negZinner=[]
365.     k=0
366.     j=0

```

```

367.     # Find all nodes in the upper left quadrant
368.     for eachnode in allnodes:
369.         coords=allnodes[k].coordinates
370.         if not (coords[1]<=0.0 or coords[0]>=0.0):
371.             archinner.append(allnodes[k])
372.             archlabelinner.append(allnodes[k].label)
373.             k=k+1
374.         else:
375.             k=k+1
376.     # Split those nodes into positive and negative
377.     for everynode in archinner:
378.         coords=archinner[j].coordinates
379.         if (coords[2]>=0.0):
380.             posZinner.append(archinner[j].label)
381.         elif(coords[2]<=0.0):
382.             negZinner.append(archinner[j].label)
383.         j=j+1
384.     p = mdb.models[modelname].parts[partnamei]
385.     p.SetFromNodeLabels(name='Arch'+str(i), nodeLabels=archlabelinner)
386.     p.SetFromNodeLabels(name='posZ'+str(i), nodeLabels=posZinner)
387.     p.SetFromNodeLabels(name='negZ'+str(i), nodeLabels=negZinner)
388.     #####
389.     ## Create the Lumen Surface
390.     a = mdb.models[modelname].rootAssembly
391.     s1 = a.instances[partnamei].faces
392.     oneface=s1.getClosest(coordinates=((-arcl[i]-
sqrt((rin[i]**2)/2+(tol)),(tol),(sqrt((rin[i]**2)/2+(tol))))),),)
393.     r=oneface[0][0]
394.     t=r.getFacesByFaceAngle(20.0)
395.     a.Surface(side1Faces=t, name='Lumen'+str(i))
396.     ## Assign Surface for the pressure to act on
397.     a = mdb.models[modelname].rootAssembly
398.     region = a-surfaces['Lumen'+str(i)]
399.     mdb.models[modelname].Pressure(name='Blood Pressure', createStepName='Step
-
1', region=region, distributionType=UNIFORM, field='', magnitude=diastolic, am
plitude=UNSET)
400.     mdb.models[modelname].loads['Blood Pressure'].setValuesInStep(magnitude=sy
stolic, stepName='Step-2')
401.     ## Find the Aortic Root & Create Geometry Set
402.     a = mdb.models[modelname].rootAssembly
403.     # Inner
404.     s1 = a.instances[partnamei].faces
405.     if float(LayerThickness)==1.0 and (float(ArchRadius)+float(WallThickness)+
float(Stiffness)+float(LayerStiffness)==0.0):
406.         rootfaceinner=s1.getClosest(coordinates=((-arcl[i]-rin[i]-((rout[i]-
rin[i])*thick[i])+tol,0.0,tol)),),)
407.     else:
408.         rootfaceinner=s1.getClosest(coordinates=((-arcl[i]-rin[i]-((rout[i]-
rin[i])/2)+tol,0.0,tol)),),)
409.         rr=rootfaceinner[0][0]
410.         tt=rr.getFacesByFaceAngle(20.0)
411.         # Outer
412.         s1 = a.instances[pouter].faces
413.         rootfaceouter=s1.getClosest(coordinates=((-arcl[i]-
rout[i]+tol,0.0,tol)),),)
414.         rrr=rootfaceouter[0][0]
415.         ttt=rrr.getFacesByFaceAngle(20.0)
416.         aaa=tt+ttt
417.         a.Set(faces=aaa, name='Root'+str(i))
418.         a.Surface(side1Faces=aaa, name='Root'+str(i))
419.         ## Find the Root Control Node & slave nodes
420.         p = mdb.models[modelname].parts[pouter].sets['Arch'+str(i)].nodes
421.         tl=0.0001
422.         # Control Node
423.         for eachnode in p:

```

```

424.     if (eachnode.coordinates[0]>=(-arcl[i]-rout[i]-
tol) and eachnode.coordinates[0]<=(-arcl[i]-rout[i]+tol)):
425.         if (eachnode.coordinates[1]>=0.0-
tl and eachnode.coordinates[1]<=0.0+tl):
426.             if (eachnode.coordinates[2]>=0.0-
tl and eachnode.coordinates[2]<=0.0+tl):
427.                 controlnode=eachnode.label
428.                 p = mdb.models[modelname].parts[pouter]
429.                 p.SetFromNodeLabels(name='ROOT_CONTROL'+str(i),nodeLabels=(((controlnode,c
ontrolnode))))
430.                 # Slave nodes
431.                 slavenode=[]
432.                 # outer
433.                 p = mdb.models[modelname].parts[pouter].sets['Arch'+str(i)].nodes
434.                 for eachnode in p:
435.                     if ((eachnode.coordinates[0]<0.0 and eachnode.coordinates[0]!=(-
arcl[i]-rout[i]))):
436.                         if (eachnode.coordinates[1]>=0.0-
tl and eachnode.coordinates[1]<=0.0+tl):
437.                             slavenode.append(eachnode.label)
438.                             p = mdb.models[modelname].parts[pouter]
439.                             p.SetFromNodeLabels(name='ROOT_SLAVE'+str(i),nodeLabels=(((slavenode))))
440.                             # Inner
441.                             slavenodeinner = []
442.                             p = mdb.models[modelname].parts[partnamei].sets['Arch'+str(i)].nodes
443.                             for eachnode in p:
444.                                 if ((eachnode.coordinates[0]<0.0 and eachnode.coordinates[0]!=(-
arcl[i]-rout[i]))):
445.                                     if (eachnode.coordinates[1]>=0.0-
tl and eachnode.coordinates[1]<=0.0+tl):
446.                                         slavenodeinner.append(eachnode.label)
447.                                         p = mdb.models[modelname].parts[partnamei]
448.                                         p.SetFromNodeLabels(name='ROOT_SLAVE'+str(i),nodeLabels=(((slavenodeinner)
)))
449.                                         #####
##### RP for Root
450.                                         ## Create Reference Point and put it in a set
451.                                         mdb.models[modelname].rootAssembly.ReferencePoint(point=(-
arcl[i], 0.0, 0.0))
452.                                         RP=mdb.models[modelname].rootAssembly.referencePoints.findAt((-
arcl[i], 0.0, 0.0),)
453.                                         mdb.models[modelname].rootAssembly.Set(name='RP'+str(i), referencePoints=(
RP, ))
454.                                         ## Hold the Root
455.                                         # Find the correct Datum
456.                                         datum=mdb.models[modelname].rootAssembly.datums
457.                                         k=0
458.                                         for origin in datum.keys():
459.                                             xorigin=datum[datum.keys()[k]].origin.pointOn[0]
460.                                             yorigin=datum[datum.keys()[k]].origin.pointOn[1]
461.                                             if abs(xorigin)==abs(arcl[i]) and yorigin==0.0:
462.                                                 datumroot=datum[datum.keys()[k]]
463.                                                 datumID=origin
464.                                                 k=k+1
465.                                         a = mdb.models[modelname].rootAssembly
466.                                         region = a.sets['RP'+str(i)]
467.                                         if float(Torsion)==1.0 and (float(Caudal)+float(Cranial)+float(Anterior)+f
loat(Posterior))==0.0):
468.                                             mdb.models[modelname].VelocityBC(amplitude=UNSET, createStepName='Step
-1', distributionType=UNIFORM, fieldName='',
469.                                             localCsys=datumroot, name='Root_Hold', region=region, v1=0.0, v2=0.0,
v3=0.0, vr1=0.0, vr2=0.0, vr3=0.0)
470.                                             mdb.models[modelname].boundaryConditions['Root_Hold'].setValuesInStep(
stepName='Step-2', vr3=torque)
471.                                         elif float(Caudal)==1.0 and (float(Torsion)+float(Cranial)+float(Anterior)
+float(Posterior))==0.0):

```

```

472.     mdb.models[modelname].VelocityBC(amplitude=UNSET, createStepName='Step
-1', distributionType=UNIFORM, fieldName='',
473.     localCsys=datumroot, name='Root_Hold', region=region, v1=0.0, v2=0.0,
v3=0.0, vr1=0.0, vr2=0.0, vr3=0.0)
474.     mdb.models[modelname].boundaryConditions['Root_Hold'].setValuesInStep(
stepName='Step-2', v3=caudal)
475.     elif float(Cranial)==1.0 and (float(Torsion)+float(Caudal)+float(Anterior)
)+float(Posterior)==0.0):
476.     mdb.models[modelname].VelocityBC(amplitude=UNSET, createStepName='Step
-1', distributionType=UNIFORM, fieldName='',
477.     localCsys=datumroot, name='Root_Hold', region=region, v1=0.0, v2=0.0,
v3=0.0, vr1=0.0, vr2=0.0, vr3=0.0)
478.     mdb.models[modelname].boundaryConditions['Root_Hold'].setValuesInStep(
stepName='Step-2', v3=cranial)
479.     elif float(Anterior)==1.0 and (float(Torsion)+float(Caudal)+float(Cranial)
)+float(Posterior)==0.0):
480.     mdb.models[modelname].VelocityBC(amplitude=UNSET, createStepName='Step
-1', distributionType=UNIFORM, fieldName='',
481.     localCsys=None, name='Root_Hold', region=region, v1=0.0, v2=0.0, v3=0.
0, vr1=0.0, vr2=0.0, vr3=0.0)
482.     mdb.models[modelname].boundaryConditions['Root_Hold'].setValuesInStep(
stepName='Step-2', v1=anterior)
483.     elif float(Posterior)==1.0 and (float(Torsion)+float(Caudal)+float(Cranial)
)+float(Anterior)==0.0):
484.     mdb.models[modelname].VelocityBC(amplitude=UNSET, createStepName='Step
-1', distributionType=UNIFORM, fieldName='',
485.     localCsys=None, name='Root_Hold', region=region, v1=0.0, v2=0.0, v3=0.
0, vr1=0.0, vr2=0.0, vr3=0.0)
486.     mdb.models[modelname].boundaryConditions['Root_Hold'].setValuesInStep(
stepName='Step-2', v1=posterior)
487.     ## Set up KINEMATIC COUPLING CONSTRAINT between Root and Reference Point
488.     mdb.models[modelname].Coupling(controlPoint=
489.     mdb.models[modelname].rootAssembly.sets['RP'+str(i)], couplingType=KINEMAT
IC,
490.     influenceRadius=WHOLE_SURFACE, localCsys=
491.     mdb.models[modelname].rootAssembly.datums[datumID], name=
492.     'KinematicCouplingConstraint_'+str(i), surface=
493.     mdb.models[modelname].rootAssembly-surfaces['Root'+str(i)], u1=OFF, u2=ON,
u3=ON, ur1=ON, ur2=ON, ur3=ON)
494.
495.     ## Define Self Contact
496.     ## Find the outside surface
497.     a = mdb.models[modelname].rootAssembly
498.     s1 = a.instances[partnamei+'_outer'].faces
499.     oneface=s1.getClosest(coordinates=((-arcl[i]-(2*sqrt((rou[i]**2)/2-
(tol))), (arcl[i]+rou[i]+tol), (sqrt((rou[i]**2)/2+(tol))),),),)
500.     r=oneface[0][0]
501.     t=r.getFacesByFaceAngle(20.0)
502.     a.Surface(side1Faces=t, name='Outside'+str(i))
503.     ## Define self-contact
504.     mdb.models[modelname].ContactProperty('IntProp-'+str(i))
505.     mdb.models[modelname].interactionProperties['IntProp-
'+str(i)].NormalBehavior(allowSeparation=ON, constraintEnforcementMethod=DEFAU
LT, pressureOverclosure=HARD)
506.     mdb.models[modelname].interactionProperties['IntProp-
'+str(i)].TangentialBehavior(formulation=FRICTIONLESS)
507.     mdb.models[modelname].SelfContactStd(createStepName='Step-1',
508.     interactionProperty='IntProp-'+str(i), name='Int-'+str(i), surface=
509.     mdb.models[modelname].rootAssembly-surfaces['Outside'+str(i)], thickness=0
N)
510.     #####
#####
511.     #####
#####
512.     ## Find the Diaphragm & create Geometry Set & Surface
513.     # Inner
514.     a = mdb.models[modelname].rootAssembly

```

```

515.     s1 = a.instances[partnamei].faces
516.     diaface=s1.getClosest(coordinates=((arcl[i]+rin[i]-((rout[i]-rin[i])/2),-
tube[i]-(tol),2*(tol))),),)
517.     rr=diaface[0][0]
518.     tt=rr.getFacesByFaceAngle(20.0)
519.     # Outer
520.     s1 = a.instances[pouter].faces
521.     diafaceouter=s1.getClosest(coordinates=((arcl[i]+rout[i]-((rout[i]-
rin[i])*0.25),-tube[i]-(tol),2*(tol))),),)
522.     rrr=diafaceouter[0][0]
523.     ttt=rrr.getFacesByFaceAngle(20.0)
524.     aaa=tt+ttt
525.     a.Set(faces=aaa, name='Dia'+str(i))
526.     a.Surface(side1Faces=aaa, name='Dia'+str(i))
527.     ## Create Reference Point and put it in a set
528.     mdb.models[modelname].rootAssembly.ReferencePoint(point=(arcl[i], -
tube[i], 0.0))
529.     RP=mdb.models[modelname].rootAssembly.referencePoints.findAt((arcl[i], -
tube[i], 0.0),)
530.     mdb.models[modelname].rootAssembly.Set(name='RP_dia'+str(i), referencePoin
ts=(RP, ))
531.     ## Hold the Dia
532.     # Find the correct Datum
533.     datum=mdb.models[modelname].rootAssembly.datums
534.     k=0
535.     for datums in datum.keys():
536.         xorigin=datum[datum.keys()[k]].origin.pointOn[0]
537.         yorigin=datum[datum.keys()[k]].origin.pointOn[1]
538.         if abs(xorigin)==abs(arcl[i]) and abs(yorigin)==abs(tube[i]):
539.             datumdia=datum[datum.keys()[k]]
540.             datumdiaID=datums
541.             k=k+1
542.     a = mdb.models[modelname].rootAssembly
543.     region = a.sets['RP_dia'+str(i)]
544.     mdb.models[modelname].VelocityBC(amplitude=UNSET, createStepName='Step-
1', distributionType=UNIFORM, fieldName='', localCsys=datumdia, name='Dia_Hold
', region=region, v1=0.0, v2=0.0, v3=0.0, vr1=0.0, vr2=0.0, vr3=UNSET)
545.     ## Set up KINEMATIC COUPLING CONSTRAINT between Dia and Reference Point
546.     mdb.models[modelname].Coupling(controlPoint=
547.     mdb.models[modelname].rootAssembly.sets['RP_dia'+str(i)], couplingType=KIN
EMATIC,
548.     influenceRadius=WHOLE_SURFACE, localCsys=
549.     mdb.models[modelname].rootAssembly.datums[datumdiaID], name=
550.     'KinematicCouplingConstraint_dia'+str(i), surface=
551.     mdb.models[modelname].rootAssembly-surfaces['Dia'+str(i)], u1=OFF, u2=ON,
u3=ON, ur1=ON, ur2=ON, ur3=ON)
552.     #####
553.     ## Supress Previous Instance and Features
554.     if i>0:
555.         mdb.models[modelname].rootAssembly.features['root'+str(i-
1)].suppress()
556.         mdb.models[modelname].rootAssembly.features['dia'+str(i-
1)].suppress()
557.         mdb.models[modelname].rootAssembly.features[partname+str(i-
1)].suppress()
558.         mdb.models[modelname].rootAssembly.features[partname+str(i-
1)+'_outer'].suppress()
559.         mdb.models['Model-
1'].constraints['KinematicCouplingConstraint_'+str(i-1)].suppress()
560.         mdb.models['Model-
1'].constraints['KinematicCouplingConstraint_dia'+str(i-1)].suppress()
561.         mdb.models['Model-1'].interactions['Int-'+str(i-1)].suppress()
562.     ## Create & write Inp File
563.     myJob = mdb.Job(name=jobnamei, model=modelname, description='', type=ANALY
SIS,
564.         atTime=None, waitMinutes=0, waitHours=0, queue=None, memory=80,

```

```

565.         memoryUnits=PERCENTAGE, getMemoryFromAnalysis=False,
566.         explicitPrecision=SINGLE, nodalOutputPrecision=SINGLE, echoPrint=OFF,
567.         modelPrint=OFF, contactPrint=OFF, historyPrint=OFF,
568.         scratch='', multiprocessingMode=MPI, numCpus=4,
569.         numDomains=4, numGPUs=0)
570.     mdb.jobs[jobnamei].writeInput(consistencyChecking=OFF)
571.     ##### Define the Cohesive Behaviour between surfaces ####
572.     #####
573.     ##### The Expression being put into the input file f
or cohesive zone model #####
574.     slave='Inner'+str(i)
575.     master='Outer'+str(i)
576.     InputExpression = (
577.         '''*CONTACT PAIR, INTERACTION=user
578.     '''
579. +str(slave)+','+str(master)+
580.     '''
581. *surface interaction, name=user, user, properties=5,unsymm,DEPVAR=11
582. 1.,
583. ''' +str(SIGM)+' '+str(DELN)+' '+str(DELT)+' '+str(SIGT)+' '+str(ZETA))
584.     InputExpression1 = (
585.         '''*Contact Output
586. SDV'''
587.         check = False
588.         check1 = False
589.         for line in fileinput.input(jobnamei+'.inp', inplace=1):
590.             if line.startswith('** STEP: Step-1'):
591.                 check = True
592.             else:
593.                 if check:
594.                     print InputExpression
595.                     check = False
596.                 if line.startswith('** HISTORY OUTPUT:'):
597.                     check1 = True
598.                 else:
599.                     if check1:
600.                         print InputExpression1
601.                         check1 = False
602.                         print line,
603.             # Submit Job and wait for completion
604.             # myJob.submit()
605.             # print('job submitted')
606.             # myJob.waitForCompletion()
607.             # print('job completed')
608.             # os.system('abaqus j='+jobname+' inp='+jobname+' cpus=4 int')
609.             print('All Models Created Successfully')
610. ##-----
611. ##
612. ## Upload inp files to ICHEC
613. ##-----
614. ## Prompt user to choose to upload inp files to server or not
615. input = (getWarningReply('Upload inp Files to ICHEC?:', (YES,NO,CANCEL)))
616. if input ==YES:
617.     print('Now Uploading inp files to ICHEC')
618.     myhost='Fionn.ichec.ie'
619.     myusername='BrianFitz'
620.     mypassword='purplemonkeydishwasher'
621.     myport=22
622.     ## open ssh Transport
623.     ssh = paramiko.SSHClient()

```

```

623.     localpath='C:\\Users\\11424912\\Documents\\Abaqus\\AortaGeom\\sb3c\\'+pout
er+str(i)+'_outer.inp'
624.     hostpath='/ichec/work/ngeng069b/BrianFitz/aorta_geom/parastudy/'+partname+
str(i)+'_outer.inp'
625.     # Allow the client to auto accept any host]
626.     ssh.set_missing_host_key_policy(paramiko.AutoAddPolicy())
627.     ssh.connect(myhost, myport, myusername, mypassword)
628.     transport = paramiko.Transport((myhost, myport))
629.     transport.connect(username=myusername, password=mypassword)
630.     # Open secure file transfer protocol
631.     sftp = paramiko.SFTPClient.from_transport(transport)
632.     sftp.chdir('/ichec/work/ngeng069b/BrianFitz/aorta_geom/parastudy')
633.     ## Loop through inp files and upload to ICHEC
634.     for i in xrange(5):
635.         sftp.put(localpath, hostpath)
636.         print(hostpath,localpath)
637.     try:
638.         hostpath='/ichec/work/ngeng069b/BrianFitz/aorta_geom/parastudy/'+jobna
me+'.PBS'
639.         localpath='C:\\Users\\11424912\\Documents\\Abaqus\\AortaGeom\\ParaStud
y\\'+jobname+'.PBS'
640.         sftp.put(localpath, hostpath)
641.         print('PBS File Uploaded')
642.     except:
643.         print('no PBS file not uploaded')
644. elif input == NO:
645.     print('Files will not be uploaded to ICHEC \nCompleted')
646. elif input == CANCEL:
647.     import delete
648.     Print ('Parts being deleted...')
649. ##-----

```

The following MATLAB and Python scripts form the basis of the residual stress optimisation scheme outlined in Chapter 7.

MATLAB Master Residual stress script.

```

%% Residual Stress Optimisation Scheme
% Optimise residual stress simulations by calling python script to interact
% with abaqus
cd('F:\Abaqus\ResidualStress\2019\BilinearModel\')
format long

%% Set path and file names
openingAngles= [140 155 170 185 200 215 230 245 260 275];
initialGuesses=[63.842559533998440 93.387194337455900 1.966288787633876e+02
750 1.422032248493601e+02...
83.783682990592440 56.594397435287455 43.827333426426080
34.848090624497370 29.636465932971113];
for i=1:length(openingAngles)
% i=1;
openingAngle=openingAngles(i);
%Define working directory
defaultFolder='F:\Abaqus\ResidualStress\2019\BilinearModel\';
savePath=fullfile(defaultFolder);

% Defining file names
abaqusInpFileNamePart=['OpeningAngle_ifea_',num2str(openingAngle)];
abaqusInpFileName=fullfile(savePath,[abaqusInpFileNamePart, '.inp']); %INP
file name
abaqusDATFileName=fullfile(savePath,[abaqusInpFileNamePart, '.dat']); %DAT
file name
umatScriptName='umat_BL_BL_Dispersion_AxialGeom_January2020';

%% write initial guess to text file for python to read in
xInitial=initialGuesses(i);
P(i)=xInitial;
pythonInputInitial=fopen('data_in.txt','w');
fprintf(pythonInputInitial,'%f',xInitial);
fclose(pythonInputInitial);

%% Define parameter bounds for optimisation
parameterBounds=[P(i)/5 P(i)*5];
%%
runMode=2;
optimizationMethod=2;
addMaterial=1; % 1 = user-defined material // 0 = no UMAT
%% What should be known to the objective function:
objectiveStruct.parNormFactors=P(i); %This will normalize the parameters to
ones(size(P))
objectiveStruct.Pb_struct.xx_c=P(i); %Parameter constraining centre
objectiveStruct.Pb_struct.xxlim=parameterBounds; %Parameter bounds
objectiveStruct.method=optimizationMethod;
objectiveStruct.plotOn=1;
objectiveStruct.abaqusInpFileName=abaqusInpFileName;
objectiveStruct.abaqusDATFileName=abaqusDATFileName;
objectiveStruct.umatScriptName=umatScriptName;
objectiveStruct.abaqusInpFileNamePart=abaqusInpFileNamePart;
objectiveStruct.i=i;
objectiveStruct.addMaterial=addMaterial;
Pn=P(i)./objectiveStruct.parNormFactors; %Normalize parameters

%Optimisation settings
maxNumberIterations=100; %Maximum number of optimization iterations

```

```

maxNumberFunctionEvaluations=maxNumberIterations*100; %Maximum number of
function evaluations, N.B. multiple evaluations are used per iteration
functionTolerance=1; %Tolerance on objective function value
parameterTolerance=1; %Tolerance on parameter variation
displayTypeIterations='iter';
% optimizationPlotOn=1;

%% Do the optimization
switch runMode
case 1 %Test, run once and view output
    [F_opt,outputStruct]=objectiveFunction_Cube(Pn,objectiveStruct);
    Pn_opt=Pn;
case 2 % STARTING OPTIMISATION

    switch objectiveStruct.method
    case 1 %fminsearch and Nelder-Mead
        OPT_options=optimset('fminsearch'); % 'Nelder-Mead simplex
direct search'
        OPT_options =
optimset(OPT_options,'MaxFunEvals',maxNumberFunctionEvaluations,...
        'MaxIter',maxNumberIterations,...
        'TolFun',functionTolerance,...
        'TolX',parameterTolerance,...
        'Display',displayTypeIterations,...
        'FinDiffRelStep',1e-3,...
        'DiffMaxChange',0.5);
        [Pn_opt,OPT_out.fval,OPT_out.exitflag,OPT_out.output]=
fminsearch(@(Pn)
objectiveFunctionResidualStressRun(Pn,objectiveStruct),Pn,OPT_options);
    case 2 %lsqnonlin and Levenberg-Marquardt
        OPT_options =
optimoptions(@lsqnonlin,'Algorithm','levenberg-marquardt');
        OPT_options =
optimoptions(OPT_options,'MaxFunEvals',maxNumberFunctionEvaluations,...
        'MaxIter',maxNumberIterations,...
        'TolFun',functionTolerance,...
        'TolX',parameterTolerance,...
        'Display',displayTypeIterations,...
        'FinDiffRelStep',1e-3,...
        'DiffMaxChange',0.5);

[Pn_opt(i),OPT_out(i).resnorm,OPT_out(i).residual,OPT_out(i).iterations]=
lsqnonlin(@(Pn)
objectiveFunctionResidualStressRun(Pn,objectiveStruct),Pn,[],[],OPT_options
);
        end

[F_opt(i),outputStruct(i)]=objectiveFunctionResidualStressRun(Pn_opt(i),obj
ectiveStruct);
end

%% Unnormalize and constrain parameters

P_opt(i)=Pn_opt(i).*objectiveStruct.parNormFactors; %Scale back, undo
normalization

disp_text=sprintf('%6.16e,',P_opt(i)); disp_text=disp_text(1:end-1);
disp(['P_opt=',disp_text]);

close all
end

```

Objective Function:

```
function
[F_opt,outputStruct]=objectiveFunctionResidualStressRun(Pn,objectiveStruct)

%% Unnormalize and constrain parameters
P=Pn.*objectiveStruct.parNormFactors; %Scale back, undo normalization
P_in=P; %Proposed P

%Constraining parameters
for q=1:1:numel(P)

[P(q)]=boxconstrain(P(q),objectiveStruct.Pb_struct.xxlim(q,1),objectiveStruct.Pb_struct.xxlim(q,2),objectiveStruct.Pb_struct.xx_c(q));
end

disp('-----');
disp('SETTING MATERIAL PARAMETERS...');
disp(['Proposed (norm.): ',sprintf(repmat('%6.16e ', [1,numel(Pn)]),Pn)]);
disp(['Proposed      : ',sprintf(repmat('%6.16e ', [1,numel(P_in)]),P_in)]);
disp(['Set (constr.)   : ',sprintf(repmat('%6.16e ', [1,numel(P)]),P)]);
disp('-----');

%% Get data from structure
abaqusInpFileName=objectiveStruct.abaqusInpFileName;
[savePath,abaqusInpFileNamePart,~]=fileparts(abaqusInpFileName);
abaqusMSGFileName=fullfile(savePath,[abaqusInpFileNamePart,'.msg']); %DAT
file name
umatScriptName=objectiveStruct.umatScriptName;
[savePath,abaqusInpFileNamePart,~]=fileparts(abaqusInpFileName);
abaqusDATFileName=fullfile(savePath,[abaqusInpFileNamePart,'.dat']); %DAT
file name
i=objectiveStruct.i;
addMaterial=objectiveStruct.addMaterial;

%%
lockFileName=fullfile(savePath,[abaqusInpFileNamePart,'.lck']);
if exist(lockFileName,'file')
    warning('Lockfile found and deleted!')
    delete(lockFileName);
end

pythonInput=fopen('data_in.txt','w');
fprintf(pythonInput,'%f',P);
fclose(pythonInput);

% Python script to generate base inp file and modify with user material and
% node print
runString0=['abaqus cae script=ResidualStress_opt_inputFileOnly.py --
',num2str(i-1)...
', ' ',num2str(addMaterial)];
system(runString0);

%% Run the job

compilerPath='"C:\Program Files
(x86)\IntelSWTools\compilers_and_libraries_2016.0.110\windows\bin\ifortvars
.bat"';
runDirectory='F:/Abaqus/ResidualStress/2019/BilinearModel/';

runString=['C:\Windows\system32\cmd.exe /K "',compilerPath,' intel64 vs2013
& cd=',runDirectory,...
' & abaqus j=',abaqusInpFileNamePart,'
inp=',abaqusInpFileNamePart,...
' user=',umatScriptName,' cpus=4 int & exit"'];
```

```

system(runString);

%% Import and visualize abaqus results
% Importing the abaqus .dat file
%
optionStruct.getElementData=1;
[abaqusData]=importAbaqusDat(abaqusDATFileName,optionStruct);

%% Check if ABAQUS terminated with an error
%Load DAT file into cell array
T=txtfile2cell(abaqusMSGFileName);
errorDetectTarget='***ERROR: THE ANALYSIS HAS BEEN TERMINATED';
logicErrorLines = ~cellfun(@isempty, regexp(T,errorDetectTarget));

%% Compute objective function
if ~any(logicErrorLines) %If the job runs successfully...

% Define Difference vector for objective function

% D=importdata('data_out.dat');
% diameter=importdata('diameter.dat');
diameter=abs(abaqusData.STEP.INCREMENT(end).nodeOutput(1).data.COOR2-...
    abaqusData.STEP.INCREMENT(end).nodeOutput(2).data.COOR2);

targetD=30.0;
area=pi*(diameter/2)^2;
targetArea=pi*(targetD/2)^2;
pct_error=(abs(diameter-targetD)/targetD)*100;
difference=targetArea-area;
D=(abs(difference)/targetArea);
F_opt=D;
outputStruct.D=D;
outputStruct.pct_error=pct_error;
outputStruct.P=P;
figure(1)
hold all
plot(P,pct_error,'o','LineWidth',2.5)
xlabel('Radius (mm)')
ylabel('% Error')
% ylim([0 0.5]); xlim([targetD*0.8 targetD*1.2]);

disp('-----');
disp(['Percentage Error: ',sprintf('%6.16f ',pct_error)]);
disp('-----');

if objectiveStruct.plotOn==1

    r=diameter/2;
    currentArea=pi*(r^2);
    rTarget=targetD/2;
    hold on
    ang=0:pi/30:2*pi;
    xCurrent=r*cos(ang);
    yCurrent=r*sin(ang);

    xTarget=rTarget*cos(ang);
    yTarget=rTarget*sin(ang);

    close(figure(2))
    figure(2)
    hold on
    plot(xCurrent,yCurrent,'-^k','MarkerFaceColor','k');
    plot(xTarget,yTarget,'-or');
    legend('Calculated','Target')

```

```
figure(3)
categories=categorical({'Target Area','Current Area'});
bar(categories,[targetArea currentArea])
ylabel('Area (mm^2)')
end
else
    F_opt=[1000];
    outputStruct=0;
end
```

The following python script is called by the objective function with updated input parameters from the optimisation scheme.

Python Model Builder Script:

```

1.  ## This Objective funtion for optimisation of residual stress calculations
2.  ## Author:: Brian FitzGibbon 02/05/2019
3.  from abaqus import *
4.  from abaqusConstants import *
5.  import sys
6.
7.  def ResidualStress_opt_inputFileOnly(argv):
8.      import os, sys, inspect
9.      import __main__
10.     import section
11.     import regionToolset
12.     import displayGroupMdbToolset as dgm
13.     import part
14.     import material
15.     import assembly
16.     import step
17.     import interaction
18.     import load
19.     import mesh
20.     import optimization
21.     import job
22.     import sketch
23.     import visualization
24.     import xyPlot
25.     import displayGroupOdbToolset as dgo
26.     import connectorBehavior
27.     import fileinput
28.     sys.argv[-2]=int(sys.argv[-2])
29.     sys.argv[-1]=int(sys.argv[-1])
30.     print("i= " , (sys.argv[-2]))
31.     i=sys.argv[-2]
32.     addMaterial=sys.argv[-
1] #receive command from matlab to add material or not. 0=not. 1=add
33.     print("addMaterial= " ,addMaterial)
34.     openingAngle=[140,155,170,185,200,215,230,245,260,275]
35.     meshSize=0.3
36.     mdb=openMdb(pathName='F:/Abaqus/ResidualStress/2019/BilinearModel/openingA
ngles_
37.     +str(openingAngle[i])+'.cae')
38.
39.     os.chdir('F:/Abaqus/ResidualStress/2019/BilinearModel/')
40.     input_file=open('data_in.txt','r')
41.     input_data=float(input_file.read())
42.     input_file.close()
43.
44.     Pn=input_data
45.     targetD=30.0
46.     targetArea=pi*(targetD/2)**2
47.     tol=targetArea*0.01
48.
49.     ## EDITING THE SKETCHES
50.     # MAIN GEOMETRY SKETCH
51.     #OPENING ANGLES
52.     p = mdb.models['Model-2'].parts['Part-1']
53.     s = p.features['Solid extrude-1'].sketch
54.     mdb.models['Model-2'].ConstrainedSketch(name='__edit__', objectToCopy=s)

```

```

55.     s1 = mdb.models['Model-2'].sketches['__edit__']
56.     g, v, d, c = s1.geometry, s1.vertices, s1.dimensions, s1.constraints
57.     s1.setPrimaryObject(option=SUPERIMPOSE)
58.     p.projectReferencesOntoSketch(sketch=s1, upToFeature=p.features['Solid extrude-1'], filter=COPLANAR_EDGES)
59.     s=mdb.models['Model-2'].sketches['__edit__']
60.     s.parameters['OpeningAngle'].setValues(expression=str(openingAngle[i]/2))

61.     s1.unsetPrimaryObject()
62.     p = mdb.models['Model-2'].parts['Part-1']
63.     p.features['Solid extrude-1'].setValues(sketch=s1)
64.     del mdb.models['Model-2'].sketches['__edit__']
65.     p = mdb.models['Model-2'].parts['Part-1']
66.
67.     # INITIAL GUESS
68.     p = mdb.models['Model-2'].parts['Part-1']
69.     s = p.features['Solid extrude-1'].sketch
70.     mdb.models['Model-2'].ConstrainedSketch(name='__edit__', objectToCopy=s)
71.     s1 = mdb.models['Model-2'].sketches['__edit__']
72.     g, v, d, c = s1.geometry, s1.vertices, s1.dimensions, s1.constraints
73.     s1.setPrimaryObject(option=SUPERIMPOSE)
74.     p.projectReferencesOntoSketch(sketch=s1,
75.     upToFeature=p.features['Solid extrude-1'], filter=COPLANAR_EDGES)
76.     s=mdb.models['Model-2'].sketches['__edit__']
77.     s.parameters['InitialGuess'].setValues(expression=str(Pn))
78.     s1.unsetPrimaryObject()
79.     p.features['Solid extrude-1'].setValues(sketch=s1)
80.     del mdb.models['Model-2'].sketches['__edit__']
81.     p = mdb.models['Model-2'].parts['Part-1']
82.     # PARTITION FACE SKETCH
83.     p = mdb.models['Model-2'].parts['Part-1']
84.     s = p.features['loose_face'].sketch
85.     mdb.models['Model-2'].ConstrainedSketch(name='__edit__', objectToCopy=s)
86.     s2 = mdb.models['Model-2'].sketches['__edit__']
87.     g, v, d, c = s2.geometry, s2.vertices, s2.dimensions, s2.constraints
88.     s2.setPrimaryObject(option=SUPERIMPOSE)
89.     p.projectReferencesOntoSketch(sketch=s2, upToFeature=p.features['loose_fac
90.     e'],
91.     filter=COPLANAR_EDGES)
92.     s=mdb.models['Model-2'].sketches['__edit__']
93.     if openingAngle[i]>180:
94.         s.parameters['PartitionFace'].setValues(expression=str(Pn))
95.     else:
96.         s.parameters['PartitionFace'].setValues(expression=str(Pn))
97.     s2.unsetPrimaryObject()
98.     p = mdb.models['Model-2'].parts['Part-1']
99.     p.features['loose_face'].setValues(sketch=s2)
100.    del mdb.models['Model-2'].sketches['__edit__']
101.    p = mdb.models['Model-2'].parts['Part-1']
102.    p.regenerate()
103.    ## BOUNDARY CONDITIONS
104.    setnames=['E3', 'E0', 'E4', 'E6', 'E8', 'E10', 'E12', 'E14', 'E16', 'E19', 'E20']
105.    # v_vals=[3,0,4,6,8,10,12,14,16,19,20]
106.    a = mdb.models['Model-2'].rootAssembly
107.    for j in xrange(len(setnames)):
108.        region = a.sets[setnames[j]]
109.        mdb.models['Model-
110.        2'].boundaryConditions[setnames[j]].setValues(region=region,
111.        u1=-a.sets[setnames[j]].edges[0].pointOn[0][0])
112.    elemType1 = mesh.ElemType(elemCode=C3D8R, elemLibrary=STANDARD,
113.        secondOrderAccuracy=OFF, distortionControl=DEFAULT)
114.    elemType2 = mesh.ElemType(elemCode=C3D6, elemLibrary=STANDARD)
115.    elemType3 = mesh.ElemType(elemCode=C3D4, elemLibrary=STANDARD)
116.    p = mdb.models['Model-2'].parts['Part-1']

```

```

117.     c = p.cells
118.     cells = c.getSequenceFromMask(mask=('[#3 ]', ), )
119.     pickedRegions =(cells, )
120.     p.setElementType(regions=pickedRegions, elemTypes=(elemType1, elemType2,
121.         elemType3))
122.     p = mdb.models['Model-2'].parts['Part-1']
123.     p.deleteMesh()
124.     p = mdb.models['Model-2'].parts['Part-1']
125.     p.seedPart(size=meshSize, deviationFactor=0.1, minSizeFactor=0.1)
126.     p = mdb.models['Model-2'].parts['Part-1']
127.     p.generateMesh()
128.
129.     # ADDITIONAL BOUNDARY CONDITIONS FOR SMALLER OPENING ANGLES
130.
131.     mdb.models['Model-2'].boundaryConditions['mid_hold_inner'].setValues(u2=-
a.sets['Mid_Inner'].edges[0].pointOn[0][1])
132.     mdb.models['Model-2'].boundaryConditions['mid_hold_outer'].setValues(u2=-
a.sets['Mid_Outer'].edges[0].pointOn[0][1])
133.     if addMaterial==1:
134.         mdb.models['Model-
2'].boundaryConditions['mid_hold_inner'].setValuesInStep(stepName='Step-6', u1=(-
15-a.sets['Mid_Inner'].edges[0].pointOn[0][0]))
135.         mdb.models['Model-
2'].boundaryConditions['mid_hold_outer'].setValuesInStep(stepName='Step-6', u1=(-
17-a.sets['Mid_Outer'].edges[0].pointOn[0][0]))
136.
137.
138.
139.     ## RUN THE JOB
140.     jobname='openingAngle_ifea_'+str(openingAngle[i])
141.     mdb.Job(name=jobname, model='Model-2', description='', type=ANALYSIS,
142.         atTime=None, waitMinutes=0, waitHours=0, queue=None, memory=90,
143.         memoryUnits=PERCENTAGE, getMemoryFromAnalysis=True,
144.         explicitPrecision=SINGLE, noda1OutputPrecision=SINGLE, echoPrint=0
FF,
145.         modelPrint=OFF, contactPrint=OFF, historyPrint=OFF, userSubroutine
='',
146.         scratch='', resultsFormat=ODB, multiprocessingMode=DEFAULT, numCpu
s=1,
147.         numGPUs=0)
148.     mdb.jobs[jobname].writeInput(consistencyChecking=OFF)
149.
150.     print('Inp File Written')
151.     ## ADD USER MATERIAL AND NODE PRINT SECTIONS TO THE INP
152.     if addMaterial==1:
153.         p=[0.15,0.9,0.075,0.5, 4.0, 1.515152,0.16,4.5,
154.         0.4,0.5,2.0,2, 28.5 ,15.0]
155.         InputExpression0 = ( '''*Solid Section, elset=Set-1, orientation=Ori-
1, controls=EC-1, material=BilinearModel \n''' )
156.         InputExpression = (
157.             '''*Section Controls, name=EC-1, hourglass=ENHANCED
158. 1., 1., 1.
159. **
160. *Material, name=BilinearModel
161. *Depvar
162. 8,
163. *User Material, constants=14
164. ''' +str(p[0])+', '+str(p[1])+', '+str(p[2])+', '+str(p[3])+', '+str(p[4])+', '+str(
p[5])+', '+str(p[6])+', '+str(p[7])
165.         +'\n'+str(p[8])+', '+str(p[9])+', '+str(p[10])+', '+str(p[11])+', '+str(p[
12])+', '+str(p[13]))
166.         InputExpression1 = (
167.             '''*Element output
168. SDV
169. *Output, history

```

```

170. *Node print, nset=Top_Node, frequency=1
171. COORD
172. *Node print, nset=Bottom_Node, frequency=1
173. COORD
174. *El print, elset=Mid_Nodes, frequency=1
175. S'''
176.     elif addMaterial==0:
177.         InputExpression0 = (
178.             '''*Solid Section, elset=Set-1, orientation=Ori-1, material=Material-1
179.             '''
180.         )
181.         InputExpression = (
182.             '''*Material, name=Material-1
183.             *Elastic
184.             0.5, 0.45'''
185.         )
186.         InputExpression1 = (
187.             '''*Element output
188.             '''
189.         )
190.         SDV
191.         *Output, history
192.         *Node print, nset=Top_Node, frequency=1
193.         COORD
194.         *Node print, nset=Bottom_Node, frequency=1
195.         COORD
196.         *El print, elset=Mid_Nodes, frequency=1
197.         S'''
198.         check0 = False
199.         check = False
200.         check1 = False
201.         for line in fileinput.input(jobname+'.inp', inplace=1):
202.             if line.startswith('*Solid Section'):
203.                 line=InputExpression0
204.                 check0 = True
205.             else:
206.                 if check0:
207.                     check0 = False
208.                 if line.startswith('*Material, name='):
209.                     check = True
210.                 else:
211.                     if check:
212.                         print InputExpression
213.                     check = False
214.                 # if line.startswith('*Static'):
215.                 #     line='*Static, stabilize, factor=0.0002, allsdtol=0, continue=NO
216.                 \n'
217.                 if line.startswith('*Output, history'):
218.                     check1 = True
219.                 else:
220.                     if check1:
221.                         print InputExpression1
222.                     check1 = False
223.                     print line,
224.             print('Inp File Modified')
225.         mdb.save()
226.         mdb.saveAs(jobname+'.cae')
227.         sys.exit()
228.
229.
230. ResidualStress_opt_inputFileOnly(sys.argv[-1])

```

The following UMAT contains the methodology for implementing residual stress in the idealised aorta model. It is implemented with the BLFM model.

Residual Stress & Bilinear Fibre Model (BLFM) UMAT:

```

SUBROUTINE UMAT(STRESS,STATEV,DDSDDE,SSE,SPD,SCD,
1 RPL,DDSDDT,DRPLDE,DRPLDT,
2 STRAN,DSTRAN,TIME,DTIME,TEMP,DTEMP,PREDEF,DPRED,CMNAME,
3 NDI,NSHR,NTENS,NSTATV,PROPS,NPROPS,COORDS,DROT,PNEWDT,
4 CELENT,DFGRD0,DFGRD1,NOEL,NPT,LAYER,KSPT,KSTEP,KINC)
C
C   INCLUDE 'ABA_PARAM.INC'
C
C   CHARACTER*80 CMNAME
C   DIMENSION STRESS(NTENS),STATEV(NSTATV),
1   DDSDDE(NTENS,NTENS),DDSDDT(NTENS),DRPLDE(NTENS),
2   STRAN(NTENS),DSTRAN(NTENS),TIME(2),PREDEF(1),DPRED(1),
3   PROPS(NPROPS),COORDS(3),DROT(3,3),DFGRD0(3,3),DFGRD1(3,3),
4   DFGRD1_m(3,3)
C
C LOCAL ARRAYS
C -----
C XKIRCH1 - KIRCHHOFF STRESS
C DFP - INCREMENT OF THE PERTURBED DEF. GRAD.
C DFGRD_PERT - PERTURBED DEF. GRAD.
C XKIRCH_PERT - PERTURBED KIRCHHOFF STRESS
C CMJ - (:,:,I,J) COMPONENTS OF MATERIAL JACOBIAN
C CMJVEC - ABOVE IN VECTOR FORM
C ILIST, JLIST - SET OF THE COMPONENTS TO BE PERTURBED UPON
C DUMSTRSS - DUMMY STRESS TENSOR
C -----
C
C   DIMENSION XKIRCH1(3,3), DFP(3,3), DFGRD_PERT(3,3),XKIRCH_PERT(3,3)
1 ,CMJ(3,3), CMJVEC(NTENS), ilist(6), jlist(6), DUMSTRSS(3,3),
1 XMDUM(3,1), XMDUM1(3,1), XI4(2),XBETAR(2),XALPHAR(2)
C   DIMENSION HOOPQ(101,101), AXIALQ(101,101), OAQ(101,101), OA(101)
C   DIMENSION TQ(101,101),RADIALQ(101,101)
C   LOGICAL, SAVE :: doOnce
C   COMMON / DATA_ARRAYS / AXIALQ, HOOPQ, OAQ, OA, TQ, RADIALQ
C
C
C   ARRAYS FOR THE POLAR DECOMPOSITION
C
C   DIMENSION spolF(3,3), spolC(3,3), spolCS(3,3), spolUINV(3,3),
& U(3,3), R(3,3), RT(3,3), VAR(1)
C
C   PARAMETER(ZERO=0.D0, ONE=1.D0, TWO=2.D0, THREE=3.D0, FOUR=4.D0,
1 SIX=6.D0)
C
C -----
C READ IN THE RESIDUAL STRESS RESULTS FILES
C -----
C
doOnce = .FALSE.
call MutexLock( 1 )
IF (.not. doOnce) THEN
OPEN(101,
file="F:\Abaqus\ResidualStress\2019\BilinearModel\Data\Axialq.txt")
READ(101,*) AXIALQ
CLOSE(101)

```

```

C
      OPEN(102,
file="F:\Abaqus\ResidualStress\2019\BilinearModel\Data\Hoopq.txt")
      READ(102,*) HOOPQ
      CLOSE(102)
C
      OPEN(106,
file="F:\Abaqus\ResidualStress\2019\BilinearModel\Data\Radialq.txt")
      READ(106,*) RADIALQ
      CLOSE(106)
C
      OPEN(103,
file="F:\Abaqus\ResidualStress\2019\BilinearModel\Data\OAq.txt")
      READ(103,*) OAQ
      CLOSE(103)
C
      OPEN(104,
file="F:\Abaqus\ResidualStress\2019\BilinearModel\Data\OA.txt")
      READ(104,*) OA
      CLOSE(104)
C
      OPEN(105,
file="F:\Abaqus\ResidualStress\2019\BilinearModel\Data\Tq.txt")
      READ(105,*) TQ
      CLOSE(105)
c
      doOnce = .TRUE.
      END IF
      call MutexUnlock( 1 )
C
C -----
C
C 3D CONTINUUM ELEMENTS
C -----
C
C   NUMBER OF FIBRE FAMILIES
C -----
C
C   NANISO = 2
C
C -----
C
C   MATERIAL PROPERTIES
C -----
C
C   ! Isotropic parameters
      xD1t = PROPS(1)
      xD2t = PROPS(2)
      xE1  = PROPS(3)
      xE2t = PROPS(4)
      xE2c = xE2t
      scale = PROPS(5)
      BulkM = PROPS(6)
C
C   ! Anisotropic parameters
      xE1f = PROPS(7)
      xE2f = PROPS(8)
      xD1f = PROPS(9)
      xD2f = PROPS(10)
      NANISO = PROPS(11)
      iswitch=int(props(12))  !=2 for global, =1 for local
      ALPHAD1 = PROPS(13)    ! mean fiber angle with respect to
circumferential direction
      xbb = PROPS(14)
C
      xP = (xE1f - xE2f)/(2.d0*(xD1f-xD2f))
      xQ = xE1f - (xD1f*(xE1f-xE2f))/(xD1f-xD2f)
      xR = xE1f*xD1f - xP*(xD1f**2.d0) - xQ*xD1f

```

```

C
      XPI = 3.14159265359d0
      XALPHAR(1)= ALPHAD1*XPI/180.d0
      XALPHAR(2)=-XALPHAR(1)
C
      teta=90.0
C!      IF ((KINC.eq.1) .AND. (KSTEP.eq.1)) THEN
C!          xp = COORDS(1)
C!          yp = COORDS(2)
C!          teta = ATAN(-xp/yp)
C!          !a0(1,1) = cos(XALPHAR)*cos(teta)
C!          !a0(1,2) = cos(XALPHAR)*sin(teta)
C!          !a0(1,3) = sin(XALPHAR)
C!          !a0(2,1) = cos(-XALPHAR)*cos(teta)
C!          !a0(2,2) = cos(-XALPHAR)*sin(teta)
C!          !a0(2,3) = sin(-XALPHAR)
C!      ELSE
C!          teta = STATEV(8)
C!          !a0(1,1)=STATEV(9)
C!          !a0(1,2)=STATEV(10)
C!          !a0(1,3)=STATEV(11)
C!          !a0(2,1)=STATEV(12)
C!          !a0(2,2)=STATEV(13)
C!          !a0(2,3)=STATEV(14)
C!      END IF
C
      iter=0
C
C-----
C      POLAR DECOMPOSITION
C-----

      spolF=dfgrd1
      DO J=1,3
          DO I = 1,3
              spolC(I,J)= 0.0D0
              DO K=1,3
                  spolC(I,J)= spolC(I,J) + spolF(K,I)*spolF(K,J)
              ENDDO
          ENDDO
      ENDDO

      DO J=1,3
          DO I=1,3
              spolCS(I,J)= 0.0D0
              DO K=1,3
                  spolCS(I,J)= spolCS(I,J) + spolC(I,K)*spolC(K,J)
              ENDDO
          ENDDO
      ENDDO

      spolC1= spolC(1,1) + spolC(2,2) + spolC(3,3)
      spolC2= 0.5D0 * (spolC1**2.0D0 - (spolCS(1,1)+spolCS(2,2)+
+      spolCS(3,3)))
      spolC3= spolC(1,1) * (spolC(2,2)*spolC(3,3)-spolC(2,3)*spolC(3,2))
      1 +spolC(1,2) * (spolC(2,3)*spolC(3,1)-spolC(2,1)*spolC(3,3))
      2 +spolC(1,3) * (spolC(2,1)*spolC(3,2)-spolC(2,2)*spolC(3,1))
      spolU3= SQRT(spolC3)
      spolX1=2.0**5.0 /27.0*(2.0*spolC1**3.0-9.0*spolC1*spolC2+
      27.0*spolC3)
      spolX2= 2.**10.0 /27.0*(4.0*spolC2**3.0-spolC1**2.0*spolC2**2.0 +
      4.0*spolC1**3.0*spolC3-18.0*spolC1*spolC2*spolC3+27.0*spolC3**2.0)

      IF (spolX2.LT.0.) spolX2= 0.0
      F1= spolX1 + SQRT(spolX2)

```

```

IFLAG2= 0
IFLAG1= 0
IF (F1.LT.0.0) IFLAG1= 1
F2= spolX1 - SQRT(spolX2)
IF (F2.LT.0.0) IFLAG2= 1
IF (IFLAG2.EQ.1) F2= -F2
IF (IFLAG1.EQ.1) F1= -F1
spolX3= -2.0/3.0*spolC1 + F1**(1.0/3.0) + F2**(1.0/3.0)
IF (IFLAG1.EQ.1) spolX3= -2.0/3.0*spolC1 + F2**(1.0/3.0) -
+      F1**(1.0/3.0)
IF (IFLAG2.EQ.1) spolX3= -2.0/3.0*spolC1 + F1**(1.0/3.0) -
+      F2**(1.0/3.0)
B= -2.0*spolC1
IF (spolX3.EQ.B) THEN
U1= SQRT(spolC1+2.0*SQRT(spolC2))
ELSE
U1= 0.5 * (SQRT(2.0*spolC1+spolX3) + SQRT(2.0*spolC1 -
+      spolX3+16.0*SQRT(spolC3)/SQRT(2.0*spolC1+spolX3)))
ENDIF
U2= SQRT(spolC2+2.0*spolU3*U1)
B1= spolU3**2.0 * (spolU3+U1*spolC1) +
&U1**2.0 * (U1*spolC3+spolU3*spolC2)
B2= U1 * (U1*U2-spolU3) / B1
B3=- (U1*U2-spolU3) * (spolU3+U1*spolC1) / B1
B4= (U2*spolU3*(spolU3+U1*spolC1) +
&U1**2.0 * (U2*spolC2+spolC3))/B1

DO J=1,3
DO I=1,3
spolUINV(I,J)= B2*spolCS(I,J) + B3*spolC(I,J)
IF (I.EQ.J) spolUINV(I,J)= spolUINV(I,J) + B4
ENDDO
ENDDO

DO J=1,3
DO I=1,3
R(I,J)=0.0
DO K=1,3
R(I,J)= R(I,J) + spolF(I,K)*spolUINV(K,J)
ENDDO
ENDDO
ENDDO
DO I=1,3
DO J=1,3
RT(I,J) = R(J,I)
ENDDO
ENDDO

U=0.0
DO I=1,3
DO J=1,3
DO M=1,3
!U(I,J)=U(I,J)+RT(I,M)*spolF(M,J) ! old version
U(I,J)=U(I,J)+spolF(I,M)*RT(M,J) ! modified
ENDDO
ENDDO
ENDDO

C
C-----
C CALCULATE THE ROTATED, a_0' VECTORS
C-----
C
IF (iswitch.EQ.1) then
DO IAN = 1,2
!XMDUM(:,1) = XMMAT(:,IAN)
!
! (M, N, L, A, KA, B, KB, C, KC)

```

```

!call KMTMS(3, 3, 1, RT, 3, XMDUM, 3, XMDUM1, 3)
!call KMTMS(3, 3, 1, RT, XMDUM, XMDUM1)
!XMMAT(:,IAN) = XMDUM1(:,1)
END DO
C
write(6,*) '*Orientation is defined!'
C
DFGRD1_m=0.0
DO I=1,3
  DO J=1,3
    DO M=1,3
      DFGRD1_m(I,J)=DFGRD1_m(I,J)+R(I,M)*U(M,J) ! modified
    ENDDO
  ENDDO
ENDDO
!DFGRD1_m = U
C
ELSE IF (iswitch.EQ.2) then
  !XMMAT(:,IAN)=XMMAT(:,IAN)
  DFGRD1_m = DFGRD1
ELSE
  WRITE (6,*) '*** ERROR: Global or local coordinate system must be'
  WRITE (6,*) 'specified in PROPS(15),=1 for local, =2 for global'
  STOP
ENDIF
C
C-----
C ZERO THE TANGENT MATRIX
C-----
C
DO I=1,NTENS
DO J=1,NTENS
  DDSDE(I,J) = ZERO
END DO
END DO
C-----
C CALCULATE THE STRESS
C-----
C
!call kstress_calc(DFGRD1, C10, D1, xA, xB, xP, xQ, xR,
!1 xD1, xD2, xbb, XKIRCH1, XJ1, XALPHAR, XBETAR, NANISO,
!2 XI1, XI2, XI3, XI4)
call kstress_calc(DFGRD1_m,PROPS,NPROPS,NANISO,
1 XKIRCH1,XJ1,XI1,XI2,XI3,XI4,nphase,RT,teta,
2 COORDS, HOOPQ, AXIALQ, OAQ,OA,TQ,RADIALQ)
C
STATEV(1) = XI1
STATEV(2) = XI2
STATEV(3) = XI3
STATEV(4) = XI4(1)
STATEV(5) = XI4(2)
STATEV(6) = XJ1
STATEV(7) = nphase
C
C-----
C CONVERT KIRCHHOFF STRESS TO CAUCHY STRESS
C-----
DUMSTRSS = XKIRCH1 / XJ1

call kmatrix2vector(DUMSTRSS, STRESS, nshr)
C
C-----
C*****
C
C-----

```

```

C CALCULATE THE PERTURBATION OF THE KIRCHHOFF STRESS
C -----
C
C     eps = 1.0e-08
C
C     ilist(1) = 1; ilist(2) = 2; ilist(3) = 3
C     ilist(4) = 1; ilist(5) = 1; ilist(6) = 2
C     jlist(1) = 1; jlist(2) = 2; jlist(3) = 3
C     jlist(4) = 2; jlist(5) = 3; jlist(6) = 3
C
C
C     Perturbation: DO iter = 1,NTENS
C
C         ii = ilist(iter)
C         jj = jlist(iter)
C
C         call kdelf(ii, jj, DFGRD1_m, eps, DFP)
C
C -----
C CREATE THE PERTURBATION OF THE DEFORMATION GRADIENT
C -----
C
C         DFGRD_PERT = DFGRD1_m + DFP
C
C -----
C CALCULATE THE STRESS BASED ON THIS NEW DEFORMATION GRADIENT
C -----
C
C     ! call kstress_calc(DFGRD_PERT, C10, D1, xA, xB, xP, xQ, xR,xD1,
C     !1 xD2, xbb, XKIRCH_PERT, XJP, XALPHAR,XBETAR,
C     !2 NANISO, XI1, XI2, XI3, XI4)
C     call kstress_calc(DFGRD_PERT,PROPS,NPROPS,NANISO,
C     1 XKIRCH_PERT, XJP,XI1,XI2,XI3,XI4,nphase,RT,teta,
C     2 COORDS, HOOPQ, AXIALQ, OAQ,OA,TQ,RADIALQ)
C
C
C -----
C DIFFERENCE BETWEEN THE PERTURBED(i,j) AND UNPERT. STRESS
C -----
C
C     do i = 1,3
C     do j = 1,3
C         CMJ(i,j) = XKIRCH_PERT(i,j) - XKIRCH1(i,j)
C     end do
C     end do
C
C     CMJ = CMJ/XJ1/eps
C
C
C -----
C VECTORISE AND INSERT INTO THE DDSDE MATRIX
C -----
C
C     call kmatrix2vector(CMJ, CMJVEC, NSHR)
C
C     do insert = 1,NTENS
C
C         DDSDE(insert,iter) = CMJVEC(insert)
C
C     end do
C
C     end do Perturbation
C
C     RETURN
C     contains
C

```

```

C-----
C          SUBROUTINES
C-----
C
C * KSTRESS_CALC - Calculate the Kirchhoff stress based on the deformation
C                  gradient and the elastic constants C10 and D1.
C
C * KDELF        - Calculate the increment of the deformation gradient for
C                  a given perturbation in (i,j), with epsilon
C
C * KPRINTER     - Print out a matrix of any size
C
C * KMTMS        - Multiply two 2nd order tensors
C
C * KMATRIX2VECTOR - Convert a 3x3 matrix to a 6x1 vector
C
C * KDOTPROD     - Dot product of two vectors
C-----
C
C      subroutine kstress_calc(DGRAD,PROPS,NPROPS,NANISO,XKIRCH,
1          DET,XI1,XI2,XI3,XI4,nphase,RT,teta,
2          COORDS, HOOPQ, AXIALQ, OAQ,OA,TQ,RADIALQ)
C
C      INCLUDE 'ABA_PARAM.INC'
C
C      intent(in) :: DGRAD, PROPS, NPROPS, NANISO, RT ,teta
C      intent(out):: XKIRCH, DET, XI1, XI2, XI3, XI4, nphase
C
C      dimension DGRAD(3,3), BMAT(3,3), XKIRCH(3,3),
1          B2MAT(3,3),aoa(3,3),RT(3,3),
2          XANISOK(3,3),XANISOTOT(3,3),XI4(NANISO),
3          PROPS(NPROPS)
C
C      parameter(n_phi=20, n_omega=10, nseg = (n_omega-1)*n_phi+1)
C
C      dimension phi_vec(n_phi), omega_vec(n_omega), xm0i(3,1),
1          xn0i_mat(nseg,3), xn0i(3,1), rho_vec(nseg), area_vec(nseg),
2          rot_mat_E2(3,3),rot_mat_E3(3,3),rot_mat(3,3),xm0i_rot(3,1),
3          xn0i_pre_rot(3,1),xn0i_rot(3,1),xn0i_rot_mat(nseg,3),xn1i(3,1),
4          rho_mat(n_omega,n_phi), rot_mat1(3,3)
14          xn0i_rot_vec(3,1),
C
C      DOUBLE PRECISION XMM(3),DUMMY1(3),BBAR(NTENS),BBARP(3),
2          BBARN(3,3),BBARMAT(3,3),XKIRCH1(3,3),STRAIN(3),
3          SBAR(3),Cauchy(3,3), BBARNT(3,3),SISOP(3,3), XALPHAR(2)
C
C      real(8) ::kiso(6),lambda2(3),na(3,3),B_a(3),
1          n11(6),n22(6),n33(6),lambda_bar(3),lambda(3)
C
C      INTEGER:: ROW_IND,COL_IND, i, ii, CNT
C      REAL(8) :: pct_y, pct_t, OA_input, T_input, archCircum,tol
C      REAL(8) :: phi, arcl, pct_arc, xcentreline, ycentreline, zcentreline
C      PARAMETER (propThorax=27.D0,propAbdomen=39.D0)
C      PARAMETER (SIX=6.D0, archR=30.D0, rin=8.D0, rout=10.D0, pi=3.1415926536)
C      PARAMETER (vert=(2*archR),tol=0.5, CNT=1000, pi2=1.570796326794897)
C      DIMENSION RESID(3),COORDS(3)
C      DIMENSION HOOPQ(101,101),AXIALQ(101,101),OAQ(101,101)
C      DIMENSION OA(101),TQ(101,101),RADIALQ(101,101)
C-----
C
C          CALCULATE THE RESIDUAL STRESS
C-----
C
C      IF ((KINC==1).AND.(KSTEP(1)==1)) THEN
C      IF (COORDS(2)<0.0) THEN

```

```

IF (COORDS(1)>0.0) THEN
-----THORACIC AORTA-----
pct_y=NINT((abs(COORDS(2))/vert)*propThorax)+propAbdomen ! 27 and 39
are the proportions of the total arch length of thoracic and
r=sqrt(COORDS(3)**2+(COORDS(1)-archR)**2)
pct_t=NINT(abs((r-rin)/(rout-rin))*100)
OA_input=OA(pct_y)
T_input=pct_t
! WRITE(7,*) 'THORACIC AORTA'
END IF
ELSE
!----- ASCENDING AORTA AND AORTIC ARCH
archCircum=archR*pi
phi=atan2(COORDS(2),COORDS(1)) ! CALCULATE SEGMENT
ANGLE
arc1=abs(((phi*(180/pi))/180)*pi*archR) ! CALCULATE ARC LENGTH
pct_arc=NINT((1-(arc1/archCircum))*propAbdomen) ! CALCULATE THE
PERCENTAGE OF THE AORTIC ARCH
IF (pct_arc==0) THEN
pct_arc=1
END IF
OA_input=OA(pct_arc)
xcentreline=sin(pi2-phi)*archR ! LOCATE THE COORDINATES OF THE
CENTRELINE OF THE ARCH
ycentreline=sin(phi)*archR
zcentreline=ZERO
! DISTANCE BETWEEN CENTRELINE AND INPUT COORDS
dfrmcentre=sqrt((xcentreline-COORDS(1))**2+(ycentreline-
COORDS(2))**2+(zcentreline-COORDS(3))**2)
pct_t=((dfrmcentre-rin)/(rout-rin))*100)
T_input=NINT(pct_t)
! WRITE(7,*) 'ASCENDING AORTA AND AORTIC ARCH'
END IF
!-----
COL_IND=0
ROW_IND=0
i=0
C !-----
C
C
DO WHILE (COL_IND==0)
! i=1,SIZE(Tq,1)
i=i+1
! INDEX THE THICKNESS DATA TABLE BASED OFF OF THE CALCULATED INPUT
IF ((T_input)>(Tq(i,1))-(tol)) THEN
IF ((T_input)<(Tq(i,1))+(tol)) THEN
COL_IND=i
END IF
END IF
END DO
!-----
ii=0
DO WHILE (ROW_IND==0)
! ii=1,SIZE(OAq,1) ! INDEX THE OPENING ANGLE DATA TABLE BASED OFF
OF THE CALCULATED INPUT
ii=ii+1
IF ((OA_input)>(OAq(1,ii))-(7.5*tol)) THEN ! 7.5*tol is a lighter tolerance
(should be replaced)
IF((OA_input)<(OAq(1,ii))+(7.5*tol)) THEN
ROW_IND=ii
END IF
END IF
END DO
!-----
C

```



```

                                BMAT(I,J) = BMAT(I,J) + DGRAD(I,K)*DGRAD(J,K)
                                END DO
                                END DO
                                END DO
C
C-----
C   CALCULATE THE INVARIANTS
C-----
C
C   XI1 = BMAT(1,1)+BMAT(2,2)+BMAT(3,3)
C
C   CALL KMTMS(3, 3, 3, BMAT, BMAT,B2MAT)
C
C   TRB2 = B2MAT(1,1)+B2MAT(2,2)+B2MAT(3,3)
C
C   XI2 = 0.5d0*((XI1**2.d0) - TRB2)
C
C   XI3=BMAT(1, 1)*BMAT(2, 2)*BMAT(3, 3)
1  -BMAT(1, 2)*BMAT(2, 1)*BMAT(3, 3)
2  +BMAT(1, 2)*BMAT(2, 3)*BMAT(3, 1)
3  +BMAT(1, 3)*BMAT(3, 2)*BMAT(2, 1)
4  -BMAT(1, 3)*BMAT(3, 1)*BMAT(2, 2)
5  -BMAT(2, 3)*BMAT(3, 2)*BMAT(1, 1)
C
C-----
C   CALCULATE THE ISOTROPIC PORTION OF THE KIRCH STRESS
C-----
C
C   Bilinear_erf
C
C   par1 = ONE/(DET**(TWO/THREE))
C   BBARMAT = par1*BMAT
C   BBAR(1) = BBARMAT(1,1)
C   BBAR(2) = BBARMAT(2,2)
C   BBAR(3) = BBARMAT(3,3)
C   BBAR(4) = BBARMAT(1,2)
C   BBAR(5) = BBARMAT(1,3)
C   BBAR(6) = BBARMAT(2,3)
C
C   Calculate eigenvalues la2(a) and eigenvectors n_a(3,3) of b
C   (Note: Jacobian algorithm destroys upper triangular components 12,13,23)
C
C   call kDSYEVJ3(BMAT,na,lambda2)
C
C   lambda(1) = lambda2(1)**0.5d0
C   lambda(2) = lambda2(2)**0.5d0
C   lambda(3) = lambda2(3)**0.5d0
C
C   lambda_bar(1) = DET**(-ONE/THREE)*lambda(1)
C   lambda_bar(2) = DET**(-ONE/THREE)*lambda(2)
C   lambda_bar(3) = DET**(-ONE/THREE)*lambda(3)
C
C   DO K=1,3
C       strain(K) = lambda_bar(K) - 1.d0
C   END Do
C
C   Calculate principal 2nd Piola-kirchoff stress
C
C   Do I=1,3
C       if (strain(I) .le. 0.d0) then
C           xD1c = -props(1)
C           xD2c = -props(2)
C       else
C           xD1c = props(1)
C           xD2c = props(2)
C       endif

```

```

C
    xmuc = xD1c + 0.5d0*(xD2c-xD1c)
    xac = xE2c-xE1
    xbc = (xD2c-xD1c)/scale
    xFD1c = erf((xD1c-xmuc)/(xbc*sqrt(2.d0)))
    xFD2c = erf((xD2c-xmuc)/(xbc*sqrt(2.d0)))
    xintfxc= erf((sqrt(2.d0)*(xmuc - strain(I)))/(2.d0*xbc)
&
&
    *exp(-(xmuc-strain(I))**2.d0/(2.d0*xbc**2.d0)))/sqrt(XPI)

    xintfx0c = erf((sqrt(2.d0)*(xmuc-0.d0))/(2.d0*xbc))*
&
&
    exp(-(xmuc - 0.d0)**2.d0/(2.d0*xbc**2.d0)))/sqrt(XPI)
    xintconstc=xac/(xFD2c-xFD1c)*xintfx0c ! constant of integration to force
s=0 at epsilon=0
C
    Sbar(I)=xE1*strain(I)
&
    + xac/(xFD2c-xFD1c)*(xintfxc-xFD1c*strain(I))-xintconstc
    END DO
C
C
    Calculate the stress coefficients B_a
DO J=1,3
    B_a(J) = (Sbar(J) - ONE/THREE*(Sbar(1)+Sbar(2)+Sbar(3)))
END DO
C
C
    Calculate the eigenvector dyadic products (eigenvalue bases)
C
C
    n11
    n11(1) = na(1,1)*na(1,1)
    n11(2) = na(2,1)*na(2,1)
    n11(3) = na(3,1)*na(3,1)
    n11(4) = na(1,1)*na(2,1)
    n11(5) = na(1,1)*na(3,1)
    n11(6) = na(2,1)*na(3,1)
C
    n22
    n22(1) = na(1,2)*na(1,2)
    n22(2) = na(2,2)*na(2,2)
    n22(3) = na(3,2)*na(3,2)
    n22(4) = na(1,2)*na(2,2)
    n22(5) = na(1,2)*na(3,2)
    n22(6) = na(2,2)*na(3,2)
C
    n33
    n33(1) = na(1,3)*na(1,3)
    n33(2) = na(2,3)*na(2,3)
    n33(3) = na(3,3)*na(3,3)
    n33(4) = na(1,3)*na(2,3)
    n33(5) = na(1,3)*na(3,3)
    n33(6) = na(2,3)*na(3,3)
C
    Do k1=1,6
    kiso(k1) = (B_a(1)*n11(k1))+(B_a(2)*n22(k1))+(B_a(3)*n33(k1))
    ENDDO
C
    COEFF3 = BulkM*(DET-ONE)*DET
C
    DO J=1,3
    kiso(J)= kiso(J)+COEFF3
    ENDDO
C
    XKIRCH(1,1)=kiso(1)
    XKIRCH(2,2)=kiso(2)
    XKIRCH(3,3)=kiso(3)
    XKIRCH(1,2)=kiso(4)
    XKIRCH(1,3)=kiso(5)
    XKIRCH(2,3)=kiso(6)
    XKIRCH(2,1)=XKIRCH(1,2)

```

```

XKIRCH(3,1)=XKIRCH(1,3)
XKIRCH(3,2)=XKIRCH(2,3)
C
C-----
C   Set up the fiber dispersion in the local coordinate system
C-----
C
  phi_vec(1)=ZERO

  DO i=2,n_phi
    phi_vec(i)=phi_vec(i-1)+TWO*xpi/n_phi
  END DO
  omega_vec = ZERO

  DO ih=2,n_omega
    omega_vec(ih)=omega_vec(ih-1)+((XPI/TWO)/(n_omega-1))
  END DO
C
  xm0i(1,1) = ZERO
  xm0i(2,1) = ZERO
  xm0i(3,1) = ONE
C
  del_phi = phi_vec(2)-phi_vec(1)
  del_omega = ((xpi/two)*(ONE/(n_omega-1)))
C
  xn0i_mat(1,1)=sin(omega_vec(1))*cos(phi_vec(1))
  xn0i_mat(1,2)=sin(omega_vec(1))*sin(phi_vec(1))
  xn0i_mat(1,3)=cos(omega_vec(1))
C
  area_1 = ((0.5d0*del_omega)**two)*xpi
C
  CALL kPDF3D1(xbb,xm0i,xm0i,xrho_1)
C
  rho_vec(1) = xrho_1
  area_vec(1) = area_1
  rho_mat(1,1:n_phi)=xrho_1
  count = 1
  area_tot = 0.d0
  DO i = 2, n_omega
    DO j = 1, n_phi

      count = count + 1

      xn0i(1,1) = sin(omega_vec(i))*cos(phi_vec(j))
      xn0i(2,1) = sin(omega_vec(i))*sin(phi_vec(j))
      xn0i(3,1) = cos(omega_vec(i))

      xn0i_mat(count,1) = xn0i(1,1)
      xn0i_mat(count,2) = xn0i(2,1)
      xn0i_mat(count,3) = xn0i(3,1)

      if (i<n_omega) then
        area_seg = del_omega*sin(omega_vec(i))*del_phi
      else
        area_seg = del_omega*sin(omega_vec(i))*del_phi*0.5d0
      endif

      area_vec(count) = area_seg
      area_tot = area_tot + area_seg

      CALL kPDF3D1(xbb,xn0i,xm0i,xrho)

      rho_vec(count) = xrho

      rho_mat(i,j) = xrho
    
```

```

        xrho_tot = xrho_tot + xrho*area_seg

        END DO
    END DO

    area_tot = area_tot + area_1
    xrho_tot = xrho_tot + xrho_1*area_1

    xrho_tot_norm = xrho_tot/area_tot
C
C-----
C-----
C    Rotate the fiber dispersion in the local coodinate system to the global
coordinate system
C-----
C-----
C
! Need to rotate M (the local mean fiber direction the distribution is distributed
around)
! so that it maps to A (the global mean fiber direction of the fiber family)
C
!xA0(1,1) = cos(XALPHAR)*cos(teta)
!xA0(1,2) = cos(XALPHAR)*sin(teta)
!xA0(1,3) = sin(XALPHAR)
C
DO I=1,3
DO J=1,3
    XANISOTOT(I,J) = ZERO
END DO
END DO
C
C LOOP OVER THE NO OF FIBRE FAMILIES
C
DO IANISO = 1,NANISO
    rot_mat_E2(1,1) = sin(xalphar(IANISO))
    rot_mat_E2(1,2) = 0.d0
    rot_mat_E2(1,3) = cos(xalphar(IANISO))
    rot_mat_E2(2,1) = 0.d0
    rot_mat_E2(2,2) = 1.d0
    rot_mat_E2(2,3) = 0.d0
    rot_mat_E2(3,1) = -cos(xalphar(IANISO))
    rot_mat_E2(3,2) = 0.d0
    rot_mat_E2(3,3) = sin(xalphar(IANISO))
C
    rot_mat_E3(1,1) = cos(teta)
    rot_mat_E3(1,2) = -sin(teta)
    rot_mat_E3(1,3) = 0.d0
    rot_mat_E3(2,1) = sin(teta)
    rot_mat_E3(2,2) = cos(teta)
    rot_mat_E3(2,3) = 0.d0
    rot_mat_E3(3,1) = 0.d0
    rot_mat_E3(3,2) = 0.d0
    rot_mat_E3(3,3) = 1.d0
C
    call KMTMS (3, 3, 3, rot_mat_E3, rot_mat_E2, rot_mat)
C
    DO i=1,3
        xm0i_rot(i,1) = 0.d0
        DO m=1,3
            xm0i_rot(i,1) = xm0i_rot(i,1)+rot_mat(i,m)*xm0i(m,1)
        END DO
    END DO
C
DO kk=1,nseg
    xn0i_pre_rot(1,1) = xn0i_mat(kk,1)
    xn0i_pre_rot(2,1) = xn0i_mat(kk,2)

```

```

        xn0i_pre_rot(3,1) = xn0i_mat(kk,3)
C
        DO i=1,3
            xn0i_rot(i,1) = 0.d0
            DO m=1,3
                xn0i_rot(i,1) = xn0i_rot(i,1)+rot_mat(i,m)*xn0i_pre_rot(m,1)
            END DO
        END DO
C
C   Calculate the Anisotropic Stress
C
        DO i=1,3
            xn1i(i,1) = 0.d0
            DO m=1,3
                ! Do k=1,3
                xn1i(i,1) = xn1i(i,1) + DGRAD(i,m)*xn0i_rot(m,1)
                ! END DO
            END DO
        END DO
C
        DO I=1,3
            DO J=1,3
                aoa(I,J) = xn1i(I,1)*xn1i(J,1)
            END DO
        END DO
C
        XI_F = aoa(1,1) + aoa(2,2) + aoa(3,3)

        if (kk==1) then
            XI4(IANISO) = XI_F
        endif
C
C-----
C   INSTATE THE TENSION CONDITION
C-----
C
        IF(XI_F>ONE) THEN
C
C   ZERO MATRICES
C
            DO I=1,3
                DO J=1,3
                    xanisok(i,j) = zero
                END DO
            END DO
C
C   CALCULATE THE VARIOUS PARTS OF THE EQUATION FOR KIRCHSTRESS
C
            fibeps = sqrt(XI_F)-1.d0

            if(fibeps<=xD1f)then
                XANISOK = xE1f*fibeps*aoa
                nphase = 1
            elseif (fibeps<=xD2f)then
                XANISOK = (xP*(fibeps**2.d0) + xQ*fibeps + xR)*aoa
                nphase = 2
            else
                XANISOK = (xE2f*(fibeps-xD2f) +
&                (xP*xD2f**2.d0 + xQ*xD2f + xR))*aoa
                nphase = 3
            endif
C
            XANISOTOT = XANISOTOT +
&            (1.d0/xrho_tot)*XANISOK*rho_vec(kk)*area_vec(kk)

        END IF

```

```

C
END DO
C
END DO
C
XKIRCH = XKIRCH + XANISOTOT
! write(6,*)'rot_mat=',rot_mat
! Add the residual stress tensor to the diagonal components of the Kirchoff
stress
IF (KSTEP(1)==1) THEN
XKIRCH(1,1)=XKIRCH(1,1)+(TIME(1)*STATEV(9))
XKIRCH(2,2)=XKIRCH(2,2)+(TIME(1)*STATEV(10))
XKIRCH(3,3)=XKIRCH(3,3)+(TIME(1)*STATEV(11))
ELSE
XKIRCH(1,1)=XKIRCH(1,1)+STATEV(9)
XKIRCH(2,2)=XKIRCH(2,2)+STATEV(10)
XKIRCH(3,3)=XKIRCH(3,3)+STATEV(11)
END IF
return
end subroutine kstress_calc

```

```

subroutine kdelF(m, n, DGRAD, eps, DF)

INCLUDE 'ABA_PARAM.INC'

intent (in) :: DGRAD, eps, m, n
intent (out):: DF

C Input: the index's i & j; The current deformation gradient (DGRAD). The
perturbation
C      increment (eps)
C
C Output: The perturbed increment DF
C
dimension dyad1(3,3), dyad2(3,3), DGRAD(3,3), DF(3,3), DFp1(3,3)

c Zero the dyad matrices
c
do i = 1,3
do j = 1,3
dyad1(i,j) = zero
dyad2(i,j) = zero
end do
end do

C Place the 1's in the correct location
dyad1(m,n) = 1.0
C
dyad2(n,m) = 1.0
C
call KMTMS (3, 3, 3,dyad1, DGRAD, DFp1)
DF = DFp1
C
call KMTMS (3, 3, 3, dyad2,DGRAD, DFp1)
DF = DF + DFp1
C
DF = 0.5*DF*eps
C
end subroutine kdelF

```

```

subroutine kprinter(tens, m, n)

```

```

INCLUDE 'ABA_PARAM.INC'

intent(in):: tens, m, n

dimension tens(m,n)

  write(6,*)
  do i = 1,m
  do j = 1,n
    write(6,'(e19.9)',advance='no'),tens(i,j)
  end do
  write(6,*)
  end do
  write(6,*)
return
end subroutine kprinter
C
C-----

SUBROUTINE KMTMS (M, N, L, A, B, C)
INCLUDE 'ABA_PARAM.INC'
C
  intent(in) :: M, N, L, A, B
  intent(out):: C
C
C
C PRODUCT OF REAL MATRICES
C
  DIMENSION A(M,N), B(N,L), C(M,L)
  DOUBLE PRECISION W
C
C
  DO 30 I = 1,M
    DO 20 J = 1,L
      W = 0.D0
      DO 10 K = 1,N
        W = W + A(I,K) * B(K,J)
10      CONTINUE
      C(I,J) = W
20    CONTINUE
30  CONTINUE
  RETURN
  END SUBROUTINE
C
C-----

subroutine kmatrix2vector(XMAT, VEC, NSHR)

INCLUDE 'ABA_PARAM.INC'

intent(in) :: XMAT, NSHR
intent(out):: VEC

dimension xmat(3,3), vec(6)

  do i=1,3
    vec(i) = xmat(i,i)
  end do

  vec(4) = xmat(1,2)

  IF (NSHR==3) then
    vec(5) = xmat(1,3)
    vec(6) = xmat(2,3)
  END IF

```

```
end subroutine kmatrix2vector
```

C-----

```
subroutine kdotprod(A, B, dotp, n)
```

```
INCLUDE 'ABA_PARAM.INC'
```

```
intent(in) :: A, B, n  
intent(out):: dotp
```

```
dimension A(n), B(n)  
dotp = 0.0
```

```
do i = 1,n  
  dotp = dotp + A(i)*B(i)  
end do
```

```
end subroutine kdotprod
```

C

C-----

C

```
SUBROUTINE kPDF3D1(xbb,xn,xm,xrho)
```

```
INCLUDE 'ABA_PARAM.INC'
```

```
intent(in) :: xbb, xn, xm  
intent(out):: xrho  
dimension xn(3,1), xm(3,1)  
REAL xpar  
XPI = 3.14159265359d0
```

```
xpar = sqrt(2.d0*xbb)  
CALL kerfi1(xpar, xerr)
```

```
xNdotM = xn(1,1)*xm(1,1)+xn(2,1)*xm(2,1)+xn(3,1)*xm(3,1)  
xq1 = 4.d0*(sqrt(xbb/(2.d0*xpi)))  
xq2 = (2.d0*xbb*(xNdotM**2.d0))  
xq3 = exp(xq2)  
xrho = xq1*xq3/xerr
```

```
return  
end subroutine kPDF3D1
```

C

C-----

C

```
subroutine kerfi1(x, xerr1)
```

```
INCLUDE 'ABA_PARAM.INC'  
INTEGER NMAX
```

```
PARAMETER (NMAX=6,H=0.4d0,A1=2.d0/3.d0,A2=0.4d0,A3=2.d0/7.d0)
```

```
INTEGER i,init,n0  
REAL d1,d2,e1,e2,sum,x2,xp,xx,c(NMAX),x  
SAVE init,c  
DATA init/0/
```

```
if(init.eq.0)then  
  init=1  
  do i=1,NMAX  
    c(i)=exp(-((2.d0*float(i)-1.d0)*H)**2.d0)  
  enddo  
endif
```

```
if (abs(x).lt.0.2) then  
  x2=x**2.d0
```

```

        dawson=x*(1.d0-A1*x2*(1.d0-A2*x2*(1.d0-A3*x2)))
    else
        xx=abs(x)
        n0=2*nint(0.5*xx/H)
        xp=xx-float(n0)*H
        e1=exp(2.d0*xp*H)
        e2=e1**2.d0
        d1=float(n0+1)
        d2=d1-2.d0
        sum=0.d0
        do i=1,NMAX
            sum=sum+c(i)*(e1/d1+1.d0/(d2*e1))
            d1=d1+2.d0
            d2=d2-2.d0
            e1=e2*e1
        enddo

        dawson=0.5641895835*sign(exp(-xp**2.d0),x)*sum
    endif

xerr1 = (2.d0/sqrt(XPI))*exp(x**2.d0)*dawson

return
END subroutine kerfi1

```

```

!*****
* -----
* Numerical diagonalization of 3x3 matrcies
* Copyright (C) 2006 Joachim Kopp
* -----
* This library is free software; you can redistribute it and/or
* modify it under the terms of the GNU Lesser General Public
* License as published by the Free Software Foundation; either
* version 2.1 of the License, or (at your option) any later version.
*
* This library is distributed in the hope that it will be useful,
* but WITHOUT ANY WARRANTY; without even the implied warranty of
* MERCHANTABILITY or FITNESS FOR A PARTICULAR PURPOSE. See the GNU
* Lesser General Public License for more details.
*
* You should have received a copy of the GNU Lesser General Public
* License along with this library; if not, write to the Free Software
* Foundation, Inc., 51 Franklin Street, Fifth Floor, Boston, MA 02110-1301 USA
* -----
SUBROUTINE KDSYEVJ3(A, Q, W)
* -----
* Calculates the eigenvalues and normalized eigenvectors of a symmetric 3x3
* matrix A using the Jacobi algorithm.
* The upper triangular part of A is destroyed during the calculation,
* the diagonal elements are read but not destroyed, and the lower
* triangular elements are not referenced at all.
* -----
* Parameters:
* A: The symmetric input matrix
* Q: Storage buffer for eigenvectors
* W: Storage buffer for eigenvalues
* -----
* .. Arguments ..
DOUBLE PRECISION A(3,3)
DOUBLE PRECISION Q(3,3)
DOUBLE PRECISION W(3)
*
* .. Parameters ..
INTEGER N
PARAMETER ( N = 3 )

```

```

*      .. Local Variables ..
      DOUBLE PRECISION SD, SO
      DOUBLE PRECISION S, C, T
      DOUBLE PRECISION G, H, Z, THETA
      DOUBLE PRECISION THRESH
      INTEGER          I, X, Y, R

*      Initialize Q to the identity matrix
*      --- This loop can be omitted if only the eigenvalues are desired ---
      DO 10 X = 1, N
        Q(X,X) = 1.0D0
        DO 11, Y = 1, X-1
          Q(X, Y) = 0.0D0
          Q(Y, X) = 0.0D0
11      CONTINUE
10     CONTINUE

*      Initialize W to diag(A)
      DO 20 X = 1, N
        W(X) = A(X, X)
20     CONTINUE

*      Calculate SQR(tr(A))
      SD = 0.0D0
      DO 30 X = 1, N
        SD = SD + ABS(W(X))
30     CONTINUE
      SD = SD**2

*      Main iteration loop
      DO 40 I = 1, 50
*      Test for convergence
      SO = 0.0D0
      DO 50 X = 1, N
        DO 51 Y = X+1, N
          SO = SO + ABS(A(X, Y))
51      CONTINUE
50     CONTINUE
      IF (SO .EQ. 0.0D0) THEN
        RETURN
      END IF

      IF (I .LT. 4) THEN
        THRESH = 0.2D0 * SO / N**2
      ELSE
        THRESH = 0.0D0
      END IF

*      Do sweep
      DO 60 X = 1, N
        DO 61 Y = X+1, N
          G = 100.0D0 * ( ABS(A(X, Y)) )
          IF ( I .GT. 4 .AND. ABS(W(X)) + G .EQ. ABS(W(X))
             .AND. ABS(W(Y)) + G .EQ. ABS(W(Y)) ) THEN
            A(X, Y) = 0.0D0
          ELSE IF (ABS(A(X, Y)) .GT. THRESH) THEN
*      Calculate Jacobi transformation
            H = W(Y) - W(X)
            IF ( ABS(H) + G .EQ. ABS(H) ) THEN
              T = A(X, Y) / H
            ELSE
              THETA = 0.5D0 * H / A(X, Y)
              IF (THETA .LT. 0.0D0) THEN
                T = -1.0D0 / (SQRT(1.0D0 + THETA**2) - THETA)
              ELSE
                T = 1.0D0 / (SQRT(1.0D0 + THETA**2) + THETA)

```

```

        END IF
    END IF

    C = 1.0D0 / SQRT( 1.0D0 + T**2 )
    S = T * C
    Z = T * A(X, Y)

*      Apply Jacobi transformation
    A(X, Y) = 0.0D0
    W(X)    = W(X) - Z
    W(Y)    = W(Y) + Z
    DO 70 R = 1, X-1
        T    = A(R, X)
        A(R, X) = C * T - S * A(R, Y)
        A(R, Y) = S * T + C * A(R, Y)
70    CONTINUE
    DO 80, R = X+1, Y-1
        T    = A(X, R)
        A(X, R) = C * T - S * A(R, Y)
        A(R, Y) = S * T + C * A(R, Y)
80    CONTINUE
    DO 90, R = Y+1, N
        T    = A(X, R)
        A(X, R) = C * T - S * A(Y, R)
        A(Y, R) = S * T + C * A(Y, R)
90    CONTINUE

*      Update eigenvectors
*      --- This loop can be omitted if only the eigenvalues are desired ---
    DO 100, R = 1, N
        T    = Q(R, X)
        Q(R, X) = C * T - S * Q(R, Y)
        Q(R, Y) = S * T + C * Q(R, Y)
100   CONTINUE
    END IF
61   CONTINUE
60   CONTINUE
40  CONTINUE

    PRINT *, "kDSYEVJ3: No convergence."

    END SUBROUTINE
* End of subroutine kDSYEVJ3
* -----

    END

```